DYNAMICS IN A FERMI LATTICE GAS

BY

WENCHAO XU

DISSERTATION

Submitted in partial fulfillment of the requirements
for the degree of Doctor of Philosophy in Physics
in the Graduate College of the
University of Illinois at Urbana-Champaign, 2018

Urbana, Illinois

Doctoral Committee:

Professor Peter Abbamonte, Chair
Professor Brian DeMarco, Director of Research
Professor David Ceperley
Associate Professor Brian Odom

Abstract

We use ^{40}K atoms trapped in a cubic optical lattice to simulate the Fermi-Hubbard model. The work in this thesis focuses on investigating dynamics in the Fermi-Hubbard model and developing techniques for engineering Hamiltonians beyond the minimal Hubbard model.

We discussed three experiments. In the first, we investigated the transport properties of a Fermi lattice gas by directly measuring the transport lifetime at various interaction strengths and temperatures. The resistivity is inferred from the measured transport lifetime. We observe anomalous transport behavior, which is analogous to bad-metal behavior in strongly correlated electronic materials.

The second experiment presents the first realization of correlated, density-dependent tunneling in a Fermi-Hubbard optical lattice model by applied Raman laser fields. This correlated tunneling involves spin-flips and the generation of doublons, which have been observed experimentally. We also confirmed that the amplitude of correlated tunneling is suppressed when neighboring lattice sites are unoccupied.

The last experiment explores the possibility to introduce long-range interactions for fermions trapped in optical lattices via Rydberg-dressed states. We developed a novel velocity-selective spectroscopy method to measure the transition between the $5P_{1/2}$ and Rydberg states via electromagnetically induced transparency. This measurement is a first step toward inducing Rydberg-dressed interactions in optical lattices.

To my Grandfather

Acknowledgments

Foremost, I am extremely grateful to my advisor Brian DeMarco for his support and academic guidance. When I joined the group, I was afraid of communicating with others and asking questions. Brian encouraged me to express my own ideas. When I was worried about my future career, Brian was the one who shared his experience and cheered me up. I will always remember when we worked together for a whole weekend on the spectroscopy measurements of Rydberg energy levels and finally succeeded.

I would like to thank Stanimir Kondov and William McGehee, who were the senior graduate students when I joined the group. They not only built the K apparatus from which I benefited, but also instructed me how to be a good experimentalist. It has also been a great pleasure to work with the other members on K team including Will Morong, Pei-Wen Tsai, and Lucas Slattery.

I want to thank the group members on Rb team, including Carrie Meldgin, David Chen, Phil Russ, and Laura Wadleigh. Carrie taught me how to measure the trap frequencies of an optical dipole trap on my first day in the lab. David, Phil, and Laura were always willing to share their progress on the Rb apparatus. I also want to thank Prof. Bryce Gadway and his group members Eric, Alex, and Jackson for helpful discussions.

Finally, I would like to thank my family for their support and love through the years, especially to my parents who listened to my feelings at midnight in China. Many thanks to my hometown, Nanjing, who always welcome me back with her nice food and beautiful planetrees.

I acknowledge generous support from the University of Illinois, NSF, ARO, and DARPA.

Table of Contents

List of Tables

List of Figures

Chapter 1

Introduction

Many challenges in condensed matter physics involve complicated materials with interconnected degrees of freedom appearing like a "black box" to us. To reveal the mysteries inside this "black box," scientists study its response to an external perturbation. Hopefully, this response carries information about the hidden characteristics. A simple example is applying voltage to a material and measuring the response as an electrical current to study the behavior of conductivity, which contains information regarding the scattering mechanisms and the symmetries of the system.

After investigating the relationship between the external perturbation and the response, we hope to replace this "black box" with a simplified model that reproduces the output for the same input. This strategy often works well. For example, Fermi liquid theory successfully explains the resistivity of electrons in simple metals. However, sometimes it is challenging to find a theoretical model that fully accommodates the properties of this "black box." One famous example is high-temperature superconductivity. Moreover, although the candidate model has been simplified, there might be no analytical solution, and numerical simulations may exceed the ability of classical computers. From the experimental prospective in condensed matter physics, difficulty in controlling individual material parameters and the unavoidable imperfections create more challenges for understanding the necessary ingredients for a successful model. Therefore, either validating or disapproving a candidate model for a given problem or a class of problems can be difficult.

Ultracold quantum gases trapped in optical lattices are a promising approach to solving the mysteries of the "black box" in condensed matter physics. Precise controllability and wide tunability of ultracold quantum gases allow the engineering of exactly the model Hamiltonian that we wish to explore. Instead of solving the model analytically or numerically on a classical computer, we explore the behavior of the ultracold quantum gases under well-known conditions. In this way, we investigate the candidate model with an analog quantum emulator and carry out model testing.

Our apparatus uses potassium ^{40}K atoms trapped in a cubic optical lattice, which (at low enough temperature) realizes a single-band Fermi-Hubbard model. As a minimal paradigm for describing strongly-correlated electronic systems, the Fermi-Hubbard model is a candidate model for high-temperature superconductors [1].

For more than one dimension and away from half-filling, the Fermi-Hubbard model is challenging to solve because of the fermion sign problem [2]. This problem motivates us to perform quantum simulation using ultracold atoms trapped in optical lattices. An additional advantage of quantum simulation using ultracold atoms is that many ingredients beyond the minimal Fermi-Hubbard model, such as artificial gauge fields (see [3] for a review), spin-orbit coupling [4–7], and long-range interactions [8–10], can be added, which opens the possibility to study novel quantum phases and even phenomena without counterparts in condensed matter systems.

My work for this thesis has focused on the dynamic properties of the Fermi-Hubbard model. In solids, typical timescales for the decay of electronic excitations is at the order of $1 - 100$fs. State-of-the-art pump-and-probe techniques can barely achieve this time resolution (see Ref. [11], for example). On the other hand, for atoms in optical lattices, the timescale of dynamical process is often on the order of milliseconds, which can be easily resolved.

The differences between conventional solid state systems and ultracold atomic systems are myriad. One of the most important constrains is the typical temperature range we explore. For metals, the temperature in unit of Fermi temperature T_F is usually below $0.01T/T_F$, since T_F is around $50000K$. On the other hand, T/T_F for ultracold quantum gases in optical lattice is much higher, larger than $0.1T/T_F$ in most experiments. Therefore, the energy scales involved in dynamical process are different.

Also, the response to external forces in solids is usually measured after the system has reached a quasi-steady state by continuously exchanging particles and energy with an external reservoir. However, ultracold quantum gases in optical lattices are isolated systems, and an external force can drive the system far from equilibrium. Oscillatory or more complicated behavior can emerge instead of a quasi-steady state [12]. Therefore, an appropriate interpretation of measurements is crucial, and whether the measured dynamical properties can be directly compared to their counterparts in condensed matter systems requires justification.

An outline of this thesis follows:

Chapter 2

This chapter briefly reviews how we produce ultracold, degenerate Fermi gases composed of ^{40}K atoms using our apparatus. I focus on the new features that have been added to the apparatus during my thesis work, including the Raman lasers that drive transitions between different spin components and the upgraded hardware for accessing a Feshbach resonance.

Chapter 3

This chapter discusses the basic concepts and tools for performing quantum simulation using ultracold

atoms trapped in optical lattices. The properties of optical lattices and how the Fermi-Hubbard model is realized are introduced. The semiclassical approach to describing the kinetic properties of Fermi lattice gases and response to external forces is discussed. I also discusses the methods we use to infer the thermodynamic properties of lattice quantum gases. The last section of this chapter gives a brief introduction to Green's functions, which are a useful theoretical formalism in condensed matter physics.

Chapter 4

We report measurements of the transport lifetime for gases trapped in optical lattices, the behavior of which is consistent with the properties of a "bad metal." A bad metal presents anomalous transport properties such as linear dependence of resistivity on temperature and the lack of a maximum resistivity. In this work, from the decay rate of a mass current created via stimulated Raman transitions, the dependence of the transport lifetime on interaction strengths and temperatures has been investigated. The qualitative failure of theoretical predictions based on Fermi's golden rule suggests behavior beyond the quasiparticle framework. We infer the effective resistivity from the measured transport lifetime. The dependence of the resistivity on temperature presents a linear scaling, which is a signature of bad-metal behavior. Moreover, with increasing temperature, the value of resistivity approaches the Mott-Ioffe-Regal limit. In addition, a comparison to dynamical mean-field theory simulations suggests that the reduction of quasiparticle weight from strong interactions is directly related to anomalous resistivity scaling.

Chapter 5

Periodic driving forces combined with optical lattices have enabled experiments to achieve physics beyond the minimal Hubbard model. In this chapter, we report the realization of correlated, density-dependent tunneling by appropriately tunning the frequency difference between a pair of Raman beams applied to a spin-polarized gas. Spin transitions and tunneling are induced that depend on the relative occupation of neighboring lattice sites. This correlated spin-flip tunneling is spectroscopically resolved, and the accompanying generation of doubly-occupied sites is measured via number loss induced by light-assisted collisions. Furthermore, by controllably introducing vacancies to a lattice gas, we demonstrate that correlated tunneling is suppressed when neighboring lattice sites are unoccupied. This work is the first time that correlated spin-flip tunneling effect has been observed in the Fermi-Hubbard model.

Chapter 6

This chapter focuses on the possibility to introduce long-range interactions in optical lattice via

Rydberg-dressed states. I discuss introducing Rydberg-dressed interactions by mixing a small amount of a Rydberg state into the ground state. For experimentally feasible parameters, it is promising to observe Rydberg-dressing in optical lattices. The second part of this chapter reports a measurement. As a first step towards realizing Rydberg-dressed states in optical lattices for ^{40}K atoms, we perform novel velocity-selective spectroscopy measurements of the transition between $5P_{1/2}$ and Rydberg states via electromagnetically induced transparency.

Publication list:

[1] W. R. McGehee, S. S. Kondov, W. Xu, J. J. Zirbel and B. DeMarco. Three-dimensional Anderson localization in variable scale disorder. *Physical Review Letters.* 111(14):145303, 2013.

[2] S. S. Kondov, W. R. McGehee, W. Xu and B. DeMarco. Disorder-induced localization in a strongly correlated atomic Hubbard gas. *Physical Review Letters.* 114(8):083002, 2015.

[3] W. Xu and B. DeMarco. Velocity-selective electromagnetically-induced-transparency measurements of potassium Rydberg states. *Physical Review A.(R)* 93(1):011801, 2016

[4] Wenchao Xu, William McGehee, William Morong, Brian DeMarco. Bad Metal in a Fermi Lattice Gas. *arXiv preprint arXiv:1606.06669.* Jun. 2016.

[5] Wenchao Xu, William Morong, Hoi-Yun Hui, Vito W Scarola, and Brian DeMarco. Correlated Spin-Flip Tunneling in a Fermi Lattice Gas. *arXiv preprint arXiv:1711.02061.* Nov. 2017

Chapter 2

Apparatus

Our apparatus for producing degenerate Fermi gases composed of ^{40}K atoms was in operation when I joined the group. Standard cooling techniques are used: atoms are collected in a magneto-optical trap (MOT) and cooled to degeneracy using microwave and optical evaporation. The main apparatus was built by Stanimir Kondov, Josh Zirbel and William McGehee. Many details can be found in Stan and William's theses [13,14]. In this chapter, after a brief description on the preparation of Fermi gases, I will focus on new features that we have added to the apparatus.

2.1 Preparing Fermi gases

The alkali atom used in our apparatus is ^{40}K. The energy levels relevant to cooling and trapping of the single valence electron in the $4S$ orbital of ^{40}K structure are shown in Fig. 2.1. ^{40}K has two hyperfine ground-state manifolds: $F = 9/2$ and $F = 7/2$. In the presence of a magnetic field, each hyperfine state splits into $2F + 1$ non-degenerate Zeeman levels. Fig. 2.1 shows the ordering of Zeeman energy levels for the $F = 9/2$ manifold. The primary trapping and cooling transitions we use are from the $4S_{1/2}$ to the $4P_{3/2}$ level, which is the D2 transition. Evaporative colling requires high collision rates, which are necessary for the rethermalization of gases to lower temperature after removing the highest energy atoms. S-wave collisions between identical Fermions are forbidden by the Pauli exclusion principle, and at temperatures lower than 200μK, p-wave scattering is energetically suppressed [15]. In our approach, atoms with $m_F = 9/2$ and $m_F = 7/2$, between which the s-wave scattering length is $a = 170a_0$ (a_0 is the Bohr radius), are used for evaporative cooling and to produce a thermalized Fermi gas.

Fig. 2.2 is a photo of the vacuum system we use to create degenerate Fermi gases. Potassium atoms, generated from a resistively heated enriched potassium metal dispenser, are trapped in a dark spot MOT in the collection cell. The MOT is a combination of a quadrupole magnetic field and three pairs of circular-polarized trap and repump laser beams. The repump beam, which drives the transition between the ground $F = 7/2$ and the excited $F' = 9/2$ state, has a dark spot in its center. The purpose of this dark spot is to

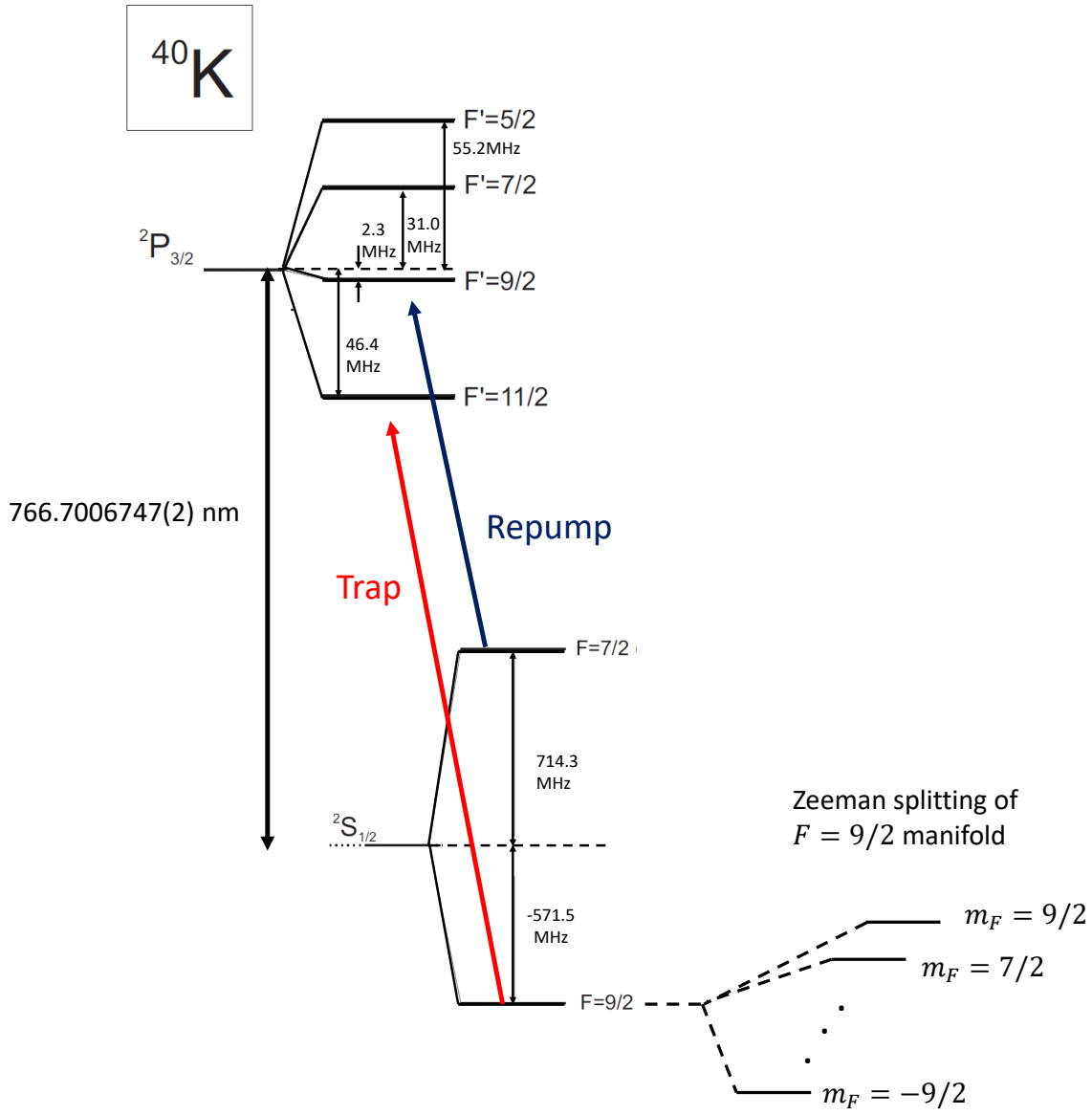

Figure 2.1: Electronic structure of ^{40}K (not to scale) [16]. The D2 transition is used for cooling and trapping. With an external magnetic field, each hyperfine state splits into $2F+1$ energy levels via the Zeeman effect. For the ground state $F = 9/2$ manifold, the energy splitting between the adjacent m_F states is about $0.31MHz/G$ at low magnetic field.

keep the atoms in the $F = 7/2$ manifold and suppresses excitation from the trap laser. This suppression reduces loses from inelastic collisions and enhances the trapped number of atoms. The disadvantage of this scheme is a long MOT loading time of $30s$.

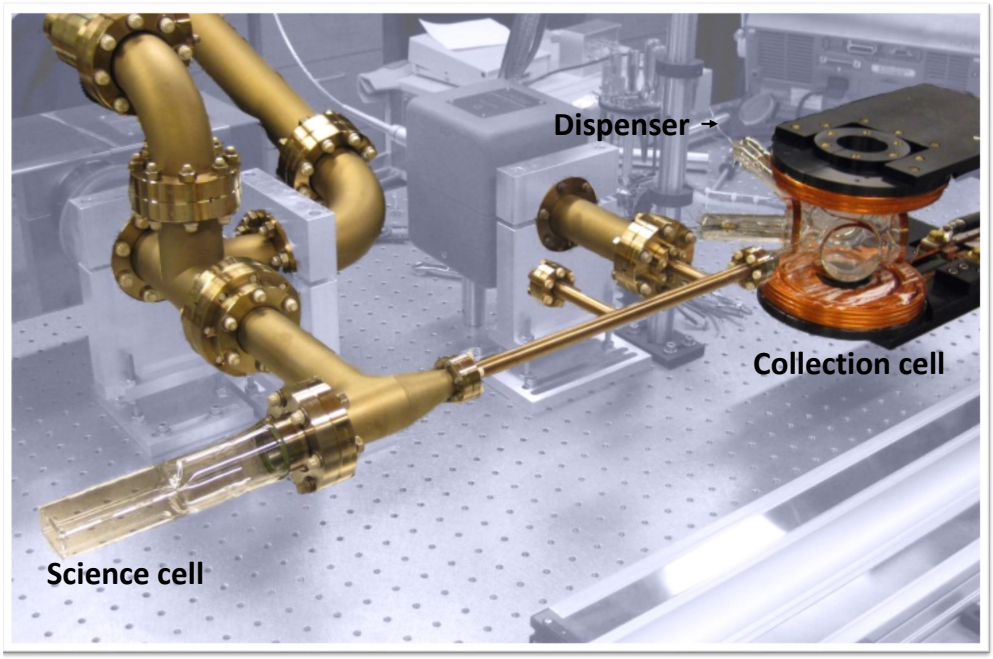

Figure 2.2: Photo (by William McGehee) of the vacuum system. The source of potassium atoms is an enriched potassium dispenser. Atoms are collected in a magneto-optic trap (MOT) in the collection cell and transferred along the tube to the science cell by the magnetic quadrupole coils that are mounted on a cart. In the science cell, forced evaporative cooling is performed in a modified QUIC trap (not shown in this figure). Finally, the atoms are captured in an optical dipole trap and cooled to below the Fermi temperature.

After collecting atoms in the MOT, several stages are used to prepare atoms in the $F = 9/2$ manifold (shown as $(1) - (4)$ in Table. 2.1). Then the current in the quadrupole coils is ramped up to produce a gradient of $240G/\text{cm}$, and atoms are transferred to the science cell by mechanically moving the cart across the optical table. The background pressure of the science cell is sufficiently low to guarantee a vacuum-limited trapping lifetime of several hundred seconds.

After transferring atoms into the magnetic trap mounted around the science cell (not shown in Fig. 2.2), the total number of atoms is on the order of 1.5×10^8, with a temperature lower than 10mK. Magnetic evaporative cooling is performed in a modified QUIC magnetic trap [17], which creates a $3G$ magnetic field. After driving high energy atoms to magnetically untrapped states via a microwave-frequency magnetic field, the total atom number is about 1.5×10^6 with a temperature around 5μK. The loading efficiency from the magnetic trap to the crossed optical dipole trap is about 50%. The waists of the dipole trap beams are

$w_x \approx 120\mu$m, $w_y \approx 98\mu$m for the first pass, and $w_x \approx 86\mu$m, $w_y \approx 96\mu$m for the second pass. Further evaporative cooling in the optical dipole trap achieves Fermi degeneracy. The coldest temperature achieved on our apparatus is about $T/T_F \approx 0.15$, with total atom number around 30000. Fig. 2.3 plots the recent evaporative cooling trajectories. Table. 2.1 summaries some primary stages of a complete experimental sequence for preparing degenerate Fermi gas.

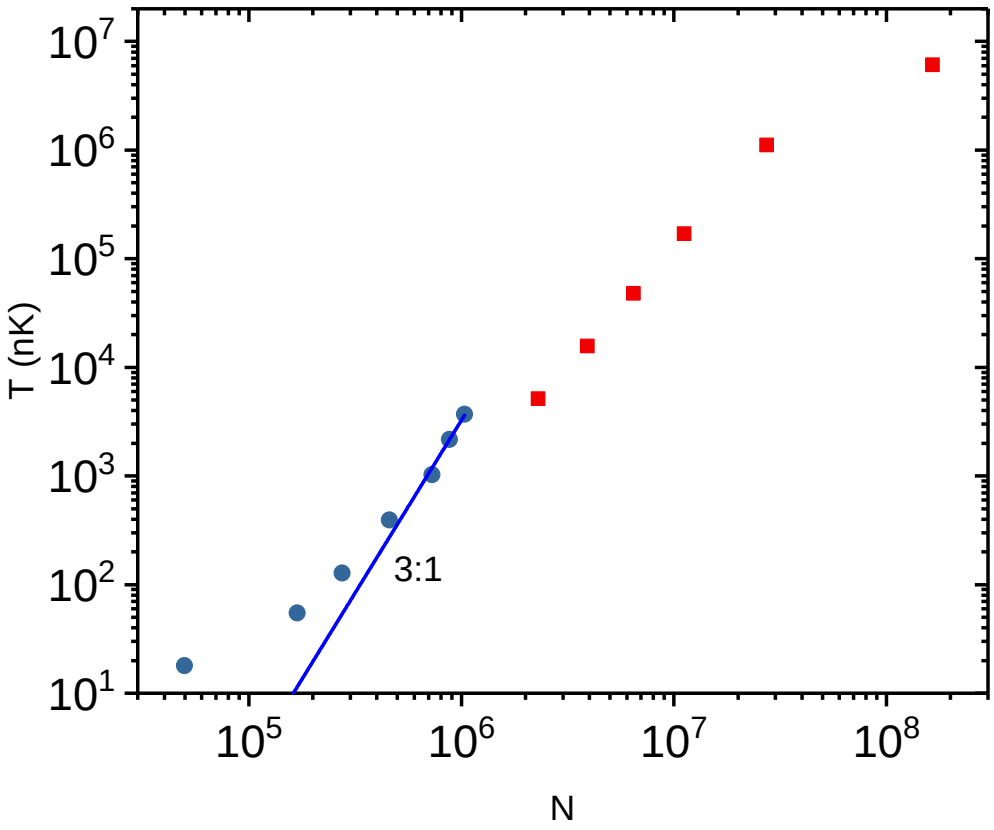

Figure 2.3: Evaporative cooling trajectory. Temperature vs. total number of atoms is plotted for the magnetic evaporative cooling stage (red square) and the optical evaporative cooling stage (blue circle). The blue line plots $T = N^\alpha$, with $\alpha \approx 3$ in this plot. Larger α indicates better cooling efficiency. As an empirical rule, $\alpha < 1$ indicates poor cooling efficiency. At the final stage of evaporative cooling in the optical dipole trap, the efficiency becomes poorer.

2.2 Stimulated Raman transitions

Stimulated Raman transitions are a coherent two-photon process: stimulated absorption and subsequent stimulated emission of photons cause transitions between internal states. Tuning the frequency difference

	Step	Time	Trap laser	Repump laser	Purpose	Other comments
1	Dark-spot MOT	30s	f^t	f^r	Loading atoms into MOT	
2	Bright MOT		f^t	$f^r + 15$MHz	Hyperfine pumping: $\|F = 7/2\rangle$ to $\|F = 9/2\rangle$	Shutter open for bright repump beams
3	Optical molasses	5ms	$f^t + 22$MHz	$f^r + 15$MHz	Laser cooling	Quadrupole coils off
4	Optical pumping	0.5ms	$(f^t - 3 + 65)$MHz	$f^r - 45$MHz	Pumping to $m_F = 9/2$ and $m_F = 7/2$	σ^+-polarized optical pumping beam on
5	Cart transfer		far detuned	$f^r - 45$MHz	Transfer to science cell	
6	Magnetic evaporative cooling	~ 50s	far detuned	$f^r - 45$MHz	Cooling to 5μK	Microwave sweep in QUIZ trap
7	Optical evaporative cooling	~ 30s	far detuned	$f^r - 45$MHz	Cooling to degeneracy	Reduce the depth of optical dipole trap
8	Imaging		on resonant $(f^t + 38.4$MHz)	far detuned	Absorption image of atoms	25μs pulse of on-resonant light

Table 2.1: A list of each experimental stage. Currently, f^t (the frequency of the trap laser during MOT loading) is ~ 35MHz red-detuned from the $F = 9/2 \rightarrow F' = 11/2$ transition, and f^r is ~ 20MHz red-detuned from the $F = 7/2 \rightarrow F' = 9/2$ transition. Steps (1)-(4) are done in the collection cell. The stability of the trap and repump laser frequency is crucial for producing enough atoms for evaporative cooling. The method for optimizing these parameters (such as the frequency detuning, light power, and timing) during each step is to optimize the total number of atoms at the beginning of magnetic trap evaporative cooling step. (5)-(6) are performed in the science cell. The parameters shown in this table are current settings for our sequence. The resonant probe frequency for imaging given in this table is for the transition between the $|F = 9/2, m_F = 9/2\rangle \rightarrow |F' = 11/2, m_F = 11/2\rangle$ state at $B \approx 3$G magnetic field. More details about each step can be found in Kondov's and McGehee's theses [13, 14].

between the two Raman beams provides access to an energy-selective transition. The change in momentum or quasimomentum between the initial and final states can be controlled independently by varying the wavevector difference between the two Raman beams.

Stimulated Raman transitions have been widely used in ultracold experiments. Raman sideband cooling has been employed for cooling the motional and vibrational degrees of freedom of ions and atoms [18–21]. The first observation of quasimomentum cooling in an optical lattice has been observed [22]. Moreover, stimulated Raman transitions can induce synthetic magnetic field [23], spin-orbit coupling [24], and artificial gauge potentials [3, 25–27]. Two of the projects in this thesis used this technique (See Chapters. 4 and 5).

2.2.1 Experimental setup

The Raman beams in our experiment are derived from a single-frequency grating stabilized diode laser (Vortex II TLB-6900), which is red-detuned $40 - 80$GHz from the $4S_{1/2} \rightarrow 4P_{1/2}$ D1 transition in ^{40}K. A schematic of the Raman beams optics is shown in Fig. 2.4. The laser beam is split into two paths, each of which goes through an acousto-optic modulator (AOM, Gooch and Housego R23080-i-LTD) operating at a nominal frequency of 80MHz. The diffracted light from the AOM is coupled into a single-mode polarization-maintaining fiber. By tuning the difference between the radio-frequency drives applied to the AOMs, the frequency difference $\Delta\omega$ between the two Raman beams can be varied. The power of each Raman beam is individually controlled by sampling a small fraction of the Raman light after the fiber on a photodetector (PDA36A), and the voltage from the photodetecotor is servoed by comparing it to a computer signal. A resonant electro-optic modulator (EOM, Newport 4421-01 @ 650MHz) can generate sidebands on the Raman beams, which can be used to drive hyperfine transitions. This EOM is not used in the experiments discussed in this thesis.

The two Raman beams are focused onto the atoms with a waist of 170μm, which provides approximately uniform light intensity over the gas. Conservation of momentum requires the momentum change $\delta\vec{k}$ between the initial and the final state to equal to the wavevector difference between the two Raman beams. In our experiment, the angle between these two beams is about 30 degrees, and therefore, the amplitude $|\delta\vec{k}| = 2|k|\sin(15°) = 0.518|k|$, with the amplitude of the Raman beam wavevector $|k| = 2\pi/770.1$nm . For our optical lattice with lattice spacing $d = 391.1$nm, $|\delta\vec{k}|$ is about half q_B, where $q_B = \hbar\pi/d$.

2.2.2 Hamiltonian for stimulated Raman transitions

The stimulated Raman transitions used in our work involve a Λ-type three-level system, as shown in Fig. 2.5 The two lower levels are states with different magnetic quantum numbers, labeled as $|\uparrow\rangle$ and $|\downarrow\rangle$ in the figure.

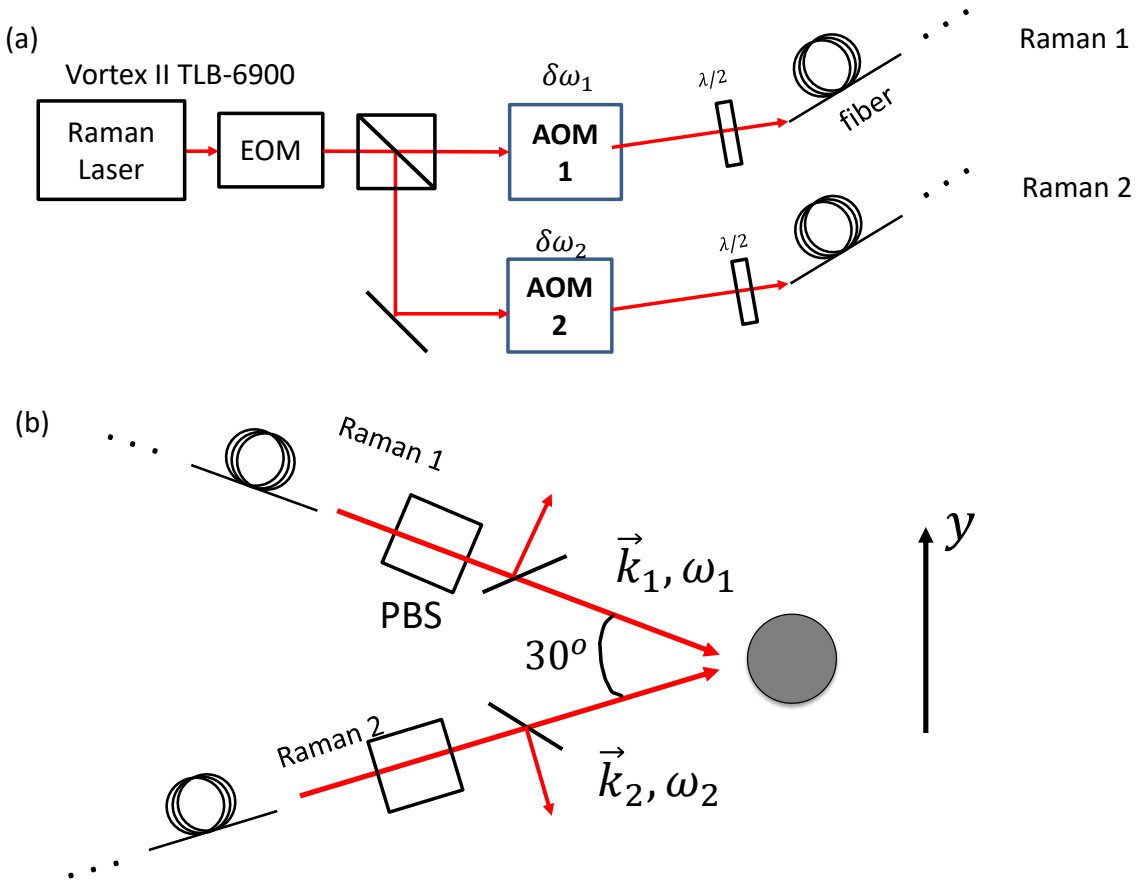

Figure 2.4: Stimulated Raman optical system. Two Raman beams are derived from a light source which is $40 - 80$GHz detuned from the D1 transition of ^{40}K. A resonant EOM can generate sidebands on the laser frequency that can be used to drive transitions between different hyperfine manifolds. This EOM is not used for the work in this thesis. The frequency of each Raman beam is controlled by an AOM. The frequency difference between the Raman beams determined by the difference in the AOM driving frequencies, the difference $\Delta\omega \equiv \omega_1 - \omega_2 = \delta\omega_1 - \delta\omega_2$ can cover a range around $2\pi \times (0 - 15)$MHz. The Raman beams are coupled into single-mode polarization-maintaining optical fibers to shorten the beam path and increase the pointing stability. At the optical fiber output, a polarizing beam splitter cube is used to purify the polarization. The polarization of the Raman beams points perpendicular to the plane of the paper. A beam sampler picks off a small amount of light for actively servoing the power of the Raman beam. Both beams are focused onto the position of the atoms with an angle of 30 degrees. The Raman vector difference $\delta\vec{k} = \vec{k}_1 - \vec{k}_2$ is along the y-direction (*i.e.*, vertical).

The upper level $|3\rangle$ is the excited $4P_{1/2}$ state. The energy splitting between the $|\uparrow\rangle$ and $|\downarrow\rangle$ states is from the Zeeman effect.

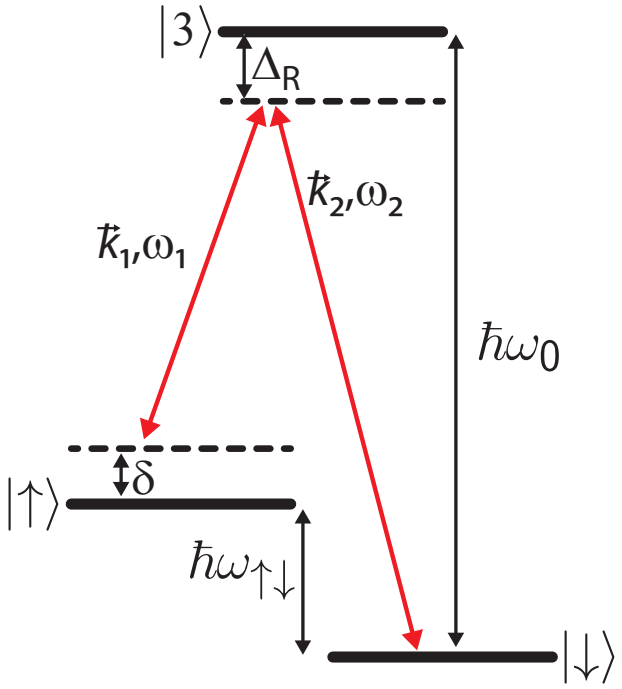

Figure 2.5: Schematic of energy levels of a 3-level Λ-system, consisting of two energy levels $|\uparrow\rangle$ and $|\downarrow\rangle$ and an excited state $|3\rangle$. The two lasers couple $|\uparrow\rangle \rightarrow |3\rangle$ and $|\downarrow\rangle \rightarrow |3\rangle$ with frequencies and wavevectors $\omega_1, \vec{k}_1$ and $\omega_2, \vec{k}_2$.

We consider a classical electric field in the form of

$$\vec{E}(\vec{r},t) = \vec{E}_1 \cos(\vec{k}_1 \cdot \vec{r} - \omega_1 t) + \vec{E}_2 \cos(\vec{k}_2 \cdot \vec{r} - \omega_2 t), \tag{2.1}$$

where $\vec{E}_{1,2}$ is electric field of the Raman laser beam. The electric field interacts with the atoms via $-e\vec{r}\cdot\vec{E}$. Therefore, the Raman-transition Hamiltonian in the basis of $|\uparrow\rangle, |\downarrow\rangle$, and $|3\rangle$, is [28]:

$$H_R^{\text{3-level}} = \begin{pmatrix} \omega_{\uparrow\downarrow} & 0 & \Omega_1^* \cos(\vec{k}_1 \cdot \vec{R} - \omega_1 t) \\ 0 & 0 & \Omega_2^* \cos(\vec{k}_2 \cdot \vec{R} - \omega_2 t) \\ \Omega_1 \cos(\vec{k}_1 \cdot \vec{R} - \omega_1 t) & \Omega_2 \cos(\vec{k}_2 \cdot \vec{R} - \omega_2 t) & \omega_0 \end{pmatrix}. \tag{2.2}$$

$$H_R^{\text{3-level}} = \begin{pmatrix} \omega_{\uparrow\downarrow} & 0 & \frac{\Omega_1^*}{2}\left[e^{i(\vec{k}_1\cdot\vec{R}-\omega_1 t)} + e^{-i(\vec{k}_1\cdot\vec{R}-\omega_1 t)}\right] \\ 0 & 0 & \frac{\Omega_2^*}{2}\left[e^{i(\vec{k}_2\cdot\vec{R}-\omega_2 t)} + e^{-i(\vec{k}_2\cdot\vec{R}-\omega_2 t)}\right] \\ \frac{\Omega_1}{2}\left[e^{i(\vec{k}_1\cdot\vec{R}-\omega_1 t)} + e^{-i(\vec{k}_1\cdot\vec{R}-\omega_1 t)}\right] & \frac{\Omega_2}{2}\left[e^{i(\vec{k}_2\cdot\vec{R}-\omega_2 t)} + e^{-i(\vec{k}_2\cdot\vec{R}-\omega_2 t)}\right] & \omega_0 \end{pmatrix}. \tag{2.3}$$

Here $\vec{R}$ is the position of atom, $\hbar\omega_0$ is the energy difference between $|\downarrow\rangle$ and $|3\rangle$, $\hbar\omega_{\uparrow\downarrow}$ is the energy difference between $|\downarrow\rangle$ and $|\uparrow\rangle$, $\Omega_{1,2} = \frac{-e}{\hbar}\langle 3|\vec{E}_{1,2}\cdot\vec{r}|\uparrow,\downarrow\rangle$ are the Rabi rates of each Raman beam. The detuning of Raman beam is defined as $\Delta_R = \hbar\omega_0 - \hbar\omega_2$. The frequency difference between two Raman beams is $\Delta\omega = \omega_1 - \omega_2 = \delta + \omega_{\uparrow\downarrow}$. We assume there is no coupling between the $|\uparrow\rangle$ ($|\downarrow\rangle$) and the $|3\rangle$ state by $\vec{E}_2$ ($\vec{E}_1$) (such coulping only causes an energy shift because of the AC stark effect).

In the interaction picture and with the rotating wave approximation (RWA), we have:

$$H_R^{\text{3-level}} = \begin{pmatrix} 0 & 0 & \frac{\Omega_1^*}{2}e^{-i(\delta+\Delta_R)t - i\vec{k}_1\cdot\vec{R}} \\ 0 & 0 & \frac{\Omega_2^*}{2}e^{-i\Delta_R t - i\vec{k}_2\cdot\vec{R}} \\ \frac{\Omega_1}{2}e^{i(\delta+\Delta_R)t + i\vec{k}_1\cdot\vec{R}} & \frac{\Omega_2}{2}e^{i\Delta_R t + i\vec{k}_2\cdot\vec{R}} & 0 \end{pmatrix}. \tag{2.4}$$

Then under a unitary transformation

$$\hat{U} = \begin{pmatrix} e^{-i\delta t} & 0 & 0 \\ 0 & 1 & 0 \\ 0 & 0 & e^{i\Delta_R t} \end{pmatrix}, \tag{2.5}$$

$H_R^{\text{3-level}}$ becomes $U^{-1}H_R^{\text{3-level}}U - iU^{-1}\frac{\partial U}{\partial t}$:

$$H_R^{\text{3-level}} = \begin{pmatrix} \delta & 0 & \frac{\Omega_1^*}{2}e^{-i\vec{k}_1\cdot\vec{R}} \\ 0 & 0 & \frac{\Omega_2^*}{2}e^{-i\vec{k}_2\cdot\vec{R}} \\ \frac{\Omega_1}{2}e^{i\vec{k}_1\cdot\vec{R}} & \frac{\Omega_2}{2}e^{i\vec{k}_2\cdot\vec{R}} & \Delta_R \end{pmatrix}. \tag{2.6}$$

If $\Delta_R \gg \Omega_1, \Omega_2$, the three-level system can be approximated as a two-level system. The 3×3 matrix can be projected onto the subspace of $\{|\uparrow\rangle, |\downarrow\rangle\}$, with the matrix element as $\langle\sigma| H_R^{\text{2-level}} |\sigma'\rangle = \langle\sigma| H_R^{\text{3-level}} |\sigma'\rangle - \frac{\langle\sigma|H_R^{\text{3-level}}|3\rangle\langle 3|H_R^{\text{3-level}}|\sigma'\rangle}{2}$. This procedure gives:

$$H_R^{\text{2-level}} = \begin{pmatrix} \delta + \frac{\Omega_1^2-\Omega_2^2}{4(\Delta_R+\delta)} & \frac{\Omega_1^*\Omega_2^*}{8}(\frac{1}{\Delta_R} + \frac{1}{\Delta_R+\delta})e^{-i\delta\vec{k}\cdot\vec{R}} \\ \frac{\Omega_1^*\Omega_2^*}{8}(\frac{1}{\Delta_R} + \frac{1}{\Delta_R+\delta})e^{i\delta\vec{k}\cdot\vec{R}} & 0 \end{pmatrix} \approx \begin{pmatrix} \delta + \frac{\Omega_1^2-\Omega_2^2}{4\Delta_R} & \frac{\Omega}{2}e^{-i\delta\vec{k}\cdot\vec{R}} \\ \frac{\Omega^*}{2}e^{i\delta\vec{k}\cdot\vec{R}} & 0 \end{pmatrix}, \tag{2.7}$$

where $\Omega = \frac{\Omega_1 \Omega_2}{2\Delta_R}$ is the effective Rabi rate for this two-level system and $\delta\vec{k} = \vec{k}_1 - \vec{k}_2$.

2.3 Feshbach resonances

Feshbach resonances have become a powerful tool in the field of AMO physics, because they can be used to vary the effective interactions between atoms by tunning an external parameter such as the magnetic field. It has been widely used for producing cold molecules and for investigating many-body physics (see Refs. [29] and [30] for reviews). Important breakthroughs enabled by Feshbach resonances in the context of quantum simulation with ultracold atoms include the numerous studies of the BEC-BCS crossover of trapped fermions (see Ref. [31], for example), measurements of the properties of unitary bosons and fermions [32–34], and the observation of superfluidity of ultracold fermions in optical lattice [35].

The capability to tune the on-site interactions via a Feshbach resonance makes ultracold fermionic atoms trapped in optical lattices an ideal platform to study the attractive Fermi Hubbard model, which is difficult to realize in solid-state systems. Compared with the extensively study on the repulsive Fermi-Hubbard model from the cold atom community, there are much less experimental works on the attractive side [36–39]. Many properties of the attractive Fermi-Hubbard model are well-known, because there is no "sign problem." For example, see Ref. [40] for a quantum Monte Carlo study of the 3D attractive Hubbard model. Still, this model provides a nice platform to study the Bose-Einstein condensation of local bound pairs and the BCS-type superfluidity in optical lattices [41–43] . In addition, the effect of disorder, which can be introduced experimentally via the speckle field in our experiment (see McGehee's thesis for more details [14]), is of great theoretical interest [44].

This motivates us to upgrade our apparatus to access a Feshbach resonance. Multiple Feshbach resonances between different magnetic quantum states in ^{40}K have been reported [45–48]. In our experiment, we plan to use the Feshbach resonance between the $|F = 9/2, m_F = -9/2\rangle$ and the $|F = 9/2, m_F = -7/2\rangle$ states, which occurs at magnetic field $|\vec{B}| = 202.1\text{G}$ [49]. In this section, after a brief introduction on the theoretical background of Feshbach resonances, I will discuss the hardware upgrades to our apparatus.

2.3.1 A brief introduction to Feshbach resonances

To illustrate the principle of a Feshbach resonance, Fig. 2.6 plots a basic two-channel model, consisting of two potential curves: $V_o(R)$ (open channel) and $V_c(R)$ (closed channel). The open channel potential $V_o(R)$ asymptotically connects to two free atoms at large interatomic distance R. The zero of energy is set to be $V_o(R)$ as $R \to \infty$. This open channel cannot support a bound state for particles with incoming energy

larger than zero. On the other hand, the closed channel can support a bound molecular state, with its energy denoted as E_c. The amount of energy shift of $V_c(R)$ as $R \to \infty$ is determined by the sum of the single-particle Zeeman energies associated with the closed-channel spin configuration of atom pairs [29]. If two atoms collide at energy E in the open channel, with E matching the E_c in the closed channel, then a strong mixing between these two channels occurs. This is the Feshbach resonance.

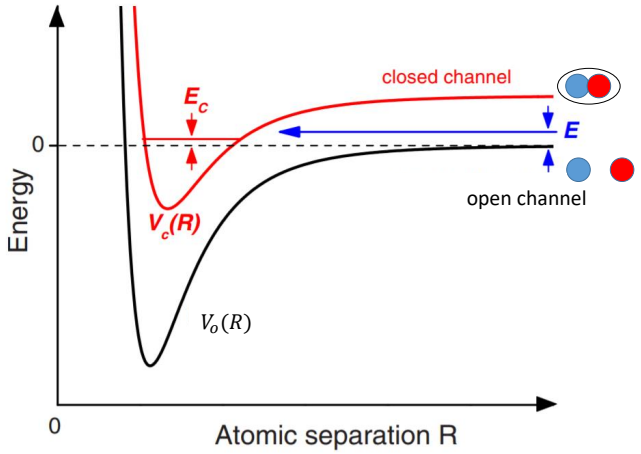

Figure 2.6: Schematic two-channel model for a Feshbach resonance. Two potential curves $V_c(R)$ and $V_o(r)$ are shown. If the energy of a molecular bound state E_c in the closed channel is close to the energy E of atoms in the open channel, the these two channels couple together and introduce strong effective interactions between atoms. This figure is adapted from Ref. [30].

The value of E_c depends on the magnetic field. Assuming that $E - E_c$ vanishes for a given magnetic field B_0, we can express the s-wave scattering length a as a function of magnetic field B near B_0 as [30]:

$$a = a_o(1 - \frac{\Delta}{B - B_0}), \tag{2.8}$$

where a_o is the scattering length associated with the open channel, and Δ is the resonance width. For the collisions between the $|F = 9/2, m_F = -9/2\rangle$ and $|F = 9/2, m_F = -7/2\rangle$ atoms in potassium ^{40}K, $B_0 = 202.1G$ and $\Delta = 7.8 \pm 0.1G$. Fig. 2.7 plots the dependence of scattering length on the magnitude of the external magnetic field. The s-wave scattering length diverges at $B = B_0$ and can become negative. This allows the study on the attractive Fermi-Hubbard model.

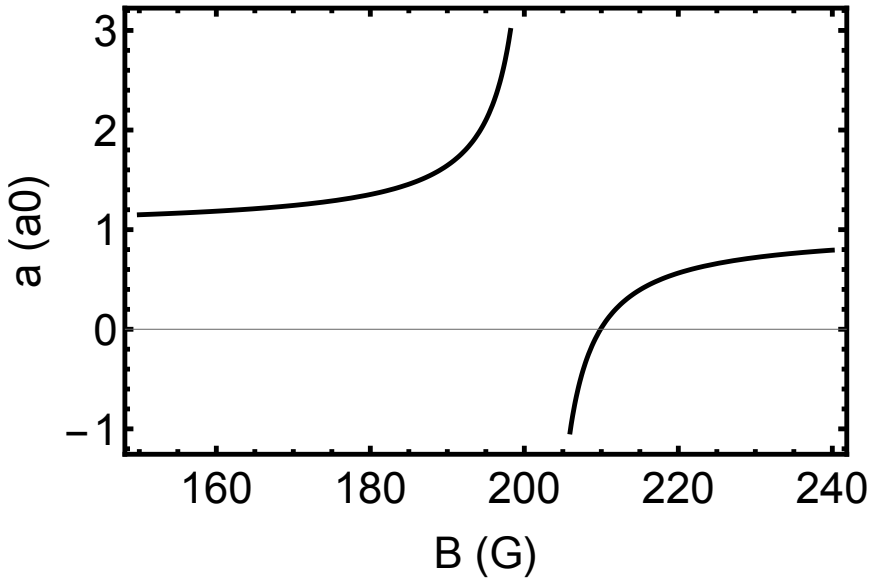

Figure 2.7: Dependence of s-wave scattering length on the external magnetic field for collisions between the $|F = 9/2, m_F = -9/2\rangle$ and $|F = 9/2, m_F = -7/2\rangle$ atoms. The scattering wavelength diverges at the Feshbach resonance magnetic field.

2.3.2 Creating Feshbach field

Magnetic coils in Helmholtz configuration

To access the Feshbach resonance using our apparatus, we require a homogeneous magnetic field with a magnitude up to 230G at the position of the atoms. We decided that the most feasible solution was to modify our existing magnetic QUIC trap [13, 14, 50]. The field minimum of a QUIC trap has an non-zero magnitude in order to avoid Majorana losses. Fig. 2.8(a) shows a drawing of our QUIC trap. It consists of a pair of coils (TQ and BQ) in a quadrupole configuration mounted above and below the science cell. The third Ioffe coil (IC) has its axis in a perpendicular plane. The three coils were connected in series through copper welding cables and machined copper bars (Fig. 2.8(b) and (c)). The currents in the QUIC magnetic coils are actively stabilized via standard PI servos (Fig. 2.8(c)) (details of the servo circuit diagram are shown in Fig. 2.13).

In the QUIC trap configuration, the currents in the TQ and the BQ coils flow in opposite directions. To generate a uniform magnetic field up to 230G, we modified the connections of the QUIC trap to allow a Helmholtz configuration and to electronically disconnect the Ioffe coil. A series of mechanical relays (TE Connectivity LEV200A4ANA) is used to switch between the QUIC trap configuration and the Feshbach configuration, as shown by the schematic diagram in Fig. 2.9. The gray circles represent the mechanical relays. P1 through P5 are copper plates used to mount the relays. Each connection consists of a pair of

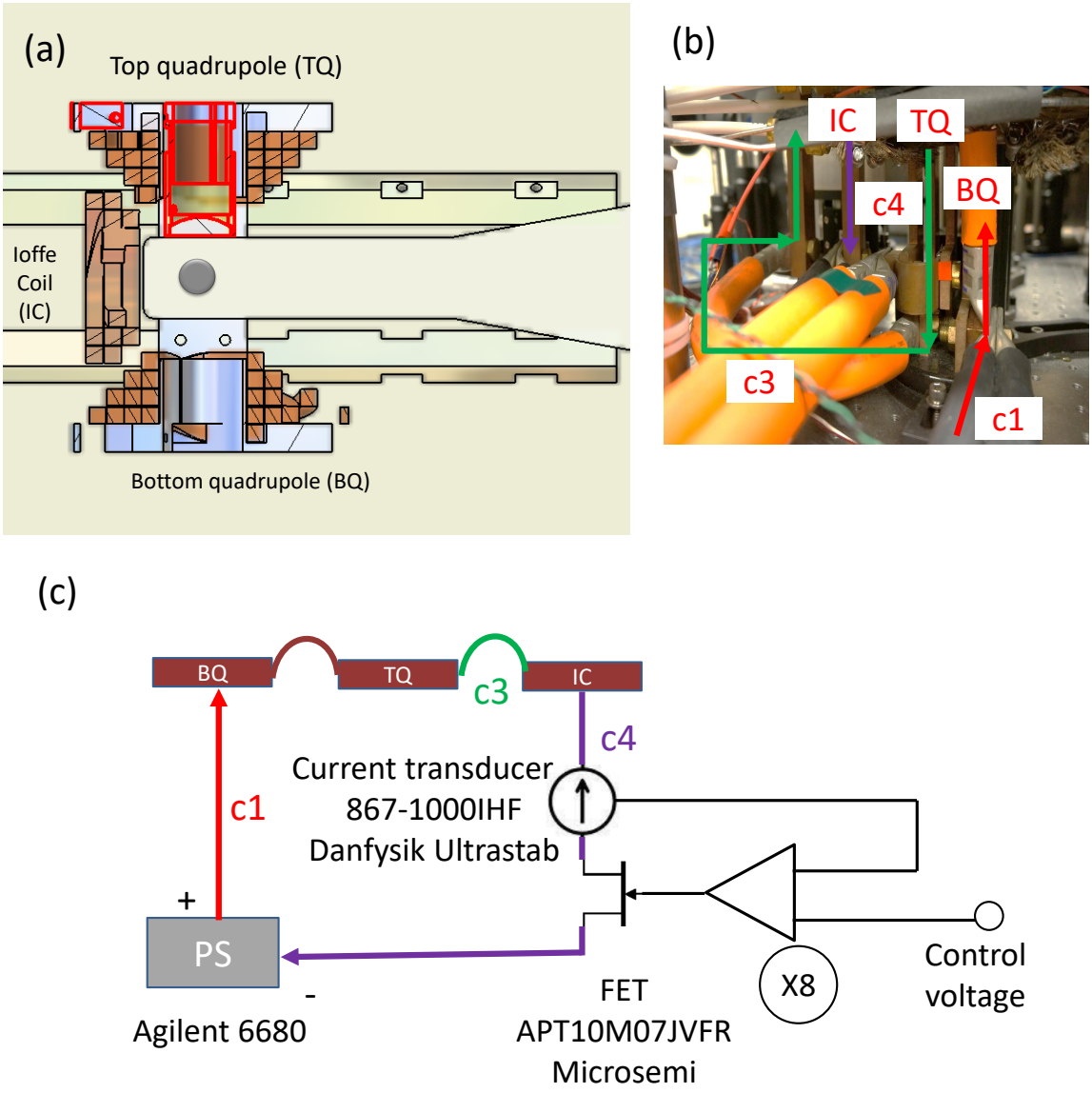

Figure 2.8: (a): Drawing of the QUIC trap, consisting of a pair of top quadrupole coil (TQ), bottom quadrupole (BQ) coil, and Ioffe coil (IC). (b) A photo showing the copper bars that connect the TQ, BQ and IQ. The orange welding 4/0 cables carry a current up to $710A$ for the QUIC trap. The colored arrows show the current direction. (c): A schematic drawing of the previous QUIC trap connection to the power supply (Agilent 6680). By controlling the gate voltage on eight FETs (APT10M07JVFR) mounted in parallel, the current flowing in the QUIC trap is servoed.

relays in parallel, in order to reduce the resistance. The open and closed status of the mechanical relays are denoted as X and $\downarrow$ in this figure. By changing the status of relays, the configuration can be switched between the QUIC trap and the Feshbach configurations by a control circuit.

Fig. 2.10(a) shows the copper plates (P1-P5); the mechanical relays are hidden below. The connections between the copper cables carry 710A and the plates are water cooled. Fig. 2.10(b) is a photo of the new connections between copper cables and copper bars at the QUIC trap.

Control circuit for switching configurations

The mechanical relays are controlled by the control circuit shown in Fig. 2.11 . A digital control signal from the computer is sent to a dual multivibrator (SN74LS221). Channel 1 (or 2) reacts to the rising (or falling) edge of the input respectively, and the output is a square wave pulse on 1Q (or 2Q), as shown by the function table in Fig. 2.11.

The system inside the dashed line is a protection circuit, that prevents switching coil configurations when the current is on. It consisting of latch 1 (SN74HCT573) and a differential comparator (LM139). The positive input to the LM139 comes from a Hall effect current sensor that monitors the current flowing in the magnetic coils. A 20mV reference voltage is applied to the LM139 negative input. The output of the comparator is sent to the latch-enable (LE) port of latch 1. If the current sensor voltage is higher than the reference voltage, then the output of the LM139 is low. The output of the latch remains as the previous value such that the magnetic coils' configuration retains. If no current flows in the magnetic coils, then the output of the comparator is high and the output of latch 1 equals the input voltage.

When latch 1 reacts to the voltage pulse from the multivibrator, depending on the input digital control signal, FET 1 (for rising edge) or FET 2 (for falling edge) is activated and current can flow. This pulse is sent to the set coils (or reset coils) in latch 2, which changes its contact mode, and therefore changes the status of the mechanical relays. The output voltage of latch 2 is from a voltage regulator (MC7805). Fig. 2.12 shows the logic diagram for the digital control circuit.

As another precaution, a uninterruptible power supply is used for the relay control box. This prevents sudden changes in the circuit configuration in case of a power outage. Since the coils store a lot of magnetic energy, this scenario could result in a large induced voltage that could cause damage. A Hall effect current sensor monitors the current flowing in the UPS. If that current is non-zero, which occurs when the UPS is on due to a power outage, then a signal will be sent to the interlock for the high-current power supply, which ramps off the current in a safe way.

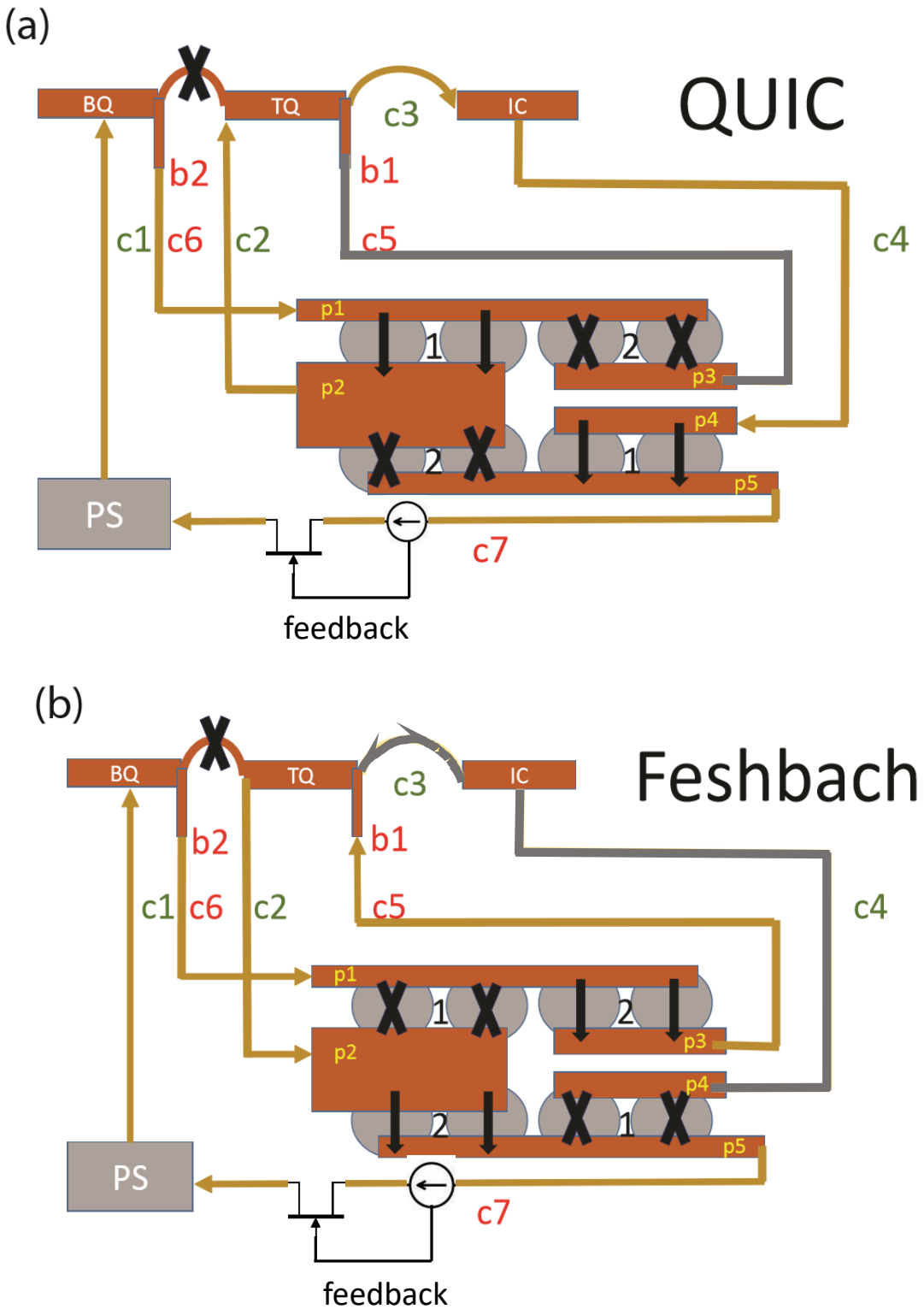

Figure 2.9: Schematic of the mechanical relays and circuit configuration for (a) QUIC trap configuration and (b) Helmholtz configuration. "X" denotes an open relay and "↓" denotes a closed relay.

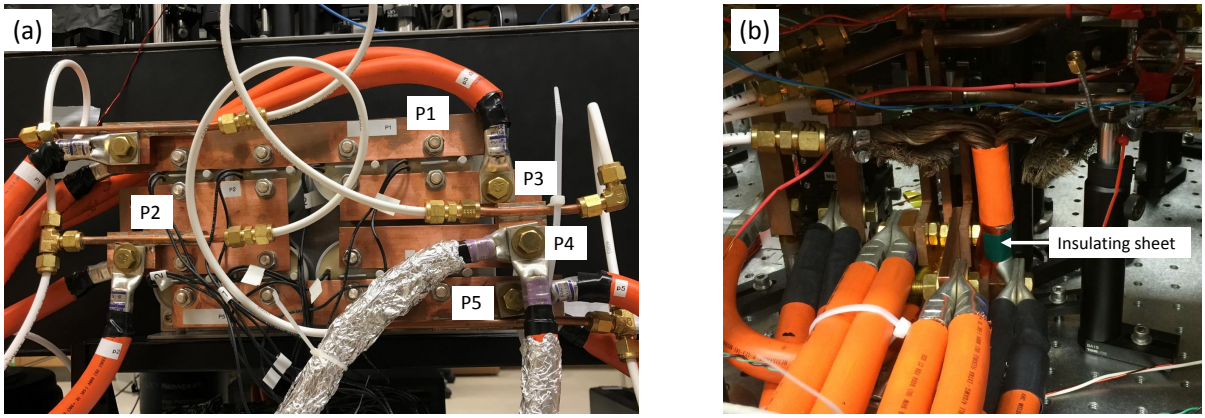

Figure 2.10: Photos for (a) the relays and copper plates and (b) the connection to copper bars. There is a sheet of plastic for insulating the two copper bars from contacting each other.

Precision voltage control

A stable magnetic field is crucial, *e.g*, for performing spectroscopy measurements at high magnetic field. The servo circuit we used before changing the coil configuration is shown in Fig. 2.13. The analog control voltage is derived from an 8-channel 16-bit DAQ board (National Instrument, NI 6733). The ratio between the magnetic field at the atoms from the Helmholtz coils and the control voltage is about 1G/4mV. The precision of the analog voltage from the DAQ board is $20\text{V}/2^{16} = 0.3mV$. Therefore, the precision of the magnetic field is 33mG. This uncertainty in the magnetic field corresponds to a 5kHz fluctuation in the Zeeman energy splitting between different m_F states. The fluctuation in the ambient magnetic field in our lab is about $3mG$, corresponding to a 0.5kHz change in Zeeman energy splittings. For performing spectroscopy measurements, the fluctuation in magnetic field should be less than 10mG. Therefore, the poor stability in magnetic field limited by the servo voltage needs to be improved.

To improve the magnetic stability and to have the ability to fine tune the magnetic field near the Feshbach resonance, we designed a precision voltage reference circuit (Fig. 2.14). The source of the control voltage is an ultra-low-noise, high-precision voltage reference (Maxim MAX6126). The control voltage for servoing is derived from a four-resistor voltage divider (*e.g.*, R1-R4). This series of resistors allows for precise adjustment of the control voltage by changing the small resistors (R2 and R4). Varying the ratio $(R1 + R2)/(R3 + R4)$ changes the control voltage. A precision 8-channel multiplexer (Maxim MAX 308) is used to switch between different settings for the control voltage. The analog output channel from the computer is connected to channel 6 on this multiplexer, which is used as a coarse control voltage. Table. 2.2 lists the corresponding currents for given settings of the digital lines.

The output of the multiplexer is sent to an inverting amplifier circuit. The output from this precision

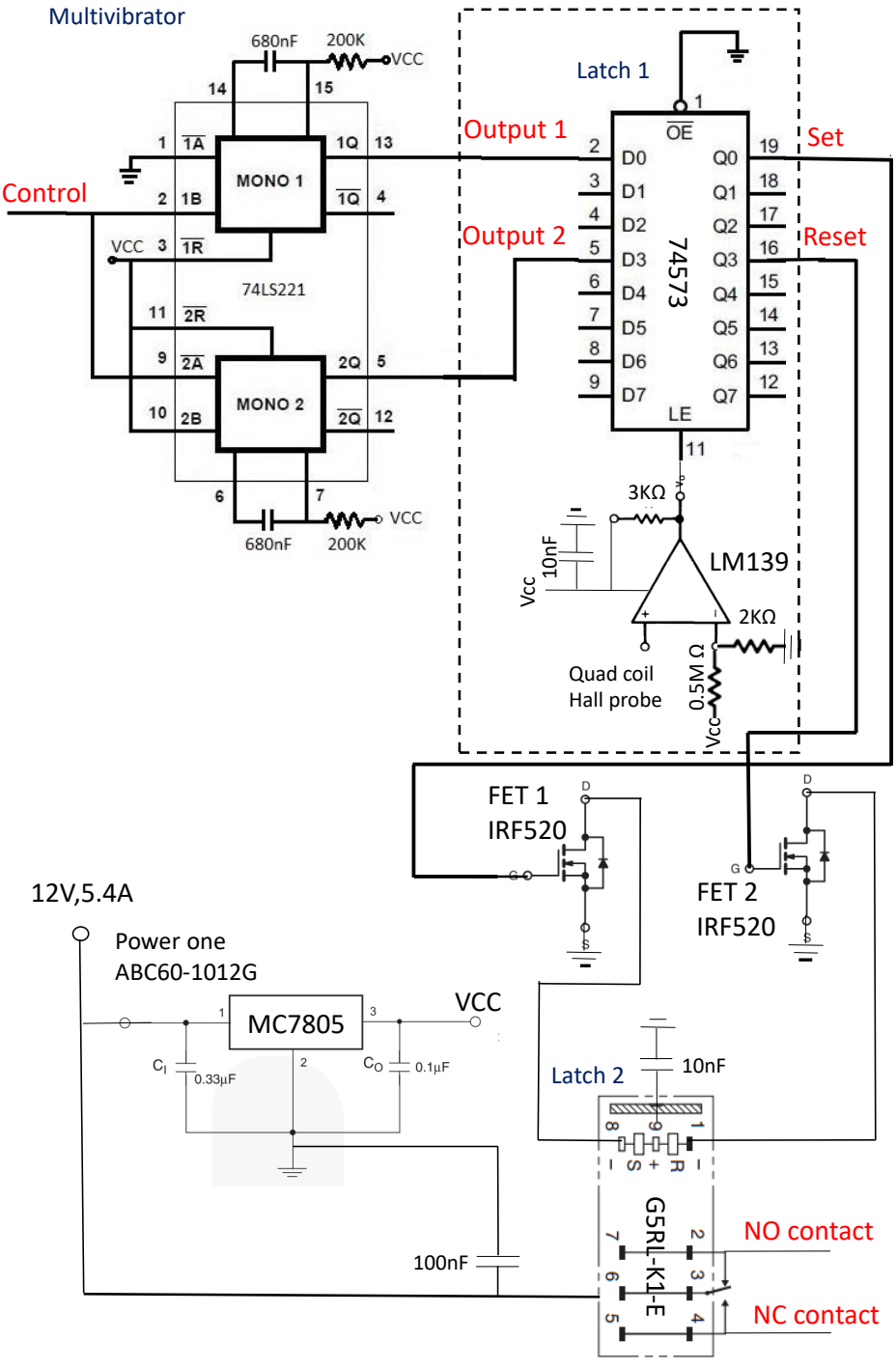

Figure 2.11: Circuit diagram of the digital circuit for controlling the mechanical relays.

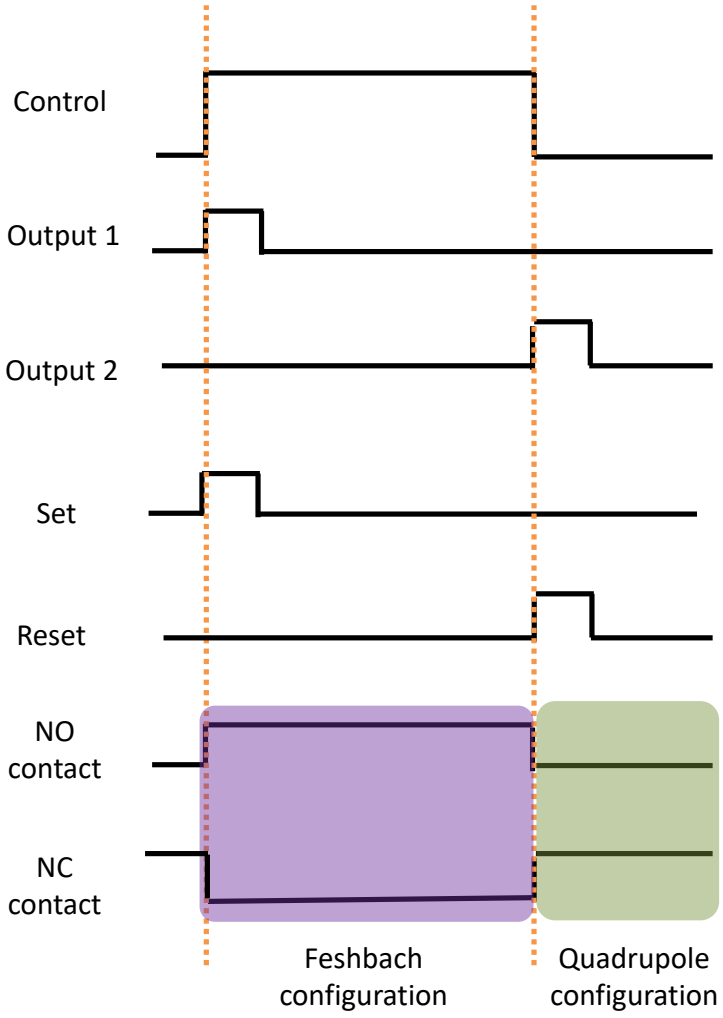

Figure 2.12: Timing diagram for the digital control circuit.

Table 2.2: Table for Feshbach coil current vs. multiplexer setting. Computer digital lines 45, 46, and 47 are used to select the input line.

#45	#46	#47	Corresponding current(A)	
1	1	0	Variable	Coarse variable current control
1	0	0	36.5	Preparing $m_F = -9/2$
0	1	1	199.75	Near Feshbach
0	0	1	208	Non-interacting
0	1	0	237	Far from resonance, for evaporation

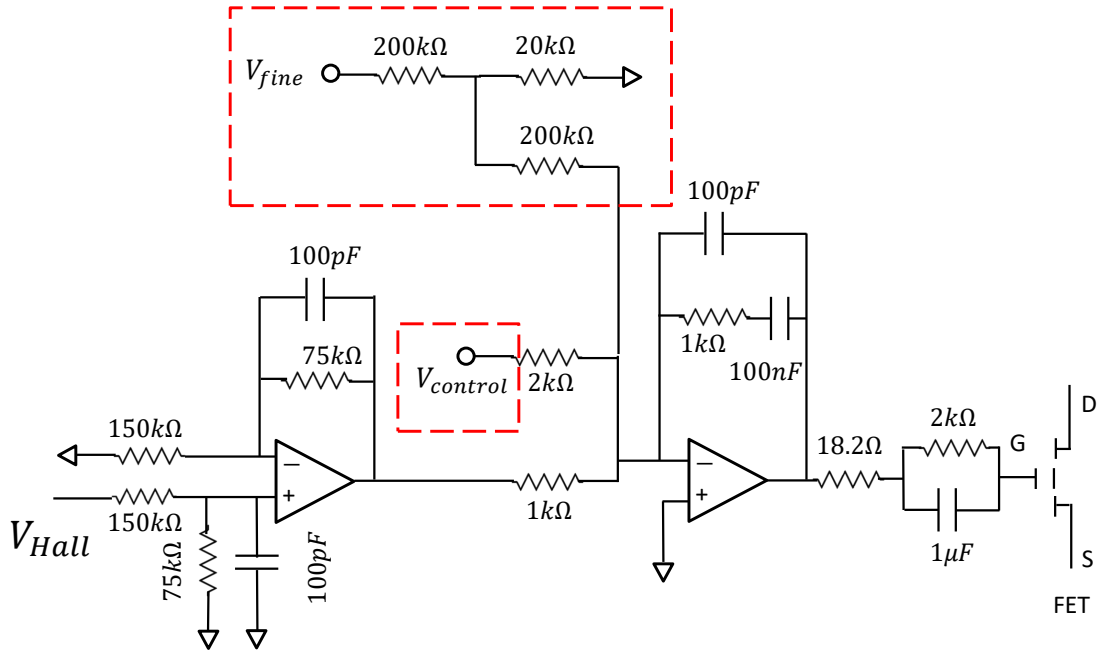

Figure 2.13: Circuit for servoing the current in the magnetic coils. The red dashed squares highlight the changes we made to the originally installed circuit in the experiment. The control voltage V_{control} was directly from a computer output analog channel. Now it is taken from the output of the precision voltage reference circuit (Fig. 2.14). V_{fine}, which is derived from the DAQ board, was added to fine tune the magnetic field within a small range.

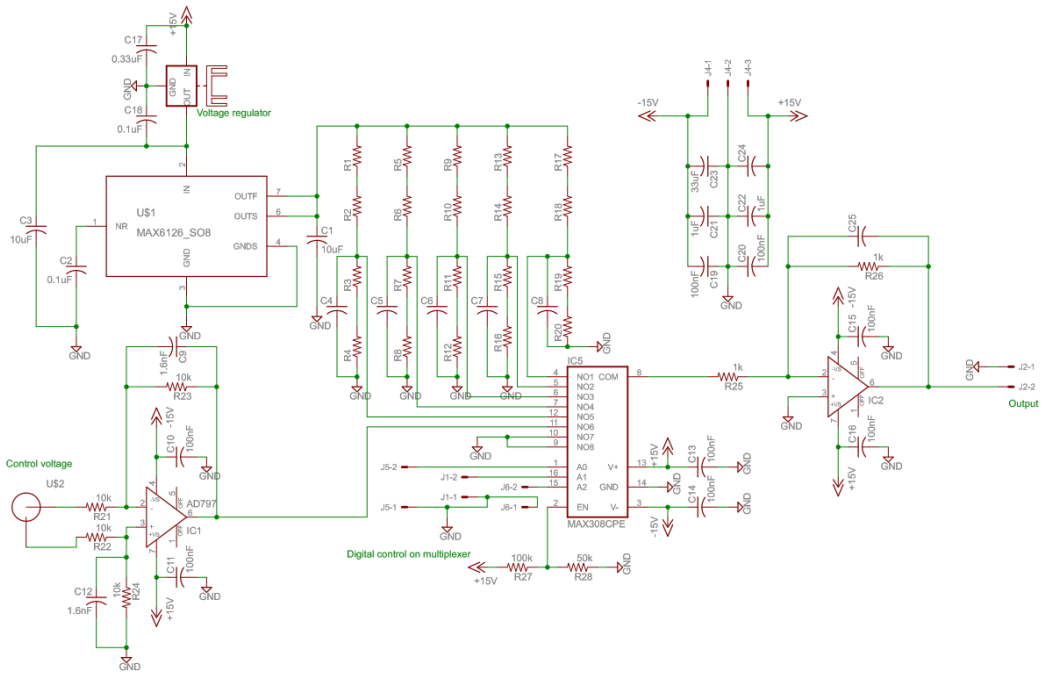

Figure 2.14: Precision voltage control circuit designed for providing a stable magnetic field.

operational amplifier (AD711) is connected to the V_{control} port, as labeled in Fig. 2.13. In addition, a fine tunning channel is added to the servo circuit (labeled as V_{fine} in Fig. 2.13). V_{fine} is derived from a computer analog output channel that is divided by a factor of 11 using resistors. It is used for precisely adjusting the current in the Feshbach coils within a small range. After using this precise voltage control circuit, the magnetic stability has been enhanced to approximately 8mG near the Feshbach resonance.

Realignment of OT and lattice beams

Before we changed the magnetic trap configuration, the center of the optical dipole trap was not aligned with the center of the Helmholtz coils. In order to obtain a homogeneous magnetic field at the atoms, we must find the position of the center of Helmholtz coils and realign the crossed optical dipole trap to it.

An approximate measurement of the center position of the Helmholtz coils can be done by loading atoms into a quadrupole magnetic trap formed from the coils. By disconnecting P3 and P4 in Fig. 2.10 and moving the P3 cable to P4, the coils can be connected in a quadrupole trap configuration. The center of this quadrupole magnetic field can be measured by trapping atoms in it.

Fine alignment of the OT position to the center of the Helmholtz coils can be performed using two methods. The first method is straightforward: by comparing the time-of-flight curves with and without currents applied to the coils, the gradient due to the magnetic field can be obtained. The second method

involves comparing the in-trap position of the atoms in a low power optical trap with and without currents applied to the coils. If a magnetic gradient is present (because the OT is not aligned to the center of the coils), the position of the potential minimum will shift. Using the optical trap frequencies and the measured displacement of the in-trap position of the atoms, the gradient from the magnetic field can be calculated. Fig. 2.15 plots the dependence of the magnetic gradient (at 200A) on the distance from the Helmholtz coil center (based on our best knowledge of coils geometry). This figure provides guidance on which direction the crossed optical trap should be moved to align the OT center.

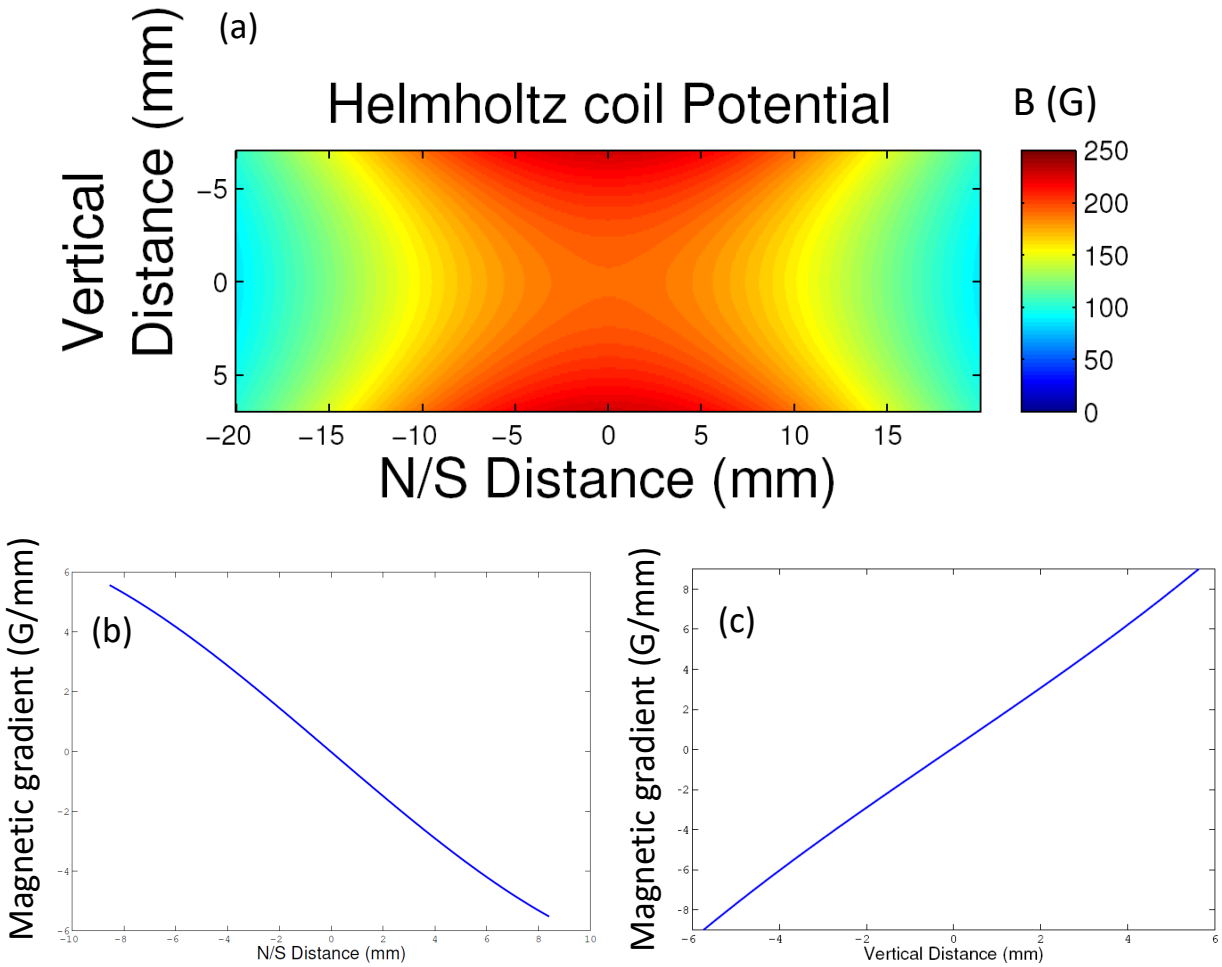

Figure 2.15: (a): Magnitude of the magnetic field generated by the Helmholtz coils in the y-z plane at 200A. Gradients of the magnetic field are plotted in unit of G/mm (b): along the z-direction (north-south in the lab), and (c): along the y-direction (up-down).

2.3.3 Radio-frequency coil for preparing spin mixtures

The Feshbach resonance in ^{40}K we use occurs between atoms with magnetic quantum numbers $m_F = -9/2$ and $m_F = -7/2$. Atoms with $m_F < 0$ are not confined in a magnetic trap. Therefore, after evaporatively cooling the atoms in the QUIC trap with $m_F = 9/2$ and $m_F = 7/2$ atoms and loading these two spin components into the crossed optical dipole trap, we transfer them to the $m_F = -9/2$ and $m_F = -7/2$ states by a radio-frequency sweep, in order to access the Feshbach resonance.

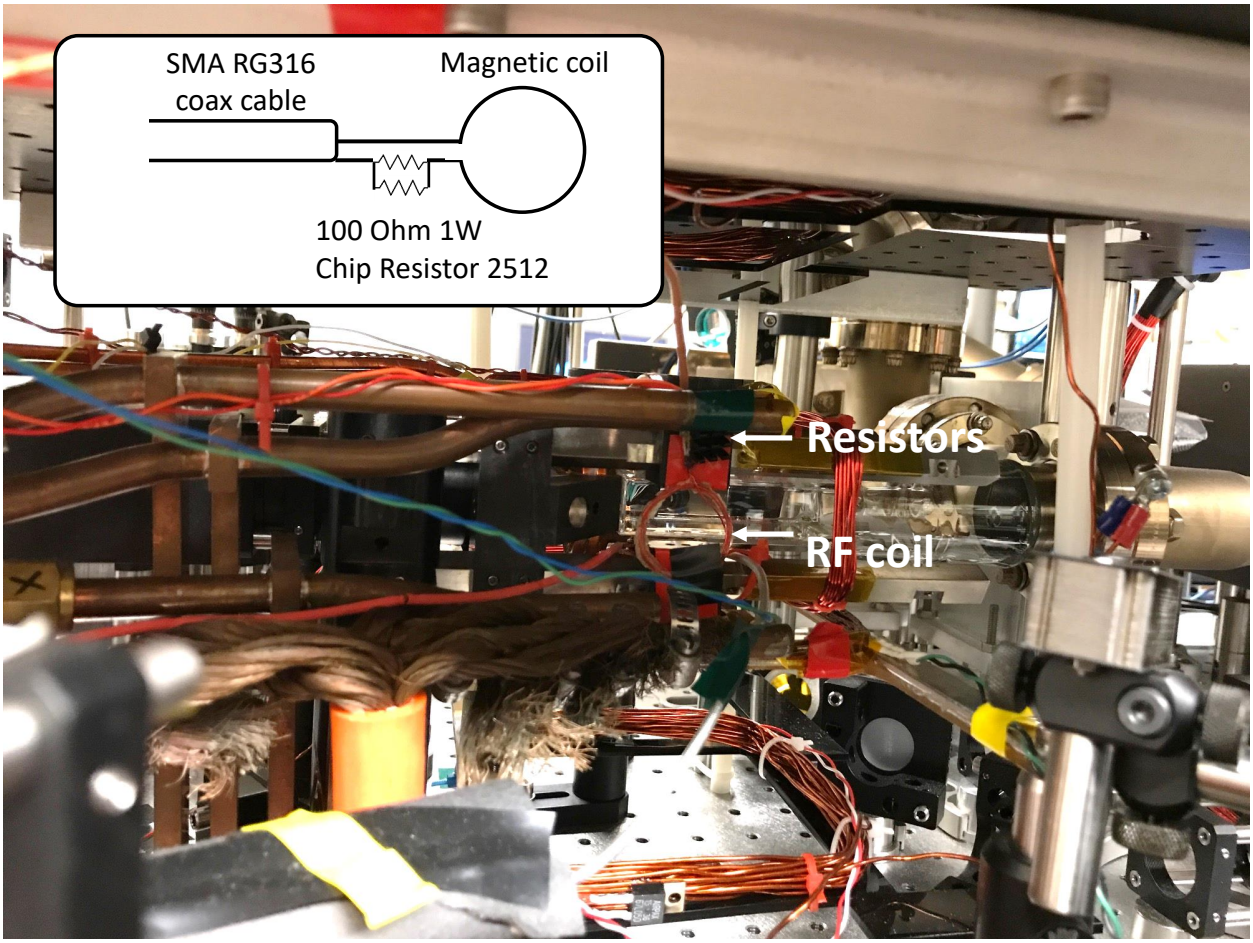

Figure 2.16: A photo showing how the radio-frequency coil is mounted. The inset shows a schematic of the connection of the RF coil to an SMA coax cable.

A small RF coil, made with 4 turns of Kapton coated magnetic wires, is installed close to the science cell (approximately 4cm) as shown in Fig. 2.16. A radio frequency signal is generated using a 300MHz direct digital synthesizer (DDS, Analog Devices AD9854 with phase coherent frequency sweeps), and amplified by a 5W amplifier (ZHL-5W-1, Mini-Circuits). Two high power 100Ω resistors (chip resistor 2512), soldered back-to-back in parallel, are used for termination. Fig. 2.17 plots the sample data for Rabi oscillations between the $|F = 9/2, m_F = -9/2\rangle$ and the $|F = 9/2, m_F = -7/2\rangle$ states at $|\vec{B}| \approx 110$G. The RF power measured

after the $5W$ amplifier for these data is 32dBm, and the π-time of this Rabi oscillation is ≈ 0.15ms.

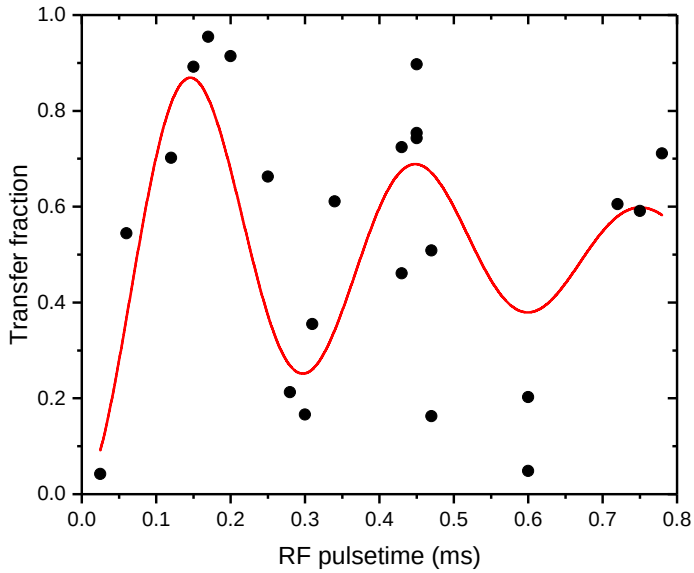

Figure 2.17: Rabi oscillations between the $|F = 9/2, m_F = -9/2\rangle$ and the $|F = 9/2, m_F = -7/2\rangle$ states at approximately a 110G magnetic field. The red curve is a fit to a damped sinusoidal function.

In our experiment, this AD9854 DDS is needed for multiple purposes. In addition to driving the radio-frequency transitions between different m_F states, it also drives one of the Raman beam AOMs (the other Raman AOM is driven by an AD9959 DDS, the frequency of which is usually fixed), and it serves as a reference frequency for the voltage controlled oscillator (VCO, Mini circuits ZX95-2500W-5+) that drives the hyperfine transitions between $F = 9/2$ and $F = 7/2$ manifolds. There is no time conflict between these applications for our current sequence. Two RF switches (ZX80-DR230-S+) and an RF splitter (ZFSC-2-1W+) are used to control the frequency chain used for these purposes (Fig. 2.18).

2.4 Beat-note locking

To have access to Feshbach-related physics, we need to take images at both high and low magnetic fields. The difference between the frequencies for imaging at low and high magnetic field is larger than 300MHz, because of the Zeeman shift (Fig. 2.19). In addition, we need a large tuning range for the probe beam in order to image atoms with different m_F at high magnetic field. To fulfill these requirements, we implement a frequency beat-note locking scheme. The difference in frequency of two laser beams with the same polarization is measured by overlapping them onto a fast photodetector. One of the laser beams (the "master laser") has

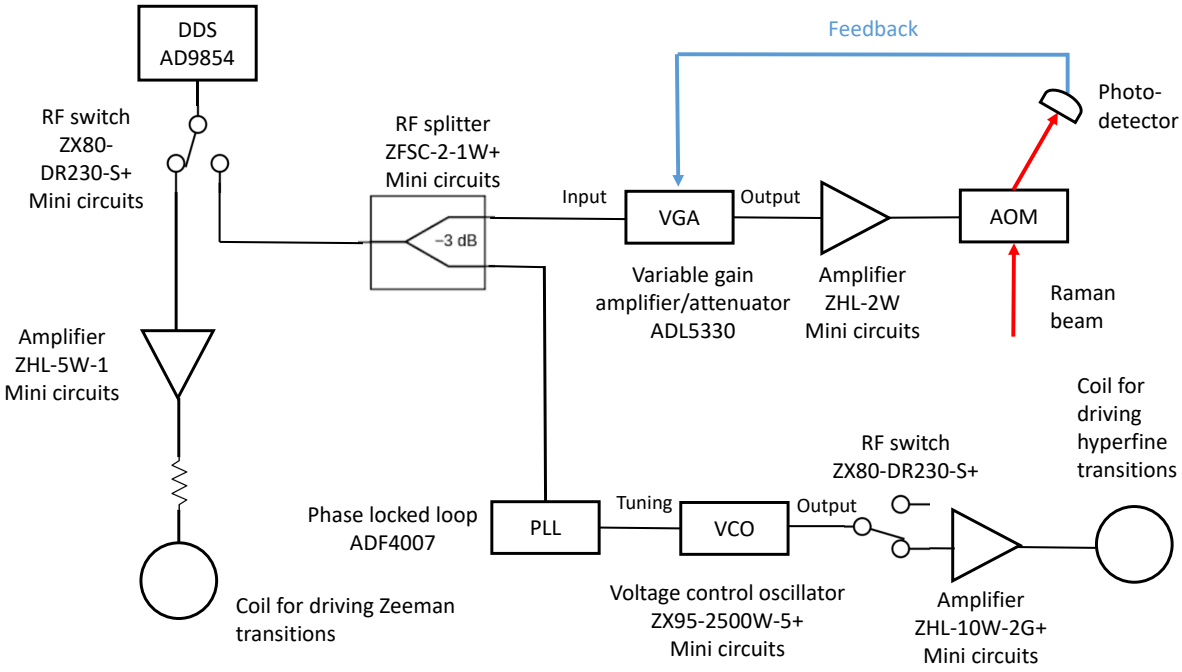

Figure 2.18: Schematic of the radio-frequency chain. A digital synthesizer (AD9854) is the radio-frequency source. The three chains shown here are for (1) driving transitions between different m_F states, (2) controlling one of the Raman AOMs, and (3) providing a reference for a PLL board that drives the hyperfine transition between the $F = 9/2$ and the $F = 7/2$ manifolds.

been frequency stabilized to an atomic transition. The comparison of the beat frequency to a reference is used as an error signal for frequency locking the other laser.

2.4.1 Optics for beating two lasers

Fig. 2.20 shows the frequencies of the features for the $D2$-line spectroscopy of the three isotopes of potassium. From 2009 to 2016, the trap laser was offset locked to the $F = 1 \rightarrow 4P_{3/2}$ transition (blue arrow in Fig. 2.20) for ^{41}K via modulation spectroscopy using a potassium vapor cell. The frequency offset was provided by double-passing the pump beam through an acousto-optic modulator (AOM), which enabled an offset frequency from 180MHz to 240MHz. The probe beam for imaging goes through another AOM, which shifts the frequency by an additional 65MHz. The total frequency offset could cover the transition frequency difference between $F = 1 \rightarrow 4P_{3/2}$ in ^{41}K and $F = 9/2 \rightarrow 4P_{3/2}$ in ^{40}K at low magnetic field. For this offset locking scheme, the tuning range of the probe beam for imaging was limited to 60MHz.

Fig. 2.21 is a schematic for the beat-note locking system. Another external cavity diode laser was added to our experiment (labeled as "Trap ECDL" in Fig. 2.21). This trap laser, which is an anti-reflection coated laser diode (Eagleyard EYP-RWE-0780-02000-1300-SOT12-0000) mounted in a home-made external cavity, is beat against the master laser (Vortex TLB-6900). Each is focused by a lens and overlapped on an AC-coupled fast photodetector (ET2030-A).

To have a beat-note frequency around 1GHz (which a working frequency range preferred by commercial RF electronics), we use the -1 diffracted order from the AOM. The master laser is locked to the $F = 9/2 \rightarrow 4P_{3/2}$ crossover in ^{39}K (black arrow in Fig. 2.20), which has a high signal-to-noise ratio due to the higher abundance of ^{39}K. For the MOT loading stage, the beat-note frequency is 1.02GHz. Fig. 2.22 shows a photo of the beat note power spectrum. The remaining light of the trap laser is sent to a tapered amplifier (EYP-TPA-0765-01500-3006- CMT03-0000), and then split into two beams for the MOT and probe beam.

2.4.2 Locking electronics

The beat-note signal from the photodetector is sent to a commercial phase locked loop (PLL) circuit (Analog Devices, ADF4007). Fig. 2.23 shows the electronics for producing the error signal, with the reference frequency coming from a DDS (Analog devices, AD9959). An zero crossing appears in the error signal if $f_{\mathrm{ref}}/8 = f_{\mathrm{RF}}/16$ (where f_{RF} is the beat note frequency from the fast photodetector, and f_{ref} is the reference frequency from DDS), as shown in Fig. 2.23. This steep and step-like feature is a desirable signal for locking.

The error signal from the output of the PLL is sent to a locking circuit (designed by Philip Russ). Two feedback loops are used to adjust the piezo voltage and current applied to the trap laser diode. The piezo

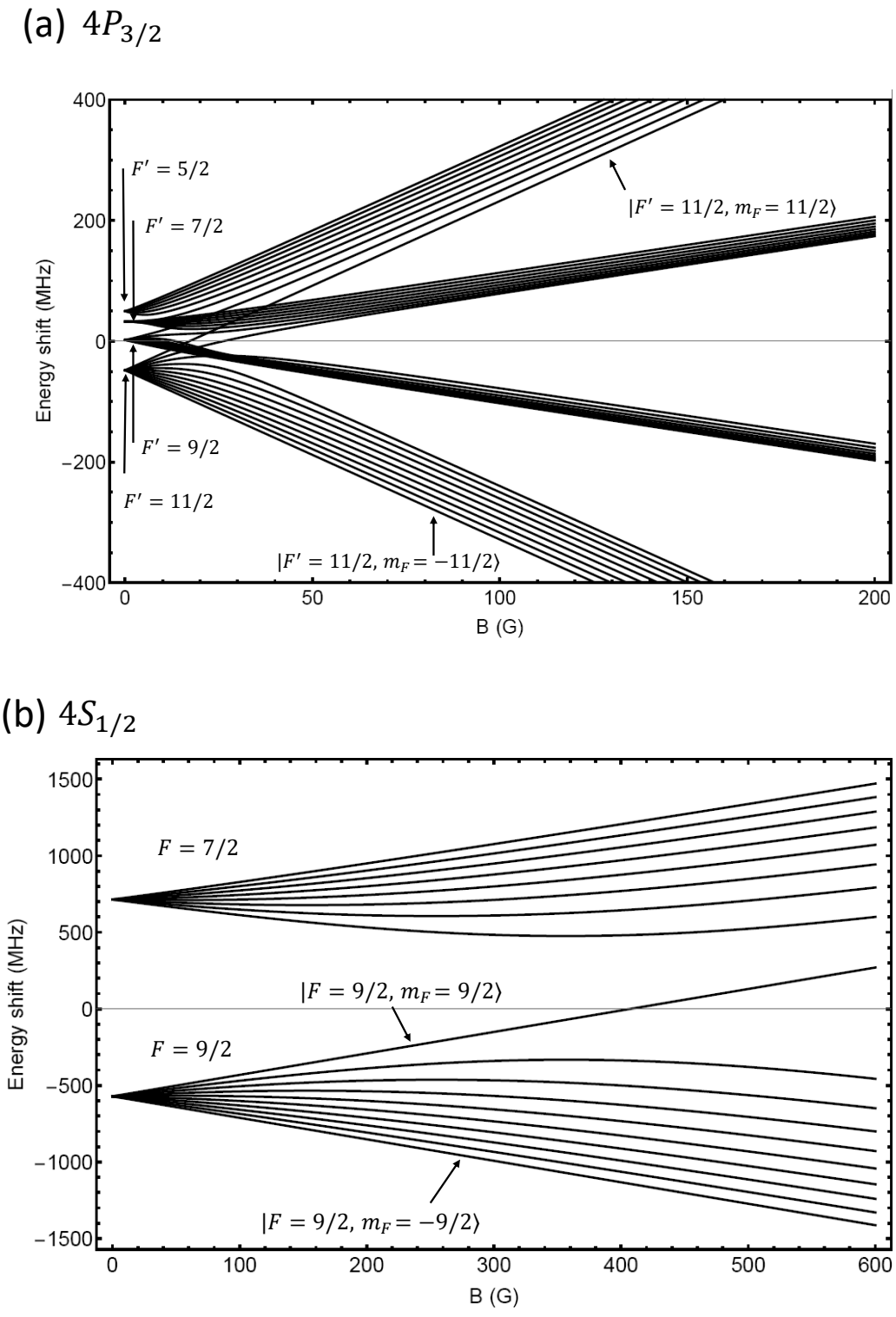

Figure 2.19: Zeeman energy shifts as a function of magnetic field for (a) the $4S_{1/2}$ ground state and (b) the $4P_{3/2}$ state.

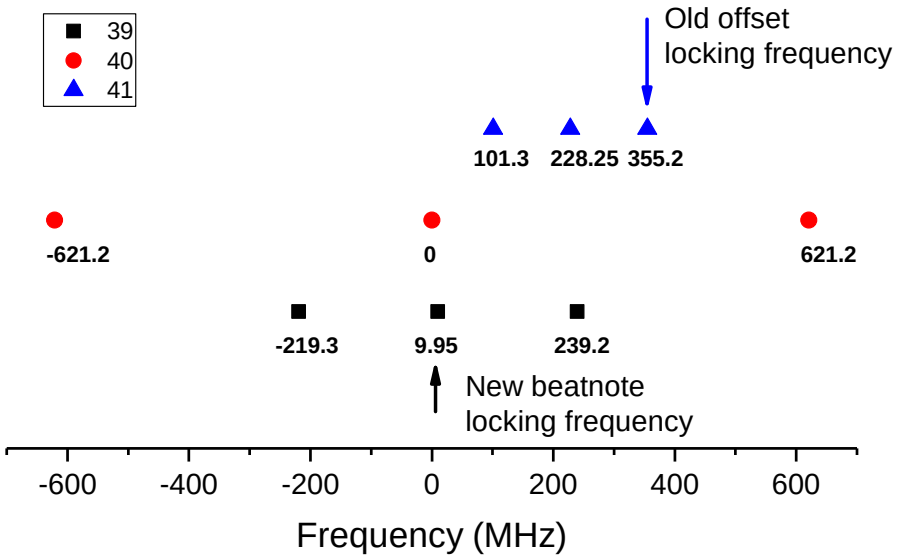

Figure 2.20: Features of D2-line transitions in potassium. For each isotope, there exists three spectroscopic features. Our previous offset locking scheme was locked to the $F = 1 \rightarrow 4P_{3/2}$ transition for ^{41}K. For the new beat-note locking scheme, the master laser is locked the crossover feature for ^{39}K.

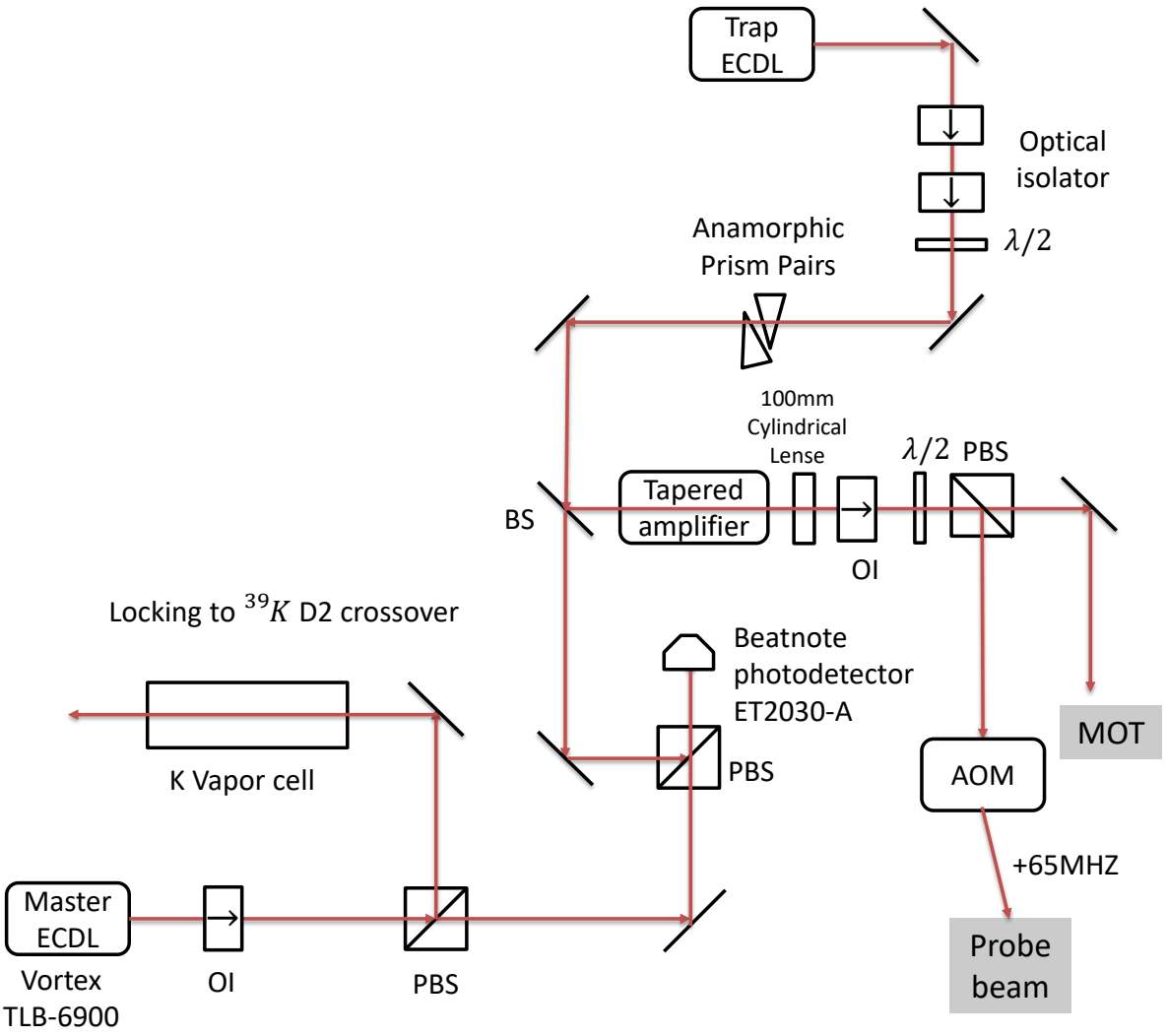

Figure 2.21: Optical system for beat-note locking. The "master" laser is an ECDL (Vortex TLB-6900), which is locked to the crossover feature of the D2 transition in ^{39}K via standard frequency modulation spectroscopy. The trap laser is a single-mode anti-reflection coated laser diode mounted in a home-made external cavity. Some of its light is picked off to beat with the trap laser. The remaining light is sent to a tapered amplifier to create the MOT trapping light and for the imaging probe beam.

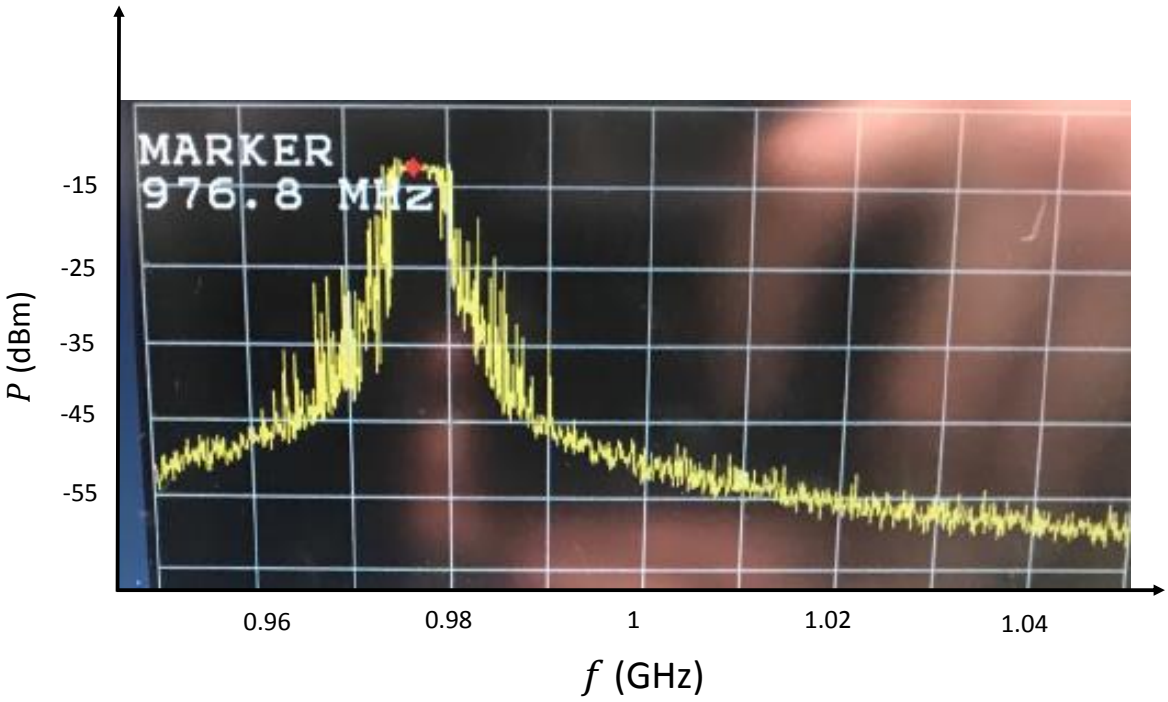

Figure 2.22: Beat note power spectrum.

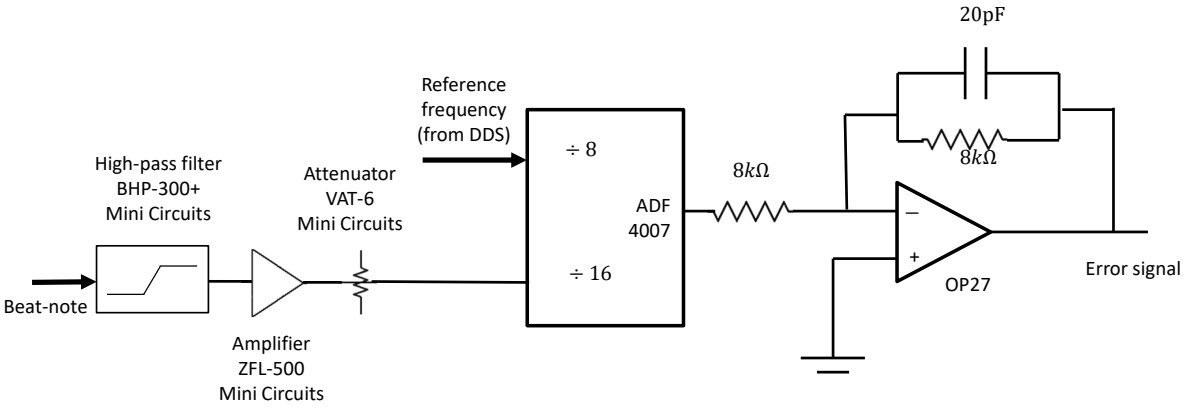

Figure 2.23: Circuit and divider setting for the PLL. The error signal is sent to a locking circuit.

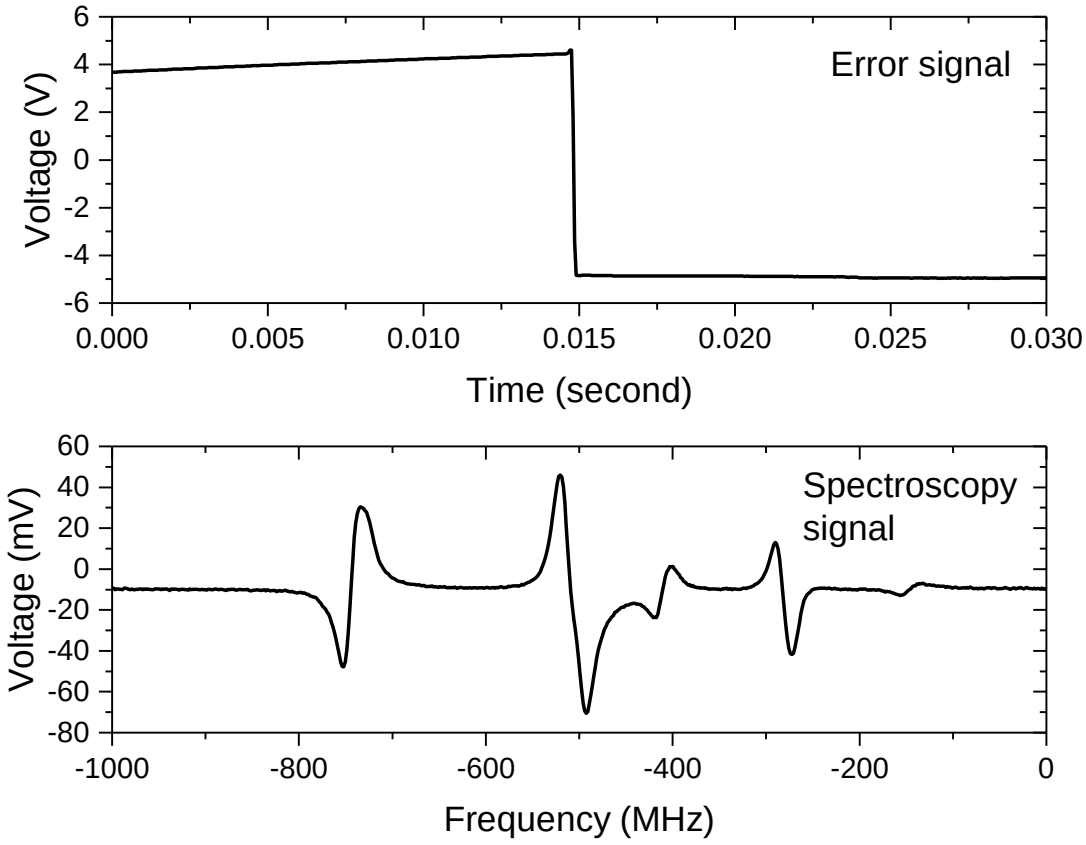

Figure 2.24: The beat-note error signal (top) with the voltage applied on piezo scanning, and the averaged standard saturated spectroscopy signal (bottom, used for master laser frequency stabilization). The trap laser frequency is stabilized to the falling edge of the error signal.

feedback loop is designed to respond to slow drift in the error signal, while the current feedback loop is for removing high frequency noise in the error signal. The values of resistors and capacitors in both feedback loops were optimized to minimize the amplitude of error signal while the laser is locked.

2.4.3 Reducing laser frequency noise

Just after switching to using beat-note locking, the frequency stability of the trap laser was degraded: the fluctuations on the MOT florescence lever was much higher (around 10%) and the fluctuation on the measured total number of atoms at the end of magnetic evaporative cooling was more than 50%. Normally the fluctuation should be around $1-2\%$ in MOT fluorescence level and the fluctuation in measured number of atoms is around $5-10\%$. We tracked down several issues and improved the laser frequency stability.

- Acoustic noise

  We noticed that the trap laser was very sensitive to acoustic noise. The MOT fluorescence level would fluctuate more than 50% when people spoke nearby the optical table. It turned out that the dimensions of the sorbothane pads under the ECDL were not optimal. We changed their dimensions based on Thorlabs' "feet selection guide."

- Optimizing gain settings of the feedback loops

  We found the best benchmark to test the servo quality is to mix the beat-note frequency down to approximately 10MHz and perform a fast Fourier transform (FFT) of this signal using an oscilloscope (Agilent Technologies MSO7034B). The center of this FFT spectrum peak should be stable to approximately 100kHz level and the full width at half maximum should be narrower than 3MHz (Fig. 2.25). Fine tunning of the gain settings for the piezo and current feedback loops can be done by adjusting the resistor values in the feedback loops while looking at this FFT spectrum. Fig. 2.25 shows the FFT spectrum after optimization. In this case, the standard deviation in the total number of atoms after magnetic evaporative cooling is less than 10%.

2.5 Imaging at high magnetic field

We use absorption imaging to obtain information such as the density or momentum distribution. The attenuation of the intensity for the imaging beam in the presence of saturation effects and for a resonant imaging light is [51]

$$\frac{dI(z)}{dz} = -n(x,y,z)\ \sigma_a\ \frac{I(z)}{1+I(z)/I_{\rm sat}}, \tag{2.9}$$

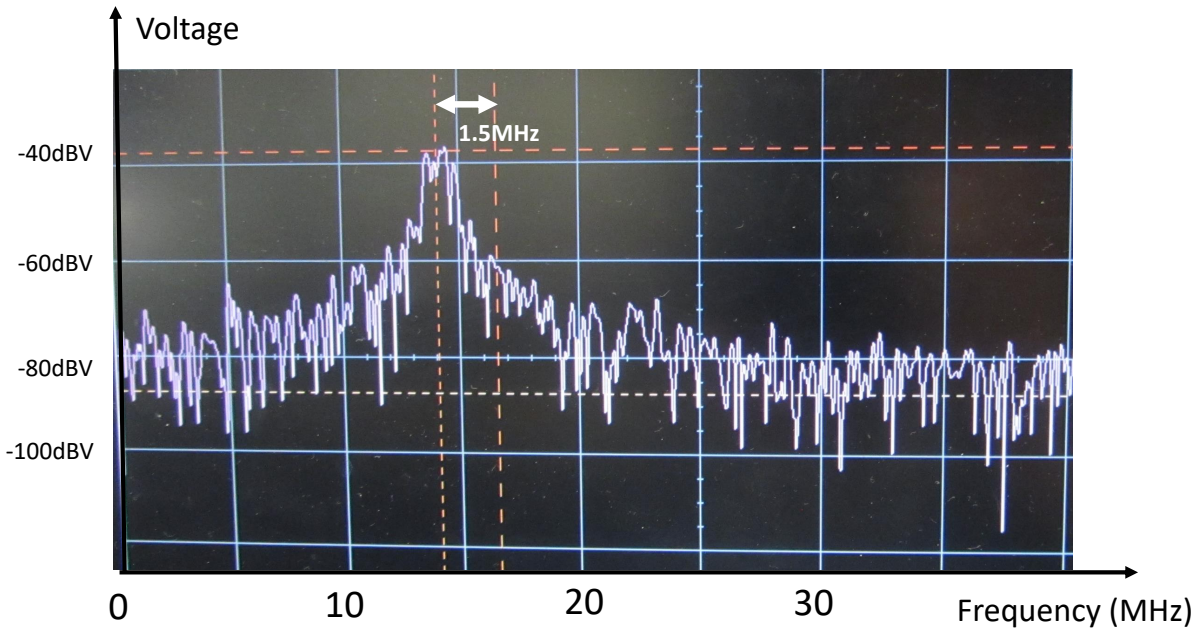

Figure 2.25: Fast Fourier transformation of beat-note frequency after mixing down to approximately 10MHz. The width and the peak stability of this spectrum directly reflects the quality of beat-note locking, and guides the optimization on gain settings for the locking circuit.

where $n(x, y, z)$ is the density of atoms, $\sigma_a = 3\lambda^2/2\pi$ is the resonant cross-section, and $I_{\text{sat}} = \pi hc\Gamma/3\lambda^3$ is the saturation intensity, with Γ the natural linewidth of the transition and c the speed of light.

To minimize the non-linear dependence of the absorption on intensity, a small I/I_{sat} is preferred. With low-intensity absorption imaging, the probe light intensity becomes $I = I_0 e^{-OD}$ after passing through the gas, where I_0 is the initial light intensity and $OD = \sigma_a \int n(x, y, z)dz$ is the optical depth (assuming the direction of the imaging beam is along z).

To obtain OD in our experiment, three images are taken at the end of each experiment sequence. For the first image (atom image A), resonant light is applied and the shadow of the atoms is imaged onto a CCD camera (Princeton Instruments Pixis 1024BR). The subsequent other two images are taken without atoms (light image L) and without laser light (background image D). The optical depth OD is determined as:

$$OD = -\ln(\frac{A - D}{L - D}). \tag{2.10}$$

In practice, we compromise between increasing the signal-to-noise ratio at high I and minimizing the non-linear effect by working at small I. For example, we take images at low I for temperature measurements, where the results are sensitive to the density profile of atoms. Other images, such as measurements on trap frequencies, may be taken at high probe power. The measured total number of atoms will be rescaled to get the correct number based on the ratio of OD/OD_m (where OD_m is the measured optical depth). As an example to obtain OD/OD_m, Fig. 2.26 plots the number of counts measured by the CCD camera per pixel for the imaging probe beam (which is proportional to the imaging light intensity) vs. the measured peak OD of the gas (which is proportional to the measured total number of atoms). By fitting the data to the expected form [52]:

$$I = I_{\text{sat}} \frac{OD - OD_m}{1 - e^{-OD_m}}, \tag{2.11}$$

we obtain OD/OD_m at given imaging light intensity.

Until recently, we imaged exclusively at low magnetic field. The quantization coils, as shown in Fig. 2.29, provide a magnetic field along the probe beam propagation direction. The polarization of the probe beam is σ^+, which drives the transition between the $|F = 9/2, m_F\rangle$ and the $|F' = 11/2, m_{F'} = m_F + 1\rangle$ states.

Now we image at high magnetic field to access Feshbach-related physics. The magnetic field produced by our Feshbach coils is perpendicular to the propagation direction of the probe beam. Therefore, the polarization of the probe beam used at low magnetic field becomes a combination of $1/2\pi$ light and $1/2$ linear polarized light in the atomic frame at high field; therefore, it cannot be fully absorbed. This limits the maximum OD to be $\ln(1/2) = 0.69$ (Fig. 2.27).

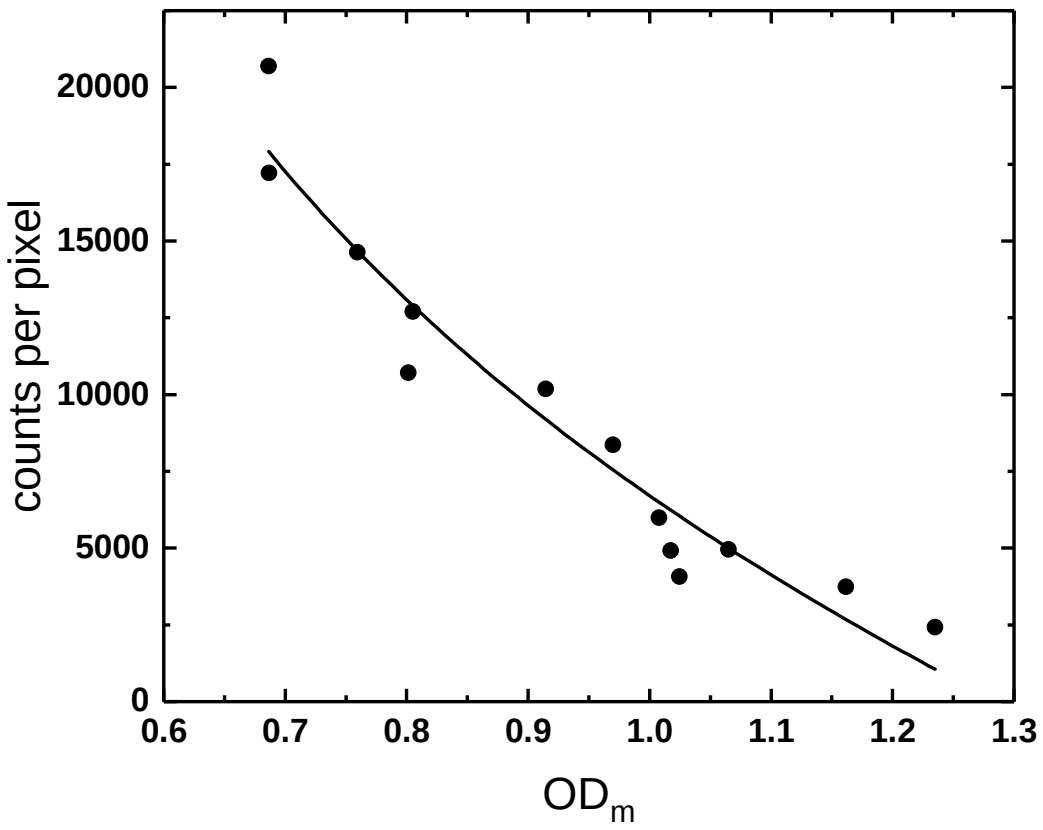

Figure 2.26: The effect of $I/I_{\rm sat}$ on the measured optical depth. The imaging light intensity, proportional to the measured counts per pixel in the CCD camera, is plotted vs. the measured peak OD, which is proportional to the measured number of atoms. A fit (solid line) to function Eq. 2.11 allows us to extract the real number at a given imaging light intensity by rescaling the measured number by a factor of OD/OD_m.

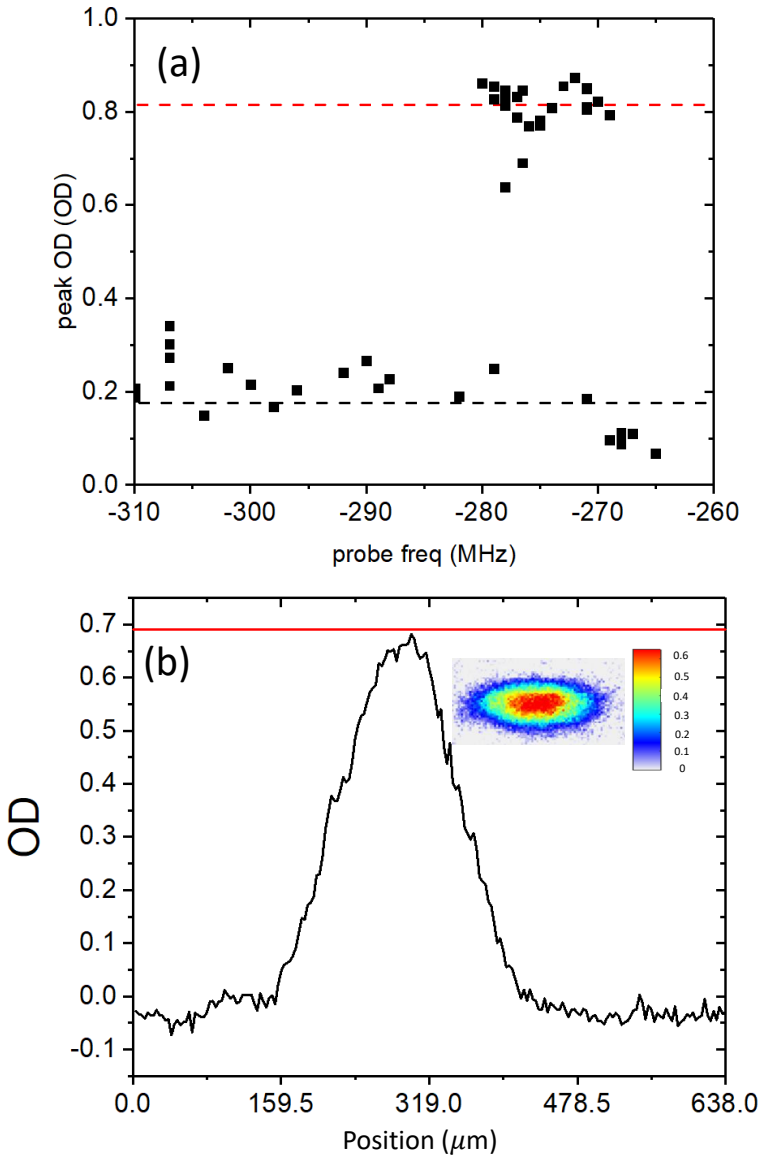

Figure 2.27: Saturation of OD at high magnetic field imaging ($|\vec{B}| \approx 180G$) with probe beam parallel to the magnetic field direction. (a): Maximum OD at different probe frequency. The saturation of maximum OD and a non-zero background are evident. (b): A slice cut through the center of the time-of-flight imaging with probe frequency at -275MHz. The red line marks the theoretical maximum OD, which is $\ln(1/2) = 0.69$. The inset shows the time-of-flight imaging of the atomic gas.

We can eliminate this imaging problem by using linearly polarized light. When the propagation direction of the probe beam is not parallel to the magnetic field, the usual convention for σ^+ and σ^- light should not be applied. This basis is not the correct for describing the electric dipole oscillation in the atom if there is an angle between the quantization axis and the light propagation direction. In the case that both the polarization direction and the light propagation direction are perpendicular to the magnetic field, linearly polarized light can be fully absorbed for a transition with $\Delta m_F = \pm 1$. In this case, the absorption cross section is reduced by a factor of two.

An easy way to understand this is to consider a reverse process: atoms at position $(x, y, z) = (0, 0, 0)$ go through transitions with $\Delta m_F = +1$ and therefore radiate electric fields. The radiated electric field is [53]

$$\vec{E} \propto [\hat{\theta}\cos\theta - i\hat{\phi}e^{-i\phi}]\cos(\omega t), \tag{2.12}$$

with spherical coordinates (r, θ, ϕ). The unit vectors $(\hat{r}, \hat{\theta}, \hat{\phi})$ are a right-handed set. The polarization of the electric dipole radiation depends on the angle of observation (Fig. 2.28). In the direction $\theta = 0$, the radiation field has a polarization as $\hat{\theta} - i\hat{\phi}$, which is right-circularly polarized. In the x-y plane, *i.e.*, $\theta = \pi/2$, the radiation field is polarized along $-i\hat{\phi}$, which is horizontally polarized (within the x-y plane). The time averaged intensity of $|\vec{E}|^2$ with $\theta = \pi/2$ is half as for the $\theta = 0$ case.

Therefore, in the case that the probe beam propagates perpendicular to the magnetic field, if its polarization is linear and within the $x - y$ plane, the light can be fully absorbed by atoms and drive transitions between $m_F \to m_F + 1$. The absorption cross section is a factor of two smaller compared with the case that a σ^+ probe beam propagates along $\hat{z}$.

In order to have the freedom to image different spin components at low and high magnetic field, we added a half and quarter wave plate in the path of probe beam, as shown in Fig. 2.29. The angle between the fast axis of these two wave-plates is fixed to be 45°. By adjusting the rotation mount that holds this pair of wave plates, the polarization of the probe beam can be σ^+ or σ^- (defined at low magnetic field, with $\vec{B}$ parallel to light propagation direction); or linear polarized along x-direction, which is used for imaging at high magnetic field. Fig. 2.29 gives the relation between the rotational mount angle setting and the polarization of light.

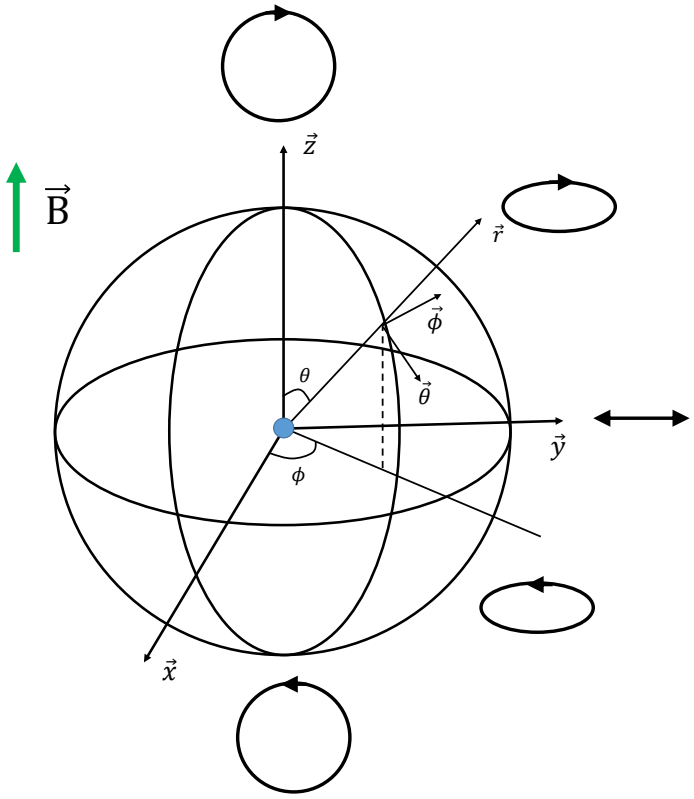

Figure 2.28: A schematic of the polarization for electric dipole radiation with $\Delta m_F = +1$. The polarization depends on the angle of observation. As θ changes from 0 to $\pi/2$, the polarization of the radiation field changes from right-circularly polarized to elliptical polarized, and to a linear polarized field. The quantization axis of the atoms is along the magnetic field direction $\hat{z}$.

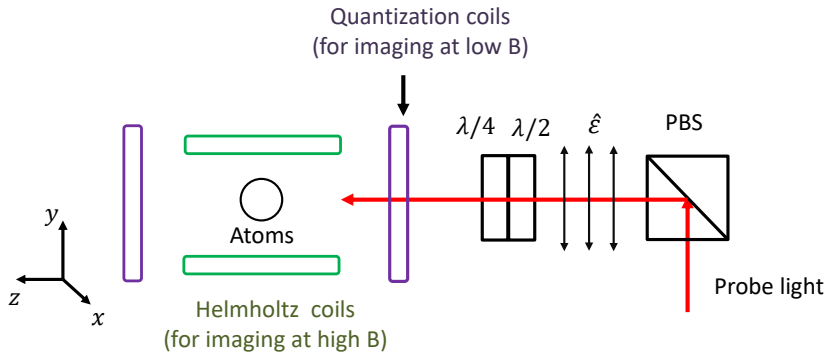

Figure 2.29: Schematic of the imaging system. The polarization of the probe beam after the polarizing beam splitter (PBS) is along the vertical direction (black arrows). A combination of a half-wave plate and a quarter-wave plate is placed after the PBS to adjust the polarization for imaging. The angle between the fast axis of these two wave plates is fixed to be 45°. This pair of wave-plates is mounted on a rotation mount, and the fast principle axis of the half-wave plate is aligned to position "0" on the rotation mount. At low magnetic field, by rotating the mount to be 90° or 0°, the probe beam can become σ^+ or σ^- polarized, which are used for imaging $|F = 9/2, m_F = 9/2\rangle$ (coupling to $|F' = 11/2, m_{F'} = 11/2\rangle$) or $|F = 9/2, m_F = -9/2\rangle$ (coupling to $|F' = 11/2, m_{F'} = -11/2\rangle$) respectively. At high magnetic field, the rotation mount is adjusted to 45° to produce a probe beam that has a linear polarization, but rotated by 90° (*i.e.*, pointing into the paper).

Chapter 3

Toolbox for quantum simulation

3.1 Introduction

The ambitious goal of quantum simulation is to simulate unsolved puzzles in quantum many-body problems that exceed the capabilities of classical supercomputers. The simulator can be made from any quantum elements that emulate the relevant Hamiltonian. A proper mapping between an experimental system to an effective Hamiltonian is essential for understanding the "program" running on the quantum emulator. For fermions trapped in an optical lattice, the corresponding Hamiltonian is the famous "Fermi-Hubbard model," as discussed in the first section of this chapter.

Moreover, we also need to develop experimental probes to "read out" a quantum emulator, and interpreting the results requires a theoretical framework. This chapter introduces the method we use to infer thermodynamic properties of a lattice gas, and we develop a semiclassical kinetic theory for the motion of atoms in an optical lattices.

The last part of this chapter gives a brief introduction to Green's function, which is a widely used theoretical method in condensed matter physics. The Green's function contains information of how a system responds to external perturbation. As experimentalists, knowledge of the Green's function helps us to relate experimental observables to the underlying microscopics. In Chapter 4, we discuss how dynamical mean-field theory, which we use to infer resistivity from our measurements, uses Green's functions.

3.2 Simulating the Fermi-Hubbard model using ultracold lattice Fermi gases

3.2.1 Optical lattices

By counter-propagating two laser beams with the same frequency and polarization, a standing-wave with period $\lambda/2$ is formed. The atoms experience a periodic potential proportional to the local intensity because

of the AC Stark effect. In our apparatus, three-dimensional cubic optical lattices are created by three pairs of counter-propagating laser beams, intersecting at the position of atoms (Fig. 3.1(a)). The lattice beams are generated from a Tekhnoscan TIS-SF-07 Ti:Sapphire laser pumped with 532nm light generated by a Coherent Verdi V18. Each beam passes through an acousto-optical modulator, which shifts its frequency by -83MHz, $+83$MHz, and -80MHz. Different frequencies are necessary to prevent cross-dimensional interference between lattice beams. A general form for the potential of this cubic optical lattice is

$$V_{\mathrm{L}}(x,y,z) = V_{L_x}\cos^2(k_L L_x) + V_{L_y}\cos^2(k_L L_y) + V_{L_z}\cos^2(k_L L_z). \tag{3.1}$$

Here, V_{L_i} and L_i $(i = x, y, z)$ are the potential depth and the coordinates in the frame of the lattice, $k_L = 2\pi/\lambda$ is the wave-vector of lattice beams, and $\lambda = 782.2$nm for our apparatus. The lattice beams are red-detuned, and we work with $V_{L1} = V_{L2} = V_{L3} \equiv -s$, where s denotes lattice depth. The recoil energy $E_R \equiv \hbar^2 k_L^2/2m$, with atomic mass m , is a natural energy scale used for optical lattices. For our apparatus, $E_R/h = 8.15$kHz.

The alignment of these three lattice beams are roughly, but not exactly orthogonal to each other in our experiment. Our best estimates for the angles between L1 and L2, L2 and L3, L3 and L1 are 89°, 88° and 84°, respectively. The rotation matrix between the coordinates of the optical lattice $(L1, L2, L3)$ and coordinates (x, y, z) as defined in Fig. 3.1(a) is:

$$\begin{pmatrix} z \\ x \\ y \end{pmatrix} = \begin{pmatrix} 0.50 & -0.72 & 0.49 \\ 0.68 & 0 & -0.65 \\ 0.50 & -0.69 & -0.58 \end{pmatrix} \begin{pmatrix} L1 \\ L2 \\ L3 \end{pmatrix}$$

and

$$\begin{pmatrix} L1 \\ L2 \\ L3 \end{pmatrix} = \begin{pmatrix} 0.50 & 0.68 & -0.54 \\ -0.72 & 0 & -0.69 \\ 0.49 & -0.65 & -0.58 \end{pmatrix} \begin{pmatrix} z \\ x \\ y \end{pmatrix}.$$

Our lab convention is that x is along east-west, y is along up-down, and z is along north-south. Our main imaging probe beam, which propagates along $\hat{z}$ in the lab frame, is along $(1, -\sqrt{2}, 1)$ in the lattice coordinate system. Chapter 5.2 in McGehee's thesis [14] discusses the alignment procedure of the lattice beams in detail.

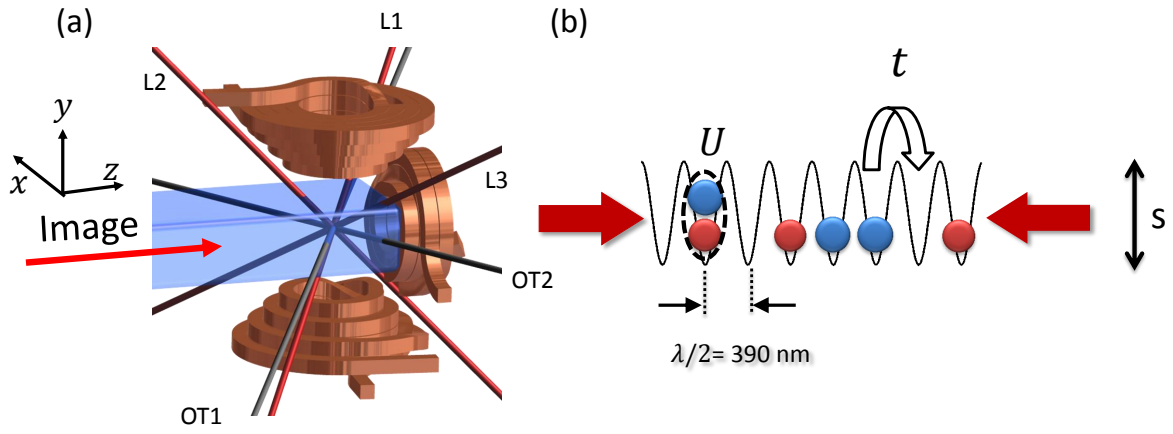

Figure 3.1: (a): Schematic of the orientation of the lattice beams relative to the (x, y, z) coordinates. The science cell and magnetic QUIC trap coils are also shown in this figure. The optical lattice beams are shown in red and optical trap beams in gray. All the beams are aligned to the position of the atomic gas. The probe beam for imaging (red arrow) travels along the z-direction. (b): A schematic of counter-propagating beams that form the lattice. Red and blue circles represent atoms with different magnetic quantum numbers. t is the tunneling energy and U is the on-site interaction energy. The ratio of U/t can be adjusted by tuning the lattice depth s.

3.2.2 Bloch waves

Generally, the eigenstates of a periodic potential $V(\vec{r})$, according to Bloch's theorem [54], have the form:

$$\psi(\vec{r}) = u_{\vec{k}}(\vec{r})e^{i\vec{k}\cdot\vec{r}}, \tag{3.2}$$

where $u_{\vec{k}}(\vec{r}) = u_{\vec{k}}(\vec{r}+\vec{R})$, and $\vec{R}$ is a lattice vector. The crystal wavevoctor $|\vec{k}| \leq k_B$, where $k_B = q_B/\hbar = \pi/d$ is the edge of Brillouin zone (BZ). The periodic function $u_{\vec{k}}(\vec{r})$ can be expanded as $u_{\vec{k}}(\vec{r}) = \frac{1}{\sqrt{V}}\sum_{\vec{K}} a_{\vec{k}}(\vec{K})e^{i\vec{K}\cdot\vec{r}}$, with V the volume of the system, and $\vec{K}$ a reciprocal lattice vector. Inserting this into the Schrödinger equation, we have

$$\left[\frac{\hbar^2}{2m}(\vec{k}+\vec{K})^2 - E(\vec{k})\right] a(\vec{k}+\vec{K}) + \sum_{\vec{K}'\neq\vec{K}} V_L(\vec{K}-\vec{K}')a(\vec{k}+\vec{K}) = 0, \tag{3.3}$$

with $V_L(\vec{K}) = \frac{1}{V}\int d^3\vec{r}V_L(\vec{r})e^{-i\vec{K}\cdot\vec{r}}$. For a standing-wave potential, $V_L(\vec{r})$ only has two frequency components in reciprocal lattice space: $V_L(|\vec{K}| = 2k_L) = V_L(|\vec{K}| = -2k_L) = -\frac{1}{4}s$ (the zero frequency component, which causes an overall energy shift, has been ignored). For a one-dimensional lattice, for given k, the elements in

the Hamiltonian matrix for this eigenvalue problem are:

$$H_{j,k} = \begin{cases} \frac{\hbar^2}{2m}(2jk_L + k)^2 & \text{if } j = k \\ -1/4s & \text{if } j = k \pm 1 \\ 0 & \text{otherwise} \end{cases} \tag{3.4}$$

Band structure

By truncating the Hilbert space, the matrix in Eq. 3.4 can be diagonalized to give the energies and eigenvectors, from which we can obtain the band structure. The cubic lattices used in this thesis are separable, and therefore the 3d band structure can be found via 1D band structure: $E_{3d,n} = E_{x,n_x} + E_{y,n_y} + E_{z,n_z}$, where n_i $(i = x, y, z)$ is the band index for the 1D band structure. Correctly labeling the 3D band structure indices requires enumerating all possible combinations of (n_x, n_y, n_z) and ordering them in energy.

To visualize the 3D bandstructure more straightforwardly, a matrix, similar to Eq. 3.4, can be constructed for a cubic lattice. Matlab code can be found in the Appendix. Figs. 3.2 and 3.3 plot equipotential surfaces for three-dimensional optical lattices at $s = 4E_R$. The top row in both figures is viewed along the $(1, 0, 0)$ direction in reciprocal lattice space, while the bottom row is along $(1, 1, 1)$. For small $\vec{q}$, the equal-energy surface is close to a sphere, similar to the free particle case. As $\vec{q}$ approaches the $\vec{q_B}$, an energy gap opens, and the equal-energy surface is always perpendicular to the boundary of the BZ.

Brillouin zone

A Brillouin zone (BZ) is defined as a Wigner-Seitz primitive cell in the reciprocal lattice space [54]. The atoms have a distribution of quasimomenta in the ground band of the first BZ, which is a cube with sides of length $2q_B$ in reciprocal space. Fig. 3.4 shows the projection of the BZ with band indices from $n = 0 - 9$, viewed along a lattice axis and along our imaging direction.

The quasimomentum distribution can be detected via the "band-mapping" technique [55–57]. By turning off the optical potential slowly enough with respect to the band gap (thereby avoiding excitation to higher bands), but quickly with respect to the harmonic trapping potential (to avoid spatial redistribution), quasimomentum is adiabatically mapped to momentum. In other words, a Bloch wave with quasimomentum k and band index n is mapped to a free particle with momentum $p_i = \text{sgn}(k_i)n \times (\hbar k_{L,i}) + \hbar k_i$ with $i = x, y, z$ and $\text{sgn}(k_i)$ the sign function. However, this band-mapping technique fails for atoms near the edge of BZ [58]. An intuitive way to understand this failure is, as the lattice depth becomes shallow, the band gap is smaller, such that the related timescale becomes longer compared to the harmonic trap period.

We implement band-mapping using a 200μs linear ramp of the lattice depth. For all temperatures

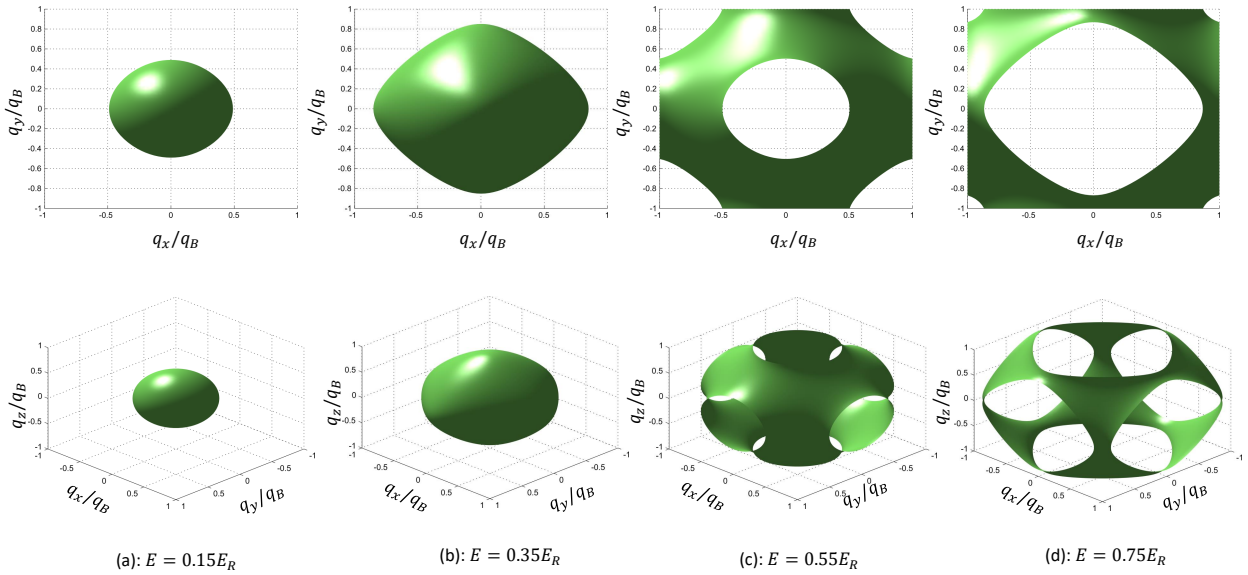

Figure 3.2: Equal energy surface for the ground band of an $s = 4E_R$ cubic lattice viewed from different angles: along $(1, 0, 0)$ (top) and along $(1, 1, 1)$ (bottom). From left to right, the corresponding energy for the surface is (a) $E = 0.15E_R$:, (b): $E = 0.35E_R$ (c): $E = 0.55E_R$ and (d)$E = 0.75E_R$, respectively. The zero energy reference is set to be $E(\vec{k} = 0)$ on the ground band.

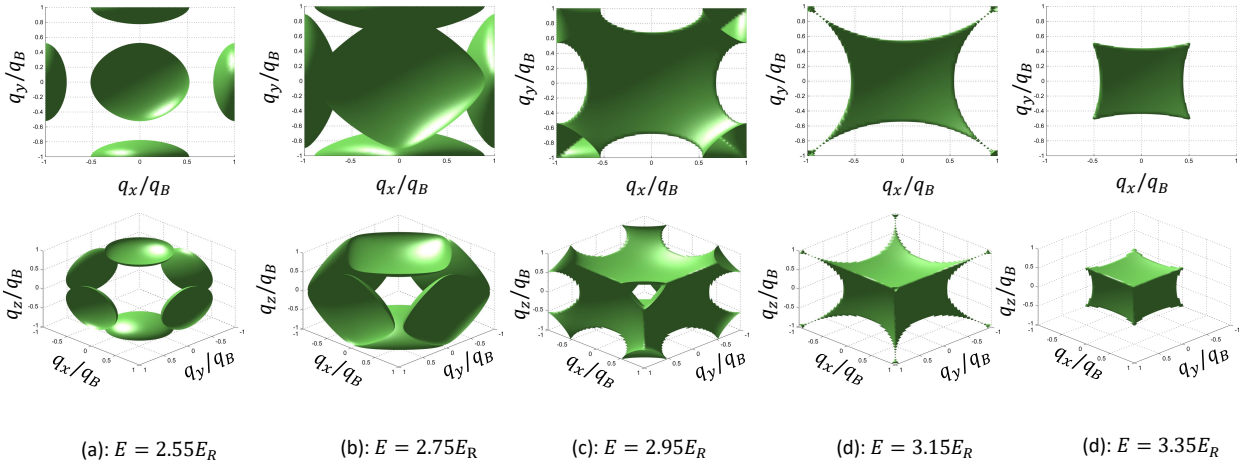

Figure 3.3: Equal energy surface for the first excited band of an $4 = 4E_R$ cubic lattice viewed from different angles: along $(1, 0, 0)$ (top) and along $(1, 1, 1)$ (bottom). From left to right, the corresponding energy for the surface is (a) $E = 2.55E_R$:, (b): $E = 2.75E_R$ (c): $E = 2.95E_R$, (d): $E = 3.15E_R$ and (e): $E = 3.35E_R$, respectively. The zero energy reference is set to be $E(\vec{k} = 0)$ on the ground band.

explored in this thesis, the atoms only occupy the ground band and populate the first BZ. A disadvantage of our lattice geometry is that the imaging beam is not along any of the primary axes of the lattices, but close to the $(1, -\sqrt{2}, 1)$ direction in the lattice coordinate. The projection of the cubic first BZ onto our image plane appears as hexagon (Fig. 3.4(b)). In addition, the projection of the BZ for higher energy bands largely overlaps with the projection of the 1st BZ, which hinders the study of dynamics involving higher band excitations.

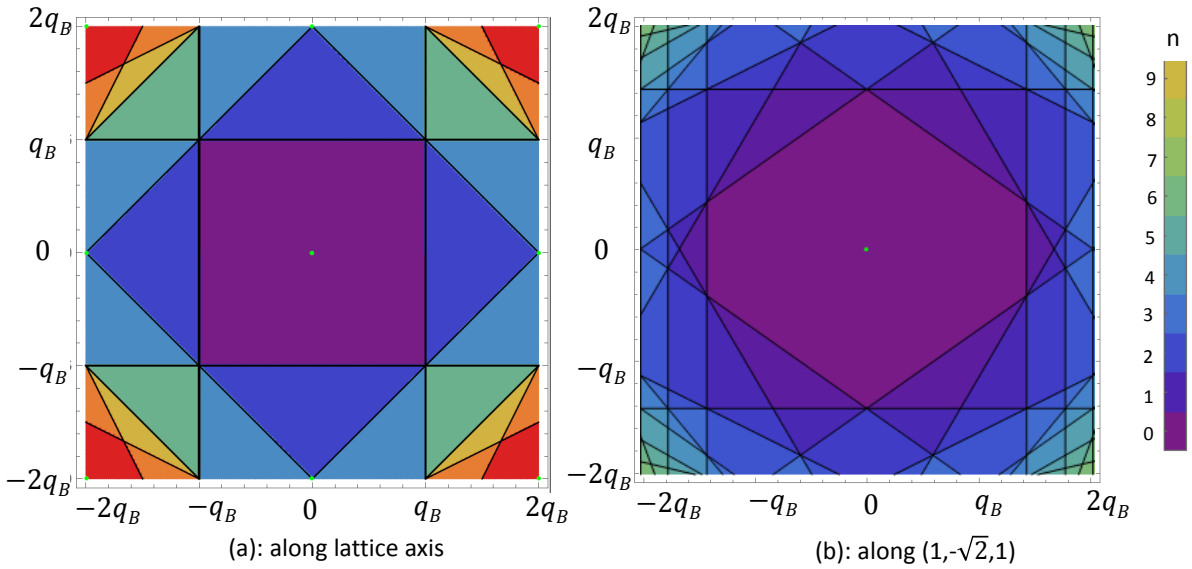

Figure 3.4: The Brillouin Zone (BZ) of a cubic lattice viewed along (a) one of the lattice axis and (b) the $(1, -\sqrt{2}, 1)$ direction. Our imaging beam is roughly along the $(1, -\sqrt{2}, 1)$ direction. Therefore, the projection of the $1st$ BZ on the imaging plane has a hexagonal shape. The color bar shows the band index. The Mathematica code used for generating the BZ is from `http://library.wolfram.com/infocenter/MathSource/8913/`.

3.2.3 Tight-binding model

For a sufficiently deep lattices ($s \geq 4E_R$), a tight-binding model is favorable to describe the physics in optical lattices. In this section, we use Wannier functions as a basis. Wannier functions, defined as

$$w(\vec{R}, \vec{r}) = \frac{1}{\sqrt{N}} \sum_{\vec{k}} e^{-i\vec{k}\cdot\vec{R}} \psi_{\vec{k}}(\vec{r}) = \frac{1}{\sqrt{N}} \sum_{\vec{k}} e^{i\vec{k}\cdot(\vec{r}-\vec{R}_l)} u_{\vec{k}}(\vec{r} - \vec{R}_l),$$

are localized around $r = \vec{R}_l$, with $\vec{R}_l$ the coordinates of the lattice sites.

Inserting this into Schrödinger equation, we have:

$$\sum_{\vec{R}_{l'}} \left[\frac{\hbar^2}{2m}\nabla^2 + V(\vec{r}) - E(\vec{k}) \right] \frac{1}{\sqrt{N}} e^{i\vec{k}\cdot\vec{R}_{l'}} w(\vec{r} - \vec{R}_{l'}) = 0, \tag{3.5}$$

where N is the total number of particles in the system. Multiplying the left handside by $w_m^*(\vec{r} - \vec{R}_l)$ and integrating over $\vec{r}$ gives:

$$E(\vec{k}) = -\sum_{\vec{R}_l} t(\vec{R}_l) e^{-i\vec{k}\cdot\vec{R}_l}, \tag{3.6}$$

with

$$t(\vec{R}_l) = \int d\vec{r} w_n^*(\vec{r} - \vec{R}_l) \left[-\frac{\hbar^2}{2m}\nabla^2 + V(\vec{r}) \right] w_n^*(\vec{r}).$$

The overlap between Wannier states on ground band with separation larger than two lattice sites is negligible for $s \geq 4E_R$, so only $t(\vec{R}_l = a_i) \equiv t$ $(i = L_x, L_y, L_z)$ is kept. For a three-dimensional optical lattices, we have the energy dispersion relationship as:

$$\begin{aligned} E(\vec{k}) &= -\sum_{i=x,y,z} t[e^{-ik_x d} + e^{ik_x d}] \\ &= -2t\left[\cos(k_x d) + \cos(k_y d) + \cos(k_z d)\right]. \end{aligned} \tag{3.7}$$

The bandwidth of ground band is $E(\vec{k} = (q_B/\hbar, q_B/\hbar, q_B/\hbar)) - E(\vec{q} = (0,0,0)) = 12t$.

Fig. 3.5 and Fig. 3.6 plot the band structure, Bloch functions, and Wannier functions for lattice depths $s = 4E_R$ and $s = 8E_R$. As the lattice depth becomes larger, the band becomes flatter and the band gaps increase. Panels (b) in Fig. 3.5 and Fig. 3.6 plot the amplitude and the real part of Bloch wavefunctions for $q = 0$ (black), $q = q_B/4$ (red) and $q = q_B/3$ (blue) for $n = 0$. The Bloch functions are similar to amplitude-modulated plane waves. For example, the dashed blue lines plot the real component of a plane wave $e^{i\pi/3}$. The periodic potential of lattice modifies its amplitude.

Wannier functions with $n = 0$ (black), $n = 1$ (red) and $n = 2$ (blue) are plotted in panels (c). For the $n = 0$ Wannier function, at $s = 4E_R$, the side lobes of the Wannier function are visible. At $s = 8E_R$, the side lobes are very small. For $n > 1$, the linewidth of Wannier functions is broader. The profile of the Wannier wavefunction becomes closer to the eigenstate of a harmonic trap potential as s increases.

The advantage of using Wannier functions is expressing the Hamiltonian in second quantizatized form (in a site basis). With field operator $\Psi(\vec{r}) = \sum_i w_i(\vec{r}) c_i$, where c_i is the annihilation operator for site i, the

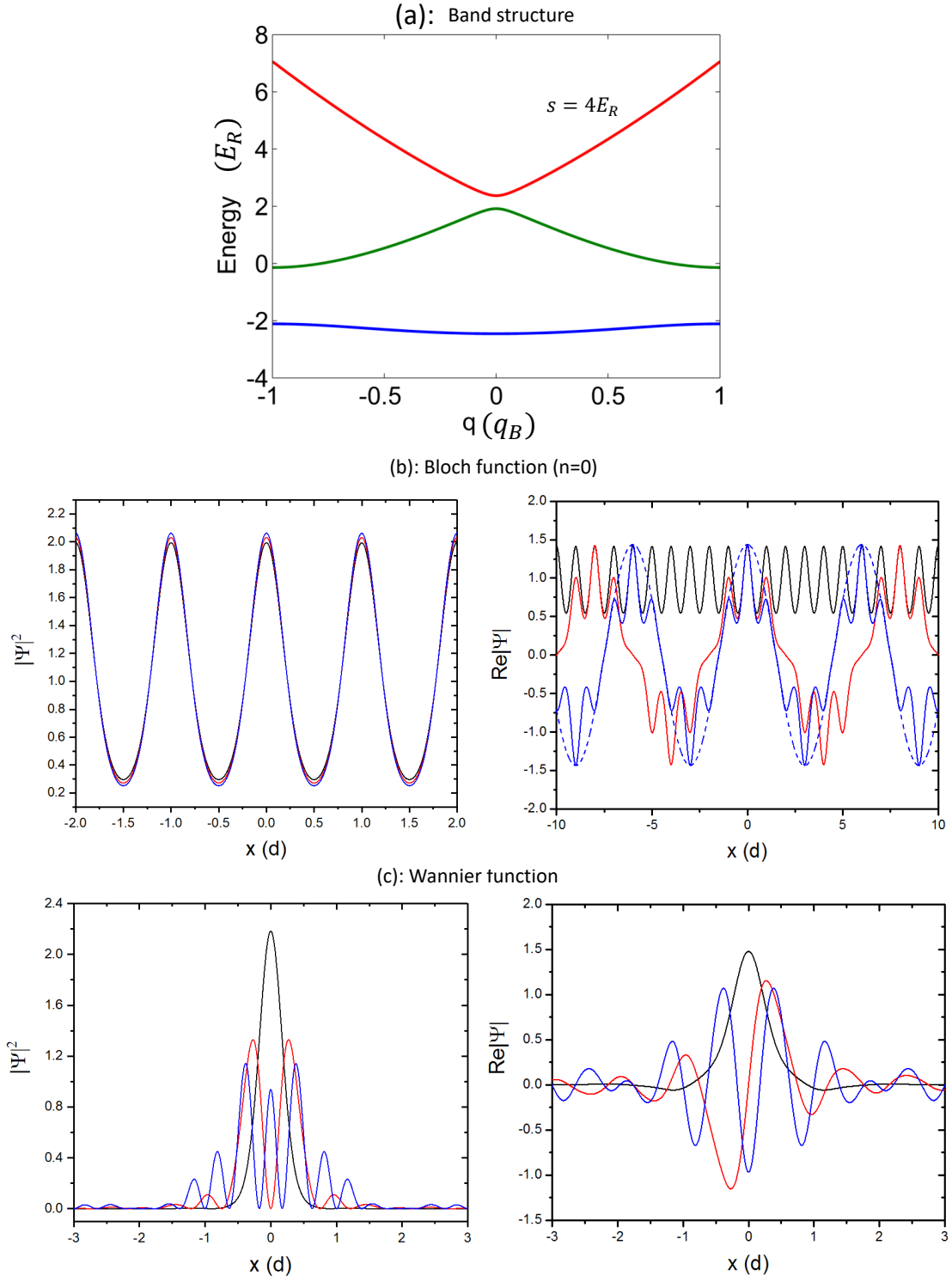

Figure 3.5: (a): Band structure at $s = 4E_R$ lattice. (b): The amplitude and the real part of Bloch functions with $n = 0$, for $q = 0$ (black), $q = q_B/4$ (red) and $q = q_B/3$ (blue). The blue dashed line plots an envelope of $e^{i\pi/3}$ (c): The amplitude and the real part of Wannier functions for $n = 0$ (black), $n = 1$ (red) and $n = 2$ (blue).

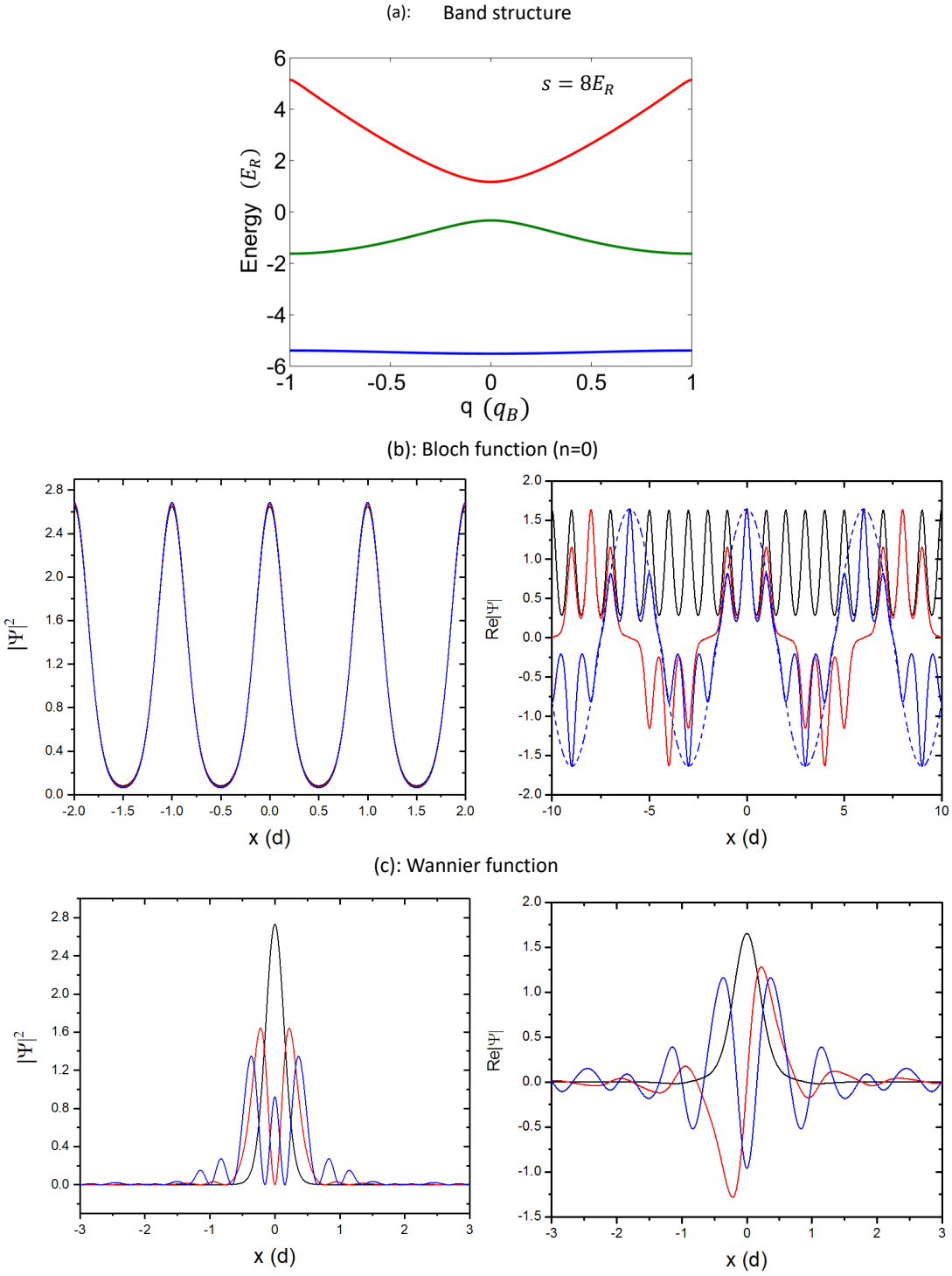

Figure 3.6: (a): Band structure at $s = 8E_R$ lattice. (b): The amplitude and the real part of Bloch functions with $n = 0$, for $q = 0$ (black), $q = q_B/4$ (red) and $q = q_B/3$ (blue). The blue dashed line plots an envelope of $e^{i\pi/3}$ (c): The amplitude and the real part of Wannier functions for $n = 0$ (black), $n = 1$ (red) and $n = 2$ (blue).

Hamiltonian is:

$$H = -t \sum_{\langle i,j \rangle} (c_i^\dagger c_j + \text{h.c.}), \tag{3.8}$$

where $\langle\rangle$ indicates a sum over neighboring sites. Eq. 3.8 is the so-called tight-binding Hamiltonian. Only tunneling between neighboring lattice sites has been kept.

3.2.4 Fermi-Hubbard model

So far, we have discussed the non-interacting case. With more than one fermionic species present, interactions between them due to collisions need to be taken into account. The temperature range we are working with is lower than the centrifugal p-wave barrier [15], and s-wave scattering only happens between fermions with different spin quantum numbers. The interaction potential between two atoms can be approximated as a contact potential $U(\vec{r} - \vec{r'}) = \delta(\vec{r} - \vec{r'}) \frac{4\pi\hbar^2 a}{m}$. Therefore, the interaction term is

$$\begin{aligned} H_{int} &= \int d^3\vec{r} d^3\vec{r'}\ \Psi_\sigma^\dagger(\vec{r}) \Psi_{\sigma'}^\dagger(\vec{r'}) U(\vec{r} - \vec{r'}) \Psi_{\sigma'}(\vec{r'}) \Psi_\sigma(\vec{r}) \\ &= \sum_i \frac{4\pi\hbar^2 a}{m} \left[\int d^3\vec{r} w_i(r)^4 \right] c_{i,\sigma}^\dagger c_{i,\sigma'}^\dagger c_{i,\sigma'} c_{i,\sigma} \qquad (3.9) \\ &= U \sum_i n_{i,\sigma} n_{i,\sigma'}, \qquad (3.10) \end{aligned}$$

with $U \equiv \frac{4\pi\hbar^2 a}{m} \left[\int d^3\vec{r} w_i(\vec{r})^4 \right]$, and $n_{i,\sigma} = \hat{c}_{i,\sigma}^\dagger \hat{c}_{i,\sigma}$ is the number operator.

Therefore, for a two-component fermionic system, the Hamiltonian involving interactions becomes:

$$H = -t \sum_{\langle i,j \rangle, \sigma} (\hat{c}_{j\sigma}^\dagger \hat{c}_{i\sigma} + h.c.) + U \sum_i n_{i,\downarrow} n_{i,\uparrow} + \sum_{i,\sigma} \frac{1}{2} m\bar{\omega}^2 r_i^2 n_{i,\sigma}, \tag{3.11}$$

where i indexes the lattice sites, $\langle\rangle$ indicates a sum over neighboring sites, and $\sigma = |\uparrow\rangle$ or $|\downarrow\rangle$ labels spin. The third term is added to take account the overall confining potential from the optical dipole trap. where $\bar{\omega}$ is the geometric mean of the dipole trap frequencies, and r_i is the distance from the site i to the trap center.

Eq. 3.11 is the famous Fermi-Hubbard model. The first term of this Hamiltonian captures the kinetic energy and tunneling between neighboring sites, with t as the Hubbard tunneling energy; the second interaction term indicates that occupying a lattice site with two atoms in opposite spin states casts an extra energy U (Fig. 3.1). The last term, which is absent in conventional solid state systems, introduces an inhomogeneous density distribution of atoms.

Experimentally, the calibration of lattice depth can be done by modulating the amplitude of lattice depth

at a few percent level. This periodic driving drives transitions between the ground and the 2nd excited band, if the modulation frequency matches the energy gap. This process adds energy to the gas, and manifests itself as number loss and reduction in the peak OD. From the dependence of the peak OD on modulation frequency, the energy gap between ground state and the 2nd excited state can be measured.The reduction in OD provides cleaner signal for locating the interband transition frequency, compared to number loss (Fig. 3.7). We calculate the lattice depth basd on a band structure calculation. The corresponding on-site interaction U an tunneling term t in Fermi-Hubbard model can be straightforwardly calculated. Table. 3.1 gives the value of U and t at various lattice depths.

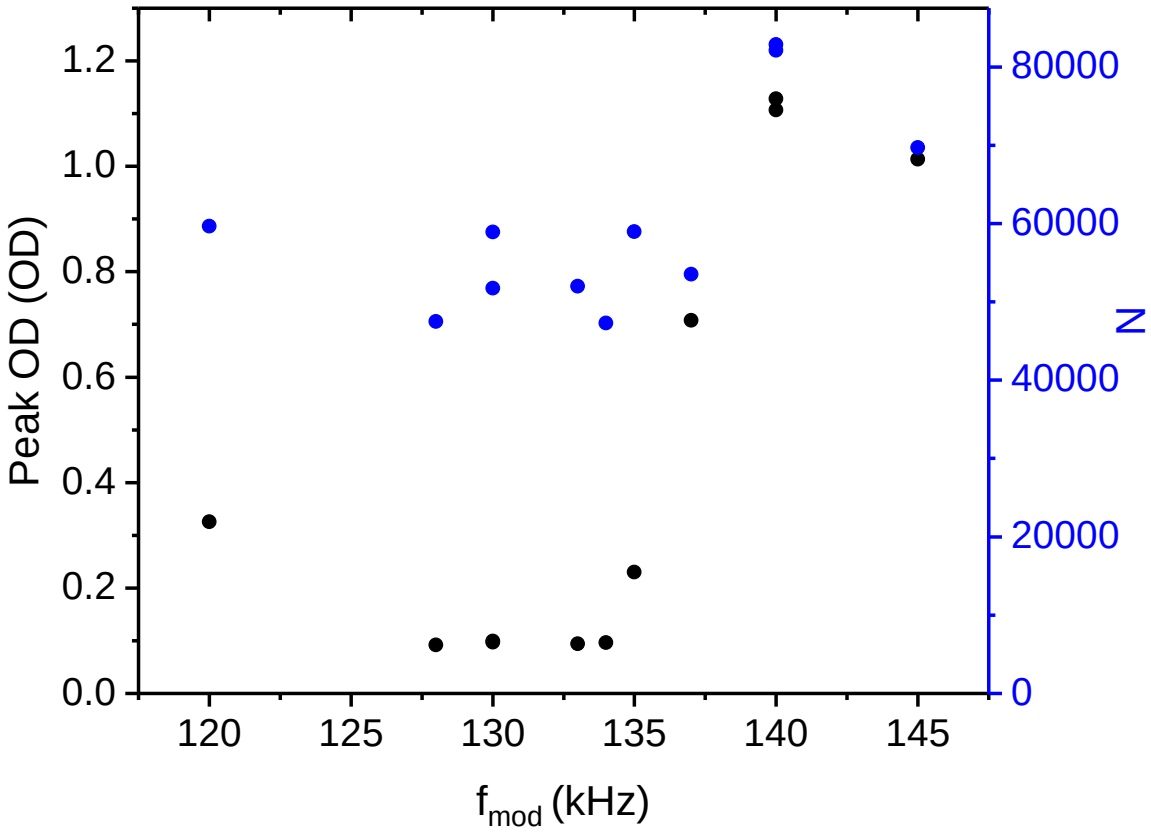

Figure 3.7: Sample data showing lattice depth calbration via lattice modulation spectroscopy for L1. The lattice intensity is modulated at a few percent level over a range of frequencies (f_{mod}). The peak OD (black circles) has a sharp reduction at $f_{\mathrm{mod}} \approx 134$kHz (corresponding to the transition from the ground to the second excited band at $s = 24E_R$). The total number of atoms (blue circle) also drops below $f_{\mathrm{mod}} \approx 134$kHz.

Table 3.1: Table of tunneling energy t and on-site energy U at various lattice depths.

Lattice depth (E_R)	t (E_R)	t/h (kHz)	U(E_R)	U/h (kHz)	U/t
4	0.0862	0.703	0.1933	1.577	2.2
5	0.0661	0.539	0.2448	1.997	2.9
6	0.0509	0.415	0.2960	2.414	3.7
7	0.0395	0.322	0.3462	2.824	4.7
8	0.0308	0.251	0.3952	3.223	5.8
9	0.0242	0.197	0.4429	3.612	7.2
10	0.0192	0.157	0.4895	3.993	8.8
11	0.0153	0.125	0.5349	4.363	10.6
12	0.0123	0.100	0.5794	4.726	12.8
13	0.0099	0.081	0.6229	5.081	15.4
14	0.0080	0.065	0.6657	5.430	18.3

3.3 Semiclassical kinetics in optical lattices

This section gives a brief discussion of the semiclassical dynamics of particles, such as their response to external field, in optical lattices. Instead of solving the Schrödinger equation, a semiclassical approach that treats the external field classically, is appropriate for describing the motion of particles in certain cases. This semiclassical approach is relevant to our study of transport phenomena in optical lattices.

3.3.1 Wavepackets

Unlike classical particles, which have a definite momentum and position, the Heisenberg uncertainty principle forbids the simultaneous determination of momentum and position for quantum particles. The eigenfunctions for particles in a periodic potential are Bloch waves, which are amplitude-modulated plane waves that have no definite position. To produce time-dependent states, we form a superposition of several eigenstates:

$$\psi_k(\vec{r},t) = \frac{1}{\Delta\vec{k}} \int_{\vec{k}_0-\frac{\Delta\vec{k}}{2}}^{\vec{k}_0+\frac{\Delta\vec{k}}{2}} u_k(\vec{r}) e^{i(\vec{k}\cdot\vec{r}-\frac{E(\vec{k})}{\hbar}t)} d\vec{k}. \tag{3.12}$$

If we assume $u_{\vec{k}}(\vec{r})$ changes very slightly with $\vec{k}$ (which is true in the tight-binding limit), then we have

$$\psi_k(\vec{r},t) \approx \frac{u_{\vec{k}_0(\vec{r})}}{\Delta\vec{k}} e^{i(\vec{k}_0\vec{r}-\frac{E(\vec{k}_0)}{\hbar}t)} d\vec{k} \int_{-\frac{\Delta\vec{k}}{2}}^{\frac{\Delta\vec{k}}{2}} u_k(\vec{r}) e^{i\delta\vec{k}(\vec{r}-\frac{\nabla_{\vec{k}}E(\vec{k}_0)}{\hbar}t)} d(\delta\vec{k}). \tag{3.13}$$

If we define the coordinates (ξ, η, ζ) as:

$$\xi = x - \frac{1}{\hbar}\left(\frac{\partial E(\vec{k})}{\partial k_x}\right)t, \tag{3.14}$$

$$\eta = y - \frac{1}{\hbar}\left(\frac{\partial E(\vec{k})}{\partial k_y}\right)t, \tag{3.15}$$

$$\zeta = z - \frac{1}{\hbar}\left(\frac{\partial E(\vec{k})}{\partial k_z}\right)t, \tag{3.16}$$

we have

$$\psi_{\vec{k}} \approx \psi_{\vec{k}_0}\frac{\sin(\Delta k_x \xi/2)}{\Delta k_x \xi/2}\frac{\sin(\Delta k_y \eta/2)}{\Delta k_y \eta/2}\frac{\sin(\Delta k_z \zeta/2)}{\Delta k_z \zeta/2}. \tag{3.17}$$

The probability to find the particle at position $\vec{r}$ is: $|\psi_{\vec{k}}|^2 = |u_{\vec{k}_0}(\vec{r})|^2 |A(\vec{r}, t)|^2$, with

$$A(\vec{r}, t) \equiv \frac{\sin(\Delta k_x \xi/2)}{\Delta k_x \xi/2}\frac{\sin(\Delta k_y \eta/2)}{\Delta k_y \eta/2}\frac{\sin(\Delta k_z \zeta/2)}{\Delta k_z \zeta/2}.$$

If $\Delta\vec{k} \neq 0$, the amplitude of the wave-packet reaches its maximum value at $\xi = \eta = \zeta = 0$, and decays as $\xi = \eta = \zeta \to \infty$. The position of the particle can be defined as the center of this wavepacket, *i.e.*, $\vec{r} = \frac{1}{\hbar}\nabla_{\vec{k}} E(\vec{k})t$. The velocity of wave-packet is

$$\vec{v} = d\vec{r}/dt = \frac{1}{\hbar}\nabla_{\vec{k}} E(\vec{k}), \tag{3.18}$$

which is the mean velocity of a Bloch wave with momentum $\vec{k}$ and energy E.

The acceleration of a wave-packet under an external force $\vec{F}$ is:

$$\begin{aligned} \frac{d\vec{v}}{dt} &= \frac{1}{\hbar}\nabla_{\vec{k}} E(\vec{k}) \\ &= \frac{1}{\hbar}(\frac{d\vec{k}}{dt}\cdot\nabla_{\vec{k}})\nabla_{\vec{k}} E(\vec{k}) \\ &= (\vec{F}\cdot\frac{1}{\hbar^2}\nabla_{\vec{k}})\nabla_{\vec{k}} E(\vec{k}) \end{aligned} \tag{3.19}$$

The equation of motion for the wave-packet still has the same classical form as Newton equation, but with an effective mass defined as

$$(\frac{1}{m})_\alpha = \frac{1}{\hbar^2}\frac{\partial^2 E(\vec{k})}{\partial k_\alpha^2}. \tag{3.20}$$

The time evolution of a wave-packet still follows the classical equations of motion, with its momentum and position defined as the mean value of the momentum and position of this wave-packet. This approach is semiclassical in the sense that we treat the external field as a classical field, and the response of the wave-

packet to the external field has the form of Newton's equation. However, the profile of the wave-packet itself, which are determined by the periodic potential, has to be treated quantum mechanically.

The validity of this semiclassical picture requires $\Delta\vec{k} \ll \pi/d$. A wave-packet with a wave vector that is well defined on the scale of the BZ must be spread in real space over many sites [54]. If the length scale of the spatial variation in the external field is much larger than the lattice spacing, then we can describe the dynamics of this system using this semiclassical approach.

3.3.2 Two simple examples

Motion of a wavepacket with an external electric field

In the presence of an external electric field, we have $\hbar\frac{d\vec{k}}{dt} = -e\vec{E}$, the solution of which is $k(\vec{t}) = \vec{k}(t=0) - \frac{e\vec{E}}{\hbar}t$. Without optical lattices, $E(\vec{k}) = \hbar^2k^2/2m$, and the relationship between the velocity of a wave-packet and $\vec{k}$ is simple: $\vec{v}(\vec{k}) = \frac{\hbar}{m}\vec{k}$. Therefore, the velocity of a wave-packet keeps increasing under a static external field as

$$\vec{v}(\vec{k}) = \frac{\hbar}{m}\vec{k}(0) - \frac{e\vec{E}}{m}t \tag{3.21}$$

The behavior of particles in optical lattices is completely different. In this case, the velocity becomes $\vec{v}(\vec{k}) = -\frac{2td}{\hbar}\sin(kd)$, which is a periodic function. There exists a maximum velocity in the lattice, and the evolution in k is periodic. This behavior is called Bloch oscillation. In real materials, there always exists a scattering process that relaxes momentum, which is much faster than the Bloch frequency, and therefore prevents the observation of Bloch oscillation. For ultracold atoms trapped in an optical lattice, because of their long coherence length, Bloch oscillations have been observed [59–62].

Motion in an optical lattice combined with a harmonic trap

The semiclassical motion of atoms in an optical lattice, combined with a harmonic trap potential follows the equations:

$$\dot{x} = \frac{\partial H}{\partial q} = 2t\frac{d}{\hbar}\sin(\frac{q}{\hbar}d) \tag{3.22}$$

$$\dot{q} = -\frac{\partial H}{\partial x} = -m\omega^2 x. \tag{3.23}$$

These equations can be solved numerically. Fig. 3.8(a) shows the evolution in phase space for different initial q. Compared to the pure harmonic trap case (Fig. 3.8)(b), the trajectories deviate from a elliptical

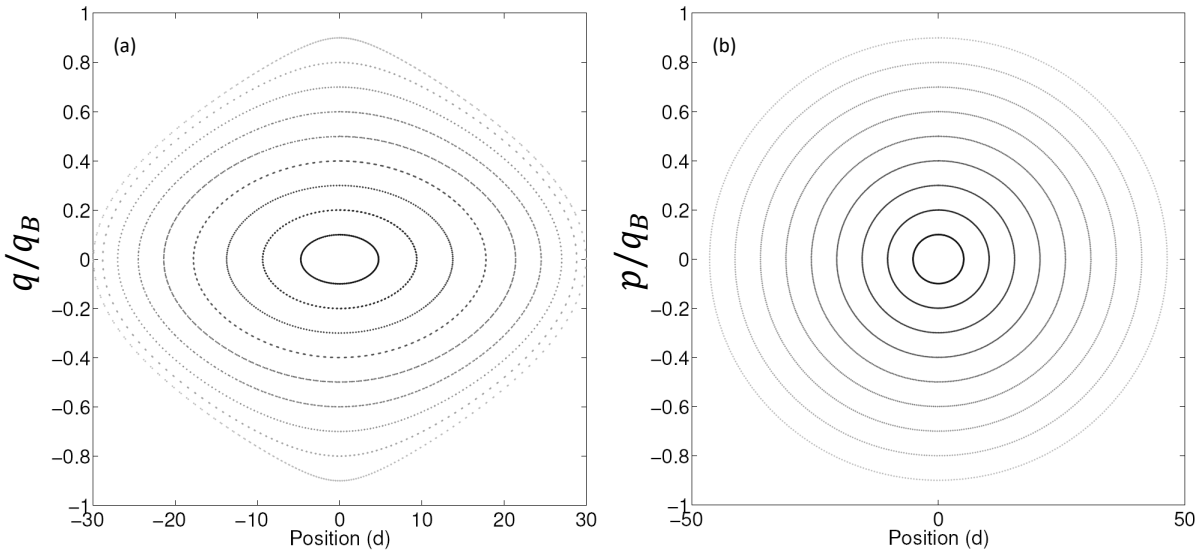

Figure 3.8: Evolution in phase space for (a) an optical lattice combined with a harmonic trap potential, and (b) a pure harmonic trap potential. Dots with different gray color scales plot the phase trajectories for constant energy contours. Time evolving Eq. 3.22 and Eq. 3.23 numerically gives the trajectories in phase space. The lattice dispersion induces anharmonic behavior. As q approaches the edge of BZ, the deviation from an elliptical trajectory is evident.

shape as q approaches the edge of BZ. Such deviation brings anharmonic behavior of atoms moving in an optical lattice. Chapter 4 will discuss this anharmonicity in detail.

3.4 Thermodynamics in optical lattices

3.4.1 Measuring temperature in optical lattices

It may be surprise to physicists outside of AMO physics that a direct probe of temperature in optical lattices is still a challenging task. For a weakly interacting gas in a harmonic trap, the temperature can be directly measured by fitting the momentum distribution of gas to analytic expressions using the semiclassical approximation [63, 64]. However, for an atomic lattice gas, this approach fails because of the rapid variation in the potential energy [64]. Directly probing of temperature of lattice gases is of great interest (see Ref. [65] for a review).

Alternatively, as an indirect technique, the thermodynamic quantities of a lattice gas can be inferred from a trapped gas. We estimate the temperature in the lattice by assuming that the optical lattice turns on slowly enough such that this process is adiabatic. Adiabaticity is only satisfied if the lattice depth is ramped

up infinitely slowly. In practice, we must use a finite ramp time, which is assumed to be slow compared to the timescales of the model. In principle, the matching in entropy and the conservation of total number of atoms during lattice loading allows the inferring of other thermodynamic quantities, such as temperature and the chemical potential, for a lattice gas. However, calculating the entropy of a lattice gas usually requires some approximations.

For a non-interacting lattice gas ($U = 0$), entropy can be calculated as a function of temperature and the chemical potential numerically (see Section.3.4.3 for details). In the case that U/t is small, mean-field methods, such as Hartree-Fock approximation, have been successfully employed for a weakly-interacting lattice gas [66]. At the limit of strong interaction ($t/U \to 0$), thermodynamic functions have analytical expressions in the atomic limit [67]. The dependence of entropy on temperature for the intermediate regime of U/t remains elusive. For works in this thesis, we load single-component non-interacting fermions confined in a harmonic trap into optical lattices. Therefore, we can numerically calculate the entropy as a function of temperature and the chemical potential and infer the thermal quantities of a lattice Fermi gas (See section.3.4.3).

3.4.2 Thermodynamics for a trapped Fermi gas

Without an optical lattice, thermodynamics quantities for a non-interacting Fermi gas confined in a harmonic potential have analytical expressions, which have been derived in references such as [52,68]. Here I summaries the expressions for frequently used quantities and how we measure them experimentally.

Semiclassically, the distribution in the phase space $(\vec{r}, \vec{p})$ follows Fermi-Dirac statistics:

$$f(\vec{r}, \vec{p}) = \frac{1}{e^{\beta(p^2/2m + \frac{1}{2}m\omega^2 r^2 - \mu)} + 1}, \tag{3.24}$$

where $\beta = 1/k_B T$ and μ is the chemical potential. The grand canonical partition function Ξ is:

$$\ln \Xi = \frac{1}{h^3} \int d^3\vec{r} \int d^3\vec{p} \, \left\{ 1 + e^{-\beta\left[p^2/2m + \frac{1}{2}m\omega^2 r^2 - \mu)\right]} \right\}. \tag{3.25}$$

Then the total number of particles is:

$$N = \frac{1}{h^3} \int d^3\vec{r} \int d^3\vec{p} \, f(\vec{p}, \vec{r}), \tag{3.26}$$

Table 3.2: Analytical expressions for thermal quantities of a trapped non-interacting Fermi gas

Fermi energy	$E_F = \hbar\bar{\omega}(6N)^{1/3}$
T/T_F	$\left[\frac{1}{6Li_3[-z]}\right]^{1/3}$
Total number	$N = (\frac{k_BT}{\hbar\bar{\omega}^3})^3 Li_3[-z]$
Entropy per particle	$S/N = k_B\left\{\frac{Li_4[-z]}{Li_3[-z]}] - \ln[z]\right\}$
Density distribution	$n(\vec{r}) = -\frac{1}{(2\pi)^{3/2}\hbar^3}(\frac{m}{\beta})^{3/2} Li_{3/2}[-ze^{-\beta V(\vec{r})}]$
Momentum distribution	$n(\vec{p}) = -\frac{1}{(2\pi)^{3/2}\hbar^3}(\frac{1}{m\omega^2})^{3/2} Li_{3/2}[-ze^{-\beta\frac{p^2}{2m}}]$
Column integrated density distribution	$n(x,y) = -\frac{\sqrt{2\pi\sigma^2}}{(2\pi)^{3/2}\hbar^3}(\frac{m}{\beta})^{3/2} Li_2[-ze^{-\frac{x^2}{2\sigma^2}-\frac{y^2}{2\sigma^2}}]$
Column integrated momentum distribution	$n(p_x,p_y) = -\frac{\sqrt{2\pi m k_BT}}{(2\pi)^{3/2}\hbar^3}(\frac{1}{m\omega^2})^{3/2} Li_2[-ze^{-\frac{p_x^2}{2mk_BT}-\frac{p_y^2}{2mk_BT}}]$

and the total entropy is

$$\begin{aligned} S &= -\frac{\partial}{\partial T}(-k_BT\ln\Xi) \\ &= \frac{1}{h^3}\int d^3\vec{r}\int d^3\vec{p}\,\left\{\ln(1+e^{-\beta(E_i-\mu)}) + \frac{\beta(E_i-\mu)}{1+e^{\beta(E_i-\mu)}}\right\}. \end{aligned} \tag{3.27}$$

Determining thermodynamic quantities requires integration over the spatial and momentum coordinates. The mathematical technique for doing this integral involves the use of a special function $Li_s[z]$, which is the polylogarithm function, defined as

$$Li_s[z] = \sum_{k=1}^{\infty}\frac{z^k}{k^s}. \tag{3.28}$$

The integral representation of $Li_s[z]$ is more useful for our purpose, which is:

$$Li_s[-z] = \frac{1}{\Gamma[s]}\int_0^{\infty}\frac{t^{s-1}}{e^t/z+1}dt, \tag{3.29}$$

where $\Gamma[s]$ is the gamma function. Another useful relation is:

$$\int_0^{\infty} Li_s[-ze^{-x^2}]dx = \frac{\sqrt{\pi}}{2}Li_{s+1/2}[-z]. \tag{3.30}$$

Table. 3.2 summaries analytical expressions for some commonly used thermal quantities, with $\sigma^2 = \frac{k_BT}{m\omega^2}$ the size of the gas.

The most widely used experimental technique to measure thermal quantities is time-of-flight imaging. The gas is released from the harmonic trap potential and allowed to expand freely for some time $t_{\rm TOF}$. Then an absorption image, as described in Chapter 2, is taken. In the absence of interactions, the motion of the atoms is purely ballistic, and the position of atoms at $t_{\rm TOF}$ reflects the momentum distribution at the

Table 3.3: Inferring thermodynamic quantities from fitting parameters. λ is the wavelength of the imaging probe beam, and M is the magnification of the imaging system.

Optical depth	$OD(x,y) = A\frac{Li_2[-ze^{-\frac{x^2}{\sigma_x^2}-\frac{y^2}{\sigma_y^2}}]}{Li_2[-z]}$
Total number	$A\sigma_x\sigma_y M^2 \frac{2\pi}{3\lambda^2}\frac{2\pi Li_3[-z]}{Li_z[-z]}$
Temperature	$k_BT = \frac{m\omega^2\sigma^2}{[1+(\omega t_{\rm TOF})^2]}$
Entropy per particle	$S/N = k_B\left\{\frac{Li_4[-z]}{Li_3[-z]}] - \ln[z]\right\}$

moment the atoms were released from the harmonic trap. It has been proven that this procedure does not change the shape of gas for non-interacting atoms [69]. Therefore, after $t_{\rm TOF}$, the distribution of atoms in space follows

$$\begin{aligned} n(\vec{r'}, t_{\rm TOF}) &= \int d^3\vec{r} f(\vec{r}, \frac{m}{t}(\vec{r'}-\vec{r})) \\ &\approx \int d^3\vec{r} \frac{1}{e^{-\beta\mu}\ e^{\frac{1}{2}m\omega^2 r^2\beta}\ e^{\beta\frac{m^2}{t_{\rm TOF}}\vec{r'}^2}+1} \\ &= \int d^3\vec{r} \frac{1}{e^{-\beta\mu}\ e^{-\frac{r^2}{2\sigma_t^2}}+1} \end{aligned} \tag{3.31}$$

with the assumption that $t_{\rm TOF}$ is sufficiently long (*i.e.*, $\sigma_{t=0} \ll \sigma_{t=t_{\rm TOF}}$). The parameter $\sigma_t^2 = \frac{1}{m\beta}(t_{\rm TOF}^2 + \frac{1}{\omega^2})$ characterises the size of the gas after time-of-flight.

The 2D absorption image corresponds to the column integrated momentum distribution. The expression for the OD is

$$OD(x,y) = A\frac{Li_2\left[-ze^{-\frac{(x-x_c)^2}{2\sigma_x^2}}\ e^{-\frac{(y-y_c)^2}{2\sigma_y^2}}\right]}{Li_2\left[-z\right]}. \tag{3.32}$$

We fit the measured OD to Eq. 3.32 with A, σ_x, σ_y, x_c, y_c, and z as free parameters. Here $\sigma_x(\sigma_y)$ is the size of the gas along $x(y)$, A is the peak OD, and $z = e^{\beta\mu}$ is the fugacity. In the classical limit, Eq. 3.32 reduces to a Gaussian distribution. Table. 3.3 summaries the relationship between thermal quantities and the fit parameters.

Combining Tables. 3.2 and 3.3 shows that there are two approaches to obtain T/T_F. First, T/T_F can be inferred from the fugacity as $T/T_F = [6Li_3[-z]]^{-1/3}$. Another method is to measuring σ at different $t_{\rm TOF}$, and fit to $\sigma(t_{\rm TOF}) = \sqrt{\frac{k_BT}{m}}\sqrt{1+(\omega t)^2}$ to determine the absolute temperature T. Because $T_F = E_F/k_B$ and $E_F = \hbar\omega(6N)^{1/3}$, T/T_F can be calculated with the knowledge of the trap frequencies and atom number N.

In practice, we usually compare T/T_F obtained from these two methods. The fugacity measured directly from the profile of the TOF imaging is most reliable for $T/T_F \approx 0.1 - 0.5$. For $T/T_F > 0.5$, the shape of

the gas is close to a classical Gaussian distribution, and therefore the fugacity is not sensitive to T/T_F. For $T/T_F < 0.1$, the fugacity diverges rapidly with T/T_F, and small fluctuations on the density profile due to noise dramatically change the fit results. Consistency between these two methods within $T/T_F \approx 0.1 - 0.5$ should be verified to ensure that Fermi gas has reached equilibrium during evaporative cooling.

3.4.3 Thermodynamics for a non-interacting Fermi lattice gas

Semiclassically, the grand canonical partition function Ξ for describing a non-interacting Fermi gas in an optical lattices is:

$$\log \Xi = \frac{1}{(2\pi)^3} \int_{-\pi}^{\pi} d^3\vec{q} \int d^3\vec{r} \log \left[1 + e^{-\beta(\epsilon(\vec{r},\vec{q})-\mu)}\right], \tag{3.33}$$

with $|q| \in [-q_B, q_B]$ the quasimomentum, and $\epsilon(\vec{r},\vec{q})$ the single-particle energy:

$$\epsilon(\vec{r},\vec{q}) = \sum_{i=x,y,z} \left[2t\left(1 - \cos(\pi \frac{q_i}{q_B})\right) + \frac{m\omega^2 r_i^2}{2}\right]. \tag{3.34}$$

Here we assume the lattice depth is equal along each direction, and the harmonic trap potential is isotropic with trap frequency ω. We also assume that the principal axes of the harmonic trap potential align with the lattice axes, which is not true in the experiment. Fermi-Dirac statistics $f(\vec{r},\vec{q}) = \frac{1}{e^{\beta[\epsilon(\vec{r},\vec{q})-\mu]}+1}$ gives:

$$\begin{aligned} N &= -\frac{\partial}{\partial \mu}(-k_B T \ln \Xi) \\ &= \frac{1}{(2\pi)^3} \int d^3\vec{r} d^3\vec{q} \frac{1}{e^{\beta[\epsilon(\vec{r},\vec{q})-\mu]}+1} \end{aligned} \tag{3.35}$$

$$\begin{aligned} S &= -\frac{\partial}{\partial T}(-k_B T \ln \Xi) \\ &= \frac{1}{(2\pi)^3} \int d^3\vec{r} d^3\vec{q} \left\{\ln(1 + e^{-\beta(\epsilon(\vec{r},\vec{q})-\mu)}) + \frac{\beta(\epsilon(\vec{r},\vec{q})-\mu)}{1+e^{\beta[\epsilon(\vec{r},\vec{q})-\mu]}}\right\}. \end{aligned} \tag{3.36}$$

In practice, we numerically integrate Eq. 3.36 and 3.36 to obtain the total number of atoms N and entropy per particle S/N, which are functions of the chemical potential and the temperature. Assuming adiabaticity, we infer the $\tilde{T}$ and $\tilde{\mu}$ in the lattice by numerically solving (simultaneously)

$$N_L(\tilde{\mu},\tilde{T}) = N_T(\mu,T), \tag{3.37}$$

and

$$S_L(\tilde{\mu},\tilde{T})/N_L(\tilde{\mu},\tilde{T}) = S_T(\mu,T)/N_T(\mu,T). \tag{3.38}$$

N_T (N_L) is the total number of atoms in the harmonic trap (in the lattice); S_T (S_L) is the total entropy of

atoms in the harmonic trap (in the lattice). N_T and S_T are functions of μ and T with analytical expressions. μ and T can be experimentally determined from time-of-flight measurements as discussed in the previous section.

With the knowledge of effective $\tilde{T}$ and $\tilde{\mu}$ in the lattices, other quantities, such as the density and momentum distributions, can be easily calculated. For example, the column integrated density profile is

$$n(x,y) = \int dz \int d^3\vec{q} \frac{1}{e^{\beta[\epsilon(\vec{r},\vec{q})-\mu]}+1}, \tag{3.39}$$

which can be measured experimentally by taking an in-situ absorption image (more details in Chapter 4).

Compared with solid crystals, a unique property of an optical lattice is that the periodic potential is accompanied by a harmonic trap potential. Although the spatial variation in the harmonic potential is small compared with the periodic potential of lattices, its effect on the properties of the system can be important. For example, it breaks the translational symmetry and modifies the single particle spectrum [70, 71].

In the work discussed in Chapter 4, we need to keep the Fermi energy E_F/t of the system fixed. For a uniform system, E_F/t solely depends on the total number of particles. However, for the combined harmonic-trap potential, this is not true. The dependence of the Fermi energy for the lattice gas on the total number of atoms N can be found via:

$$N(E_F) = \int_0^{E_F} \frac{1}{(2\pi)^3} \int d^3\vec{q} \int d^3\vec{r}\Theta(E_F - E(\vec{r},\vec{q})), \tag{3.40}$$

where $\Theta(x)$ is the Heaviside step function.

Fig. 3.9(a) plots the the dependence of total number of atoms N on the tunneling energy t, for $E_F = 4t$ (black), $E_F = 6t$ (red), and $E_F = 8t$ (blue), with $\omega = 2\pi \times 81$Hz. The dependence of N on t at given E_F/t is obvious when t is small. As t becomes larger, the single-particle energy is dominated by the lattice dispersion, and therefore N is less sensitive to t.

Moreover, in our experiment, varying t is realized by changing the lattice depth s. Besides the confinement from the crossed dipole trap, the lattice beams apply additional force on atoms. Therefore, with larger lattice depth s, the trap frequencies (ω in Eq. 3.34) increases. The harmonic-lattice combined trap frequencies are [72]:

$$\omega^2 = \omega_{\mathrm{OT}}^2 + \frac{4E_R^2}{mw_L}\left(2\frac{s}{E_R} - \sqrt{\frac{s}{E_R}}\right) \tag{3.41}$$

where ω_{OT} is the trap frequency of the optical dipole trap, w_L is the beam waist of the optical lattices, and E_R is the recoil energy. The dashed lines in Fig. 3.9(b) plot N vs t, with the dependence of ω on s being

taken into consideration. The solid lines are with fix $\omega = 2\pi \times 81$Hz. It is evident that for high lattice depth (*i.e.*, small t), the change in overall trap frequencies has a significant effect on the relationship between N and E_F.

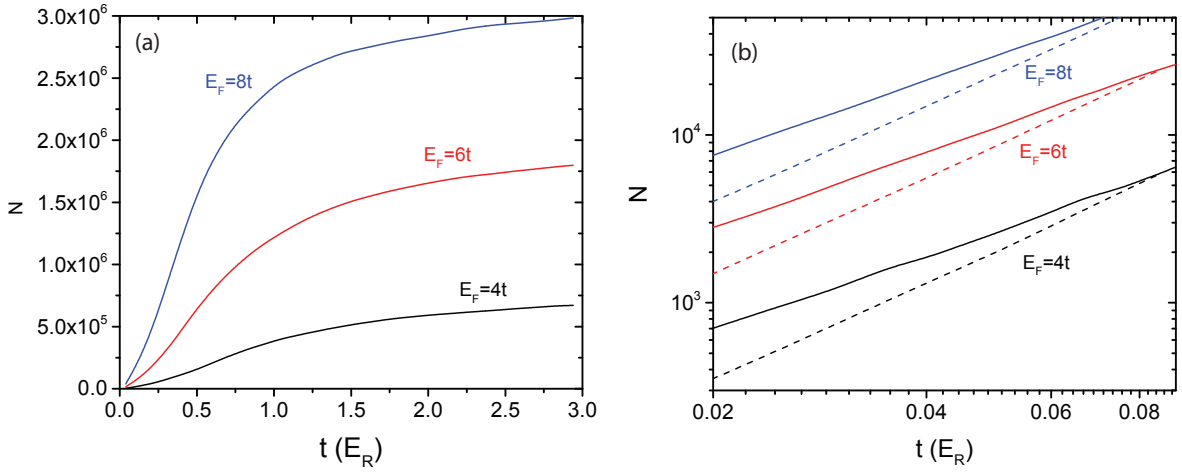

Figure 3.9: Total number of atoms vs tunneling energy at $E_F = 4t$ (black), $E_F = 6t$ (red), and $E_F = 8t$ (blue). (a): The trap frequencies are fixed to be $2\pi \times 81Hz$. (b): In our experiment, varying t is realized by changing the lattice depth, which changes the trap frequencies. The dashed lines include the dependence of ω on t. At small t, derivation from the fixed ω case (solid lines) is evident.

In the work discussed in Chapter 4, we control the total number of atoms, in order to have E_F within the range of $5t$ to $7t$. Fig. 3.10 plots the dependence of E_F (in unit of t) on N at different lattice depths. Between the two dashed lines are the range of N we post-selected for the work discussed in Chapter 4.

3.5 Green's function in a nutshell

As an important theoretical formalism for solving many-body problems, Green's functions are widely used in condensed matter theory. They are more than a mathematical method for solving differential equations. Green's functions have a direct physical interpretation that helps to reveal the microscopic underpinnings of experimental measurements. This section introduces the basics of Green's functions. Chapter 4 uses Green's functions to show the relationship between the Drude model and Kubo formula and to perform dynamical mean-field theory calculations.

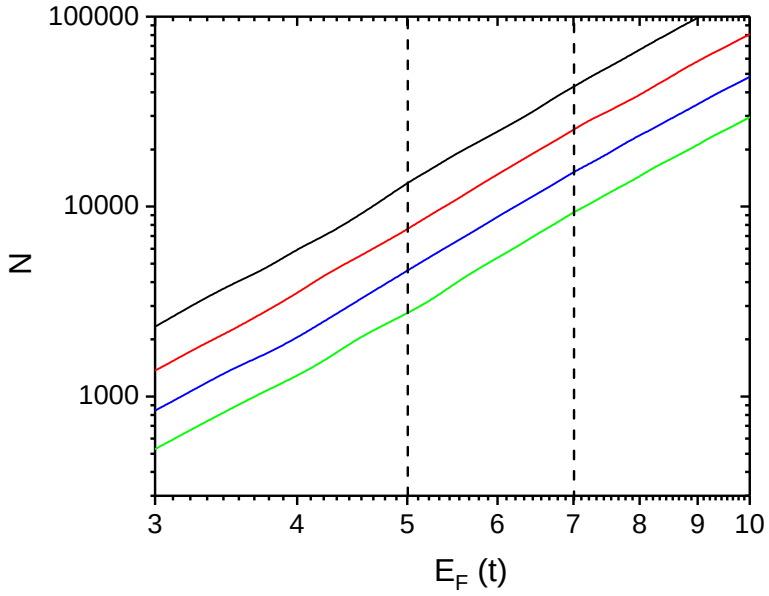

Figure 3.10: Dependence of the Fermi energy on atom number at lattice depth of $4E_R$ (black), $5E_R$ (red), $6E_R$ (blue), and $7E_R$ (green). E_F approximately scales as $N^{1/3}$ at given lattice depth, the same scaling as in a harmonic trap potential.

3.5.1 Single-particle Green's function

Generally, the single-particle Green's function is defined as

$$G(\nu, tt') = -i \left\langle \mathcal{T}(c_\nu(t) c_\nu^\dagger(t')) \right\rangle . \tag{3.42}$$

The quantum number ν can be anything (such as position $\vec{r}$, or momentum $\vec{p}$), depending on the problem of interest. The operators $c_\nu(t)$, $c^\dagger(t)$ are the creation and annihilation operators defined in the Heisenberg representation. $\mathcal{T}$ is the time-ordering operator which arranges operators with earlier times to appear on the right. For example, $\mathcal{T}(c_\nu(t)c_\nu^\dagger(t')) = c_\nu(t)c_\nu^\dagger(t')$ if $t > t'$, and $\mathcal{T}(c_\nu(t)c_\nu^\dagger(t')) = \pm c_\nu^\dagger(t')c_\nu(t)$ if $t < t'$. The $+$ $(-)$ sign is for bosons (fermions) to guarantee the correct commutation relations. The notation $\langle X \rangle$ represents the thermal average of X as

$$\langle X \rangle = \frac{Tr[e^{-\beta(H-\mu N)}X]}{Tr[e^{-\beta(H-\mu N)}]}.$$

As an example, let us consider the degenerate Fermi gas at zero temperature. In this case, it is easy to

show that

$$G(\vec{k}, tt') \quad = \quad -i\left[\theta(t-t')\theta(k-k_F) - \theta(t'-t)\theta(k_F-k)\right] e^{-i(\epsilon_k-\mu)(t-t')}, \tag{3.43}$$

where k_F is the Fermi wave vector and ϵ_k is the free-particle energy. For $t > t'$ and $k > k_F$, $G(\vec{k}, tt') = -ie^{-i(\epsilon_k-\mu)(t-t')}$. This is the propagator for free-particles, *i.e.* $\psi_k(t) = G(k, tt')\psi_k(t')$, representing the probability that we can find a particle with momentum k at time t, if we add a particle with that momentum at time t'. Of course, for the non-interacting case, this probability is unity. Similarly, for the $t < t'$ case, the Green's function gives the information about holes. In this case, we remove a particle from the system first at time t, and then put it back later at time t'.

More generally, with interactions, a basis such as $|k\rangle$ may not be eigenstates of the system. The added particle or hole can interact with other particles in the system during the time interval $t - t'$ and scatter into other states.

To be more formal, for an N-particle system with ground-state $|\Psi_0\rangle$, we want to probe excitations by injecting a fermion at time t'. The state of the $N+1$-particle system becomes

$$|\Psi(r', t'=0)\rangle \equiv \psi^\dagger(\vec{r'}, t'=0)\,|\Psi_0\rangle = \sum_{\vec{k}} \phi^*_{\vec{k}}(\vec{r'}) c^\dagger_{\vec{k}}\,|\Psi_0\rangle\,, \tag{3.44}$$

in the Schrödinger picture.

With interactions, the wavefunctions on the right-hand side are not the eigenstates of this new $N+1$-particle system. Hence, to get the time evolution, $|\Psi(r', 0)\rangle$ must be expanded onto the exact eigenstates of this $N+1$-particle system:

$$\left|\Psi(\vec{r'}, t'=0)\right\rangle = \sum_{\vec{k}} \phi^*_{\vec{k}}(\vec{r'}) \sum_A \langle\Psi_A|\, c^\dagger_{\vec{k}}\,|\Psi_0\rangle\,|\Psi_A\rangle \tag{3.45}$$

where A denotes the basis for the eigensates of the $N+1$ system. Time evolution of this state gives $|\Psi(\vec{r}, t)\rangle = e^{-\frac{i}{\hbar}(\hat{H}-\mu\hat{N})t}\,|\Psi(\vec{r}, 0)\rangle$. Here $\hat{H}$ is a many-body Hamiltonian for the whole system, and $\hat{N}$ is the number operator. We want to compare this state to another state, corresponding to the case that a fermion is injected into this time at time t:

$$\psi^\dagger(\vec{r}, t)\,|\Psi_0\rangle \to \psi^\dagger(\vec{r}) e^{-\frac{i}{\hbar}(\hat{H}-\mu\hat{N})t}\,|\Psi_0\rangle \tag{3.46}$$

in the Schrödinger picture.

Computing the overlap between these two states yields:

$$\langle\Psi_0|\,\psi(\vec{r},t)\psi^\dagger(\vec{r'},0)\,|\Psi_0\rangle = \sum_{\vec{k}} \phi_{\vec{k}}(\vec{r})\phi^*_{\vec{k}}(\vec{r'}) \sum_A |\,\langle\Psi_A|\,c_{\vec{k}^\dagger}\,|\Psi_0\rangle\,|^2 e^{-\frac{i}{\hbar}[E_A-(E_0+\mu)]t}, \tag{3.47}$$

where $\mu = \partial E_0/\partial N$. For a gapless system, the ground state energy of the $N+1$-particle system is $E_0+\mu$, therefore the right hand side of this equation contains information on the time evolution of an excited state with excitation energy $\hbar\omega = E_A - (E_0+\mu)$. The effect of interactions appear in $|\,\langle\Psi_A|\,c_{\vec{k}^\dagger}\,|\Psi_0\rangle\,|^2$.

3.5.2 Correlation function

The one-particle Green's function defined in Eq. 3.42 is seldom, if never, an experimental observable, because it requires the creation and destruction of a particle. Instead, a two-particle Green's function $-\left\langle \mathcal{T}\left[c_{\nu_4}(t)c_{\nu_3}(t)c^\dagger_{\nu_2}(t')c^\dagger_{\nu_1}(t')\right]\right\rangle$ is more useful from the experimental point of view, since it describes the process that a particle changes its state by scattering with another particle. This kind of two-particle Green's function often manifests as a correlation function in linear response theory, as discussed in details in Chapter 4.

Here we introduce the definition of the retarded correlation function as

$$C^R_{AB}(tt') = -i\theta(t-t')\,\langle[A(t),B(t')]\rangle\,. \tag{3.48}$$

Its importance comes from the fact that almost all experimental observables, such as conductivity, are related to retarded correlation functions. This correlator contains the information about the response of a measurable quantity at time t to an external perturbation that happened at time t'.

A convenient method for writing down a formal result for retarded correlation function is to use the so-called "Lehmann representation," which chooses a set of eigenstates of the full Hamiltonian as the basis set. By using this representation, we have

$$\begin{aligned}
\left\langle\left[\hat{A}(t),\hat{B}(t')\right]\right\rangle &= \sum_n \frac{e^{-\beta E_n}}{Z}\,\langle n|\left[\hat{A}(t),\hat{B}(t')\right]|n\rangle \\
&= \sum_{n,m}\frac{e^{-\beta E_n}}{Z}\{\langle n|\,\hat{A}(t)\,|m\rangle\,\langle m|\,\hat{B}(t')\,|n\rangle - \langle n|\,\hat{B}(t')\,|m\rangle\,\langle m|\,\hat{A}(t)\,|n\rangle\} \\
&= \sum_{n,m}\frac{e^{-\beta E_n}}{Z}\{\langle n|\,\hat{A}\,|m\rangle\,\langle m|\,\hat{B}\,|n\rangle\,e^{i(E_n-E_m)(t-t')} - \langle n|\,\hat{B}\,|m\rangle\,\langle m|\,\hat{A}\,|n\rangle\,e^{-i(E_n-E_m)(t-t')}\},
\end{aligned}$$

where $Z = \sum_n e^{-\beta E_n}$. Therefore

$$\begin{aligned}
C^R_{AB}(\omega) &= \int d(t-t')e^{i\omega(t-t')}(-i\theta(t-t'))\left\langle\left[\hat{A}(t),\hat{B}(t')\right]\right\rangle \\
&= \int_0^\infty \sum_{n,m}(-i\theta(t-t'))\{\frac{e^{-\beta E_n}}{Z}\langle n|\hat{A}|m\rangle\langle m|\hat{B}|n\rangle e^{i(E_n-E_m+\omega)t} \\
&\quad -\frac{e^{-\beta E_n}}{Z}\langle n|\hat{B}|m\rangle\langle m|\hat{A}|n\rangle e^{-i(E_n-E_m+\omega)t}\} \\
&= \int_0^\infty \sum_{n,m}(-i\theta(t-t'))\frac{e^{-\beta E_n}-e^{-\beta E_m}}{Z}\langle n|\hat{A}|m\rangle\langle m|\hat{B}|n\rangle e^{i(E_n-E_m+\omega)t} \\
&= \sum_{n,m}\frac{1}{E_n-E_m+\omega-i\eta}\langle n|\hat{A}|m\rangle\langle m|\hat{B}|n\rangle\frac{e^{-\beta E_n}-e^{-\beta E_m}}{Z}.
\end{aligned}$$

In the last equation, a small positive η is added to make the integral over time well-defined.

3.5.3 Green's function in imaginary time

At finite temperature, the thermal average over $\left\langle e^{-\beta H}\hat{X}\right\rangle$ is a tedious calculation. A mathematical trick to work at finite temperature is introducing the so-called "imaginary time". Although more subtle in its conception, using imaginary time makes the calculation of Green's functions much easier. The imaginary time Green's function is defined as: $\mathcal{G}(\nu\nu', tt') = -\left\langle\mathcal{T}_\tau(c_\nu(\tau)c^\dagger_{\nu'}(\tau'))\right\rangle$. The definition of correlation function with imaginary time becomes:

$$C_{AB}(\tau,\tau') = -\left\langle\mathcal{T}_\tau(\hat{A}(\tau)\hat{B}(\tau'))\right\rangle \tag{3.49}$$

where $\tau = it$ within domain $-\beta \leqslant \tau \leqslant \beta$. An operator in the Heisenberg picture is $\hat{A}(\tau) = e^{H\tau}\hat{A}e^{-H\tau}$, which has the property $C_{AB}(\tau) = \pm C_{AB}(\tau+\beta)$ (with "+" for bosons and "−" for fermions).

The Fourier transformation from imaginary time to the frequency domain is:

$$C_{AB}(i\omega_n) = \int_0^\beta d\tau C_{AB}(\tau)e^{i\omega_n\tau}, \tag{3.50}$$

where ω_n is the Matsubara frequency, with $\omega_n = \frac{(2n+1)\pi}{\beta}$ for fermions and $\omega_n = \frac{2n\pi}{\beta}$ for bosons.

Now we can check the correlation function with imaginary time in the Lehmann representation, with

$\tau' = 0$ and $\tau > 0$

$$\begin{aligned} C_{AB}(\tau) &= -\left\langle \hat{A}(\tau)\hat{B}(0)\right\rangle \\ &= -\frac{1}{Z}\sum_{m,n} e^{-\beta\epsilon_n} \langle n|\, \hat{A}(\tau)\, |m\rangle \langle m|\, \hat{B}(0)\, |n\rangle \\ &= -\frac{1}{Z}\sum_{m,n} e^{-\beta\epsilon_n} \langle n|\, e^{\hat{H}\tau}\hat{A}e^{-\hat{H}\tau}\, |m\rangle \langle m|\, \hat{B}\, |n\rangle \\ &= -\frac{1}{Z}\sum_{m,n} e^{-\beta\epsilon_n} e^{(\epsilon_n-\epsilon_m)\tau} \langle n|\, \hat{A}\, |m\rangle \langle m|\, \hat{B}\, |n\rangle\,. \end{aligned}$$

Transforming to the frequency domain, we have

$$\begin{aligned} C_{AB}(i\omega_n) &= \int_0^\beta d\tau e^{i\omega_n\tau}\left[-\frac{1}{Z}\sum_{m,n} e^{-\beta\epsilon_n} e^{(\epsilon_n-\epsilon_m)\tau} \langle n|\, \hat{A}\, |m\rangle \langle m|\, \hat{B}\, |n\rangle\right] \\ &= \sum_{m,n}\frac{1}{i\omega_n+\epsilon_n-\epsilon_m}\frac{e^{-\beta\epsilon_n}-e^{-\beta\epsilon_m}}{Z} \langle n|\, \hat{A}\, |m\rangle \langle m|\, \hat{B}\, |n\rangle\,, \end{aligned} \tag{3.51}$$

where $e^{i\omega_n\beta} = \pm 1$ has been used. If we take $i\omega_n$ approaches $\omega + i\eta$, this correlator becomes the retarded Green's function with real time in Eq. 3.49.

The benefit of using imaginary time is its convenience for integrating over the coordinates in the Green's function. For example, calculating the correlation function often involves a summation over Matsubara frequency ω_n, such as $\frac{1}{\beta}\sum_{i\omega_n} g(i\omega_n)$, where the $g(i\omega_n)$ usually has a form of $\Pi_j \frac{1}{i\omega_n - z_j}$ (a product of Green's function), containing finite poles at $z = z_j$ in the complex plane.

Combining a contour integral and the residue theorem,

$$\begin{aligned} \oint_C \frac{dz}{2\pi i} f(z)g(z) &= \sum_{i\omega_n} \operatorname*{Res}_{z=i\omega_n}[f(z)]g(i\omega_n) + \sum_j \operatorname*{Res}_{z=z_j}[g(z)]f(z_j) \\ &= -\frac{1}{\beta}\sum_{i\omega_n} g(ik_n) + \sum_j \operatorname*{Res}_{z=z_j}[g(z)]f(z_j). \end{aligned} \tag{3.52}$$

where $f(z_j) = \frac{1}{e^{\beta z}+1}$ is the Fermi distribution function, with poles at $z = i(2n+1)\pi/\beta$. If $f(z)g(z) \to 0$ as $|z| \to \infty$, then we have

$$\frac{1}{\beta}\sum_{i\omega_n} g(i\omega_n) = -\sum_j \operatorname*{Res}_{z=z_j}[g_0(z)]f(z_j). \tag{3.53}$$

This mathematical trick is used for calculating resistivity in Chapter 4.

Chapter 4

Bad Metal in a Fermi Lattice Gas

4.1 Introduction

One famous long-standing puzzle in physics is the vanishing of resistivity in high-temperature superconductors. In 1986, IBM researchers Georg Bednorz and Alex Müller discovered high-temperature superconductivity in copper oxide compounds. Unlike conventional metals, which become superconducting via the well understood Bardeen-Cooper-Schrieffer (BCS) paradigm, the mechanism underlying high T_c superconductivity is not fully known.

One of the ambitious goals in the field of quantum simulation is using ultracold atoms or molecules in optical lattices to provide insight into the mysteries of high-T_c superconductivity. As the schematic phase diagram of high-T_c superconductivity (Fig. 4.1) shows, the material without doping is an insulator with anti-ferromagnetic order below the Neel temperature. Recently, several groups have successfully observed the anti-ferromagnetic phase in optical lattices in 3D [73] and 2D [74–77]. While these encouraging results allow experiments to take a step further to approaching the high-T_c state, the coldest temperature achieved so far is still not sufficiently low to observe the possible d-wave pairing phase in the Hubbard model.

However, there are also mysteries at relatively high temperature. Above the superconducting "dome," there exist three metallic phases depending on the doping: the pseudogap phase, the strange metal (also known as the "bad metal"), and the Fermi liquid phase (*i.e.*, a conventional metal). To some extent, the pseudogap and strange metal phases are even less well understood compared with the superconducting state. Numerous puzzles are debated, such as the relation between the pseudogap and superconducting phase [78] and the lack of quasiparticles in the strange metal phase [79, 80].

The strange metal presents abnormal electrical and thermal conductivity. For example, they show anomalous scaling of resistivity with temperature and can appear as a quantum soup in which the electrons have lost their individual character (see more details in Section 4.4). This "strange metal" phase continues to be of theoretical interest. Theoretical approaches based on marginal Fermi liquid phenomenology [82], DMFT (see Refs. [2, 83], for example), and AdS-CFT holographic duality [84–86] have shown T-linear resistivity at

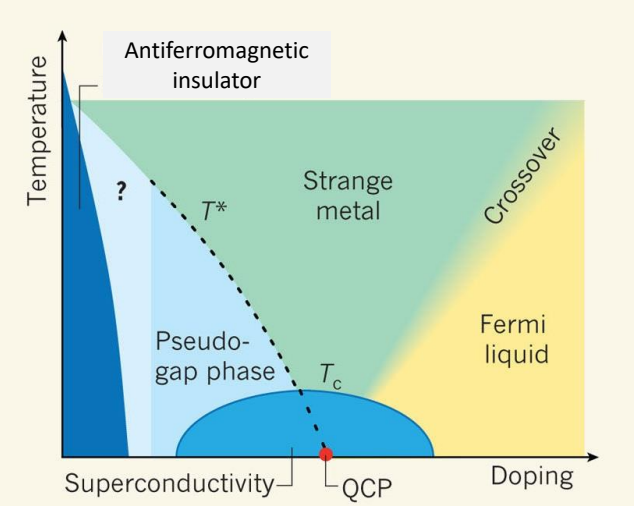

Figure 4.1: A schematic phase diagram of high-temperature superconductivity. Below the critical temperature T_c, the material becomes superconducting for doping. Above T_c, there are several metallic phases: the pseudogap, the strange metal, and the conventional metal. The transition between the Fermi-liquid phase and the strange metal phase is a crossover. This figure is reproduced from Ref. [81].

high temperature. A complete understanding of how these behaviors arise is debated.

Some people believe that understanding the origin of bad-metal behavior is crucial to resolve the mysteries of high-T_c superconductivity. Although most physicists agree that the strong electron-electron interactions are necessary for a bad metal, the importance of other ingredients such as electron-phonon interactions [87] is debated. This uncertainty motivates us to perform transport measurements with ultracold fermions trapped in optical lattices. For ultracold fermionic atoms trapped in optical lattices, which realize the Fermi-Hubbard model, phonons are absent, and the interactions are short-ranged. Whether or not we observe anomalous transport in our system will be helpful to understanding the origin of bad-metal behavior.

In previous ultracold gas experiments with fermionic atoms, the analog of photoemission spectroscopy was used to probe the spectral function in the BEC-BCS crossover for a trapped gas, and a failure of Fermi liquid theory was discovered [88]. Transport measurements such as diffusion in a 2D lattice gas [38], shear viscosity in a unitary Fermi gas [89], and spin diffusion [90] have also explored the effect of strong interactions on various relaxation processes.

In this chapter, I describe a method for measuring the decay rate of a mass current and inferring the analog of electrical resistivity for a two-component fermionic gas composed of ^{40}K atoms trapped in a cubic optical lattice. A net current consisting of a flow of spin-polarized atoms shifted in quasimomentum is created using stimulated Raman transitions. By fully resolving the decay dynamics of the current, we deduce the transport lifetime induced by collisions with atoms in the other spin state. The analog of resistivity is

inferred from the transport lifetime and the atomic density.

4.2 Theories for DC conductivity

Electrical current is the flow of charge carriers. Collisions between these particles can change their momentum $\vec{p}$. For a perfectly translationally invariant system, the DC conductivity is infinite, because of the conservation of momentum. In crystalline solid materials, there are three major sources that give rise to finite resistivity: scattering with impurities, Umklapp scattering between electrons, and scattering with phonon modes. In this section, I will discuss three theoretical approaches for understanding the DC conductivity: the Drude model, the Boltzmann equation, and the Kubo formula.

The Drude model provides a simple physics picture that relates the origin of resistivity to momentum relaxation. In Section. 4.5, we fit the decay of the mass current to the solution of the Boltzmann equation. Furthermore, in Section. 4.8, we use dynamical mean-field theory, which evaluates resistivity from the Kubo formula, to predict the scaling behavior of resistivity under our experimental conditions. Therefore, discussion of these complimentary theoretical approaches is important.

4.2.1 Drude model: an intuitive picture to understand the origin of resistivity

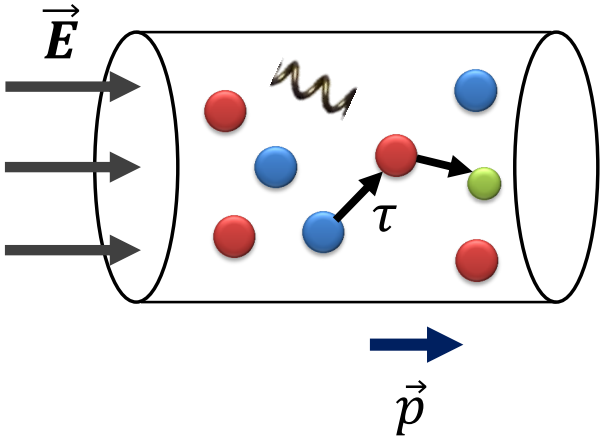

Figure 4.2: In the Drude model, a charge carrier (blue circle) constantly scatters from other electrons (red circle), impurities (green circle), or ions (spring), and loses momentum. τ is the average time between two collisions.

Without any external electric field, the velocity of the electrons in a material points toward each direction randomly, and therefore the net momentum $\langle\vec{p}\rangle$ is zero. After applying an external field $\vec{E}$, electrons start to accelerate along the direction of $\vec{E}$, and $\langle\vec{p}(t)\rangle = -e\vec{E}t$. After traveling for some time τ, the charge carrier collides with another particle (which can be another electron, impurity, or phonon) and changes its momentum. The equation describing this motion is:

$$\frac{d}{dt}\langle\vec{p}(t)\rangle = -e\vec{E} - \frac{\langle\vec{p}(t)\rangle}{\tau}, \tag{4.1}$$

where τ is a characteristic timescale corresponding to the relaxation rate of momentum $\vec{p}$.

A steady state solution requires $\frac{d}{dt}\langle\vec{p}(t)\rangle = 0$, *i.e.*, $\langle\vec{p}\rangle = -e\tau\vec{E}$. The average velocity of electrons is $\langle\vec{v}\rangle = -e\tau\vec{E}/m$, and the corresponding current density is $\left\langle\vec{j}\right\rangle = n(-e)\langle\vec{v}\rangle = (\frac{ne^2\tau}{m})\vec{E}$. Since $\vec{j} = \sigma\vec{E}$, the conductivity is:

$$\sigma = \frac{ne^2\tau}{m}. \tag{4.2}$$

The Drude model is very simple in terms of physics: interactions between electrons and ions or between the electrons are neglected. This approach is appealing because by just assuming that there is a scattering mechanism, instead of developing any specific microscopic formula to calculate τ, the Drude model can successfully explain the Hall effect, and Wiedemann–Franz law [54].

4.2.2 A semiclassical approach: the Boltzmann equation

The Boltzmann equation provides a semiclssical approach for studying transport properties. It assumes that there are particle-like excitations, and therefore we can use a phase space distribution function $f(\vec{r},\vec{k},t)$ to describe the system. The time-rate-of-change of this distribution function $f(\vec{r},\vec{k},t)$ obeys

$$\frac{df}{dt} = \frac{\partial f}{\partial t} + \frac{\partial\vec{r}}{\partial t}\nabla_{\vec{r}}f + \frac{\partial\vec{k}}{\partial t}\nabla_{\vec{k}}f. \tag{4.3}$$

Because we express the distribution function in terms of position $\vec{r}$ and crystal wavevectors of the lattice $\vec{k}$, Boltzmann equation is a semiclassical approach as it assumes that the position and the momentum of a particle can be defined simultaneously.

For simplicity, we assume spatial homogeneity, *i.e.*, $\nabla_{\vec{r}}f = 0$. With the appearance of an external electric field $\vec{F} = -e\vec{E} = \hbar\frac{\partial\vec{k}}{\partial t}$, and if there are no collisions between particles, $\dot{\vec{k}} = -e\vec{E}/\hbar$, which leads to Bloch oscillations in a lattice [1]. If there are collisions randomizing the momentum that balance the external

[1] It is interesting that the relaxation of momentum due to collisions is the origin of resistivity and conductivity at the same time. Conductivity is an interplay between Bloch oscillations and relaxation processes.

electrical field, then the distribution function f reaches a static state, *i.e.*, $\frac{\partial f}{\partial t} = 0$. Now we have

$$\frac{df}{dt} = -\frac{e\vec{E}}{\hbar} \cdot \nabla_{\vec{k}} f(\vec{k}) = b - a, \tag{4.4}$$

where a and b take collisions into account. The parameter $a = \frac{1}{(2\pi)^3} \int d^3\vec{k}\ f(\vec{k})(1 - f(\vec{k'}))\theta(\vec{k'}, \vec{k})$ is the rate of scattering out of state $\vec{k}$, and $b = \frac{1}{(2\pi)^3} \int d^3\vec{k}\ (1 - f(\vec{k}))f(\vec{k'})\theta(\vec{k}, \vec{k'})$ is the rate for particles scattering into $\vec{k}$ from other states $\vec{k'}$. The parameter $\theta(\vec{k}, \vec{k'})$ is the scattering rate between $\vec{k}$ and $\vec{k'}$.

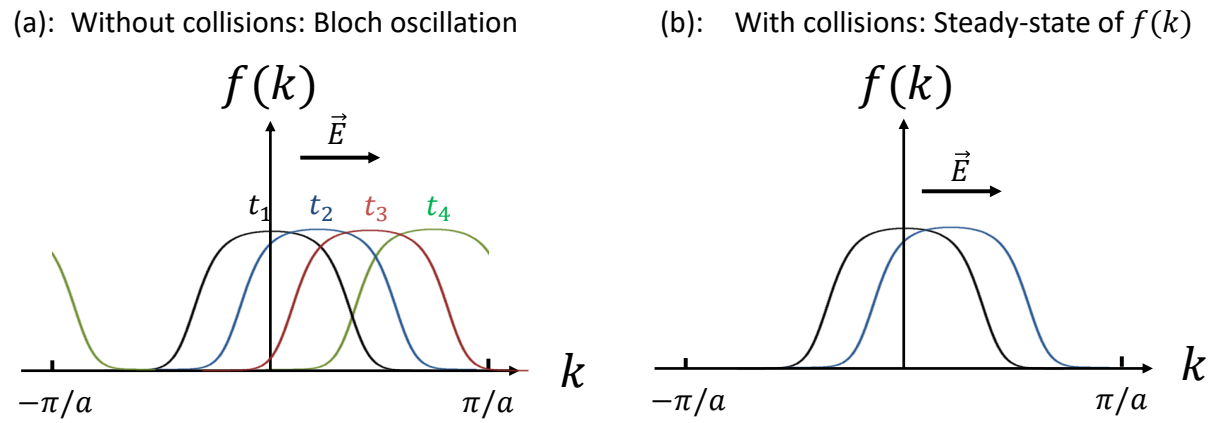

Figure 4.3: (a): Without collisions, the motion of electrons will be oscillatory (*i.e.*, Bloch oscillations). (b): With collisions, the distribution in momentum space can reach a steady state, i.e. $\frac{\partial f}{\partial t} = 0$.

Assuming the steady state $f(\vec{k})$ is close to the equilibrium phase space distribution $n(\vec{k})$, then up to a linear order in $\vec{E}$, we expand $f(\vec{k})$ as $n(\vec{k}) + \delta f(\vec{k})$, where $n(\vec{k})$ is the Fermi-Dirac distribution $\frac{1}{e^{\beta[\epsilon(\vec{k})-\mu]}+1}$ (where $\beta = 1/k_B T$, and μ is the chemical potential). With $\nabla_{\vec{k}} f(\vec{k}) = \nabla_{\vec{k}} \epsilon(\vec{k}) \frac{\partial f(\vec{k})}{\partial \epsilon(\vec{k})} = \hbar \vec{v}(\vec{k}) \frac{\partial f(\vec{k})}{\partial \epsilon(\vec{k})}$, up to linear order in $\delta f(\vec{k})$, we have

$$-e\vec{E} \cdot \vec{v}(\vec{k})\ \frac{\partial n(\vec{k})}{\partial \epsilon(\vec{k})} = b - a \equiv -\frac{\delta f(\vec{k})}{\tau(\vec{k})}, \tag{4.5}$$

where we introduce the k-dependent relaxation timescale $\tau(\vec{k})$. We assume that collisions between particles act to return the system back to its equilibrium configuration. The rate of change in $f(\vec{k})$ is proportional to its deviation from $n(\vec{k})$. The expression for current is therefore:

$$\vec{j} = -\frac{e}{(2\pi)^3} \int d^3\vec{k}\ \vec{v}(\vec{k}) f(\vec{k}) = -\frac{e}{(2\pi)^3} \int d^3\vec{k}\ \vec{v}(\vec{k})\ \delta f(\vec{k}) \tag{4.6}$$

$$= -\frac{e^2}{(2\pi)^3} \int d^3\vec{k}\ \vec{v}(\vec{k}) \tau(\vec{k}) (\vec{v}(\vec{k}) \cdot \vec{E}) \frac{\partial n(\vec{k})}{\partial \epsilon(\vec{k})}. \tag{4.7}$$

The integral over $d^3\vec{k}$ can be rewritten as $dS dk_\perp$, where dS is the equal energy surface, and $dk_\perp$ is perpen-

dicular to that surface. Moreover, since $dk_\perp = dE\frac{dk_\perp}{dE} = \frac{dE}{\hbar|\vec{v}(\vec{k})|}$, we have

$$\vec{j} = \frac{e^2}{(2\pi)^3}\int \frac{dSdE}{\hbar|\vec{v}(\vec{k})|}\tau(\vec{k})\vec{v}(\vec{k})(\vec{v}(\vec{k})\cdot\vec{E})(-\frac{\partial n(\vec{k})}{\partial\epsilon(\vec{k})}). \tag{4.8}$$

Then the conductivity tensor, defined by $j_\alpha = \sum_\beta \sigma_{\alpha\beta}E_\beta$ $(\alpha,\beta = x,y,z)$ is:

$$\sigma_{\alpha\beta} = \frac{e^2}{(2\pi)^3}\int dSdE\ \tau(\vec{k})\frac{\vec{v}(\vec{k})_\alpha\vec{v}(\vec{k})_\beta}{\hbar|\vec{v}(\vec{k})|}(-\frac{\partial n(\vec{k})}{\partial\epsilon(\vec{k})}). \tag{4.9}$$

As temperature $T\to 0$, $-\frac{\partial n(\vec{k})}{\partial\epsilon(\vec{k})} = \delta(\epsilon(\vec{k})-\epsilon(k_F))$, and only $\vec{k}$ states near the Fermi surface contribute to this integral. If we assume a spherical Fermi surface, and the off-diagonal elements of $\sigma_{\alpha,\beta}$ are zero, and with $\sigma_{xx} = \sigma_{yy} = \sigma_{zz}$, we have:

$$\sigma_{\alpha\alpha} = \frac{e^2}{(2\pi)^3}\frac{1}{3}\frac{v_F}{\hbar}4\pi k_F^2\tau(k_F). \tag{4.10}$$

With $k_F = (3\pi^2 n)^{1/3}$ and $v_F = \hbar k_F/m$, we have $\sigma = \frac{ne^2\tau}{m}$, which is the Drude formula. Surprisingly, the conductivity depends on the density of all the carriers in the system through v_F, even though only the scattering near the Fermi surface contributes to the conductivity.

Next, we will discuss the calculation of τ. Recall that

$$-\frac{\delta f(\vec{k})}{\tau(\vec{k})} = \int d^3\vec{k}'\ \theta(\vec{k},\vec{k}')f(\vec{k}')(1-f(\vec{k})) - \int d^3\vec{k}'\ \theta(\vec{k},\vec{k}')f(\vec{k})(1-f(\vec{k}')). \tag{4.11}$$

Since at equilibrium

$$\int d^3\vec{k}'\ \theta(\vec{k},\vec{k}')n(\vec{k}')(1-n(\vec{k})) = \int d^3\vec{k}'\ \theta(\vec{k},\vec{k}')n(\vec{k})(1-n(\vec{k}')),$$

we have

$$\theta(\vec{k},\vec{k}')e^{\beta(\epsilon(\vec{k})-\epsilon(\vec{k}'))} = \theta(\vec{k}',\vec{k}).$$

For elastic scattering, $\epsilon(\vec{k}) = \epsilon(\vec{k}')$, therefore $\theta(\vec{k},\vec{k}') = \theta(\vec{k}',\vec{k})$. Eq. 4.11 therefore becomes:

$$\frac{1}{\tau(\vec{k})} \quad = \quad \frac{1}{(2\pi)^3}\int d^3\vec{k}'\ \theta(\vec{k},\vec{k}')\left[1-\frac{\delta f(\vec{k}')}{\delta f(\vec{k})}\right]\delta\left[\epsilon(\vec{k})-\epsilon(\vec{k}')\right]. \tag{4.12}$$

Under the assumption of a weak electrical field, $\delta f(\vec{k})$ is proportional to $\vec{k}\cdot\vec{E}$. After doing some geometry, we have:

$$\frac{1}{\tau(\vec{k})} = \frac{1}{(2\pi)^3}\int d^3\vec{k}'\ \theta(\vec{k},\vec{k}')(1-\cos\eta)\delta\left[\epsilon(\vec{k})-\epsilon(\vec{k}')\right], \tag{4.13}$$

where η is the angle between $\vec{k}$ and $\vec{k'}$, and $\cos(\eta) = \vec{k} \cdot \vec{k'}/|\vec{k}||\vec{k'}|$. The weighting factor $1 - \cos(\eta)$ affects the contribution to resistivity based on the change in angle after scattering. Small-angle scattering is relatively unimportant. Due to this factor, the relaxation time in the transport equation is not identical to the average scattering rate. The evaluation of $\theta(\vec{k}, \vec{k'})$ depends on the microscopic details of the scattering mechanism, which may be very complicated.

Notice that this derivation of the Boltzmann equation does not require momentum conservation during collisions. It assumes the electrons scatter with "pinned" impurities.

4.2.3 Kubo formula: linear response theory

Linear response theory is widely used theoretical concept. The basic idea is that the response of a system to a weak external perturbation is proportional to that perturbation. This section discusses the derivation of DC conductivity based on linear response theory.

Current operator in second quantization language

For particles with charge e in electromagnetic field, the kinetic energy operator is:

$$\begin{aligned} \hat{T} &= \frac{1}{2m} \sum_{\sigma} \int d\vec{r}\, \Psi_{\sigma}^{\dagger}(\vec{r}) (\frac{\hbar}{i} \nabla_r - e\vec{A})^2 \Psi_{\sigma}(\vec{r}) \\ &= \hat{T_0} + \sum_{\sigma} \int d\vec{r}\, \frac{e\hbar}{2mi} \vec{A} \left[(\nabla_r \Psi_{\sigma}^{\dagger}(\vec{r})) \Psi_{\sigma}(\vec{r}) - \Psi_{\sigma}^{\dagger}(\vec{r}) (\nabla_r \Psi_{\sigma}(\vec{r})) \right] \\ &\quad + \frac{e^2}{2m} \sum_{\sigma} \int d\vec{r}\, (\vec{A})^2 \Psi_{\sigma}^{\dagger}(\vec{r}) \Psi_{\sigma}(\vec{r}), \end{aligned} \tag{4.14}$$

where $\Psi_{\sigma}(\vec{r})$ and $\Psi_{\sigma}^{\dagger}(\vec{r})$ are the quantum field operators, and $\vec{A}$ is the vector potential.

Suppose the magnitude of $\vec{A}$ is small enough such that we are only interested in linear response. Then the current operator can be written as:

$$\hat{j} = -\delta \hat{T} / \delta \vec{A} = \frac{e\hbar}{2mi} \left[\Psi_{\sigma}^{\dagger}(\vec{r}) (\nabla \Psi_{\sigma}(\vec{r})) - (\nabla \Psi_{\sigma}^{\dagger}(\vec{r})) \Psi_{\sigma}(\vec{r}) \right]. \tag{4.15}$$

The momentum representation of the current operator is,

$$\hat{j} = \frac{e\hbar}{mV} \sum_{\vec{k}\vec{q}} (\vec{k} + \frac{1}{2}\vec{q}) e^{i\vec{q}\vec{r}} c_{\vec{k}\sigma}^{\dagger} c_{\vec{k}+\vec{q}\sigma}, \tag{4.16}$$

where V is volume of the system. For DC conductivity, we will assume the limits $q \to 0$ and $\omega \to 0$.

Kubo formula for DC conductivity

Now the goal is to study how a system responds to an external field. For a general Hamiltonian, $H(t) = H_{eq} + \theta(t-t_0)H'(t)$, where H_{eq} is the Hamiltonian for the original equilibrium state, and $H'(t)$ is an external field turned on at $t = t_0$.

We derive to calculate how the observables in this system respond to $H'(t)$. It is convenient to go to the interaction picture, where operators become time-dependent as $\hat{A}(t) = e^{iH_{eq}t}\hat{A}e^{-iH_{eq}t}$. Here, the interaction representation with the presence of the external perturbation field is actually the Heisenberg representation of the original equilibrium system. The unitary transformation is with the full H_{eq}, which can have interaction terms.

In interaction picture, to first order in $\hat{H}'(t)$, we have

$$\begin{aligned} \delta\hat{A}(t) &\equiv \langle\hat{A}(t)\rangle - \langle\hat{A}\rangle_{eq} \\ &= -i\int_{t_0}^{t} dt' \left\langle \left[\hat{A}(t), \hat{H}'(t')\right]\right\rangle_{eq}. \end{aligned} \tag{4.17}$$

We can define a response correlation function as $C^R_{AH'} = -i\theta(t-t')\left\langle\left[\hat{A}(t), \hat{H}'(t)\right]\right\rangle_{eq}$, and rewrite the linear response function as $\delta\hat{A}(t) = \int_{t_0}^{\infty} dt' C^R_{AH'}(t,t')$.

Consider an external electrical field $H'(t) = \hat{B}f(t)$ (in the Schrödinger picture). Notice that $\hat{B}$ is independent of time and $f(t)$ is not an operator, and thus we expect $C^R_{AH'}(t,t')$ to be dependent only on the time difference $t-t'$. So

$$\delta\hat{A}(t) = \int_{t_0}^{\infty} dt' C^R_{AB}(t,t')f(t') = \int_{t_0}^{\infty} dt' C^R_{AB}(t-t')f(t'), \tag{4.18}$$

which is a convolution of C^R_{AB} and f. After a Fourier transform, we have $\delta\hat{A}(\omega) = C^R_{AB}(\omega)f(\omega)$. In the Lehmann representation (Eq. 3.49),

$$C^R_{AB}(\omega) = \sum_{n,m}\frac{e^{-\beta E_n}}{Z}\{\langle n|\hat{A}|m\rangle\langle m|\hat{B}|n\rangle e^{i(E_n-E_m)(t-t')} - \langle n|\hat{B}|m\rangle\langle m|\hat{A}|n\rangle e^{-i(E_n-E_m)(t-t')}\},$$

where $|n\rangle$ is a set of eigenstates of the full Hamiltonian.

If an external electric field $H'(\omega) = \frac{e}{i\omega}\hat{j}E_{ext}(\omega)$ is applied, with $\delta\langle\hat{j}(t)\rangle = \frac{e}{i\omega}C^R_{jj}(\omega)E(\omega)$, the conductivity

is

$$\begin{aligned}\sigma(\omega)_{\alpha\beta} &= \mathrm{Re}[\frac{e}{i\omega}C^R_{jj}(\omega)] = \frac{e}{\omega}\mathrm{Im}[C^R_{jj}(\omega)] \\ &= \sum_{m,n}\frac{e}{\omega}\pi\delta(E_n - E_m + \omega)\left\langle n\right|\hat{j_\alpha}\left|m\right\rangle\left\langle m\right|\hat{j_\beta}\left|n\right\rangle\frac{e^{-\beta E_n} - e^{-\beta E_m}}{Z},\end{aligned} \tag{4.19}$$

where $\alpha(\beta) = x, y, z$ denote the spatial directions.

A comment on Kubo formula for conductivity: the effect of interactions on conductivity enters via the equilibrium eigenstates. The states $|m\rangle$ in Eq. 4.19 should be the eigenstates for the Hamiltonian including interactions. Some textbooks use the notation $\langle ...\rangle_0$ for Eq.(4.17), which may be misleading, since the correlation function should not be evaluated for the non-interacting Hamiltonian. So here, I emphasize this point by using the notation as $\langle ...\rangle_{eq}$.

4.2.4 Link between the Boltzmann equation, Kubo formula, and Drude model

How to link the Boltzmann equation to the Kubo formula is not easily understood. The form of these two approaches look different. The Boltzmann equation, where the scattering rate among different states plays a vital role, contains one-particle Green's functions. In contrast, the Kubo formula involves the current-current correlation and is similar to a two-particle (*i.e.*, four-point) Green's function.

It seems that Thouless was first to make a simple argument to demonstrate that the Boltzmann equation and the Kubo formula are equivalent to each other under some assumptions [91].

In the following discussion, we consider a simple case: $\hat{H} = \hat{H_0} + \hat{V}$, where $\hat{H_0} = \sum_k \epsilon_k c_k^\dagger c_k$, and $V = \sum_i V\delta(r - r_i)$ for the impurity potential. For DC conductivity, the current operator becomes $\hat{j} = e\sum_k \vec{v}(k)c_k^\dagger c_k = \frac{e}{\hbar}\sum_k \frac{\partial\epsilon(\vec{k})}{\partial\vec{k}}c_k^\dagger c_k$. The key point is to evaluate $\langle m|\,\hat{j}\,|n\rangle\langle n|\,\hat{j}\,|n\rangle$ in Eq.(4.19). As emphasized earlier, the state $|m\rangle$ is the eigenstate of H (and not of H_0).

We can expand the eigenstates of $\hat{H}$ in the basis of eigenstates of $\hat{H_0}$:

$$|m\rangle = \sum_k a_k^{(m)}\,|k\rangle\,, \tag{4.20}$$

where $|k\rangle$ is a plane-wave state. It is assumed that the $a_k^{(m)}$ are independent normally distributed random variables, with a mean value of zero and a standard deviation $\sigma_n = \left[\frac{1}{V}\frac{\pi}{lk_m^2}\frac{1}{(k-k_m)^2 + l^2/4}\right]^{1/2}$, where l is the mean-free path, and V is the volume. The expected value of the product of two normally-distributed random variables is:

$$a_k^{(m)}a_{k'}^{(n)} = \delta_{kk'}\delta_{mn}\sigma_n^2. \tag{4.21}$$

The physical meaning becomes clear now. We assume that $|m\rangle$ spreads out as a wave-packet, with the probability to have momentum k as $\frac{1}{V}\frac{\pi}{lk_m^2}\frac{1}{(k-k_m)^2+l^2/4}$. Also, this assumption ensures $\langle m|n\rangle = \delta_{mn}$. The basis states of $\hat{H}$ are therefore orthogonal to each other. We have justified that $|m\rangle$ form a complete orthonormal basis. To evaluate current-current correlation, we calculate

$$\begin{aligned} |\hat{j}_{mn}|^2 &\equiv \langle m|\,\hat{j}\,|n\rangle\,\langle n|\,\hat{j}\,|m\rangle = \sum_{k,k'} \langle m|\,k\rangle\,\langle k|\,\hat{j}\,|k\rangle\,\langle k\,|n\rangle\,\langle n|\,k'\rangle\,\langle k'|\,\hat{j}\,|k'\rangle\,\langle k'\,|m\rangle \\ &= e^2 \sum_{k,k'} a_k^{(m)} a_k^{(n)} a_{k'}^{(n)} a_{k'}^{(m)} \vec{v}(k)\vec{v}(k'). \end{aligned} \tag{4.22}$$

Only the terms with $k = k'$ contribute to Eq. 4.22, so the expectation value is

$$\begin{aligned} \left\langle |\hat{j}_{mn}|^2 \right\rangle &= \frac{e^2}{m^2}\frac{\pi^2}{l^2V^2k_m^2k_n^2}\sum_k \frac{\hbar^2k^2/3}{[(k-k_m)^2+l^2/4]\,[(k-k_n)^2+l^2/4]} \\ &\approx \frac{e^2}{m^2}\frac{2\hbar^2\pi l}{3V}\frac{1}{1+(k_m-k_n)^2l^2}, \end{aligned} \tag{4.23}$$

for large k and l. Substitution of this expression into the Kubo formula gives the conductivity $\sigma(\omega)$ as:

$$\begin{aligned} \sigma(\omega) &= \frac{1}{4\pi^4}\frac{2\pi e^2}{m\omega^2}2\hbar^2\pi l/3\int_0^{k_F} k_m^2dk_m\int_{k_F}^{\infty} k_n^2dk_n \\ &\quad \times\frac{1}{[1+(k_m-k_n)^2l^2]}\delta(\hbar^2k_m^2/2m-\hbar^2k_j^2/2m-\hbar\omega) \\ &= \frac{e^2k_F^2l}{3\hbar\pi^2}\frac{1}{1+m^2\omega^2l^2/\hbar^2k_F^2}. \end{aligned} \tag{4.24}$$

With $l = \frac{\hbar k_F\tau}{m}$ and $k_F = (3\pi^2n)^{1/3}$, $\sigma(\omega) = \frac{1}{ne^2\tau}\frac{1}{1+\omega^2\tau^2}$, which is the Drude model result for AC conductivity!

A caveat: In this derivation, τ is the scattering rate between electrons and impurities, which is not exactly the same τ used in the Boltzmann equation. In the Boltzmann equation, τ is weighted by the angle change of momentum before and after a collision. A more sophisticated (and maybe more general) derivation is given in Ref. [92]. Eqs.(23) and (24) in this reference give expressions for DC conductivity, where $1/\tau = 2\pi\sum_k' |V_{kk'}|^2\delta(\epsilon_k-\epsilon_k')(1-\cos(\eta))$, which matches the Boltzmann equation as derived in the previous section.

4.2.5 Summary

The relaxation time τ in the Drude formula, the Boltzmann equation, and the Kubo formula are the same quantity. The Boltzmann equation and the Kubo formula provide a microscopic picture to understand

transport. As I will show later in this chapter, our measurements directly probe the relaxation rate for a mass current consisting of $|\downarrow\rangle$ atoms, due to the collisions between $|\uparrow\rangle$ and $|\downarrow\rangle$ atoms. Although we do not have a static external force to maintain a DC current, the measured relaxation rate is still directly related to resistivity.

To some extent, the condensed matter community uses a "top-down" approach to infer the transport lifetime from resistivity measurements, and to obtain information about the microscopic scattering mechanism. In contrast, we use a "bottom-up" approach: we directly measure the transport lifetime and infer resistivity to compare with phenomena in solids.

4.3 Fermi liquid theory

This section gives a brief introduction to Fermi liquid theory, which was developed by Landau. It successfully describes the behavior of interacting fermionic particles for a wide range of materials, such as electrons in conventional metals and liquid helium-3 [93]. The central conclusion of Fermi-liquid theory is that a system consisting of interacting particles can be described using almost non-interacting quasiparticles. This explains why the electrons in a metal can be regarded as a gas of almost non-interacting particles, in spite of the Coulomb interaction. Fermi-liquid theory is the theoretical foundation for the semiclassical methods discussed in the previous section.

The central assumption of Fermi liquid theory rests on the concept of "adiabatic continuity" [94]: although the eigenstates may be changed significantly by a perturbation, the "good" quantum numbers associated with the eigenstates are more robust. Laudau proposed that if the interactions between particles can be turned on slowly, there would be a one-to-one correspondence between the new eigenstates of an interacting system with the original eigenstates for the non-interacting system.

In an interacting system, the counterpart of a free electron is called "quasiparticle." Quasiparticles incorporate the influence of interactions on different properties, such as energy and effective mass. Quasiparticles are not stationary states: they are excitations above the ground state of an interacting system. Therefore, there exists a time window for the concept of a "quasiparticle" to make sense: short enough that quasiparticle does not decay from scattering with other quasiparticles, but long enough to have a well-defined energy, as illustrated in Fig. 4.4.

Fermi liquid theory and the concept of "quasiparticles" are suitable for describing electrons in conventional metals. The associated good quantum numbers are spin and momentum. This paradigm has successfully explained the transport property of conventional metals. In the remainder of this section, I will

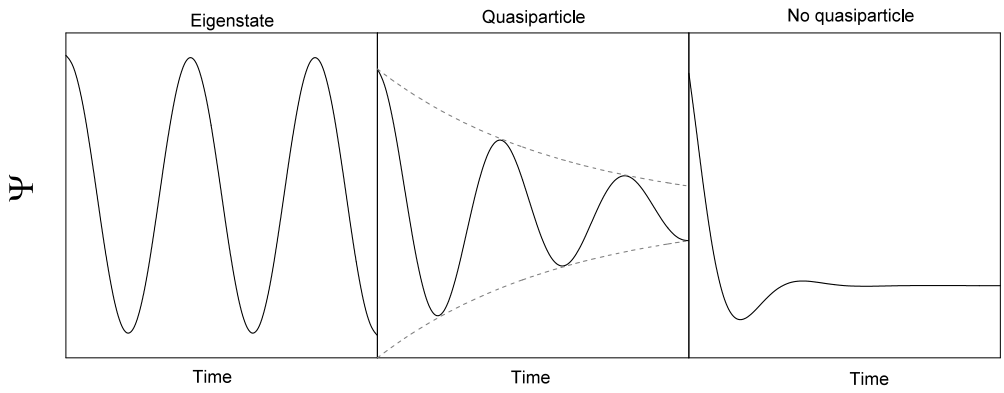

Figure 4.4: Generic time evolution of a wavefunction. The temporal oscillation of the wavefunction is controlled by the energy E_k and lifetime τ. Left: For free particle, τ is infinite. Middle: For an interacting system, when we say a quasiparticle is well-defined, it means that the wavefunction oscillates several times before being damped by electron-electron interactions. This underdamped behavior enables the definition of a corresponding excitation energy. Right: Fermi liquid theory fails if the damping is too fast. Such fast decay forbids the association of a precise excitation energy with this state, which is no longer particle-like. This figure is recreated from the ideas in Ref. [95].

discuss an approach to understanding the behavior of resistivity based on Fermi liquid theory.

4.3.1 Single-particle Green's function in Fermi liquid theory

In Fermi liquid theory, the retarded Green's function can generally be written as (see Chapter 3 for more details regarding the Green's function):

$$G^R(\vec{k},\omega) = \frac{1}{\omega - \xi_k - \Sigma(\vec{k},\omega)}, \tag{4.25}$$

where $\xi_k = \epsilon_k - \mu$ is the free-particle energy measured relative to the chemical potential, and $\Sigma(\vec{k},\omega)$ is the self-energy. The real part of the self-energy modifies the dispersion relationship. We define the normalized Fermi wave number $\vec{k_F^*}$ by the condition that $\xi_{\vec{k_F^*}} + \Re\Sigma(\vec{k_F^*},0) = 0$. The imaginary part of $\Sigma(\vec{k},\omega)$ is non-zero due to interactions that gives the quasiparticle a finite lifetime.

At low temperature and near the Fermi energy, we can expand $G^R(\vec{k},\omega)$ as

$$\begin{aligned} G^R(\vec{k},\omega) &= \frac{1}{\omega - (\epsilon_k + \Re\Sigma(\vec{k},\omega)) - i\Im\Sigma(\vec{k},\omega)} \\ &\approx \frac{1}{\omega - \omega\frac{\partial(\Re\Sigma^R)}{\partial\omega}|_{\omega=0} - (k-k_F^*)\frac{\partial(\xi_k+\Re\Sigma^R)}{\partial k}|_{k=k_F^*} - i\Im\Sigma^R} \\ &\equiv \frac{\mathcal{Z}}{\omega - \xi_k^* + \frac{i}{2\tau_k^*(\omega)}}, \end{aligned} \tag{4.26}$$

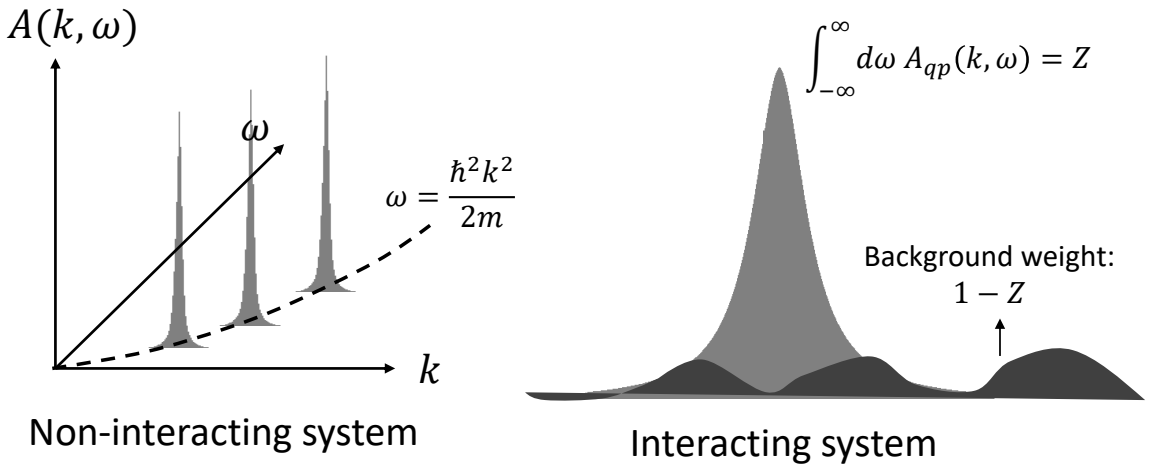

Figure 4.5: Schematic spectral functions for a free Fermi gas (left) and a quasiparticle in an interacting system (right). In a free Fermi gas, $A(k,\omega)$ is a delta function $2\pi\delta(\omega - \frac{\hbar^2 k^2}{2m})$. With interactions, the spectral function has a finite width, which inversely proportional to the lifetime of the quasiparticles. The spectral function consists of a Lorentzian function (corresponding to a quasiparticle) and a smooth background (*i.e.*, the incoherent component).

where

$$\mathcal{Z} = \frac{1}{1 - \frac{\partial}{\partial\omega}\Re\Sigma(k_F^*,\omega)|_{\omega=0}} \tag{4.27}$$

$$\xi_k^* = (k - k_F^*)\mathcal{Z}\frac{\partial}{\partial k}(\xi_k + \Re\Sigma(k,0))|_{k=k_F^*} \tag{4.28}$$

$$\frac{1}{\tau_k^*(\omega)} = -2\mathcal{Z}\Im\Sigma(k,\omega). \tag{4.29}$$

$\mathcal{Z}$ is the quasiparticle spectral weight, ξ_k^* is the effective energy near the Fermi surface, and $\tau_k^*(\omega)$ is the lifetime of a quasiparticle. The corresponding spectral function is:

$$A(\vec{k},\omega) = -2\Im G^R(k,\omega) \approx 2\pi\mathcal{Z}\delta(\omega - \xi_k^*). \tag{4.30}$$

The integral over ω gives $\int_{-\infty}^{\infty}\frac{d\omega}{2\pi}A(k,\omega) = \mathcal{Z}$. However, the general sum rule requires $\int_{-\infty}^{\infty}\frac{d\omega}{2\pi}A(k,\omega) = 1$. Therefore, there must exist another component of the spectral function, denoted as $A_{\rm ic}$, which satisfies $\int_{-\infty}^{\infty}\frac{d\omega}{2\pi}A_{ic} = 1 - \mathcal{Z}$. This component cannot be treated as a particle-like peak, and contains complicated many-body excitations. As shown by the schematic drawing in Fig. 4.5, the spectral function consists of a distinct peak (corresponding to the quasiparticle) and a smooth background (corresponding to "incoherent

excitations").

4.3.2 Random phase approximation

Until now, we have not given any specific form for the self-energy $\Sigma(k,\omega)$. Exactly calculating the self-energy for an interacting system is generally impossible (and not necessary in many cases). Some approximations are usually required.

The most important (and simplest) approximation that gives a finite quasiparticle lifetime is the random phase approximation (RPA). The basic diagram of RPA is the so-called pair-bubble diagram (Fig. 4.6(c)). Its physical interpretation is that a particle with momentum k and ω excites another particle with momentum k', generating a particle–hole excitation.

To evaluate the pair-bubble diagram, it is convenient to use the imaginary-time Green's function:

$$\begin{aligned}
\chi_0(\vec{q}, iq_n) &= \frac{1}{\beta}\sum_{ik'_n}\int \frac{d^3\vec{k}'}{(2\pi)^3} G_0(\vec{k}'+\vec{q}, ik'_n+iq_n)G_0(\vec{k}', ik'_n) \\
&= \frac{1}{\beta}\sum_{ik'_n}\int \frac{d^3\vec{k}'}{(2\pi)^3} \frac{1}{ik'_n+iq_n-\xi_{\vec{k}'+\vec{q}}}\frac{1}{ik'_n-\xi_{\vec{k}'}} \\
&= \int \frac{d^3\vec{k}'}{(2\pi)^3} \frac{n_F(\xi_{\vec{k}'+\vec{q}})-n_F(\xi_{\vec{k}'})}{\xi_{\vec{k}'+\vec{q}}-\xi_{\vec{k}'}-iq_n}.
\end{aligned} \tag{4.31}$$

The sum over ik'_n is done using a contour integral.

As shown in Fig. 4.6(b), the self-energy under the RPA approximation includes a summation over a series of pair-bubble diagrams:

$$\Sigma(\vec{k}, i\omega_n) = -\frac{1}{\beta}\sum_i q_n \int \frac{d^3\vec{q}}{(2\pi)^3} G_0(\vec{k}+\vec{q}, i\omega_n+iq_n)\chi(\vec{q}, iq_n), \tag{4.32}$$

with $\chi(\vec{q}, iq_n) = \frac{V(\vec{q})}{1-V(\vec{q})\chi_0(\vec{q},iq_n)}$. $V(\vec{q}) = \int d\vec{r}\; V(\vec{r})\; e^{i\vec{q}\cdot\vec{r}}$, which is the Fourier transform of the interaction $V(\vec{r})$.

For the on-site interaction in the Hubbard model, $V(\vec{q}) = U$. Up to the linear order in $\chi_0(\vec{q}, iq_n)$, we have $\chi(\vec{q}, iq_n) \approx U + U^2\chi_0(\vec{q}, iq_n) + ...$ Since we only care about the component of $\Sigma(\vec{k}, i\omega_n)$ that has an

imaginary part, denoted as $\triangle\Sigma(\vec{k}, i\omega_n)$, we have

$$\begin{aligned}
\triangle\Sigma(\vec{k}, i\omega_n) &= -\frac{1}{\beta}U^2 \sum_{iq_n} \int \frac{d^3\vec{q}}{(2\pi)^3} G_0(\vec{k}+\vec{q}, i\omega_n + iq_n)\chi_0(\vec{q}, iq_n) \\
&= -\frac{1}{\beta}U^2 \sum_{iq_n} \int \frac{d^3\vec{q}}{(2\pi)^3} \int \frac{d^3\vec{k}'}{(2\pi)^3} \frac{1}{i\omega_n + iq_n - \xi_{\vec{k}+\vec{q}}} \frac{n(\xi_{\vec{k}'+\vec{q}}) - n(\xi_{\vec{k}'})}{\xi_{\vec{k}'+\vec{q}} - \xi_{\vec{k}'} - iq_n} \\
&= U^2 \int \frac{d^3\vec{q}}{(2\pi)^3} \int \frac{d^3\vec{k}'}{(2\pi)^3} \frac{\alpha}{i\omega_n - \left[\xi_{\vec{k}+\vec{q}} + \xi_{\vec{k}'} - \xi_{\vec{k}'+\vec{q}}\right]},
\end{aligned} \tag{4.33}$$

where $\alpha = -n(\xi_{\vec{k}'}) \left[1 - n(\xi_{\vec{k}'+\vec{q}})\right] \left[1 - n(\xi_{\vec{k}'-\vec{q}})\right] - \left[1 - n(\xi_{\vec{k}'})\right] n(\xi_{\vec{k}'+\vec{q}}) n(\xi_{\vec{k}'+\vec{q}})$. Again, a contour integral has been used. By letting $i\omega_n \to \xi_{\vec{k}} + i\eta$ (*i.e.*, analytical continuation), we obtain the imaginary part of the self-energy $\triangle\Sigma(\vec{k}, \xi_{\vec{k}})$ as:

$$\int U^2 \left\{ -n(\xi_{\vec{k}'}) \left[1 - n(\xi_{\vec{k}'+\vec{q}})\right] \left[1 - n(\xi_{\vec{k}'-\vec{q}})\right] - \left[1 - n(\xi_{\vec{k}'})\right] n(\xi_{\vec{k}'+\vec{q}}) n(\xi_{\vec{k}'+\vec{q}}) \right\} \delta(\omega - (\xi_{\vec{k}+\vec{q}} + \xi_{\vec{k}'} - \xi_{\vec{k}'+\vec{q}})), \tag{4.34}$$

which is the scattering rate for Fermi's golden rule! The first term in the bracket is for scattering out of state $\left|\vec{k}\right\rangle$, and the second term corresponds to events scattering into $\left|\vec{k}\right\rangle$. The validity of Fermi liquid theory justifies the Boltzmann equation.

4.3.3 Conductivity

An explicit calculation of Eq. 4.32 can been found in Refs. [96, 97]. Here I just give a simple argument regarding the dependence of τ on the typical energy scale present in the system.

Consider the case with a particle above the Fermi sea, with energy $\omega > 0$ and momentum $\vec{k}$ (where $E_F = 0$). This particle scatters with one particle below the Fermi sea with energy $\omega_1 < 0$ and momentum $\vec{k}'$, and knock it out of the Fermi sea, thereby generating a particle-hole excitation. Constrained by energy conservation, the possible energy for $\xi(\vec{k}')$ must be higher than $-\omega$, and its final state cannot have an energy higher than $\omega + \omega_1$. The area of the allowed phase-space, therefore, is proportional to

$$\int_{-\omega}^{0} d\omega_1 \int_{0}^{\omega+\omega_1} d\omega_2 = \frac{1}{2}\omega^2. \tag{4.35}$$

In other words, the allowed phase-space for scattering events is proportional to the square of the typical excitation energy in the system. If the temperature is above ω, then the typical excitation energy is $k_B T$, and $1/\tau \propto T^2$. Since resistivity is proportional to $1/\tau$, we have $\rho \propto \max(\omega^2, T^2)$.

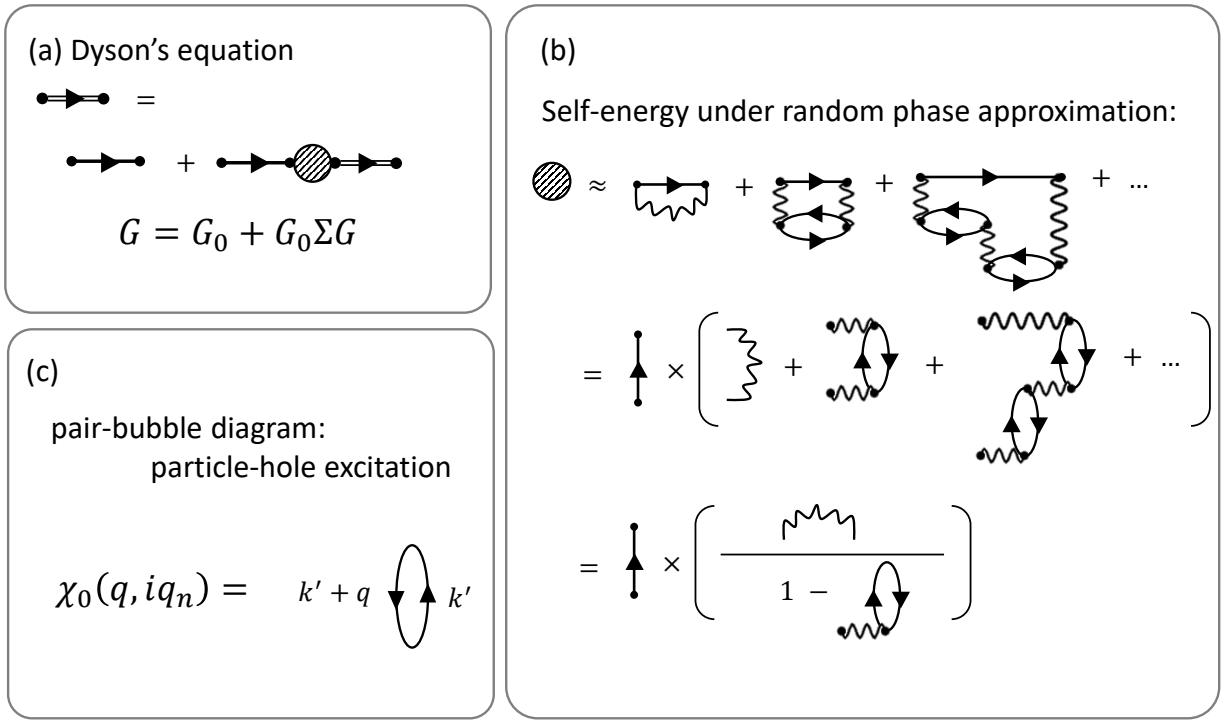

Figure 4.6: (a): Dyson's equation for a single-particle Green's function with a self-energy correction. (b): Feynman diagrams for the random-phase approximation. (c): Pair-bubble diagram, representing a particle-hole excitation.

4.3.4 Summary

We have discussed a microscopic picture of Fermi liquid theory. These arguments predict resistivity should follow a T^2 scaling due to electron-electron interactions, which has been confirmed in conventional metals. The origin of T^2 scaling arises from phase-space constraints related to momentum and energy conservation for electron-electron scattering.

The RPA approximation is the minimal known correction to the single-particle Green's function (beyond the Hartree-Fock approximation) that gives a finite lifetime of quasiparticles. There are more complicated diagrams that takes into account vertex corrections and higher orders of interactions. Nevertheless, the basic concept of a Fermi liquid is still based on the existence of long-lived quasiparticles, which fails for strongly correlated systems or near quantum critical points.

4.4 Anomalous transport phenomena beyond Fermi liquid theory

4.4.1 Good vs. bad metal

Despite its success in a wide range of materials, Fermi liquid theory fails when strong correlations or fluctuations are present [98]. Bad metals, also known as strange metals, are a prime example that cannot be accommodated by Fermi-liquid theory. Indeed, the origins of bad-metal behavior remain a puzzle.

The reason that we can explain the transport properties of conventional, or "good", metals is because scattering between electrons is rare, and therefore the electrons behave as a degenerate quantum gas. Although some approximations are usually necessary for calculating scattering matrix elements, the fact that electrons are still at least particle-like allows us to build up a microscopic picture for the scattering mechanism.

However, for bad metals, which are strongly correlated materials such as the high–temperature superconductors and the Mott-insulator-metal transition system [99], scattering between electrons is so strong that the electron starts to lose its individual identity. This section focuses on introducing the properties of bad metals beyond the framework of Fermi-liquid theory, especially its anomalous transport behavior.

4.4.2 Absence of quasiparticles

Photoemission spectroscopy is a central experimental tool used to measure the single-particle spectral function. For conventional metals, the presence of quasiparticles and their small scattering rate have been confirmed using photoemission experiments. However, for bad metals, although photoemission data show

the existence of a Fermi surface, long-lived quasiparticles are no longer well defined (see the review paper by A. Damascelli, *et al.* [81] and references within). As an example, Fig. 4.7 plots the spectral functions of $Bi_2Sr_2CaCu_2O_{8+\delta}$ measured by angle-resolved photoemission spectroscopy (ARPES) for the strange-metal and superconducting phases. The broadened feature and a long incoherent tail for the normal state around optimal doping indicate the breakdown of Landau quasiparticles.

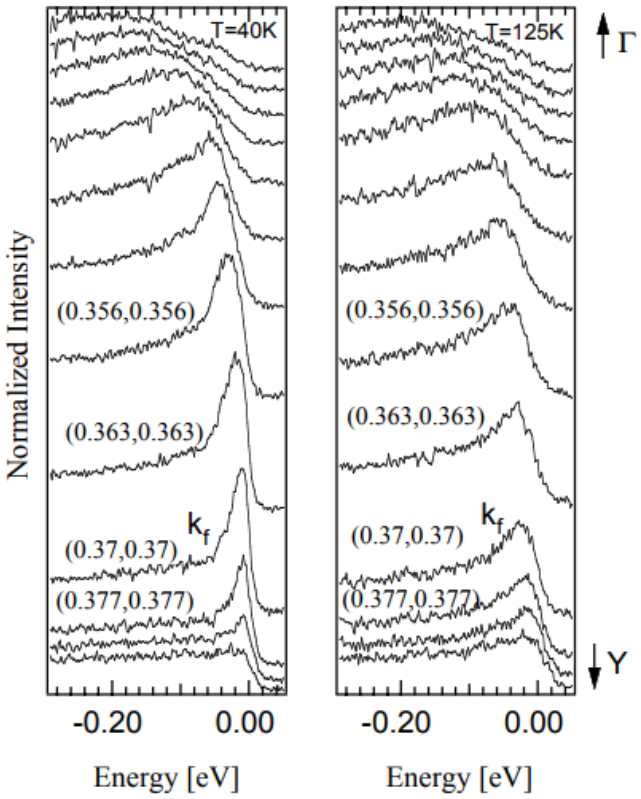

Figure 4.7: Momentum dependence of the spectral function of $Bi_2Sr_2CaCu_2O_{8+\delta}$ in the superconducting ($40K$) and normal state ($125K$) along the (π, π) direction. The spectral function presents a sharp peak near the Fermi surface (labeled as k_f) for the superconducting state. In contrast, the spectral function for the normal state is much broader, with a width that can not be explained by thermal broadening alone. Quasiparticles are no longer well-defined. This figure is reproduced from Ref. [79].

Experimental results have proven that strange metals still conduct electricity and heat like conventional metals, but not via particle-like excitations. Electronic interactions in the strange metal are so strong that electrons seem to lose their individual identity. The lack of quasiparticles demands a theory beyond Fermi liquid theory.

4.4.3 Abnormal temperature scaling of resistivity

Many strongly correlated materials exhibit an abnormal scaling of resistivity with temperature that does not follow the Fermi liquid theory prediction. A linear temperature scaling has been observed in certain doping regime for high-temperature superconductors and in some heavy fermion materials.

A summary of the "normal" temperature scaling of resistivity due to various scattering processes follows:

- Impurities (or defects) in crystals:

  The scattering rate mainly depends on the density of impurities, and therefore is not sensitive to temperature. Close to zero temperature, all the other scattering processes are strongly suppressed by Pauli blocking, and the residual resistivity is due to impurities and/or defects in crystals.

- Electrons

  As we have discussed, Fermi liquid theory predicts a low-temperature DC resistivity that scales as T^2 because of electron-electron interactions.

- Phonons:

  In materials, oscillations of ions induce a time-dependent electric field that deviates from a perfect periodic potential. This electric field distortion, or phonon, causes electrons to transition between their eigenstates.

  An analytical derivation can be found in many condensed matter textbooks (*e.g.*, Ref. [54]). Here I only present an intuitive picture of electron-phonon scattering: at high temperature (*i.e.*, $T \gg T_D$, where T_D is Debye temperature), all the phonon modes are populated and therefore contribute to scattering. The scattering rate is roughly proportional to the density of phonon modes, which is $n(\vec{q}_p) = \frac{1}{e^{\hbar\omega(\vec{q}_p)}-1} \approx \frac{k_B T}{\beta\hbar\omega(\vec{q}_p)}$, where $\vec{q}_p$ is the phonon wavevector. This is the reason that the resistivity of Cu scales linearly with temperature at room temperature (as shown in Fig. 4.8). At low temperature, only phonons with small wavevectors are populated, and they generate a resistivity that scales as T^5.

In the regime where the electron-photon process dominates, a linear dependence of scattering rate on temperature is exhibited. However, many experiments have shown that the origin of T-linear resistivity in bad metal is purely electronic in origin (for example, see Ref. [100]). Also, the scattering rate per kelvin in the T-linear resistivity regime is similar in many different materials, in spite of the large differences in the microscopic details [101]. This universal behavior cannot be explained by the electron-phonon scattering mechanism. A full understanding of the origin of T-linear resistivity remains elusive. Many different

mechanisms have been proposed to explain the microscopic origin of linear-T resistivity behavior, including quantum criticality [102, 103] and AdS/CFT calculations [104–106].

4.4.4 Mott-Ioffe-Regel Limit

The saturation of resistivity with temperature has been observed for many metals. Fig. 4.8(a) shows several experimental results suggesting saturation of resistivity.

Semi-classical transport theory provides an intuitive picture to understand saturation. Since collisions between particles lead to the relaxation of momentum, the mean-free-path—the average distance one charge carrier can travel between collisions—should not be shorter than the average interparticle spacing. This restriction constrains the maximum value of resistivity. This argument was first proposed by Ioffe and Regel [107] and later by Mott [108], and is often known as Mott-Ioffe-Regel (MIR) limit [107]. As Fig. 4.8(a) shows, the measured resistivity for Nb is consistent with the MIR prediction, where the minimum mean-free-path is assumed to be the separation between Nb atoms.

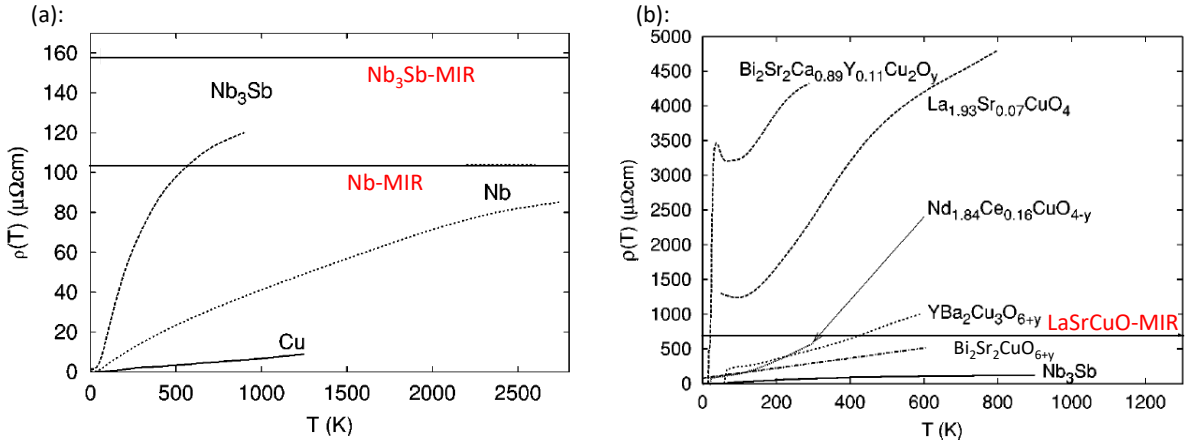

Figure 4.8: (a): Resistivity of Cu, Nb, and Nb_3Sb. The maximum resistivity corresponding to the Mott-Ioffe-Regel limit is calculated by setting the mean free path equal to the distance between Nb atoms. The MIR resistivity for Cu is about $260\mu\Omega$cm, which falls outside this figure. (b): Lack of resistivity saturation in some strongly correlated materials. The MIR resistivity for $La_{1.93}Sr_{0.07}CuO_4$ is shown by a line. Note the difference in vertical scales between (a) and (b). Both figures are adapted from [109].

However, violation of the MIR criterion has been found in a wide range of strongly correlated materials, including unconventional high-temperature superconductors and the ruthenate family (see Ref. [110] for more examples). Fig 4.8 shows the lack of resistivity saturation in some materials. There is no indication that the slope of ρ vs. T will decrease within the experimental accessible temperature range for strongly correlated materials (Fig. 4.8), and the MIR limit has been broken.

4.5 Experimental measurements of transport lifetime

The transport lifetime τ plays an essential role, as shown in the different theoretical approaches for determining DC resistivity. Theoretically, predicting τ is challenging when strong interactions are involved, since, generally, we do not know the eigenstates, and calculating all possible scattering processes is impossible. It is difficult to measure τ directly in solids because the typical dynamical timescale is on the order of a few to a hundred femtoseconds. Achieving the time resolution to resolve dynamics is at the frontier of ultrafast laser techniques. In most cases, the transport lifetime in solids is inferred from other observables, such as resistivity and spectroscopy.

One advantage in optical lattices is the accessibility of all dynamical timescales. For example, the tunneling timescale is on the order of milliseconds. In addition, the absence of phonons in optical lattices and the ability to track the motion of atoms with different spin components allows us to resolve the relaxation mechanism due to the Hubbard on-site interaction term. In this section, I will show how we directly measure the transport lifetime for a Fermi lattice gas.

4.5.1 Generating current via stimulated Raman transitions

To measure the transport lifetime, we prepare an initial state consisting of a spin-polarized gas trapped in an optical dipole trap. All the atoms are in the $|F = 9/2, m_F = 9/2\rangle \equiv |\uparrow\rangle$ state. After slowly turning on the optical lattice, we apply a 25μs Raman pulse that transfers atoms from $|\uparrow\rangle$ to $|F = 9/2, m_F = 7/2\rangle \equiv |\downarrow\rangle$ state. More details regarding simulated Raman transitions can be found in Chapter 2.

The Raman pulse time is chosen to be 25μs, so that it is short enough to transfer atoms from the $|\uparrow\rangle$ to the $|\downarrow\rangle$ state uniformly across the whole Brillouin zone. The width of the ground band ranges from 3.86kHz to 8.44kHz for our measurements.

About 1/3 of the atoms flip their spin after the Raman pulse. Momentum conservation leads to a non-zero average momentum $\Delta q_\downarrow$ for the spin-down component. The spin-down atoms move in a bath of spin-up atoms, as shown in Fig. 4.9(b). Via this stimulated Raman transition, we generate a flow of mass current consisting of $|\downarrow\rangle$ atoms in optical lattices. Collisions between $|\uparrow\rangle$ and $|\downarrow\rangle$ atoms lead to the relaxation of momentum, and, therefore, we expect to observe $\Delta q_\downarrow$ shrink as time progresses after the Raman pulse.

To track how the mass current decays with time, we measure the averaged quasimomentum of the atoms in the $|\downarrow\rangle$ state after various evolution times in the lattice. Fig. 4.9(d)-(f) schematically show the quasimomentum distribution at different stages of the evolution to equilibrium. After releasing the gas by turning off the optical dipole trap, a magnetic field with spatial gradient is applied during time-of-flight (TOF), and therefore two spin-components are separated spatially during TOF. By using bandmapping [58]

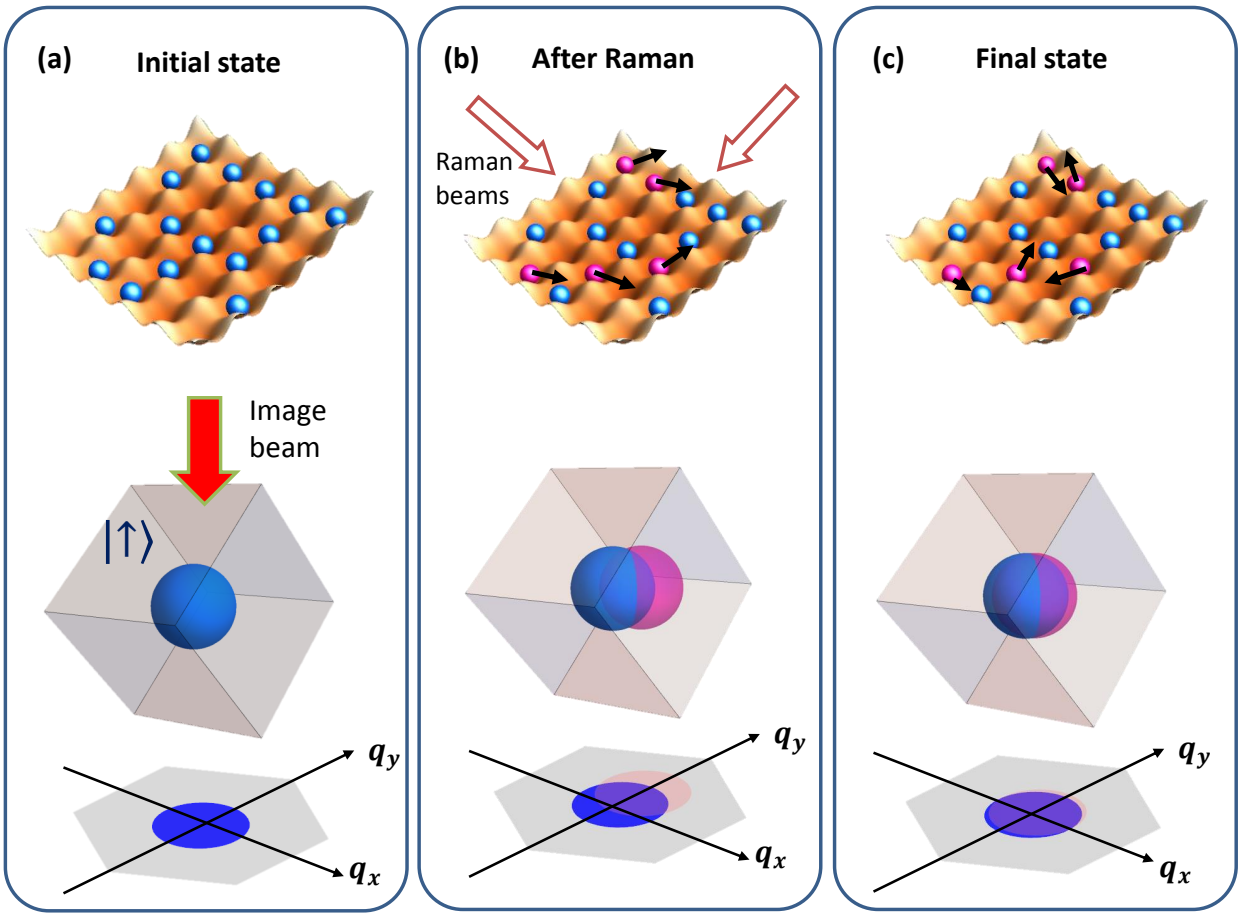

Figure 4.9: Schematic of the distribution of atoms in real space (top row) and in quasimomentum space (bottom row) at three different stages of the experimental sequence. (a): The initial state is prepared as a spin-polarized gas. All atoms are in spin-up state (blue) with no net momentum. (b): A pair of Raman beams is used to transfer 1/3 of the atoms in $|\uparrow\rangle$ to the $|\downarrow\rangle$ state (red). Conservation of momentum induces an non-zero average momentum, which is determined by the Raman wavevector difference, for the spin-down atoms. Therefore, there exists a net relative velocity between the $|\uparrow\rangle$ and $|\downarrow\rangle$ atoms. The flow of $|\downarrow\rangle$ atoms is a mass current. (c): Collisions between $|\uparrow\rangle$ and $|\downarrow\rangle$ atoms randomize the velocity of $|\downarrow\rangle$ atoms, such that $\Delta q_\downarrow$ will relax to zero. (d)-(f): The corresponding quasimomentum distribution in the 3D Brilloun zone. In our experiment, the imaging beam is along the $(1, -\sqrt{2}, 1)$ direction of the cubic lattice. The projection of the 1^{st} BZ has a hexagonal shape in the imaging plane. The pair of Raman beams is aligned such that Δq is roughly along the $(-1, -1, -1)$ direction of the cubic lattice, therefore projecting equally on the three principle axes of the lattices. Via band-mapping imaging, we obtain the quansimomentum distribution of each spin component integrated along the imaging beam direction. The initial quasimomentum shift has approximate magnitude $0.5q_B$, with $q_B = \hbar\pi/d$ (where d is the lattice spacing).

and spin-resolved TOF imaging, we acquire information on the quasimomentum distribution integrated along the imaging direction for each spin component.

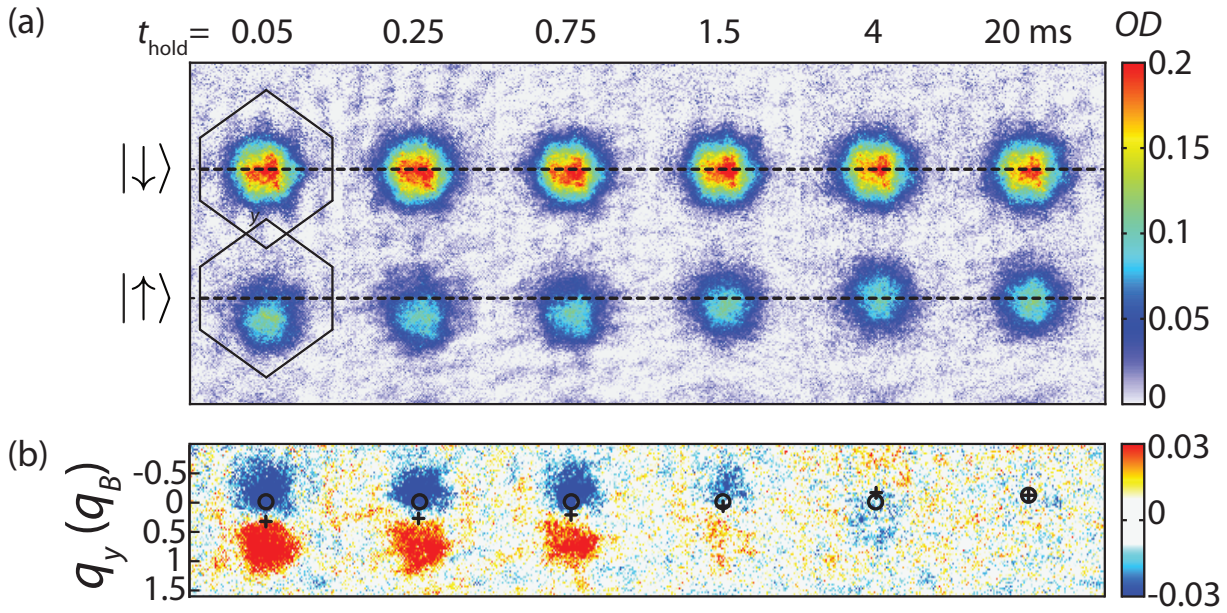

Figure 4.10: Sample data showing momentum relaxation at $s = 4E_R$ and $T/T_F = 0.23$ (measured before loading into the lattice). (a): Quasimomentum distributions of the $|\uparrow\rangle$ and $|\downarrow\rangle$ components at various evolution times after the Raman pulse. The black dashed lines mark the position for $q = 0$, and the hexagons are the projection of the 1^{st} Brillouin zone (BZ) onto the image plane. The color scale represents the measured optical depth. (b): The momentum excitation for the $|\downarrow\rangle$ atoms generated by Raman transitions. These images are produced by subtracting the quasimomentum profile for the $|\downarrow\rangle$ component from the equilibrium profile measured at t_{hold} with a spin-mixture gas subjected to a Raman pulse far from resonance. The cross indicates the center of the $|\downarrow\rangle$ component for each t_{hold}, and the circle is for the center of the equilibrium distribution. Red indicates higher occupation compared with the equilibrium momentum distribution (*i.e.*, particle-like excitations), while blue indicates fewer atoms (*i.e.*, hole-like excitations).

Fig. 4.10(a) shows sample images of the quasimomentum distribution for both spin components at different evolution times at $s = 4E_R$ and $T/T_F = 0.23$. At 0.05ms after the Raman pulse, the $|\downarrow\rangle$ atoms are shifted in average momentum; $q = 0$ is marked as the black dashed line. The effect of the Raman pulse on the momentum distribution of the $|\uparrow\rangle$ atoms is negligible. The decay of the current caused by momentum-changing collisions between atoms in $|\downarrow\rangle$ and $|\uparrow\rangle$ states is apparent, as shown by Fig. 4.10(a). The averaged momentum of $|\downarrow\rangle$ atoms has returned nearly back to 0 by $t_{hold} = 20$ms. Fig. 4.10(b) shows the excitation in momentum space generated by the Raman transition, visible in images formed by subtracting the equilibrium quasimomentum distribution of $|\downarrow\rangle$ atoms. The excitation dissipates within a few milliseconds.

4.5.2 Determination of the relaxation rate

To quantitatively analyze the relaxation of quasimomentum, we fit the quasimomentum distribution for each spin component to a Gaussian function. The center of the Gaussian distribution determines the average momentum. Fig. 4.11(a) shows the decay of $\Delta q_\downarrow$ and $\Delta q_\uparrow$ at a lattice depth $s = 4E_R$ and for $T/T_F = 0.23$. Slight non-zero drift of $\Delta q_\uparrow$ at $t = 0.05$ms is caused by the AC Stark effect from the Raman laser beams. Compared to the initial $\Delta q_\downarrow$, $\Delta q_\uparrow$ is negligible. Momentum changing collisions between atoms in $|\uparrow\rangle$ and $|\downarrow\rangle$ atoms lead to a rapid decay of $\Delta q_\downarrow$ on a millisecond timescale. At long evolution times, both $\Delta q_\uparrow$ and $\Delta q_\downarrow$ have relaxed back to zero. The total momentum is not conserved because of Umkalpp scattering and the trapping potential.

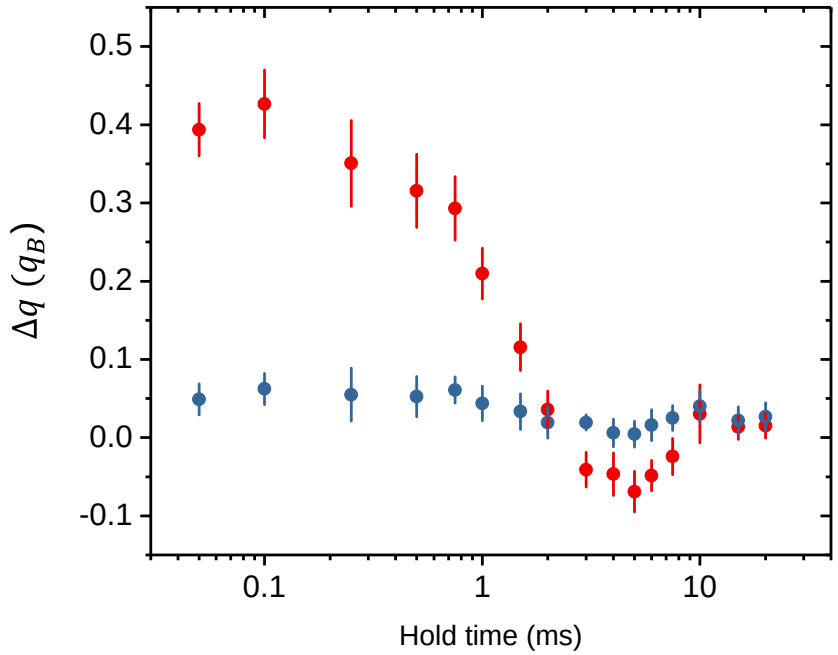

Figure 4.11: The average quasimomentum for $|\uparrow\rangle$ (blue) and $|\downarrow\rangle$ (red) states at various evolution times after the Raman pulse. The data points in this figure are obtained by fitting Guassian functions to images such as those shown in Fig. 4.10(a). The x-axis is displayed using a log scale to show the dynamics at short timescales. Compared to the change in momentum for $|\downarrow\rangle$ atoms, $\Delta q_\uparrow$ is negligible. Each point is the average of 5-10 measurements, and the error bars show the standard error of the mean.

We extract the timescale for current decay by tracking the motion of $\Delta q_\downarrow$ (Fig. 4.12) (We also did a similar analysis by meaning $\Delta q_\downarrow - \Delta q_\uparrow$, and found no significant change in the relaxation time). The time

evolution of $q_\downarrow$ can be described by Boltzmann equation [54]:

$$\frac{\partial}{\partial t} q_\downarrow(t) = -m\Omega^2 y_\downarrow(t) - \frac{q_\downarrow(t)}{\tau}. \tag{4.36}$$

The first term on the right-hand side accounts for the harmonic trap, where m is the atomic mass. The parameter $y_\downarrow$ is the in-trap position relative to the trap center, and $\frac{dy}{dt} = q_\downarrow/m$. The second term on the right-hand side is the damping force from collisions between atoms in different spin states, and τ is the transport lifetime. The solution to this equation with initial condition $y_\downarrow(t=0) = 0$ and $q_\downarrow(t=0) = q_0$ is:

$$q_\downarrow(t) = \frac{q_0}{2\sqrt{\Xi}} \left[(1+\sqrt{\Xi}) e^{-\frac{t}{2\tau_t}(1+\sqrt{\Xi})} + (-1+\sqrt{\Xi}) e^{-\frac{t}{2\tau_t}(1-\sqrt{\Xi})} \right], \tag{4.37}$$

where $\Xi = 1 - 4\tau_t^2\Omega^2$. The variables τ_t, Ω, q_0, and an offset are free parameters in the fit (red curve in Fig. 4.12) to the data.

We can apply the same procedure for a lattice gas at different lattice depths and loading temperatures to determine the dependence of the relaxation rate on interaction strength and temperature (data are shown in Fig. 4.25 and Fig. 4.27). Before discussing these data, there are several issues to clarify in order to justify that we are investigating the transport lifetime for a strongly correlated Fermi gas.

4.5.3 Linear response

The momentum displacement generated by stimulated Raman transitions is $q_B/2\sqrt{3}$ along each lattice direction. One concern is whether we have driven the system too far from equilibrium such that the response has become nonlinear. An ideal way to check for linearity would be to vary the angle between the Raman beams. This procedure requires realignment of the optics and is time consuming.

Instead of changing the geometry of Raman beams to change the initial Δq, we can obtain the transport lifetime for a smaller momentum shift by masking data at the early stage of relaxation and fitting the remaining points. Fig. 4.13(a) shows an example for this procedure. After dropping data points with $t_{\rm hold} < t(n_d)$, where $t(n_d)$ is the (n_d+1)-th shortest holdtime in our measurements, we fit the remaining data points to obtain the transport lifetime. As shown in Fig. 4.13(b), the dependence of the transport lifetime on the initial Δq is minor. The response is in the linear regime.

4.5.4 Other possible effects besides interactions

Fig. 4.12 shows an obvious decay of current, and we have explained how we extracted the corresponding relaxation timescale. An important issue is whether or not this rapid decay is mainly induced by the

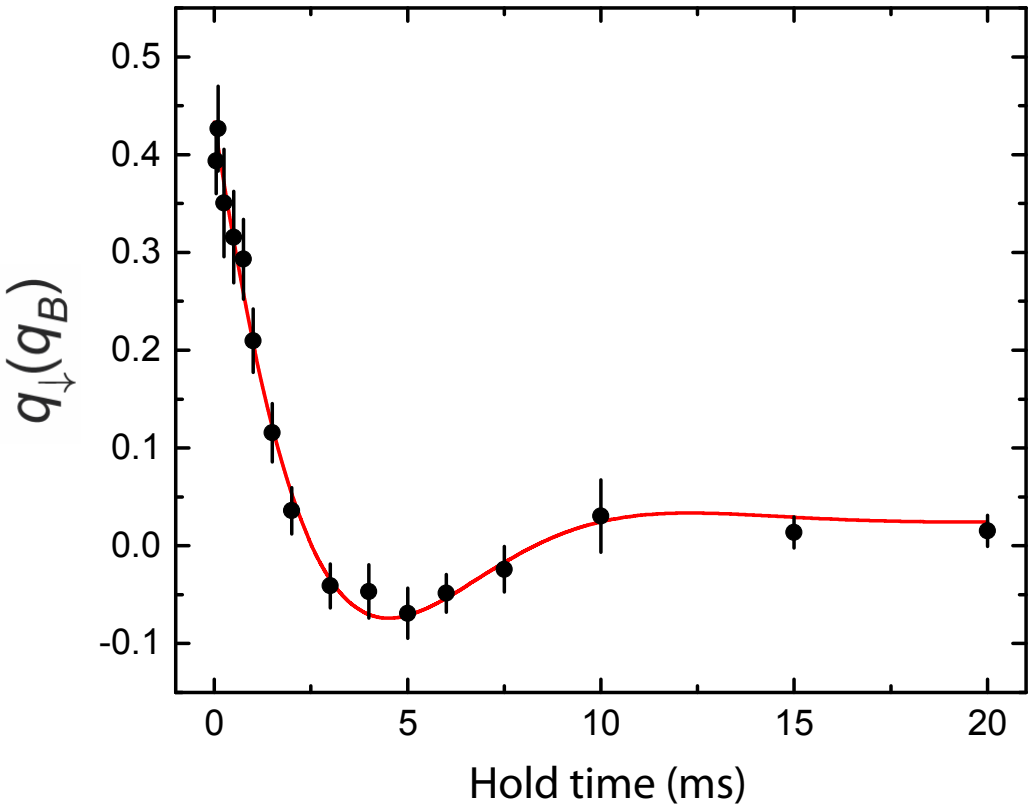

Figure 4.12: Sample data showing the decay of $\Delta q_\downarrow$ at $s = 4E_R$ and $T/T_F = 0.23$ (measured before loading into the lattice) and the fit used to determine the transport lifetime. The momentum $q_\downarrow(t)$ is fit to a solution of the Boltzmann equation to determine the transport lifetime (red solid line). The relaxation timescale determined from this fit is $\tau = 1.5 \pm 0.1$ms.

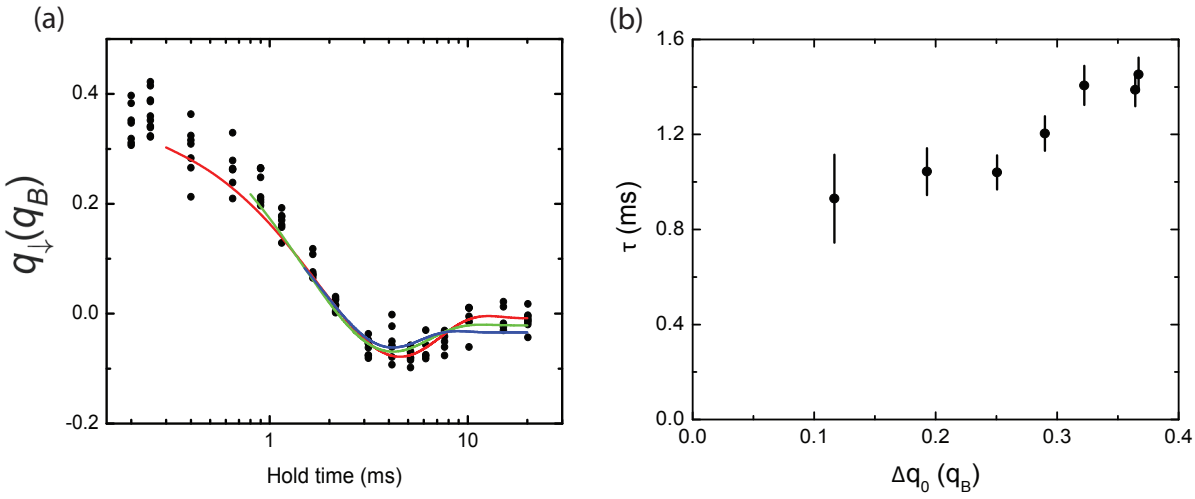

Figure 4.13: Linear response to the Raman transition. (a): Sample figure showing the fit curves after the first n_d points are removed at $s = 4E_R$ and $T/T_F = 0.23$. Fit curves are shown by red, green and blue lines, with $t(n_d) = 0.25, 0.75$, and 1.5ms, respectively. (b): The transport lifetime τ determined from fit at various Δq_0, where Δq_0 is the momentum shift at $t_{\rm hold} = t(n_d)$, determined from the fit. The value of τ does not change significantly as points are dropped. The error bars represent the fit uncertainty in fit.

interactions between the $|\uparrow\rangle$ and $|\downarrow\rangle$ components. Are there any other effects besides interactions involved in this relaxation process?

Decoherence time of a superposition state

Indeed, there is one problem we should discuss before worrying about anything else: why can atoms collide at all after the Raman transition? It seems the Raman transition should prepare a superposition of the $|\uparrow\rangle$ and $|\downarrow\rangle$ states, and if these spin-rotated states are still identical, then collisions are prevented by the Pauli exclusion principle. Nevertheless, the observed momentum damping indicates that collisions do occur. To resolve this puzzle, we compute the time evolution of the spin degree of freedoms component by using the optical Bloch equations [111]. The density matrix in the basis of the $|\uparrow\rangle$ and $|\downarrow\rangle$ states is:

$$\hat{\sigma} = \begin{pmatrix} \sigma_\uparrow & \sigma_{\uparrow\downarrow} \\ \sigma_{\downarrow\uparrow} & \sigma_\downarrow \end{pmatrix}.$$

The corresponding Bloch vector $(u, v, w) = (2\Re\sigma_{\uparrow\downarrow}, 2\Im\sigma_{\uparrow\downarrow}, \sigma_\uparrow - \sigma_\downarrow)$. The Raman Hamiltonian (in the RWA and rotating frame) is:

$$\hat{H}_R = \begin{pmatrix} 0 & \Omega_R/2 \\ \Omega_R/2 & \Delta(\vec{q}) \end{pmatrix},$$

where the detuning $\Delta(\vec{q}) = \epsilon(\vec{q} + \hbar\Delta\vec{k}) - \epsilon(\vec{q})$, and $\epsilon(\vec{q}) = 2t\left[3 - \cos(\frac{q_x}{\hbar}d) - \cos(\frac{q_y}{\hbar}d) - \cos(\frac{q_z}{\hbar}d)\right]$. The time evolution of $\hat{\sigma}$ follows:

$$\frac{\partial\hat{\sigma}}{\partial t} = -i[\hat{H}, \hat{\sigma}],$$

with initial condition that Bloch vector points towards the north pole of the Bloch sphere, *i.e.*, $\hat{\sigma}(t=0) = \begin{pmatrix} 1 & 0 \\ 0 & 0 \end{pmatrix}$.

Because of the momentum change $\delta\vec{k}$ induced by the Raman beams, the detuning is q-dependent. In other words, the time evolution of the spin state depends on its initial quasimomentum. As shown in Fig. 4.14, the final Bloch vectors for different $\vec{q}$ have different longitudes on the Bloch sphere, after evolution time $t\Omega_R = \pi/3$ (this time is chosen to match the observed 1/3 transferring of atoms to the $|\downarrow\rangle$ state). The final states are not identical to each other, and atoms can collide.

Another approach to check whether collisions can happen between two states is to check the overlap between their wavefunctions. Consider two initial states $\psi_1(r_1) = e^{ik_1r_1}|\uparrow\rangle_1$ and $\psi_2(r_2) = e^{ik_2r_2}|\uparrow\rangle_2$. After a Raman transition, they become $\psi_1(r_1) = e^{ik_1r_1}|\uparrow\rangle_1 + \alpha_{k_1}e^{i(k_1+\Delta k)r_1}|\downarrow\rangle_1$ and $\psi_2(r_2) = e^{ik_2r_2}|\uparrow\rangle_2 + \alpha_{k_2}e^{i(k_2+\Delta k)r_2}|\downarrow\rangle_2$. The Slater determinant of this two-particle system gives the wavefunction as $\psi(r1, r2) = \psi_1(r_1)\psi_2(r_2) - \psi_1(r_2)\psi_2(r_1)$. To see whether or not two fermions can collide with each other, the straightforward way is to check the value of $\psi(r1, r2)$ as r_1 approaches r_2.

With $r_1 = r_2 = r$, we have $\psi(r, r) = e^{i(k_1+k_2+\Delta k)r}\left[(\alpha_{k_2} - \alpha_{k_1})(|\uparrow_1\downarrow_2\rangle - |\downarrow_1\uparrow_2\rangle\right]$. In our case, $\alpha_{k1} \neq \alpha_{k2}$, so $\psi(r, r) \neq 0$. For a radio frequency transition, where the prefactor α_k does not depend on k, then $\psi(r, r) = 0$, and no collision is allowed.

To estimate the decoherence time for the superposition state, we perform a Ramsey interferometry measurement. We start from polarized $|\uparrow\rangle$ atoms, and apply two subsequent $\pi/2$ Raman pulses separated by a variable time. The dependence of the visibility, $\frac{N_\downarrow - N_\uparrow}{N_\downarrow + N_\uparrow}$ is plotted in Fig. 4.15 for various wait times between these $\pi/2$ pulses. A fit to an exponential function gives a decoherence time of $75 \pm 9\mu$s, which is much faster than the current decay process. This timescale seems to be determined by $\hbar/U$, which is $100\mu s$ at $s = 4E_R$.

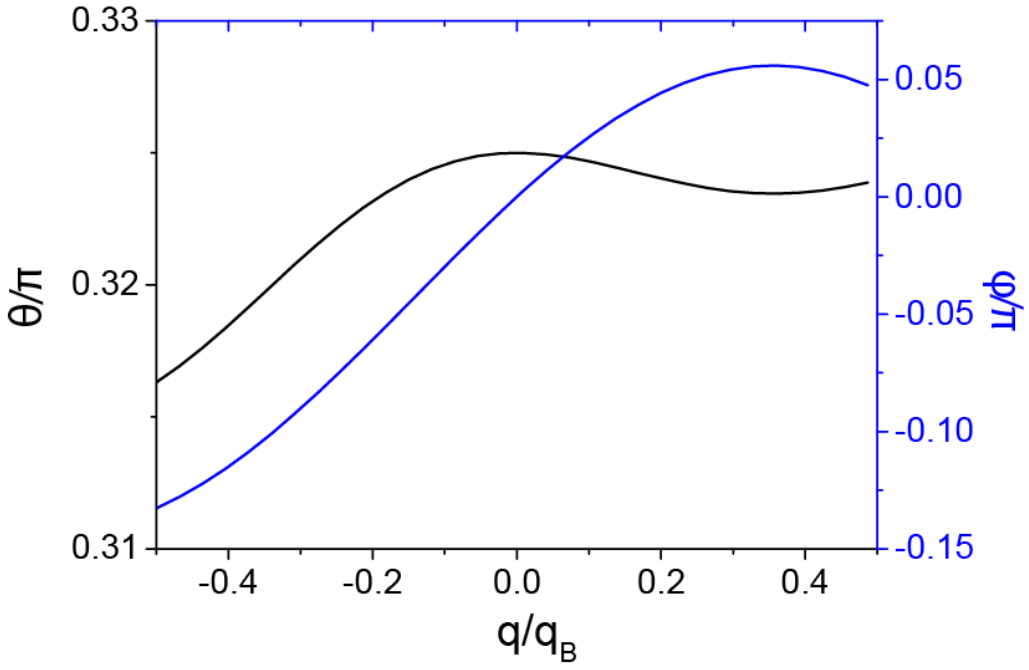

Figure 4.14: The dependence of the spherical coordinates θ and ϕ of the Bloch vector on initial quasimomentum after the Raman pulse with pulse time $t = \frac{\pi}{3}\frac{1}{\Omega_R}$, where Ω_R is the Rabi rate of the Raman transition. While θ (black curve) is roughly independent of q, (*i.e.*, the probability to find it the $|\downarrow\rangle$ state is a constant), ϕ (blue curve) covers a range of about 0.2π from $q = -0.5q_B$ to $q = 0.5q_B$. For this plot, we assume the Raman transition is resonant with the $q = 0$ state.

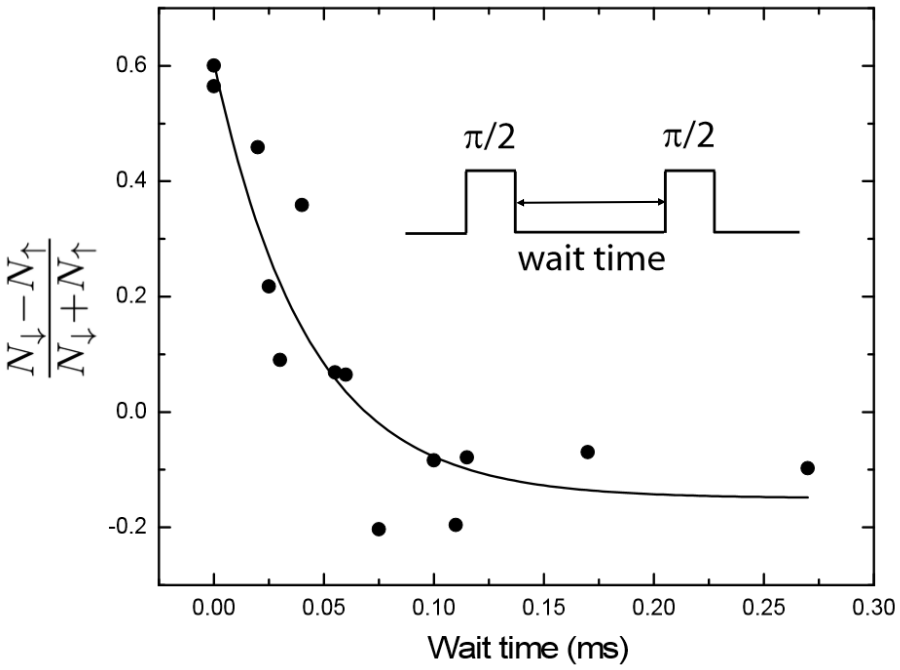

Figure 4.15: Measurement of the decoherence time for the superposition state generated by stimulated Raman transitions at $s = 4E_R$. A $\pi/2$ Raman pulse is applied to $|\uparrow\rangle$ atoms, creating a superposition state. After a variable wait time, another $\pi/2$ pulse is applied. This plot shows the visibility $(N_\downarrow - N_\uparrow)/(N_\downarrow + N_\uparrow)$ at various wait times. We fit the measurements to an exponential decay function $A_0 + Ae^{-t/\tau_d}$, as shown by the solid curve. In this case, $\tau_d = 75 \pm 9\mu$s.

Dephasing due to anharmonicity

Anharmonicity is also a source of dephasing of the atomic center-of-mass (COM) motion. For our measurements, there are two sources of anharmonicity. One is from the Gaussian profile of the crossed optical dipole trap beams. Another is from the lattice dispersion. We check the timescale related to these two dephasing mechanism using a spin-polarized gas, which is not interacting because of the Pauli exclusion principle. In this way, we isolate the anharmonicity-induced dephasing.

To measure the dephasing time, we apply an impulse to a spin-polarized gas trapped in the lattice. A force generated via a magnetic field gradient is applied to the atoms along the same direction as the Raman wavevector difference. The strength of the force is tuned to transfer approximately the same momentum to the gas as the Raman excitation. Without the lattice, the COM of the gas can last up to 100ms, which is much longer than the current decay time (Fig. 4.16).

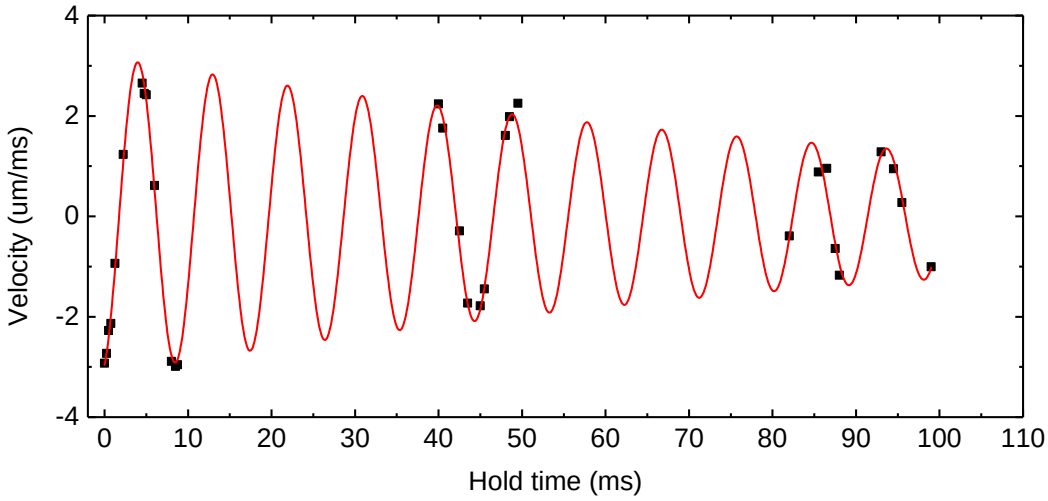

Figure 4.16: Damping of oscillations of a spin-polarized gas in the optical trap (without a lattice). Center-of-mass motion is generated by applying a magnetic field gradient. The position of the COM is measured at different hold times in optical dipole trap. The red curve is a fit to a damped sin function. The damping time here is 107 ± 9ms, which is much slower than the current decay process in Fig. 4.12.

With optical lattices, the variation in effective mass $1/m^* = \frac{1}{\hbar^2}\frac{\partial^2 E(\vec{k})}{\partial k^2}$ from the tight-binding dispersion means the oscillation frequency depends on momentum. Therefore, center-of-mass motion such as we excite will decay as individual atomic trajectories dephase.

We can theoretically model this dephasing process semi-classically. The time evolution of the phase-space

distributions can be simulated numerically. The equations of motion for a 1D lattice are:

$$\dot{q} = -\frac{\partial H}{\partial \dot{x}} = -m\omega^2 x, \tag{4.38}$$

$$\dot{x} = \frac{\partial H}{\partial \dot{q}} = \frac{2\pi t}{q_B}\sin(\pi\frac{q}{q_B}), \tag{4.39}$$

with $H = m\omega^2 x^2/2 + 2t\,[1-\cos(\pi q/q_B)]$.

We perform numerical simulation to time evolve the equations of motion with initial conditions $x(t = 0) = 0$ and $q(t = 0) = q_i$. Fig. 4.17 shows individual trajectories for different initial q_i. For small initial quasimomentum, the trajectories exhibit harmonic motion. As q_i approaches the boundary of Brillouin zone (BZ), anharmonic behavior with an amplitude-dependent period of oscillation becomes evident, and the motion does not follow a simple oscillatory function.

To simulate the motion of the entire gas, we propagate classical trajectories for a thermal distribution of initial quasimomenta subjected to the same impulse as in the experiment. For this simulation, we work in 1D, use 3000 particles, and propagate the position and quasimomentum of each particle according to Eq. 4.38 and 4.39. We weight the quasimomentum of the particles by a FD distribution and determine the average quasimomentum for different propagation times. The results of a simulation for a range of $\tilde{\mu}$ and $\tilde{T}$ (in the lattice) are shown in Fig. 4.18(a)-(c). We choose thermodynamic parameters a factor of three times smaller than the corresponding experimental points to account for the three times smaller bandwidth in 1D compared with 3D (*i.e.*, the parameters $\tilde{T}$ and $\tilde{\mu}$ match in units of the band width). With this adjustment, the parameters used for Fig. 4.18(a)-(c) cover the experimental conditions that we have explored in this work. For example, Fig. 4.18(a) corresponds to Fig. 4.12 in terms of T/t.

Sample measurements of the average quasimomentum of the gas for different hold times in the lattice after the impulse is applied are shown in the right column of Fig. 4.18, for approximately the same conditions as its simulated counterpart in the left column. We analyze the data in the same way as we did for Fig. 4.12: a fit to Eq. 4.37 is used to determine a timescale τ.

A summary of the measured and simulated dephasing times is shown in Fig. 4.19 for different temperatures in an $s = 4E_R$ lattice. For comparison, the corresponding measured relaxation rates are also displayed. As expected, since a wider range of quasimomenta are present at higher temperature, the population of atoms with q near the edge of BZ accelerates the dephasing due to anharmonicity. The agreement between simulated and measured dephasing times for spin-polarized gases indicates that the simulation accurately describes the dephasing dynamics. The simulated dephasing times have much smaller uncertainties than the measurements and therefore are a useful benchmark for estimating the impact of dephasing on

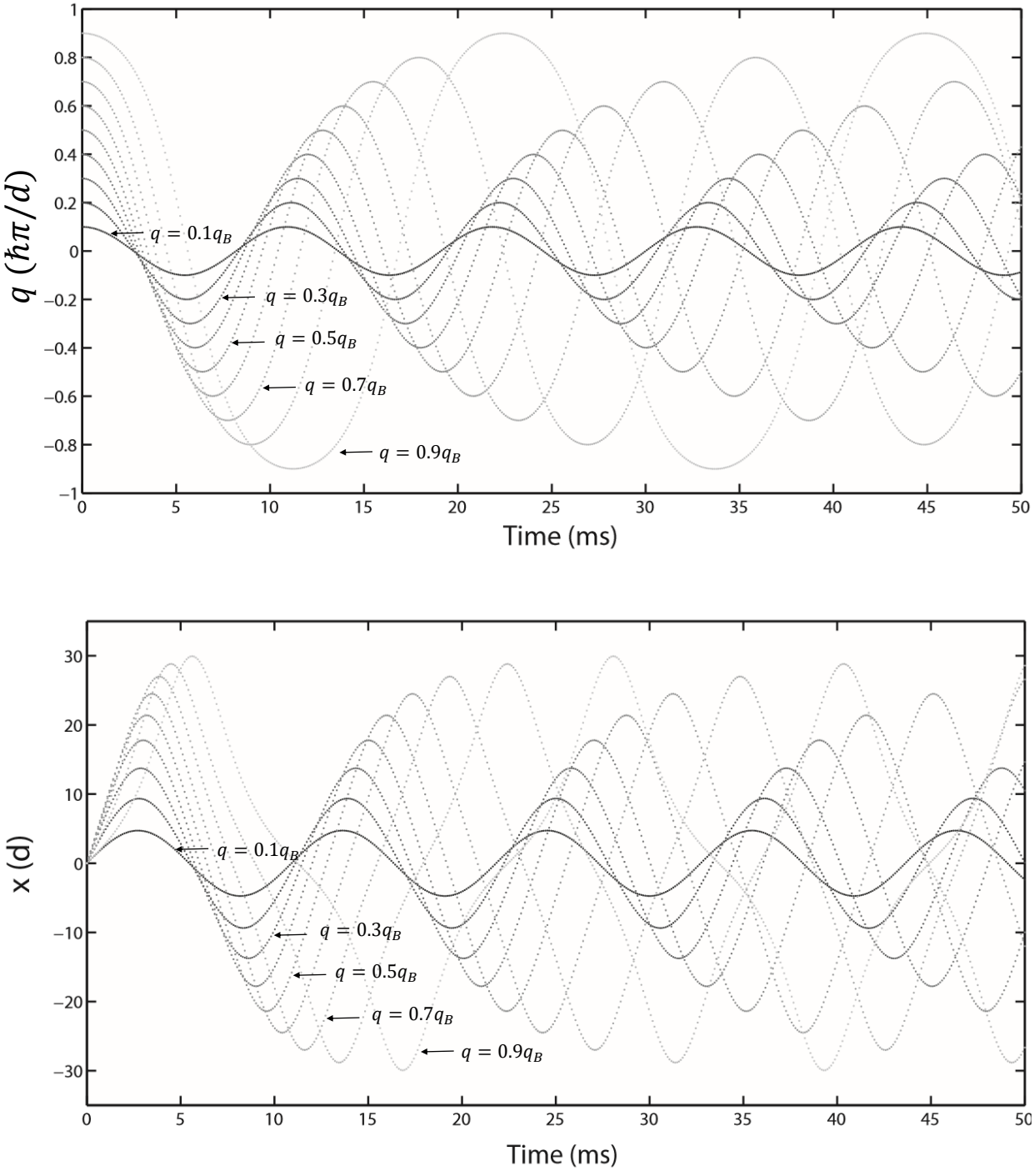

Figure 4.17: Oscillation of quasimomentum (top) and position (bottom) with time in optical lattices, with different initial quasimomentum. In addition to a different oscillation frequency for different initial q, the oscillation curve deviates from a purely sinusoidal function as q approaches the edge of the Brillouin zone.

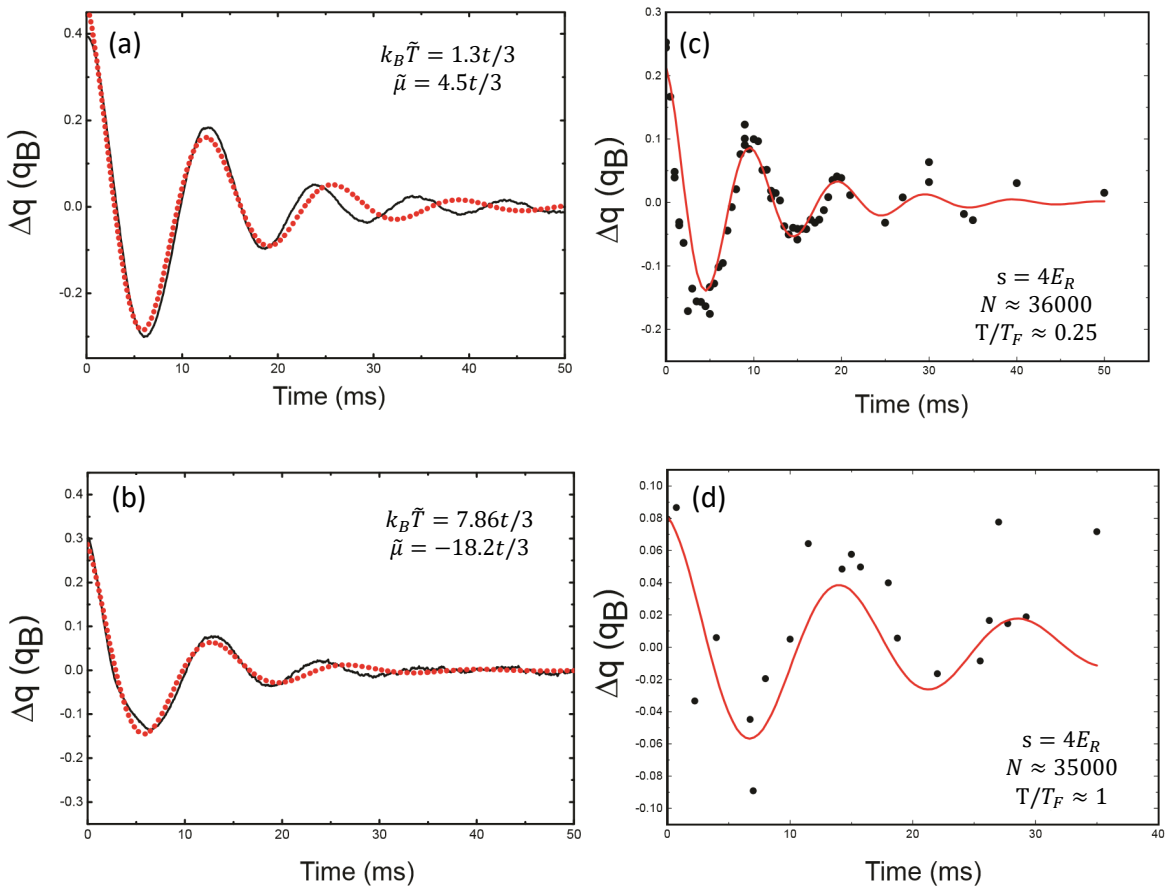

Figure 4.18: Simulation ((a)-(b)) and measurements ((c)-(d)) of damping of motion for non-interacting Fermi gas in an optical lattice. The parameters used in the left column roughly match the experimental conditions in the right column. Panels (a) and (b): Simulated average quasimomentum (black line) performed by averaging individual trajectories over quasimomenta weighted by a Fermi-Dirac distribution in one-dimensional lattice. The red curve is a fit to the simulated q. The deviation of the fit at long times is a result of the anharmonicity induced by the optical lattices. Panels (c) and (d): Corresponding measurements of damping. The center-of-mass motion is generated by applying a magnetic field gradient, which causes a quasimomentum shift roughly equal to that generated via a Raman pulse. The red curve is a fit used to determine the dephasing time.

our measurements. The simulated dephasing time is at least 4 times longer than the measured relaxation rate. Hence we conclude that dephasing has a minor impact on our measurements. The relaxation we measure is dominated by interaction-induced scattering between quasimomentum states. We are measuring the transport lifetime in a strongly-correlated lattice gas!

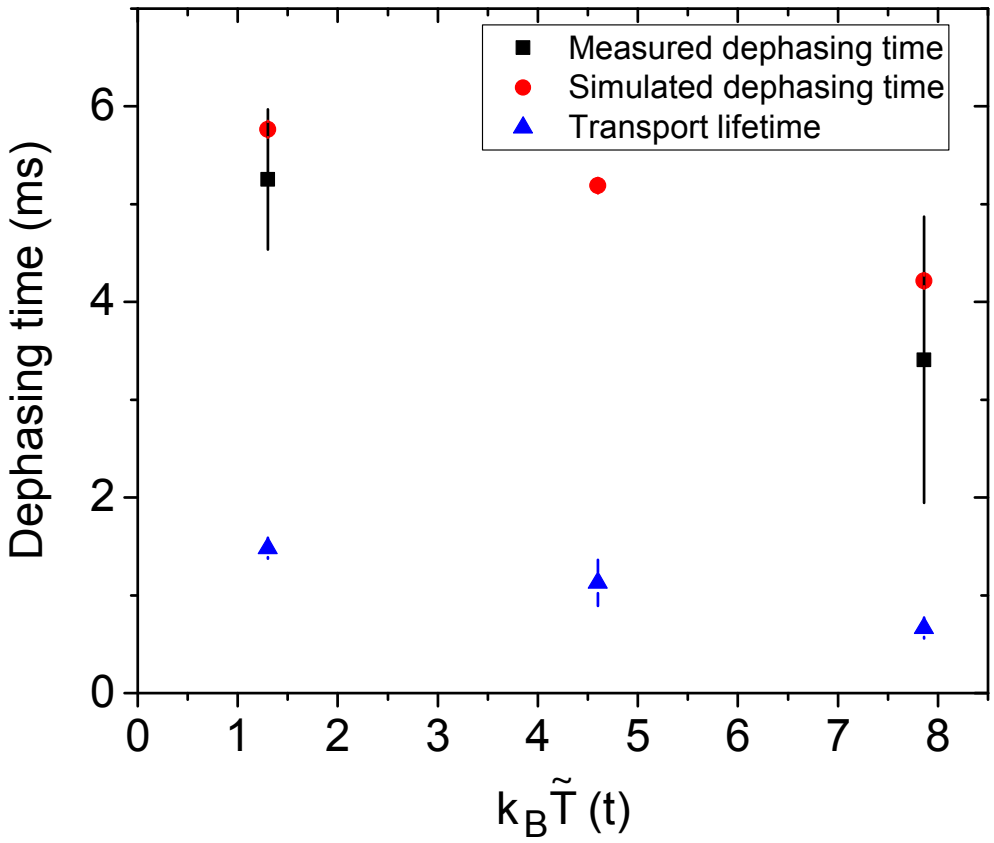

Figure 4.19: Comparison of dephasing and transport lifetime τ at different temperatures in an $s = 4E_R$ lattice. The dephasing times measured using a spin-polarized gas are shown using black squares, and the measured relaxation rate for a spin-mixed gas is shown using blue triangles. The simulated dephasing time is plotted using red circles. For the simulated time, the temperature is three times smaller than the value on the abscissa. The chemical potentials used in the simulation are $4.5t/3$, $-4.5t/3$, and $-18.2t/3$. The error bars represent the uncertainty in the fit used to determine τ.

4.6 Dependence of the transport lifetime on interactions and temperature

In this section, we study the dependence of the transport lifetime on interaction strength and temperature. To change the interaction strength, we adjust the lattice depth from $s = 4E_R$ to $7E_R$, and the corresponding U/t varies from 2.3 to 9. To tune temperature, we change the final optical depth during the evaporation cooling stage, such that $T \approx 0.2 - 1.2T_F$ before turning on the lattice. The temperature of the gas is still sufficiently low for the atoms to realize a single-band Hubbard model. To stay in the metallic phase of Hubbard model, we tune the total number of atoms N so that $E_F \approx 6t$ (*i.e.*, half-filling at $T = 0$). The relationship between E_F and N at different lattice depths can be found in Chapter 3.

4.6.1 Effective temperature and chemical potential in optical lattices

Knowledge of the initial conditions of the lattice Fermi gas is necessary for interpreting our measurements. In order to create a well characterized initial state, the gas is spin-polarized by removing the $|\downarrow\rangle$ atoms before turning on the lattice. Using a spin-polarized, non-interacting gas enables accurate knowledge of the quasimomentum and density distributions before an excitation is generated, because this model has an exact solution [58, 71].

A caveat of this approach is loading a non-interacting atomic gas into lattices invalidates the thermodynamic method as discussed in Chapter 3, because the system cannot equilibrate as the lattice is turned on. Therefore, it is necessary to check for a lattice gas whether thermodynamics properties, such as temperature and chemical potential, can still be defined. Here, we use the solution from Ref. [58, 71], measurements of N and T, and a straightforward application of the adiabatic theorem of quantum mechanics to estimate an effective chemical potential $\tilde{\mu}$ and temperature $\tilde{T}$ of the initial metallic lattice gas. The method discussed in this section was developed by Brian DeMarco.

Before turning on the optical lattice potential, the spin-polarized, non-interacting gas is trapped in a parabolic potential. The distribution of atoms in the single-particle eigenstates, characterized by three quantum numbers n_x, n_y, and n_z, is therefore well described by a Fermi-Dirac distribution $f_{n_x,n_y,n_z} = 1/\left[e^{\left(\epsilon_{n_x,n_y,n_z}-\mu\right)/k_BT}+1\right]$, with x, y, and z correspond to the lattice axes. To determine the occupations f_{n_x,n_y,n_x} in the eigenstates for $n_i = 1...300$, we used the measured number N and temperature of the gas obtained via time-of-flight imaging. The chemical potential μ is calculated by enforcing the constraint $N = \sum_{n_x,n_y,n_z} f_{n_x,n_y,n_z}$. We have checked that including more states does not significantly affect our results. We treat the trap as spherically symmetric, so that the energies are $\epsilon_{n_x,n_y,n_z} = \hbar\tilde{\omega}\left(n_x + n_y + n_z\right)$, where $\tilde{\omega}$

is the geometric mean of the trap frequencies. We have also verified that taking into account the different trap frequencies does not affect the best estimate for $\tilde{\mu}$ and $\tilde{T}$.

The single-particle eigenstates in the combined lattice–trap potential are also characterized by three quantum numbers [58, 71]. The lattice is turned on over 100 ms, which is much slower than all other timescales: $\hbar/t \approx 0.5$ ms, $\hbar/U \approx 55$ μs, and $\hbar/E_{bg} \approx 4$ μs (at lattice depth $s = 7E_R$), where E_{bg} is the bandgap. We therefore assume that the adiabatic theorem of quantum mechanics is satisfied, so that the distribution of particles in the lattice–trap eigenstates is unchanged, i.e. $\tilde{f}_{n_x,n_y,n_z} = f_{n_x,n_y,n_z}$. The corresponding eigenenergies are $\tilde{E}_{n_x,n_y,n_z} = \tilde{E}_{n_x} + \tilde{E}_{n_y} + \tilde{E}_{n_z}$, with

$$\tilde{E}_i = \begin{cases} \frac{\bar{\Omega}}{4} a_i(\alpha), & i \text{ even} \\ \frac{\bar{\Omega}}{4} b_{i+1}(\alpha), & i \text{ odd} \end{cases} \tag{4.40}$$

in the lattice–trap potential, where $\bar{\Omega} = m\bar{\omega}^2 d^2/2$, $\bar{\omega}$ is the geometric mean of the trap frequencies with the lattice light present, d is the lattice spacing, $\alpha = 4t\bar{\Omega}$, and $a_i(\alpha)$ and $b_{i+1}(\alpha)$ are the Mathieu characteristic values [58, 71]. We group and order the populations by energy to form a distribution $\tilde{f}_{\tilde{\epsilon}_j} = \sum_{\tilde{E}_{n_x,n_y,n_z}=\tilde{\epsilon}_j} \tilde{f}_{n_x,n_y,n_z}$, where j indexes the ordered, unique energies. We fit the distribution of occupations $\tilde{f}_{\tilde{\epsilon}_j}$ to a FD function $1/\left[e^{(\tilde{\epsilon}_j-\tilde{\mu})/k_B\tilde{T}}+1\right]$ with an effective chemical potential $\tilde{\mu}$ and temperature $\tilde{T}$ as free parameters. The fit minimizes the sum of the squared difference at each $\tilde{\epsilon}_j$ between $\tilde{f}_{\tilde{\epsilon}_j}$ and the FD distribution.

Fig. 4.20 shows calculated $\tilde{f}_{\tilde{\epsilon}_j}$ and fitted FD distributions for $s = 4$, $N = 26,400$, and $T/T_F = 0.22$, 0.44, and 1.16, which spans the full range of temperatures we sampled. The agreement between the computed $\tilde{f}_{\tilde{\epsilon}_j}$ and the fitted distributions are excellent, justifying using $\tilde{T}$ and $\tilde{\mu}$ to describe the system, except for the highest temperature points. At the highest temperatures, the procedure we use generates a distribution that underestimates the occupancy for the lowest and highest energy states (Fig. 4.20c). As we will discuss, despite this issue, we find that our procedure provides a density distribution that closely matches the experiment.

In Fig. 4.21, we show the predicted $\tilde{\mu}$ and $\tilde{T}$ for the conditions of Fig. 4.27 for different values of T/T_F before the lattice is turned on. The effective degeneracy is approximately conserved as the lattice is turned on (i.e., $\tilde{T}/\tilde{T_F} \approx T/T_F$), and the effective chemical potential becomes negative for $T/T_F \gtrsim 0.5$, as for a trapped gas.

With the knowledge of effective temperature $\tilde{T}$ and chemical potential $\tilde{\mu}$, and assuming that the semi-

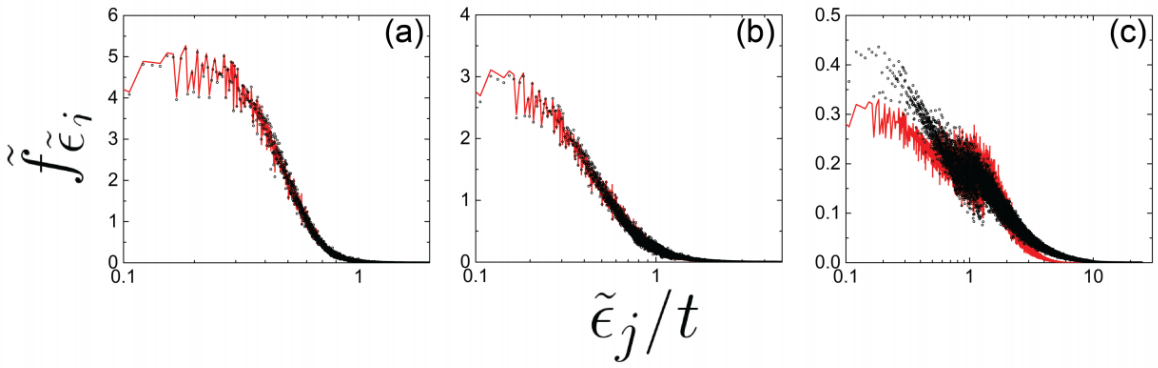

Figure 4.20: Numerical data to determine effective chemical potentials and temperatures. The computed $\tilde{f}_{\tilde{\epsilon}_j}$ is shown for $s = 4$ and $T/T_F = 0.22$ (a), 0.44 (b), and 1.16 (c) as open circles, and the fitted FD distribution is shown as a red line. A 20-point moving average filter is used to smooth the data, and approximately only one out of every 300 points are shown. Note the difference in vertical and horizontal scales.

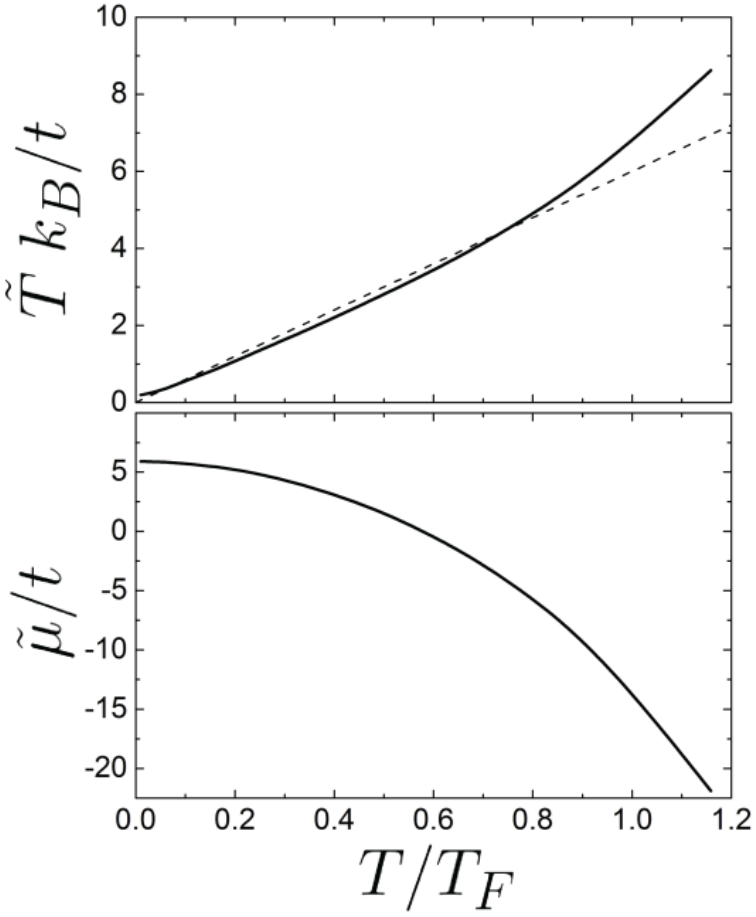

Figure 4.21: The effective chemical potential and temperature scaled to the tunneling energy are shown as solid lines. The dashed line marks the condition for T/T_F to remain unchanged when the lattice is superimposed on the gas, where $T_F \approx 6t/k_B$ in the lattice (according to a non-interacting calculation).

classical phase-space distribution in the lattice follows a FD distribution

$$\tilde{\rho}\left(\vec{r},\vec{q},\tilde{\mu},\tilde{T}\right)=1/\left[e^{\left(m\bar{\omega}^2r^2/2-6t+2t\sum\limits_{j=x,y,z}\cos(\pi q_j/q_B)-\tilde{\mu}\right)/k_B\tilde{T}}+1\right],$$

any observable we are interested in can be evaluated as:

$$\langle O\rangle=\int d^3\vec{r}\int\frac{d^3\vec{q}}{h^3}\tilde{\rho}\left(\vec{r},\vec{q},\tilde{\mu},\tilde{T}\right)O.$$

Next, we calculate several important quantities that are necessary for interpreting the measured transport lifetime, and the comparison to experiments can justify the method applied here to determine $\tilde{T}$ and $\tilde{\mu}$.

- Density profile

  In the semi-classical approximation, the density profile $n\left(\vec{r}\right)=\int d^3\vec{q}\,\tilde{\rho}\left(\vec{r},\vec{q},\tilde{\mu},\tilde{T}\right)/h^3$. The calculated shape of density profile is shown as the black solid curve in Fig. 4.22. To verify our approach, we compare predicted and measured density profiles for a spin-polarized gas in the lattice-trap potential. Comparing measured quasimomentum profiles is complicated by the failure of bandmapping at the edge of the Brilloun zone (BZ) [112]. To measure the density profile, we first transfer approximately 90% of the atoms to the $F=7/2$ state using adiabatic rapid passage driven by a microwave-frequency magnetic field. This step is necessary to reduce the optical depth (OD) of the gas. We then image the gas in situ. The images are angularly averaged (along ellipses that match the aspect ratio of the image) to produce a radial density profile. The measured radial profiles for s = 4 and $T/T_F=0.25,0.41$, and 1.1 shown in Fig. 4.22 agree well with predicted profiles based on the estimated $\tilde{\mu}$ and $\tilde{T}$ and the semi-classical approximation.

- Kinetic energy:

  To estimate the total energy added by the Raman excitation, we approximate the Raman pulse as instantaneous, and use semiclassical distributions

  $$\tilde{\rho}_\uparrow\left(\vec{r},\vec{q}\right)=\left(1-\gamma\right)\tilde{\rho}\left(\vec{r},\vec{q},\tilde{\mu},\tilde{T}\right)$$

  and

  $$\tilde{\rho}_\downarrow\left(\vec{r},\vec{q}\right)=\gamma\,\tilde{\rho}\left(\vec{r},\vec{q}-\delta\vec{q},\tilde{\mu},\tilde{T}\right).$$

  Here, $\gamma\approx0.35$ is the fraction of atoms transferred to the $|\downarrow\rangle$ state by the Raman pulse and $\delta\vec{q}=$

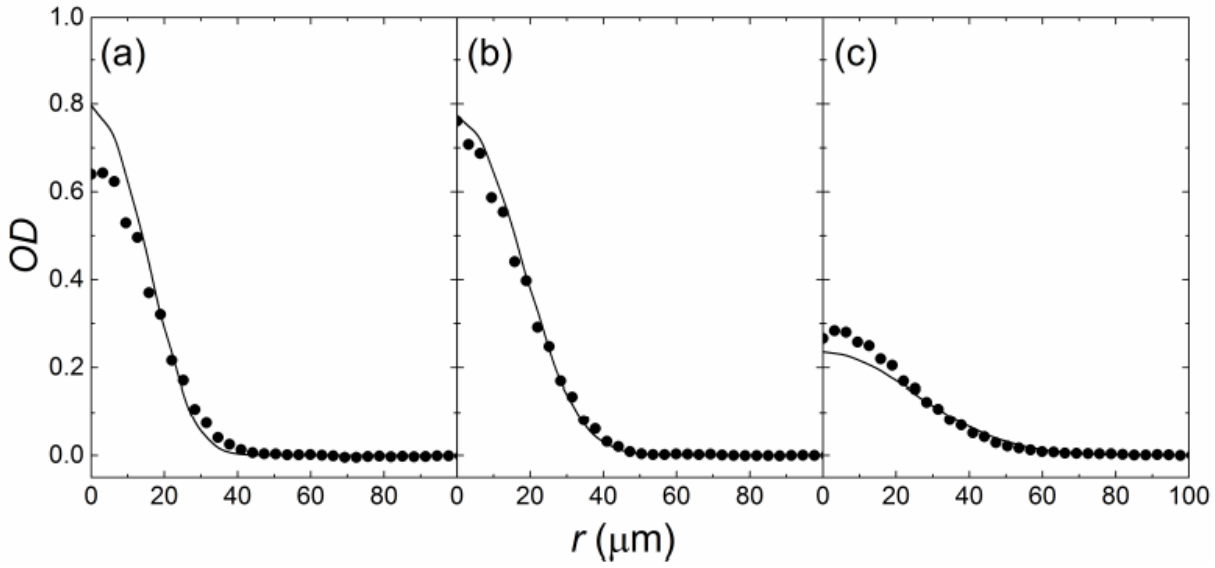

Figure 4.22: Column-integrated radial density profiles for a spin-polarized gas at $s = 4E_R$ and $T/T_F = 0.25$ (a), 0.41 (b), and 1.1 (c) shown as the measured optical depth (OD) in the trap. The measured profiles (solid circles) are created from averages of 3–4 images, and the prediction (solid line) is based on $\tilde{\mu}$ and $\tilde{T}$. The predicted profile is scaled to match the number of atoms for each case: N=16500 (a), 22600 (b), and 15700 (c). In this figure, r is a scaled radius that follows contours of constant OD.

$(\frac{1}{2\sqrt{3}}, \frac{1}{2\sqrt{3}}, \frac{1}{2\sqrt{3}})q_B$. The shifted momentum $\vec{q} - \vec{\delta q}$ of the $|\downarrow\rangle$ particles is re-mapped to the first BZ by subtracting reciprocal lattice vectors if it exceeds the first BZ boundary. Time-of-flight measurements indicate that the Raman lasers do not transfer atoms out of the first BZ, which is expected since the Raman Rabi rate is small compared with the bandgap. The increase in kinetic energy of the gas is:

$$\langle \Delta E_K \rangle = \langle E_{K\uparrow} \rangle + \langle E_{K\downarrow} \rangle - \langle E_K \rangle \tag{4.41}$$

where $E_K = \int d^3\vec{r} \int \frac{d^3\vec{q}}{h^3} \tilde{\rho}\left(\vec{r}, \vec{q}, \tilde{\mu}, \tilde{T}\right) \epsilon(\vec{q})$ is the total kinetic energy of the atoms before Raman transition; $E_{K\downarrow,\uparrow} = \int d^3\vec{r} \int \frac{d^3\vec{q}}{h^3} \tilde{\rho}_{\downarrow,\uparrow}(\vec{r}, \vec{q})\, \epsilon(\vec{q})$ are the kinetic energy for $|\downarrow\rangle$ or $|\uparrow\rangle$ atoms after Raman transition.

Fig. 4.23 shows $\langle \Delta E_K \rangle / \langle E_K \rangle$ at various initial $\tilde{T}$. Within the temperature range we sample, the increase in kinetic energy is less than 10%. The increase in absolute temperature after the Raman pulse depends on $\tilde{T}$, which is about 20% for the lowest $\tilde{T}$.

- Density-weighted density:

  The density-weighted density is defined as $n_{dwd} = \int d^3\vec{r} \frac{1}{N_\downarrow} n_\downarrow(\vec{r}) n_\uparrow(\vec{r})$, which calculates the overlap between the density distributions for $|\uparrow\rangle$ and $|\downarrow\rangle$ atoms confined in a harmonic trap potential. It

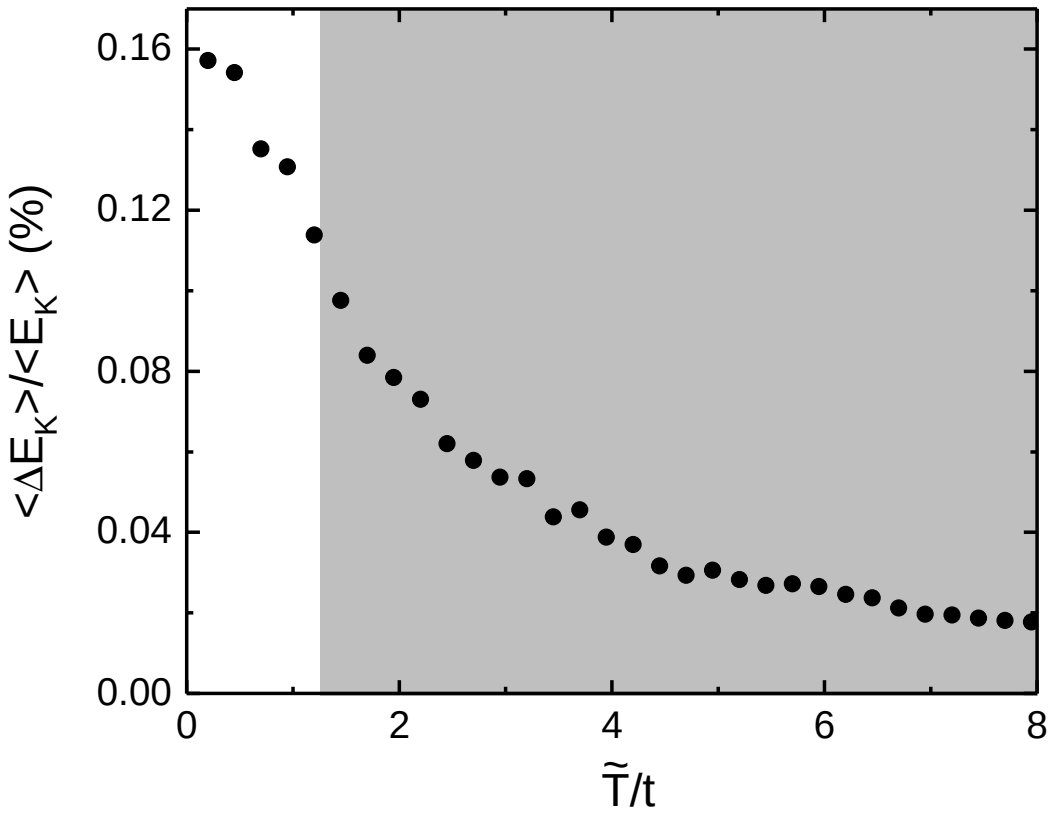

Figure 4.23: The change in kinetic energy per atom due to the Raman transition. For our measurements, $k_B\tilde{T}/t = 1.2-8.6$. The Raman excitation increases the total energy of the gas by less than 10%. The shaded region shows the area of this plot relevant to the experiment.

directly relates to the scattering rate between atoms. Fig. 4.24 plots the dependence of the calculated n_{dwd} on $\tilde{T}/t$ for the conditions of data in Fig. 4.27. Later I will discuss how to infer effective resistivity from n_{dwd} and the measured transport lifetime.

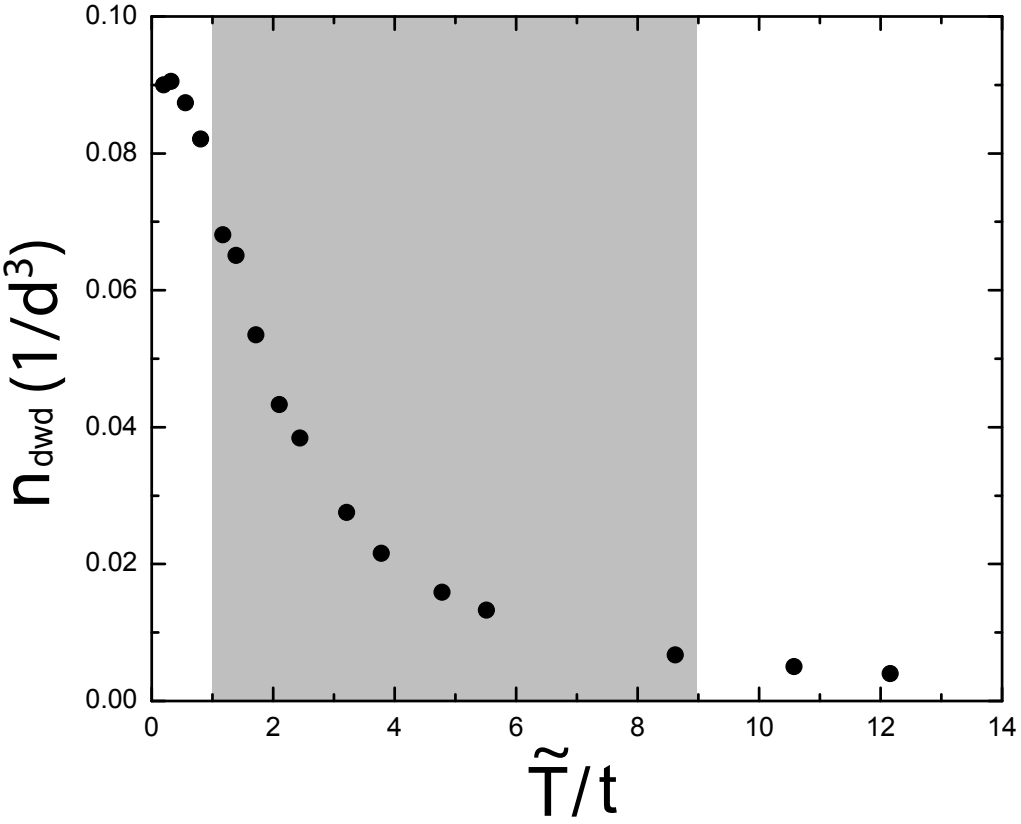

Figure 4.24: Calculated density-weighted-density from semi-classical thermodynamics. The gray region marks the temperature range we sampled in this work.

There are several potential problems with our approach to creating a phase-space distribution. First, violations of adiabaticity and heating from scattering of lattice light will modify the distribution of atoms in the energy eigenstates. Also, Eq. 4.40 assumes that the principal axes of the trap are aligned with the lattice directions; a solution for the eigenstates without this constraint is unknown. In our experiment, these axes are not aligned, however. Finally, we assume that the trapping potential is spherically symmetric. In our experiment, the ratio of trap frequencies is 2.4:2.1:1. As the lattice is turned on, the overall trap potential becomes more spherically symmetric. Because the gas is collisionless, cross-dimensional thermalization is

not possible [15], and the aspect ratio of the gas remains unchanged as the lattice is superimposed on the gas. We have verified this behavior for the images used to create Fig. 4.22. The two principal axes of the trap with trap frequencies in a 2.4:1 ratio lie within the imaging plane. We observe that the density profile of the gas before turning on the lattice has an aspect ratio of approximately 2 along these directions. This aspect ratio remains unchanged at $s = 4E_R$, even though the ratio of trap frequencies along the imaging directions is 1.6:1. The good agreement apparent in Fig. 4.22 suggests that all of these complications are minor effects.

4.6.2 Transport lifetime calculation using weak-scattering theory

Here we introduce the method we use to predict τ based on weak-scattering theory. The basic idea of this approach is to calculate the scattering rate between particles based on Fermi's golden rule, which treats the interactions between particles as a perturbation. It has been used to accurately calculate the relaxation times for trapped gas in the weakly interacting regime [15, 113, 114]. Although it may be expected to fail for our experimental conditions (since our $U/t > 2$ is not a small parameter), it still provides a baseline for understanding our measurements.

We use a standard technique to calculate the transport lifetime rate based on Fermi's Golden Rule (FGR) that closely follows the approach used in Refs. [112] and [115]. We allow for no free parameters in the calculation of the relaxation rate—experimentally measured values are used for all quantities. We use FGR to calculate the rate at which the Hubbard interaction term $H_I = U \sum_i n_{i,\downarrow} n_{i,\uparrow}$ scatters particles between states of different quasimomentum. In this method, H_I is treated as a perturbation to the tight binding Hamiltonian $-t \sum_{\langle ij \rangle, \sigma} \left(\hat{c}^\dagger_{i\sigma} \hat{c}_{j\sigma} + h.c. \right)$. This approximation is only valid in the weakly interacting limit and is not satisfied in the experiment.

For this calculation we treat the $|\uparrow\rangle$ gas as stationary (i.e., possessing no net quasimomentum). We use FGR to compute the time rate of change of the total quasimomentum of the $|\downarrow\rangle$ component $\left\langle \partial \left(\vec{q}_\downarrow \cdot \hat{\delta k} \right) / \partial t \right\rangle$ along the direction of $\hat{\delta k}$, where $\langle\rangle$ represents a thermodynamic sum over all possible scattering events, and $\hat{\delta k}$ is a unit vector along the Raman wavevector difference. We assume that the total quasimomentum $\left\langle \vec{q}_\downarrow \cdot \hat{\delta k} \right\rangle = \int d^3\vec{r} \int d^3\vec{q}\ \tilde{\rho}_\downarrow \left(\vec{r}, \vec{q}, \tilde{\mu}, \tilde{T} \right) \vec{q} \cdot \hat{\delta q} / h^3$ of the $|\downarrow\rangle$ gas decays exponentially, so that the transport lifetime is $\frac{1}{\tau} = -\frac{1}{\left\langle \vec{q}_\downarrow \cdot \hat{\delta k} \right\rangle} \left\langle \frac{\partial \left(\vec{q}_\downarrow \cdot \hat{\delta k} \right)}{\partial t} \right\rangle$.

We use dimensionless spatial and quasimomentum coordinates $\vec{\mathcal{R}} = \vec{r}/d$ and $\vec{\mathcal{Q}} = \pi \vec{q}/q_B$, respectively, to carry out this calculation, such that $\frac{1}{\tau} = -\frac{1}{\left\langle \vec{\mathcal{Q}}_\downarrow \cdot \hat{\delta k} \right\rangle} \left\langle \frac{\partial \left(\vec{\mathcal{Q}}_\downarrow \cdot \hat{\delta k} \right)}{\partial t} \right\rangle$. FGR is used to calculate the time-rate-

of-change of momentum as

$$\left\langle \frac{\partial\left(\vec{\mathcal{Q}}_{\downarrow}\cdot\delta\hat{k}\right)}{\partial t}\right\rangle = \frac{1}{2}\frac{2\pi}{\hbar}\frac{U^2}{2t}\int d^3\vec{\mathcal{R}}\int\frac{d^3\vec{\mathcal{Q}}_{1\downarrow}}{(2\pi)^3}\int\frac{d^3\vec{\mathcal{Q}}_{2\uparrow}}{(2\pi)^3}\int\frac{d^3\vec{\mathcal{Q}}_{3\downarrow}}{(2\pi)^3}\,\tilde{\rho}_{\downarrow}\left(\vec{\mathcal{Q}}_{1\downarrow},\vec{\mathcal{R}}\right)\tilde{\rho}_{\uparrow}\left(\vec{\mathcal{Q}}_{2\uparrow},\vec{\mathcal{R}}\right)\times \left[1-\tilde{\rho}_{\downarrow}\left(\vec{\mathcal{Q}}_{3\downarrow},\vec{\mathcal{R}}\right)\right]\left[1-\tilde{\rho}_{\downarrow}\left(\vec{\mathcal{Q}}_{4\uparrow},\vec{\mathcal{R}}\right)\right]\left(\vec{\mathcal{Q}}_{3\downarrow}-\vec{\mathcal{Q}}_{4\downarrow}\right)\cdot\delta\hat{k}\times \delta\left[\tilde{\epsilon}\left(\vec{\mathcal{Q}}_{1\downarrow}\right)+\tilde{\epsilon}\left(\vec{\mathcal{Q}}_{2\uparrow}\right)-\tilde{\epsilon}\left(\vec{\mathcal{Q}}_{3\downarrow}\right)-\tilde{\epsilon}\left(\vec{\mathcal{Q}}_{4\uparrow}\right)\right]. \tag{4.42}$$

Eq. 4.42 integrates over scattering events between $|\uparrow\rangle$ and $|\downarrow\rangle$ atoms with initial momenta $\vec{\mathcal{Q}}_{1\downarrow}$ and $\vec{\mathcal{Q}}_{2\uparrow}$ and final momenta $\vec{\mathcal{Q}}_{3\downarrow}$ and $\vec{\mathcal{Q}}_{4\uparrow}=\vec{\mathcal{Q}}_{3\downarrow}-\vec{\mathcal{Q}}_{1\downarrow}-\vec{\mathcal{Q}}_{2\uparrow}$. The value of $\vec{\mathcal{Q}}_{4\uparrow}$ is mapped into the first BZ by subtracting reciprocal lattice vectors if it exceeds the first BZ boundary. The dimensionless tight-binding energies are $\tilde{\epsilon}\left(\vec{\mathcal{Q}}\right)=2\left(3-\cos\mathcal{Q}_x-\cos\mathcal{Q}_y-\cos\mathcal{Q}_z\right)$.

We evaluate Eq. 4.42 using Markov-chain Monte Carlo integration. The energy-conserving delta function is represented as a decaying exponential proportional to $e^{-|\tilde{\epsilon}|/l}$. We make l sufficiently small such that the error introduced by representing the delta function this way is smaller than the Monte Carlo integration uncertainty, which is approximately 1%. In the following section, we use this method to calculate transport lifetime under different experimental conditions.

4.6.3 Dependence of transport lifetime on interaction strength

Fig. 4.25(a) shows the measured transport lifetime at various lattice depths, together with the prediction from weak scattering theory (solid black line). Although this simple calculation based on FGR gives the correct trend, it is obvious that the dependence of transport lifetime on interaction strength cannot be fully accommodated by weak-scattering theory. At the lowest interaction strength, the measured τ agrees within 10% to the weak scattering theory. However, it does not decrease as rapidly as the theory predicts. Across the interaction range we sample, τ given by weak scattering theory reduces by a factor of 10, while our measurements change only by a factor 2. This deviation, to some extent, is expected: weak scattering theory regards the ratio between U and t as a perturbation. This approximation becomes less and less correct as the interaction strength gets stronger.

A typical dynamical timescale in optical lattices is the tunneling time $\hbar/t$, which is the time for one atom to tunnel to its nearest neighbor site. Fig. 4.25(b) plots the measured τ normalized to tunneling time vs. t^2/U^2 (which is determined by lattice depth s). The prediction from weak-scattering calculation is approximately a line on this plot. As shown in Fig. 4.25, as the effective interaction strength increases, the measured τ approaches the tunneling timescale. This is a signature of incoherent transport, which suggests

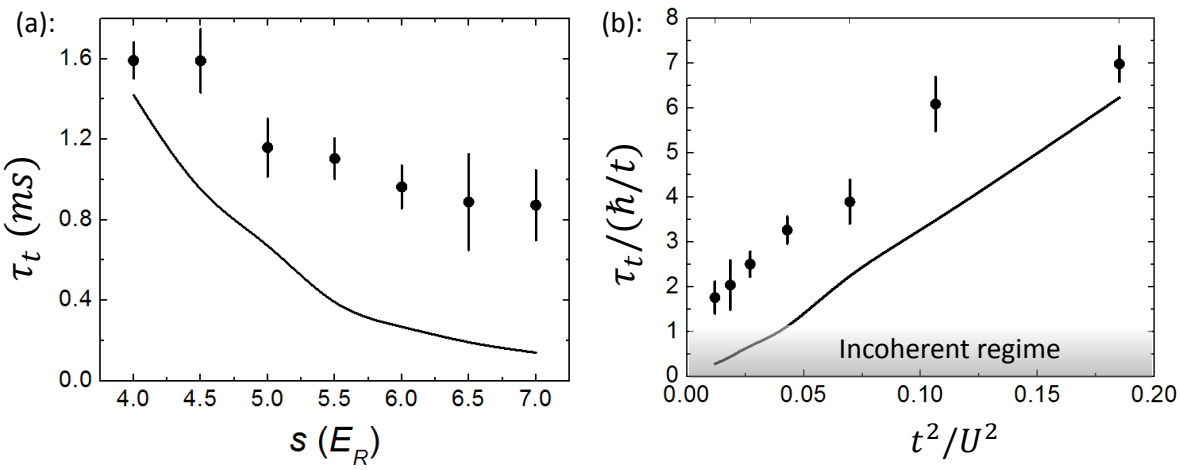

Figure 4.25: Dependence of transport lifetime at varied interaction strength and fixed temperature ($T/T_F \approx 0.23$ before loading into lattices). (a): Transport lifetime at different lattice depth s. τ are determined from fits to data such as those shown in Fig, 4.12. (b): The transport lifetime normalized to the tunneling time. In both plots, the vertical error bars show the uncertainty in the fit used to determine τ. The measurements are compared with a weak-scattering calculation (black solid line).

that momentum is not a well-defined quantity. Incoherent transport refers to the regime in which the decay rate of momentum is comparable to the characteristic single-particle timescale.

4.6.4 Dependence of transport lifetime on temperature

We can explore the dependence of τ on temperature. Because the relationship between temperature in the lattice is not a linear function of T in the trap, we convert T/T_F measured by time-of-flight imaging to $\tilde{T}/t$ in the lattice using the method introduced in Section. 4.6.1. Fig. 4.26 gives a table with the conversion between T/T_F before loading into lattice and the effective $\tilde{T}/t$ and $\tilde{\mu}$ in lattice for the conditions of Fig. 4.27. The average value of atom number N for each temperature data set is used. The figure on right shows the corresponding curves.

Astonishingly, the measured transport lifetime shows an opposite trend with temperature compared to the prediction of weak scattering theory (Fig. 4.27). The measured τ decreases monotonically with a temperature comparable to the Fermi temperature. The measured transport lifetime agrees with weak scattering theory within 30% at the lowest temperatures. However, at the highest temperature, the measured τ decreases by roughly a factor of two, while the weak scattering calculations predicts that τ increases by a factor of 6, leading to a disagreement of over 60 standard errors at the highest temperature! This discrepancy cannot be explained by an error in density or anharmonicity because of lattice dispersion—we have verified that the density of the gas decreases across this range and is consistent with thermodynamic calculations via in–situ

T/T_F	$\tilde{T}/t$	$\tilde{\mu}/t$
0.217	1.17	5.07
0.256	1.39	4.74
0.315	1.72	4.14
0.382	2.1	3.32
0.439	2.44	2.5
0.564	3.21	0.28
0.784	4.78	-5.26
1.159	8.62	-21.9

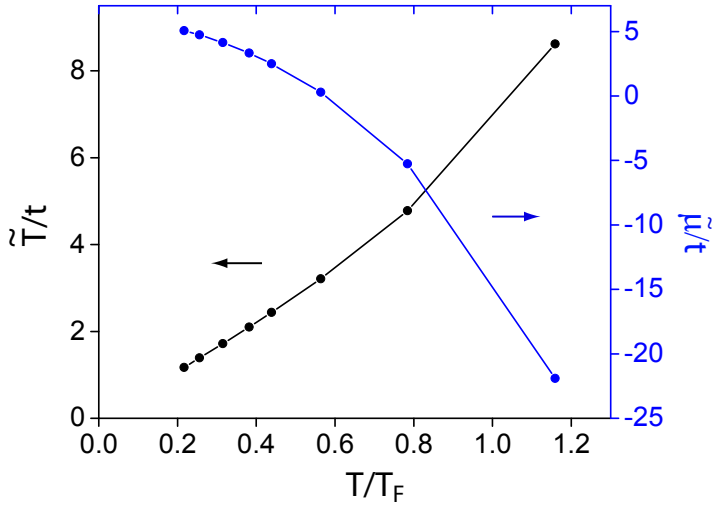

Figure 4.26: A table and a plot showing the relation between $\tilde{T}$ in optical lattices and the temperature for a trapped Fermi gas before loading into lattice. The effective temeprature (black circles) and effective chemical potential (blue circles) are calculated by assuming that the lattice turn-on satisfies the adiabatic theorem of quantum mechanics.

imaging (Fig. 4.22). The simulated dephasing time is 6 times longer than the measured transport lifetime (Fig. 4.19).

From the condensed matter perspective, an increasing value of resistivity with increasing temperature is typical. Indeed, exhibiting a positive slope for resistivity vs. temperature is the very definition of a metal. However, the temperature range sampled in solids is low in terms of T/T_F. In solids, the reason why resistivity increases as T increases is because Pauli blocking is suppressed. There are more allowed scattering final states in momentum space as the Fermi surface is smeared out with increasing T. However, for the temperature regime we sample, Pauli blocking is negligible. Furthermore, our weak scattering calculation has taken the Fermi statistics into account (indicated by the $1-\tilde{\rho}$ term in Eq. 4.42). In our experiment, τ remains finite at $T=0$ is because the Raman excitation creates unfilled quantum states; the collision rate does not vanish completely at $T=0$.

The dominant contribution to the increasing trend of the transport lifetime in the weak scattering calculation is the decrease in density as the size of the gas expands into a larger volume. This is a distinguishing feature compared with solid state materials. For a trapped gas, a quantity proportional to the mean time between collisions is expected to increase at high temperature.

To be more specific, in weak scattering theory, the scattering rate $1/\tau$ can be written as:

$$1/\tau = n_{\mathrm{dwd}}\sigma_s v_{\mathrm{rel}} \tag{4.43}$$

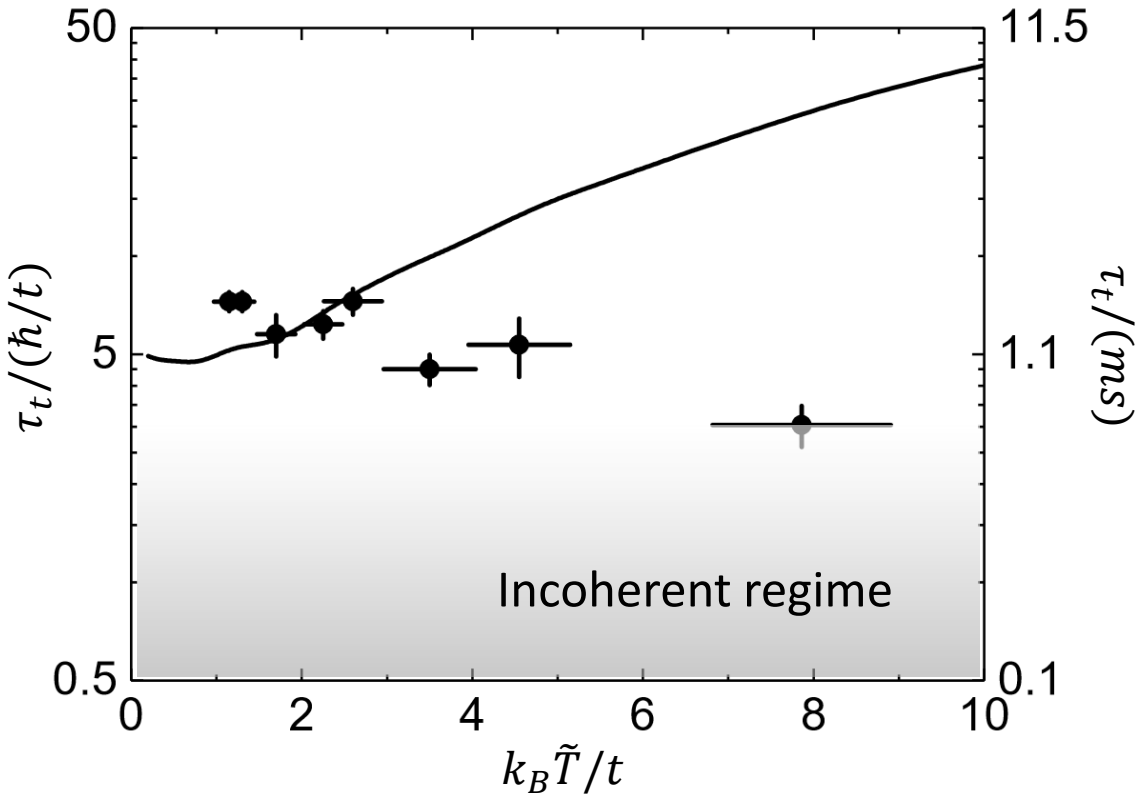

Figure 4.27: Dependence of transport lifetime on temperature at fixed interaction strength ($s = 4E_R$, $U/t = 2.3$). τ is determined from fits to data such as those shown in Fig, 4.12. The vertical error bars show the uncertainty in the fit used to determine τ, and the uncertainty in $\tilde{T}$ is from time-of-flight measurements.

Here n_{dwd} is the density-weighted-density, σ_s is the collision cross section, and v_{rel} is the mean relative speed between colliding particles.

We consider few simple scenarios:

- Classical limit for trapped atoms

  In the classical limit (*i.e.*, $T > T_F$) for a trapped gas, the thermally averaged density $n_{\mathrm{dwd}} \propto T^{-3/2}$, because the radius of the gas scales as $T^{1/2}$. The speed $\langle v_{\mathrm{rel}} \rangle \propto T^{1/2}$, and the collision cross section is constant. The scattering time τ therefore increases linearly with temperature. The dependence of $1/\tau$ has been measured in Ref. [113], which shows nice agreement with theory.

- Classical limit for a lattice Fermi gas

  The argument for a trapped gas is slightly modified for the single-band lattice Fermi gas in the classical limit. Because of the band dispersion, the mean velocity $\langle v \rangle = \left\langle |\vec{\nabla}\epsilon| \right\rangle$ is nearly independent of temperature when $E_F \approx 6t$. Therefore, τ scales as $T^{3/2}$.

- Fermi liquid

  As discussed earlier, at low temperature, Fermi liquid theory predicts $1/\tau$ scales as T^2, based on the allowed phase-space area that satisfies momentum and energy conservation. This argument must be modified in our case: the Raman excitation creates unfilled quantum states for both spin components, and generates a momentum shift for the $|\downarrow\rangle$ atoms. Therefore, even at zero temperature, τ remains finite, and the restriction on the allowed phase-space for scattering is much less important. In addition, n_{dwd} is constant at very low temperature. Hence, $1/\tau$ is not sensitive to temperature at very low T, as Fig. 4.27 shows.

In contrast to these three scenarios, the measured τ has a decreasing trend with increasing temperature, even up to a temperature comparable to the Fermi temperature. Such behavior suggests the analog of resistivity increases more rapidly than expected, just like what occurs in a bad metal. This quantitative and qualitative failure of weak scattering theory suggests that we have observed some phenomena related to strongly correlated physics.

4.7 Inferring resistivity from the transport lifetime

Our transport lifetime measurements indicate that the particles in this system cannot be described as quasiparticles labeled by a well-defined quasimomentum. To achieve a more direct comparison to observables in solids, we would like to link the measured transport lifetime to the analog of resistivity.

As shown in Fig. 4.28, the existence of a harmonic trap potential in our experiment casts additional complexities in converting the measured τ to resistivity. Two features absent in bulk solids appear: a spatially inhomogeneous density profile and a temperature-dependent density. The influence from the change in density on transport lifetime is simple, compared to the change in the underlying scattering mechanism. The goal of this section is to explain how we infer a quantity that reflects the resistivity of a uniform system, which is directly related to the scattering mechanism.

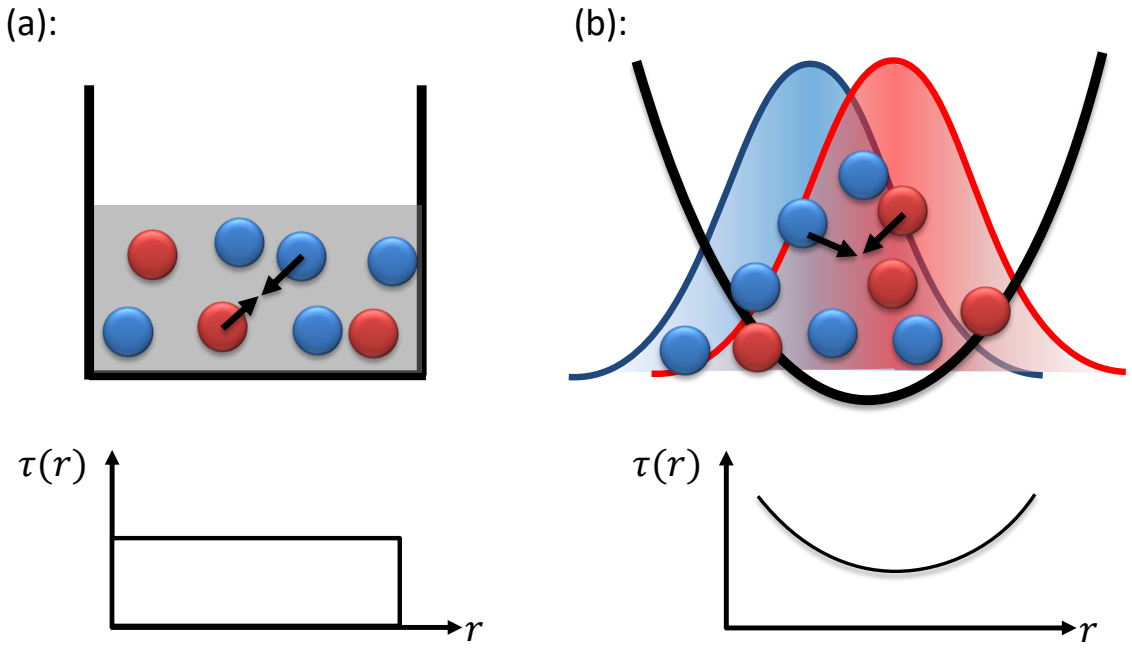

Figure 4.28: Schematic illustration showing the difference between (a) a bulk solid and (b) an atomic gas in a harmonic trap. The density of electrons is uniform across the bulk system and the transport lifetime is not position dependent. On the other hand, the harmonic trap in our experiment brings an inhomogeneous density profile. The possibility that two particles can collide shrinks at the edge of the trap, and the transport lifetime $\tau(r)$ depends on position.

4.7.1 What we have actually measured

The method we applied to obtain the transport lifetime, as discussed in Section. 4.5, measures the decay of the **average** momentum of $|\downarrow\rangle$ atoms, which can be expressed as:

$$\begin{aligned}
\frac{\partial}{\partial t}\langle\vec{q}_\downarrow\rangle &= \frac{\partial}{\partial t}\left\{\frac{1}{N_\downarrow}\int \vec{q}_\downarrow n_\downarrow(\vec{r})d^3\vec{r}\right\} \\
&= \frac{1}{N_\downarrow}\int \vec{q}_\downarrow \frac{\partial n_\downarrow(\vec{r})}{\partial t}d^3\vec{r} + \frac{1}{N_\downarrow}\int \frac{\partial \vec{q}_\downarrow}{\partial t} n_\downarrow(\vec{r})d^3\vec{r} \\
&= \frac{1}{N_\downarrow}\int \vec{q}_\downarrow \frac{\partial n_\downarrow(\vec{r})}{\partial t}d^3\vec{r} + \frac{1}{N_\downarrow}\int (-\frac{\vec{q}_\downarrow}{\tau(\vec{r})} - m\omega^2\vec{r}) n_\downarrow(\vec{r})d^3\vec{r} \\
&= \frac{1}{N_\downarrow}\int \vec{q}_\downarrow \frac{\partial n_\downarrow(\vec{r})}{\partial t}d^3\vec{r} - \vec{q}_\downarrow\langle\frac{1}{\tau(\vec{r})}\rangle - m\omega^2\langle\vec{r}\rangle, \qquad (4.44)
\end{aligned}$$

where $\frac{\partial \vec{q}_\downarrow}{\partial t} = -\frac{\vec{q}_\downarrow}{\tau(\vec{r})} + \vec{F}(\vec{r})$ (which is the solution of the Boltzmann equation) has been used.

In addition, we also have:

$$\begin{aligned}
\frac{\partial}{\partial t}\langle\vec{q}_\downarrow\rangle &= \frac{\partial}{\partial t}\left\{\frac{1}{N_\downarrow}\int \frac{\partial\vec{r}}{\partial t} n_\downarrow(\vec{r})d^3\vec{r}\right\} \\
&= \frac{1}{N_\downarrow}\int \frac{\partial^2\vec{r}}{\partial t^2} n_\downarrow(\vec{r})d^3\vec{r} + \frac{1}{N_\downarrow}\int \frac{\partial\vec{r}}{\partial t}\frac{\partial n(\vec{r})}{\partial t}d^3\vec{r} \\
&= \frac{\partial^2}{\partial t^2}\langle\vec{r}\rangle + \frac{1}{N_\downarrow}\int \vec{q}_\downarrow \frac{\partial n_\downarrow(\vec{r})}{\partial t}d^3\vec{r} \qquad (4.45)
\end{aligned}$$

Combining Eqs.4.44 and 4.45, we have

$$\frac{\partial^2}{\partial t^2}\langle\vec{r}\rangle = -\vec{q}\langle\frac{1}{\tau(\vec{r})}\rangle - m\omega^2\langle\vec{r}\rangle, \qquad (4.46)$$

which is the equation we have used to fit the data as shown in Fig. 4.12. It is clear now that the reciprocal of our measured transport lifetime is an average over the local $1/\tau(\vec{r})$ across the density profile. That is to say:

$$1/\tau = \langle 1/\tau(\vec{r})\rangle = \frac{1}{N_\downarrow}\int \frac{1}{\tau(\vec{r})} n_\downarrow(\vec{r})d^3\vec{r}. \qquad (4.47)$$

For any process that generates resistivity through independent two-body scattering, without losing generality, we can write $1/\tau = n_s M$, where M is an integral (over momenta) of scattering matrix elements that contribute to the decay of current, and n_s is the density of scatterers. The challenge in predicting the transport behavior of a strongly-correlated materials lies in the calculation of M, which carries all the information about scattering.

In our case, $n_s = n_\uparrow(\vec{r})$. So Eq.(4.47) becomes

$$\begin{aligned} \tau &= \frac{1}{N_\downarrow} \int n_\downarrow(\vec{r}) n_\uparrow(\vec{r}) M d^3\vec{r} \\ &= n_{\mathrm{dwd}} M \end{aligned} \tag{4.48}$$

For a uniform system with fixed electron density, resistivity is proportional to the scattering matrix M/m^*, where m^* is the effective mass. In our case, $m^* \propto t$, where t is the tunneling term in Hubbard model. We can define a dimensionless resistivity as

$$\varrho = \frac{1}{\frac{\tau}{\hbar/t} n_{\mathrm{dwd}} d^3}, \tag{4.49}$$

where d is the lattice spacing. $n_{\mathrm{dwd}} d^3$ indicates the averaged occupation number per lattice site.

Our analysis of ϱ assumes that the thermally averaged relative speed between colliding partners is independent of temperature. Variation in the thermally averaged speeds of the particles is suppressed because $E_F \approx 6t$ and there is a maximum allowed speed in this single-band system. As shown in Fig. 4.29, the thermally averaged speeds are independent of temperature to an excellent approximation for our parameter regime.

4.7.2 Saturation of resistivity

Fig. 4.30(b) and Fig. 4.31(b) plot the dependence of the inferred resistivity on interaction strength and temperature, respectively. The data correspond to those shown in Fig. 4.25 and Fig. 4.27. The uncertainty in ϱ comes from two variables: the measured transport lifetime τ and the density-weighted density n_{dwd}. A fit to the raw data gives the uncertainty in τ directly (as shown in Fig. 4.12). The uncertainty in n_{dwd} is determined from the uncertainty in the measured T/T_F and the fluctuation in total number of atoms.

To emphasize the failure of weak scattering theory, we show the resistivity corresponding to the weak scattering calculation using dash-dot blue curves in both figures. As expected, weak scattering theory predicts a temperature insensitive resistivity when $\tilde{T} > 0.5T_F$, because the collision rate is constant in this temperature range.

As we have discussed, one of the key signatures of bad-metal behavior is the lack of resistivity saturation as the Mott-Ioffe-Regel limit is approached. The MIR limit defines the regime in which semiclassical transport theory is valid and current-carrying particles are a legitimate concept [4, 6]. In solids, the MIR limit is $l \approx d$ [6], where l is the mean-free path and d is the atomic lattice spacing. This condition must be modified to $l \approx n^{-1/3}$ for optical lattices, because the system is free from impurities and phonons, and the only scattering is between particles with separation $n^{-1/3}$.

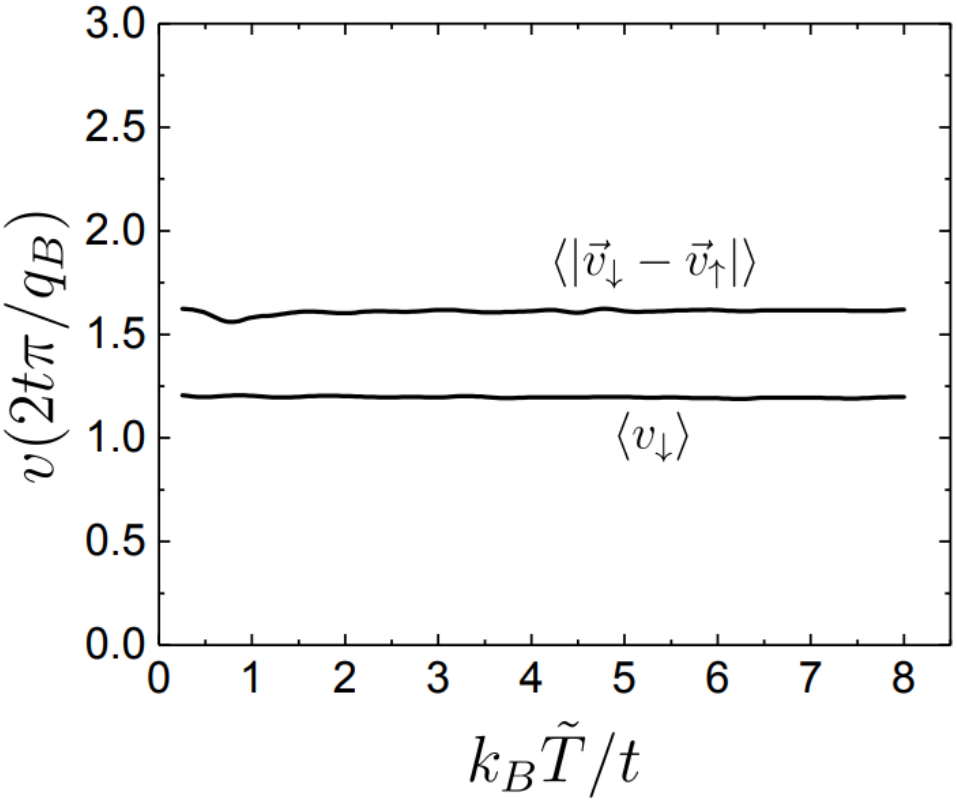

Figure 4.29: The thermally averaged speed between colliding partners and for the $|\downarrow\rangle$ component. These parameters are determined using $\tilde{T}$ and $\tilde{\mu}$.

We evaluate $\langle \vec{v}_\downarrow \rangle$ and $\left\langle n_\uparrow^{-1/3} \right\rangle$ based on the calculated density profile at corresponding $\tilde{T}$ and U/t. Fig. 4.30(a) and Fig. 4.31(a) show the mean velocity of $|\downarrow\rangle$ atoms and the average distance between $|\uparrow\rangle$ atoms. For the interaction-dependence data, the density is roughly constant, but the mean velocity decreases as the effective mass $1/m^* = \frac{1}{\hbar^2}\frac{\partial^2 E}{\partial k^2}$ increases. On the other hand, for the temperature-dependence data, $\left\langle n_\downarrow^{-1/3} \right\rangle$ drops significantly with increasing T as the size of the gas expands in the harmonic trap potential. In contrast, $\langle v_\downarrow \rangle = \left\langle |\vec{\nabla}_{\vec{q}}\, \epsilon| \right\rangle$ is independent of temperature (at constant s), because the lattice dispersion puts bounds on the allowed maximum velocity.

We define the Mott-Ioffe-Regel-limited resistivity ϱ_{MIR} from $\tau_{\mathrm{MIR}} = \left\langle n_\downarrow^{-1/3} \right\rangle / \langle v_\uparrow \rangle$. Comparison to ϱ_{MIR} (red dashed curves in Fig. 4.30(b) and Fig. 4.31(b)) shows a steady escalation toward the MIR limit. At the highest temperature, ϱ has approached ϱ_{MIR}. Furthermore, there is no sign that the increasing trend in ϱ changes with increasing T. The ratio of $\varrho/\varrho_{\mathrm{MIR}}$ shown in Fig. 4.31(c) is consistent with the absence of resistivity saturation.

4.8 Anomalous scaling of resistivity and comparison to DMFT

The failure of weak scattering theory and the absence of resistivity saturation suggest that we have observed anomalous transport in a Fermi lattice gas. To obtain deeper insight into these phenomena, I will introduce a more advanced theoretical approach—dynamical mean field theory (DMFT)—to calculate the dependence of resistivity on interactions and temperature for our experimental conditions. We compare the inferred resistivity based on transport lifetime measurements to the DMFT predictions.

4.8.1 Dynamical mean field theory

Introduction to dynamical mean field theory

Dynamical mean filed theory (DMFT) maps a many-body lattice model to a local single-site problem [2]. The influence from adjacent sites is treated as an effective coupling between this local site and an external bath. As depicted by the schematic diagram in Fig. 4.32, the hybridization V_ν between a single site and the external bath gives the probability that one electron may hop in or out of that site. Compared to mean field theory, DMFT, as suggested by the word "dynamical" in its name, uses a frequency-dependent hybridization function. Although DMFT does not incorporate spatial fluctuations (which may be important for low-dimension systems), it becomes exact in the limit of infinite dimensions or infinite coordination number (in which case the spatial fluctuation becomes negligible) [116].

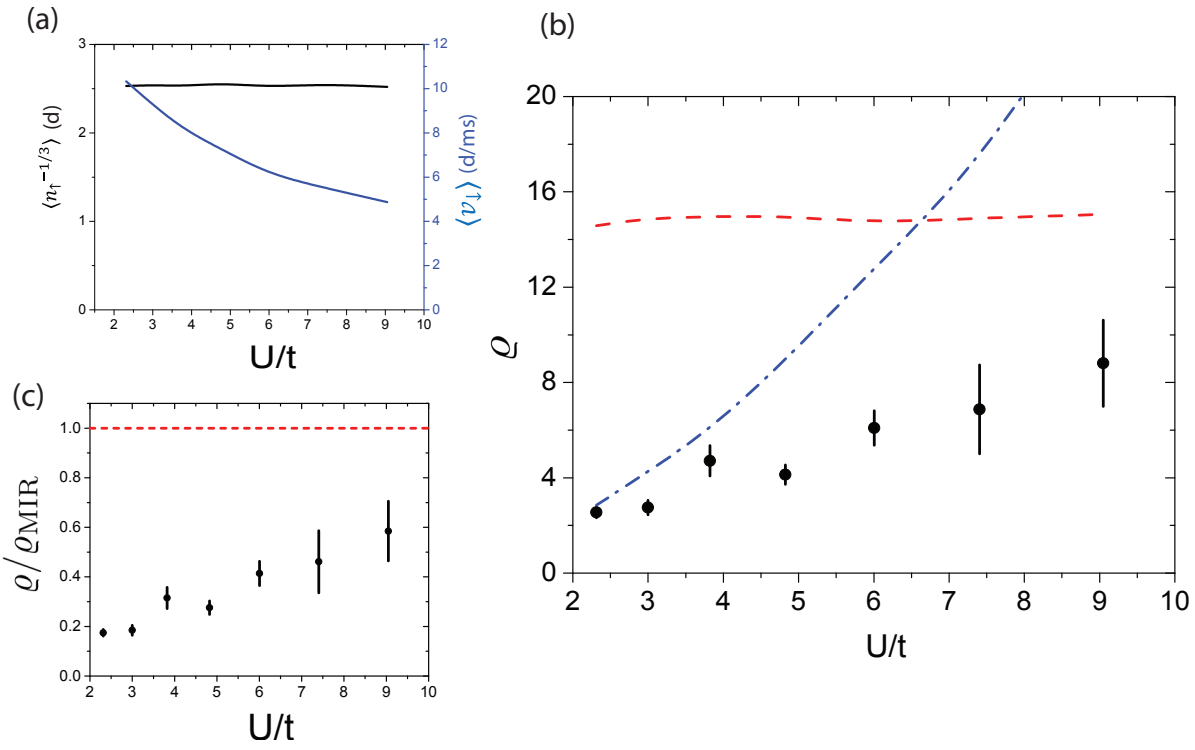

Figure 4.30: (a): The mean velocity of spin-down atoms $\langle \vec{v}_\downarrow \rangle$ and the mean separation between spin-up atoms $\left\langle n_\uparrow^{-1/3} \right\rangle$ at various interaction strengths for fixed $T/T_F \approx 0.23$. $\left\langle n_\uparrow^{-1/3} \right\rangle$ is approximately constant, since temperature and Fermi energy fixed for this data set. The mean velocity decreases because the effective mass of the atoms becomes larger as the lattice depth increases. (b): Interaction dependence of dimensionless resistivity ϱ, inferred from the data points in Fig. 4.25. The blue dash-dot line is the resistivity corresponding to the transport lifetime predicted by weak-scattering theory (black solid line in Fig. 4.25). The resistivity corresponding to the Mott-Ioffe-Regel limit ϱ_{MIR} is shown by red dashed line. (c): The ratio between the dimensionless resistivity and the MIR limit.

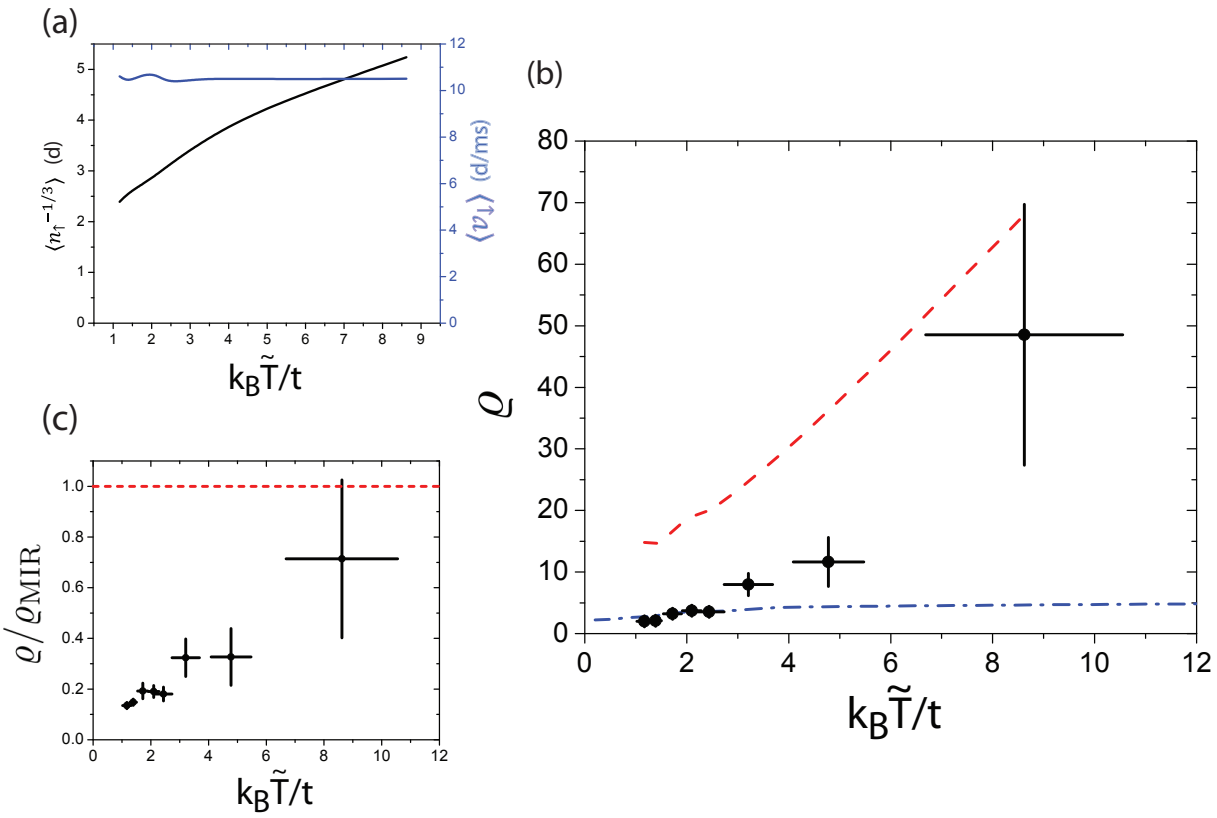

Figure 4.31: (a): The mean velocity of spin-down atoms $\langle \vec{v}_\downarrow \rangle$ and the mean separation between spin-up atoms $\left\langle n_\uparrow^{-1/3} \right\rangle$ at various temperatures for fixed interaction strength. In this regime, the mean velocity is independent of temperature, while $n_\uparrow^{-1/3}$ measures significantly due to the expansion of the gas. (b): Temperature dependence of dimensionless resistivity ϱ, inferred from the data points in Fig. 4.27. The blue dash-dot line is the resistivity corresponding to the transport lifetime predicted by weak scattering theory. The resistivity corresponding to the Mott-Ioffe-Regel limit is shown by a red-dashed line. (c): The ratio between the dimensionless resistivity and the MIR limit. The approach of the measurements toward the MIR limit at high temperature suggests the lack of resistivity saturation.

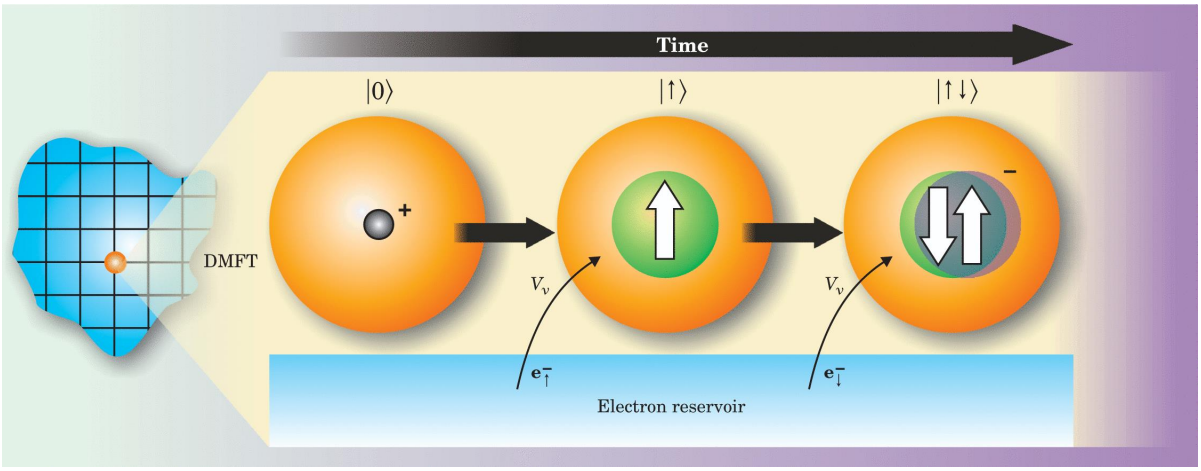

Figure 4.32: A cartoon showing the principle of dynamical mean-field theory (DMFT). The full lattice is replaced with a single lattice site (orange) imagined to exist in a bath of electrons. In our case, there are four possible configurations for this lattice site: $|0\rangle$ (empty), $|\uparrow\rangle$, $|\downarrow\rangle$ and $|\uparrow\downarrow\rangle$. The hybridization V_ν specifies how likely a state flips between different configurations by absorbing an electron from the reservoir or emitting one into the reservoir. DMFT approximately captures the dynamics of electrons on this lattice site as it fluctuates among these configurations. When the coupling between this lattice site and the bath is strong, electrons are more like free particles; the other extreme case is when hybridization is very weak and electron is localized on this lattice site. This figure is reproduced from Ref. [117]

The effective action for the single-site DMFT problem can be written as:

$$S_{eff} = -\int_0^\beta d\tau \int_0^\beta d\tau' \sum_\sigma c^\dagger_\sigma(\tau) G_0^{-1}(\tau-\tau') c_\sigma(\tau') + U\int_0^\beta c^\dagger_{\sigma'}(\tau)c_\sigma(\tau), \tag{4.50}$$

where $G_0(\tau-\tau')$ is the imaginary time Green's function, which contains information about particles in the external bath (whose degrees of freedom has been integrated out). $G_0(\tau-\tau')$ describes the following process: at time τ one particle leaves and wanders into the external bath, and then later a particle returns to the site at τ'. The form of $G_0(\tau-\tau')$ depends on the original lattice model. This effective action does not have a tunneling term, and therefore the corresponding Green's function for this single-site model $G(\tau)$ is k-independent.

The Green's function for the original Hubbard model, which is momentum-dependent, is denoted as $G_{\text{Hubbard}}(\vec{k}, i\omega_n) = \frac{1}{i\omega_n+\mu-\epsilon_k-\Sigma(i\omega_n)}$, where $\Sigma(i\omega_n)$ is the self-energy. The self-consistency condition requires the summation over $\vec{k}$ for $G_{\text{Hubbard}}(\vec{k}, i\omega_n)$ yields $G(i\omega_n)$. This gives:

$$G(i\omega_n) = \int_\infty^\infty d\epsilon \frac{D(\epsilon)}{i\omega_n+\mu-\Sigma(i\omega_n)-\epsilon}, \tag{4.51}$$

where $G(i\omega_n) = \int_0^\beta d\tau G(\tau)e^{i\omega_n\tau}$, and $D(\epsilon)$ is the density of states. The nature of the original Hubbard

model enters this single-site model via $D(\epsilon)$. For a Bethe lattice, the density of states has the semi-circular form $D(\epsilon) = \frac{2}{\pi W^2}(1 - (\frac{\epsilon}{W})^2)^{1/2}\Theta(W - \epsilon)$, where W is half-bandwidth, and $\Theta(x)$ is the Heaviside step function [118]. We use Bethe lattice geometry because of its convenience.

Since the on-site interaction term is the same for both the lattice Hubbard model and the single-site problem, the self-energy in $G(i\omega_n)$ should equal the self-energy in original lattice Hubbard model. Therefore we have $G^{-1}(i\omega_n) = G_0^{-1}(i\omega_n) - \Sigma(i\omega_n)$.

The remaining difficulty is to find G_0 that satisfies the self-consistency conditions. Many approximate methods have been developed, such as numerical renormalization group and quantum Monte Carlo [2]. Here we use iterated perturbation theory. It uses second-order perturbation theory in the Hubbard interaction U to approximate the self-energy for the single-site model. For the half-filling case, it gives [119]

$$\Sigma(\tau) = U^2 G_0^3(\tau). \tag{4.52}$$

As a brief summary, iteration for solving the single-site problem works in the following way:

- Initialize $G(i\omega_n)$ with a guess value.
- Compute $G_0(i\omega_n) = \frac{1}{i\omega_n - t^2 G(i\omega_n)}$ (for a Bethe lattice at half filling).
- Perform a Fourier transform to obtain $G_0(\tau)$ from $G_0(i\omega_n)$.
- Calculate the self-energy $\Sigma(i\omega_n) = U^2 \int_0^\tau d\tau e^{i\omega_n \tau} G_0^3(\tau)$.
- Update $G(i\omega_n)$ according to $G(i\omega_n) = \frac{1}{G_0^{-1}(i\omega_n) - \Sigma(i\omega_n)}$.

A main success of DMFT is describing the phase transition from a metal to a Mott-insulator as the ratio of the interaction strength U to the bandwidth increases. Fig. 4.33 shows a schematic phase diagram of the Hubbard model based on DMFT [117]. At low temperature, where long-range order exists, the solutions of DMFT are material- and model-dependent. At higher temperature—the regime where our experiments are done—the phase diagram is more universal. Higher temperature (path 2) enables more quasiparticle excitations, while stronger interactions (path 3) induces more scattering events. Both effects can lead to the breakdown of Fermi liquid behavior and drive the system into the "bad metal" regime.

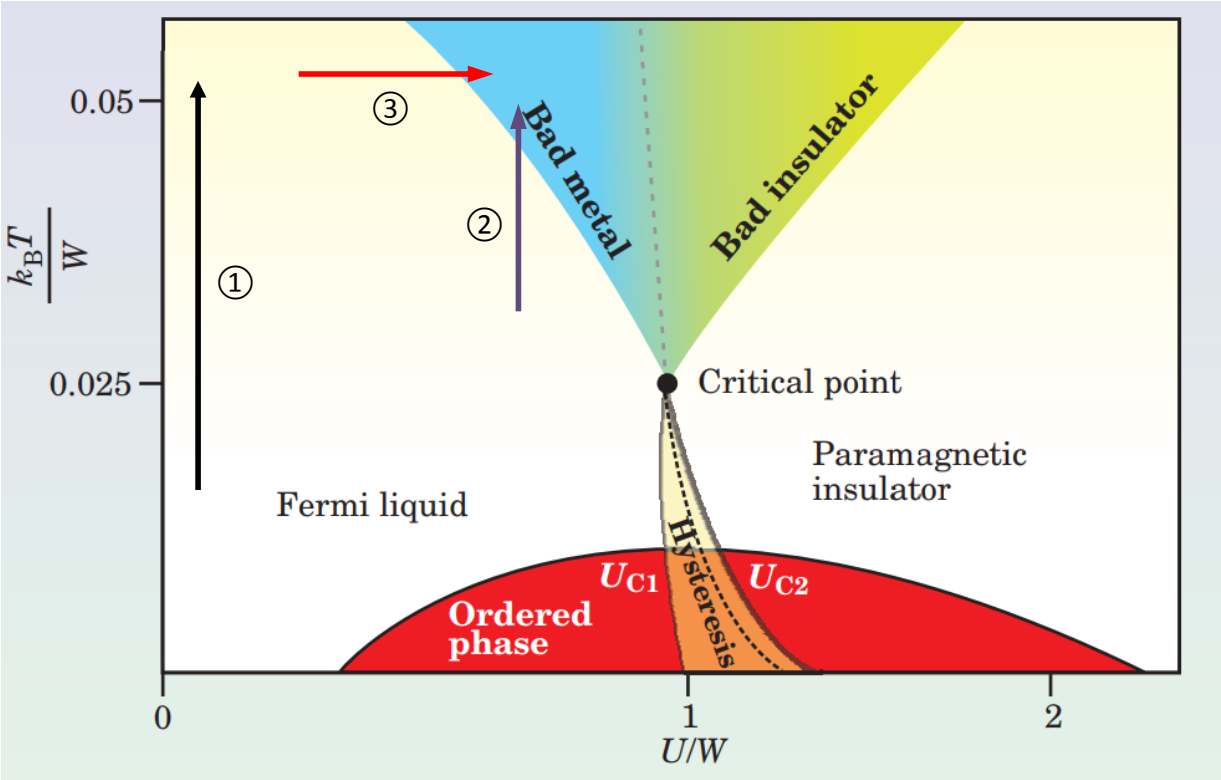

Figure 4.33: DMFT schematic phase diagram of a strongly correlated material, with temperature and strength of on-site interaction as axes. W is the half bandwidth. We are interested in the relatively high temperature regime with $U/W < 1$. Along path 1, without any interactions, the system remains a Fermi liquid. However, along path 2 and path 3, a cross-over from Fermi liquid to a bad metal occurs. The reason that high temperature and/or strong interaction induce non-Fermi liquid bad metal behavior can be attributed to more rapid scattering between particles, which reduces the coherence time. When itinerant motion is hindered due to decoherence, localized behavior is enhanced, leading to the suppression of spectral weight at the Fermi level. This figure is adapted from Ref. [117].

Conductivity

DMFT uses the Kubo formula to calculate conductivity. We calculate conductivity $\sigma(\omega)$ via the bubble-pair approximation, which gives [83]:

$$\sigma(\omega) = \frac{\pi e^2}{\hbar} \int_{-\infty}^{\infty} d\epsilon \Psi(\epsilon) \int_{-\infty}^{\infty} d\omega' (\frac{f(\omega') - f(\omega + \omega')}{\omega}) A(\omega', \epsilon) A(\omega' + \omega, \epsilon), \tag{4.53}$$

where e is the carrier charge, $A(\omega, \epsilon) = -1/\pi \Im(\frac{1}{\omega + \mu - \Sigma(\omega) - \epsilon})$ (notice that it is NOT the same as the local spectral function!), $f(\omega) = \frac{1}{e^{\beta\omega}+1}$ (with the Fermi energy set to zero), and $\Psi(\epsilon) = \sum_k (\frac{\partial \epsilon_k}{\partial k})^2 \delta(\epsilon - \epsilon_k)$ is the transport density of states. For a Bethe lattice, $\Psi(\epsilon) = \frac{1}{3d}(W^2 - \epsilon^2) D(\epsilon)$.

The limit $\omega \to 0$ gives the DC conductivity, which is:

$$\sigma_{DC} = \frac{\pi e^2}{\hbar} \int_{-\infty}^{\infty} d\epsilon \Psi(\epsilon) \int_{-\infty}^{\infty} d\omega (-\frac{\partial f(\omega)}{\partial \omega}) A^2(\omega, \epsilon). \tag{4.54}$$

4.8.2 Results of DMFT

We adapted the code provided in the Toolbox for Research on Interacting Quantum Systems (TRIQS) [120, 121] to calculate spectral functions and conductivity for our experimental conditions. The code employs iterated perturbation theory to obtain the Greens functions for the Hubbard model with a Bethe lattice geometry and particle-hole symmetry. Despite the simplicity of this method, it is believed to give a qualitatively correct result and scalings for physical quantities [2, 119]. The bandwidth of a Bethe lattice geometry is $4t^*$ (t^* denotes the hopping term in Bethe lattice), while the bandwidth of a 3D Hubbard model is $12t$. In our DMFT calculation, the temperature and energies are all in unit of the half-bandwidth W. We therefore scale the temperature and energy in units of t by a factor of 3.

Spectral function and self-energy

Fig. 4.34 and Fig. 4.35 plot the local spectral functions $-\frac{1}{\pi}\Im[G(\omega)]$ and the imaginary part of the self-energy $-\Im[\Sigma(\omega)]$. In these plots, $\omega = 0$ is the Fermi energy. With fixed temperature $T/W = 0.248$ (Fig. 4.34), the spectral function becomes broader as U/W increases, and the quasiparticle weight at the Fermi energy decreases. The spectral function retains its single-peak feature, suggesting the existence of quasiparticles. However, the imaginary part of the self-energy, proportional to $1/\tau_{\mathrm{QP}}$ (where τ_{QP} is the quasiparticle lifetime), increases significantly. We therefore expect to observe stronger deviations from Fermi liquid theory at high U, since the quasiparticles are not long-lived.

Fig. 4.35, with fixed $U/W = 0.383$, reveals more interesting features as the temperature increases. At

low temperature, the spectral function is dominated by a peak centered at $\omega = 0$, and the imaginary part of self-energy is small. Fermi liquid theory is therefore valid. As the temperature increases, a broader spectral function, lower quasiparticle weight, shorter lifetime, and a three-peak structure appear. The weight of the quasiparticle peak at $\omega = 0$ is transferred to the Hubbard bands located at $\pm U/2$. The appearance of these additional peaks indicates the breakdown of the quasiparticle picture.

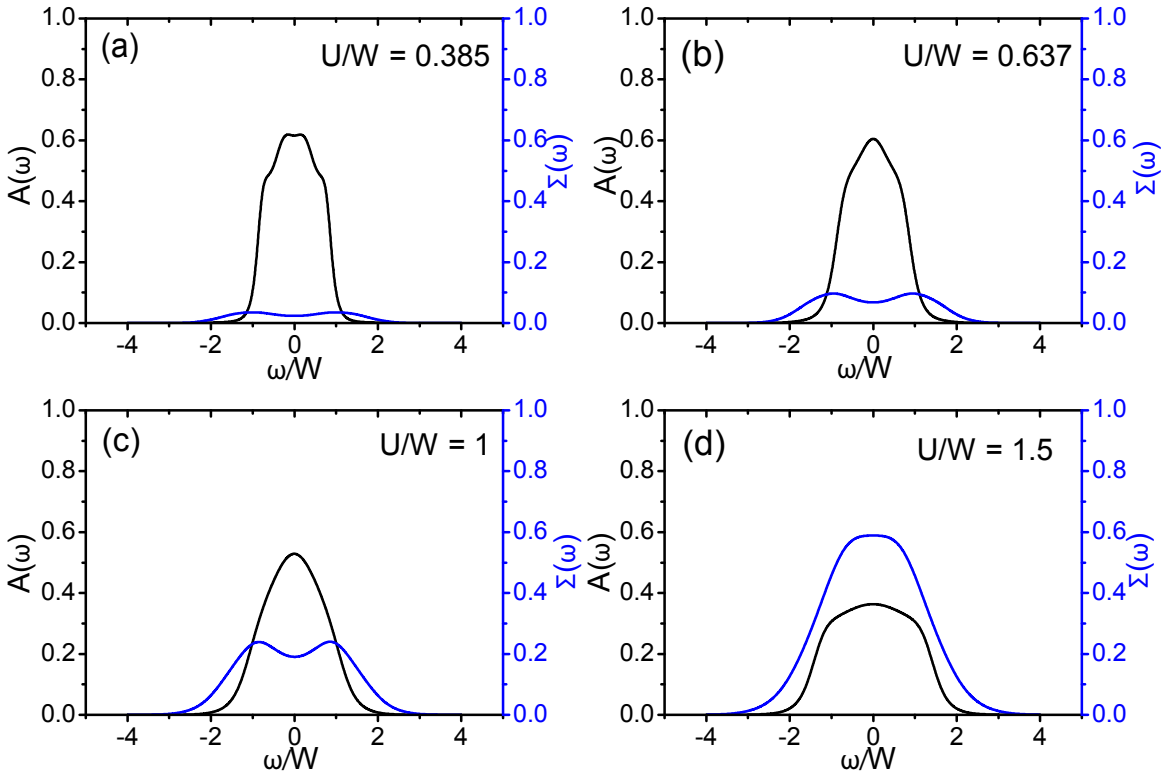

Figure 4.34: Local spectral function (black) and the imaginary part of self-energy (blue) at various interaction strengths with $k_B T/W = 0.248$. (a)-(d): U in units of the half-bandwidth W are 0.385, 0.637, 1 and 1.5, respectively. Increasing temperature broadens the spectral function and reduces the quasiparticle weight. The increasing value of $\Im\Sigma(\omega)$ at $\omega = 0$ indicates a shorter quasiparticle lifetime, suggesting that Fermi liquid theory may fail.

Scaling of resistivity

Fig. 4.36 shows the DMFT DC resistivity (in arbitrary units) dependence on the interaction strength at $T/W = 0.248$, which corresponds to the conditions for Fig 4.25. Within the interaction range that our measurements explored, the resistivity ρ follows a $(U/W)^2$ scaling for $U/W < 1$. This dependence is consistent with Fermi-liquid theory. At higher U, a slight deviation from quadratic scaling is observed.

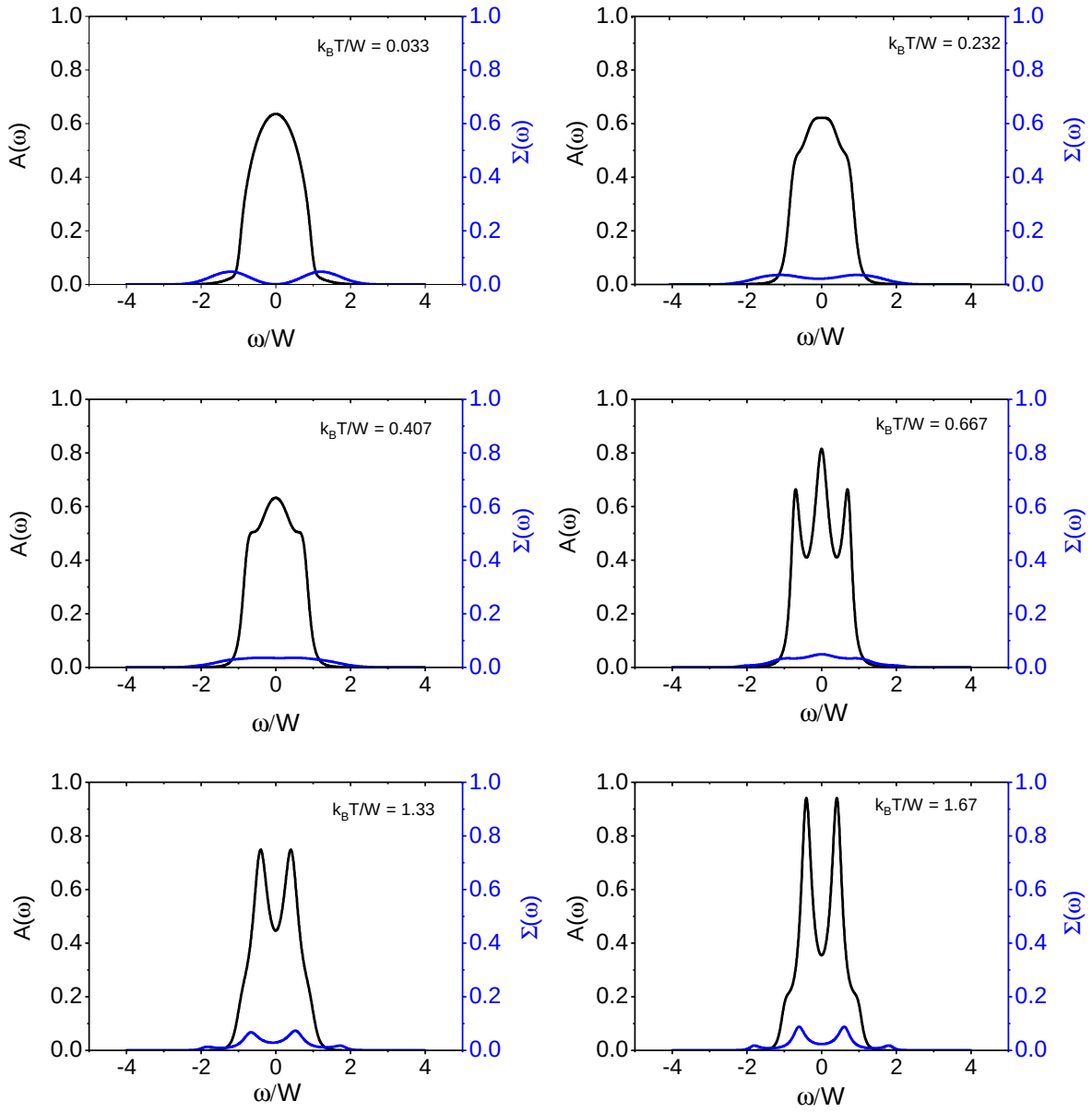

Figure 4.35: Local spectral function (black) and the imaginary part of self-energy (blue) at various temperatures, with $U/W = 0.383$. (a)-(f): Temperatures in unit of half-bandwidth W are: 0.033, 0.232, 0.407, 0.667, 1.33, and 1.67. In this plot, $\Im\Sigma(\omega)$ is scaled by a factor of 5 for a clearer view. The increase in temperature not only broadens $A(\omega)$, but leads to multiple peaks. A three-peak structure, as shown in (d), is characteristic of DMFT calculations. The other two peaks are precursors of the Hubbard bands, originating from local "atomic" excitations.

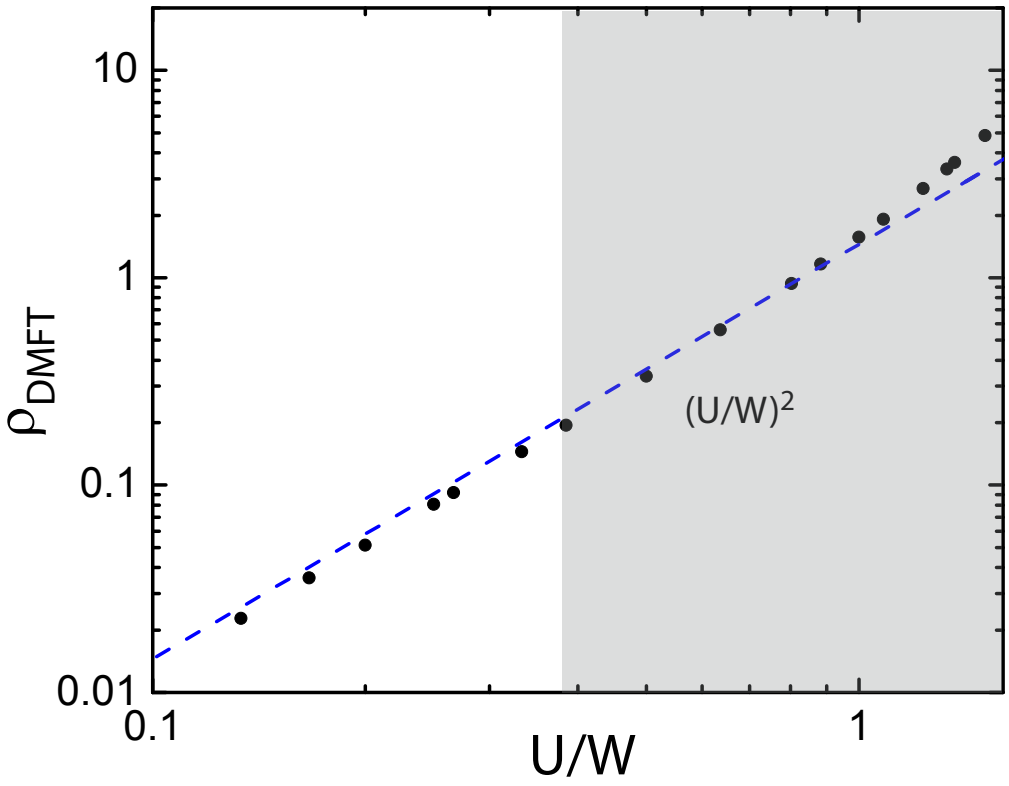

Figure 4.36: Dependence of resistivity on interaction strength with $k_B T/W = 0.248$, corresponding to the averaged temperature for the transport lifetime measurements shown in Fig. 4.25. The blue dashed line is a fit to $(U/W)^2$ for $U/W < 1$. The shaded region shows the area of this plot relevant to the experiment, which samples U/W from $0.4 - 1.5$.

Fig. 4.37 shows the dependence of resistivity on temeprature at $U/W = 0.383$, which corresponds to the conditions for Fig. 4.27. At low enough T, the resistivity shows a quadratic scaling of T, which, as expected, matches the prediction from Fermi-liquid theory. As temperature increases, a T-linear dependence appears, indicating that the picture describing transport as coherent scattering among quasiparticles with well-defined momentum is invalid. A linear dependence of ρ on temperature is a key signature of the bad metal behavior.

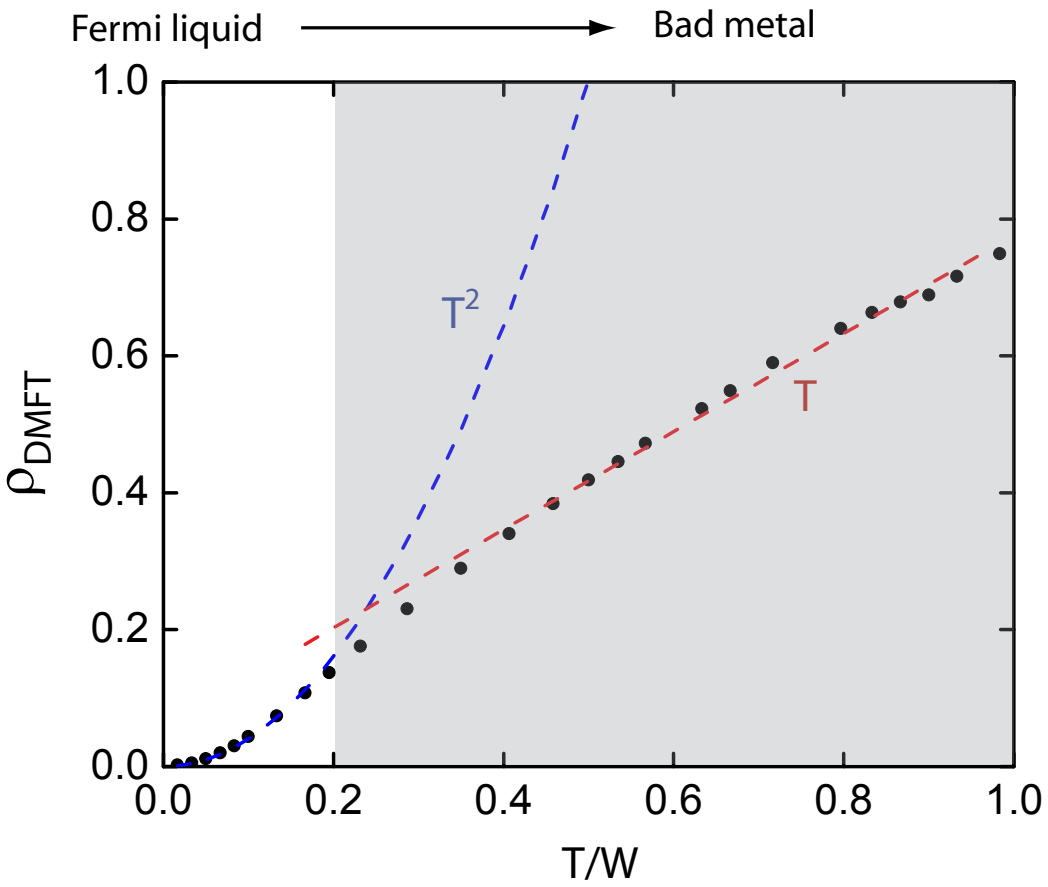

Figure 4.37: Temperature dependence of resistivity at $t/W = 0.383$, which corresponds to a lattice depth $s = 4E_R$. At very low temperature ($T/W < 0.1$), the resistivity scales as T^2. This matches the Fermi-liquid theory prediction, indicating coherent scattering between long-lived quasiparticles. As T increases, the scaling behavior deviates from T^2, and instead presents a linear dependence on temperature. The blue dashed line is a fit to a quadratic function for $T/W < 0.1$, and the red dashed line is a linear fit for $T/W > 0.1$. The shaded region shows the area of this plot relevant to the experiment, which samples T/W from $0.2 - 1.3$.

Our DMFT calculation assumes particle-hole symmetry and half-filling. The experiment, however, involves an unequal number of $|\uparrow\rangle$ and $|\downarrow\rangle$ atoms and an inhomogeneous density profile. While the particle-hole asymmetry is known to modify the spectral function $A(\omega)$ [122] and affect the absolute value of resistivity, more sophisticated DMFT calculations indicate that T-linear resistivity still appears within the tempera-

ture range we sample [123]. Other methods, such as quantum Monte Carlo calculations [124], also show the existence of T-linear scaling within a wide range of filling factors.

4.8.3 Scaling behavior comparison

We compare our measurements with predictions from dynamical mean field theory (DMFT) simulations of the Hubbard model for our lattice parameters and regime of temperature. The strategy applied here is to fit the resistivity inferred from transport lifetime measurements to a power law function, with the exponent fixed to be the value predicted by DMFT calculation. The reduced chi-squared χ^2 is used in our goodness of fit testing.

Fig. 4.38 shows the comparison for the interaction dependence of resistivity. The data fit well to the DMFT scaling prediction $\varrho = b_U + g_U(U/t)^2$ (reduced $\chi^2 = 0.99$), with an offset g_U and proportionality constant g_U as free parameters (black curve in Fig. 4.38). An offset is necessary because the Hubbard approximation and the tight-binding limit fail in the $s \to 0$ limit. The bottom of Fig. 4.38 shows the spectral function $A(\omega)$ and the imaginary part of the self-energy predicted by DMFT calculation. At low temperature and low interaction strength, $A(\omega)$ consists of a well-defined single peak centered at the Fermi energy, which is broadened by interactions. The reduction of quasiparticle weight explains the derivation of weak-scattering theory at higher U/t.

For the temperature dependence data, since our sampling of temperature is in the T-linear region, the data are fit to a linear function (black curve in Fig. 4.39). In the $T \to 0$ limit, the system is expected to cross-over to the Fermi liquid T^2 scaling. An offset is therefore required here for fitting to T-linear behavior at high T. Reduced $\chi^2 = 1.76$ of this fit indicates the scaling is consistent with T-linear, which is evident in Fig. 4.39. This T-linear scaling is contradictory with Fermi liquid theory and is a signature of a bad metal. The bottom panel of Fig. 4.39 plots the spectral function $A(\omega)$ and the imaginary part of the self-energy $\Im(\Sigma(\omega))$. The qualitative change in the spectral function $A(\omega)$ from a single-peak to a three-peak structure provides insight into how bad metal behavior arise [117] and indicate the failure of weak scattering theory. At relatively low temperature, the states are still quasiparticle-like and retain the character of free electrons, but with a finite lifetime due to interactions. At high T, the transfer of spectral weight to peaks centered at approximately $\pm U/2$ is indicative of the breakdown of quasiparticles. The states become localized, giving rise to a resistivity that increases more rapidly with temperature than the Fermi-liquid prediction. This effect is responsible for the anomalous scaling of transport lifetime evident in Fig. 4.27. The breakdown of quasiparticles is consistent with the qualitative failure of the weak scattering calculation, because the origin of resistivity can no longer be treated as a result of collisions between particles with well-defined momenta.

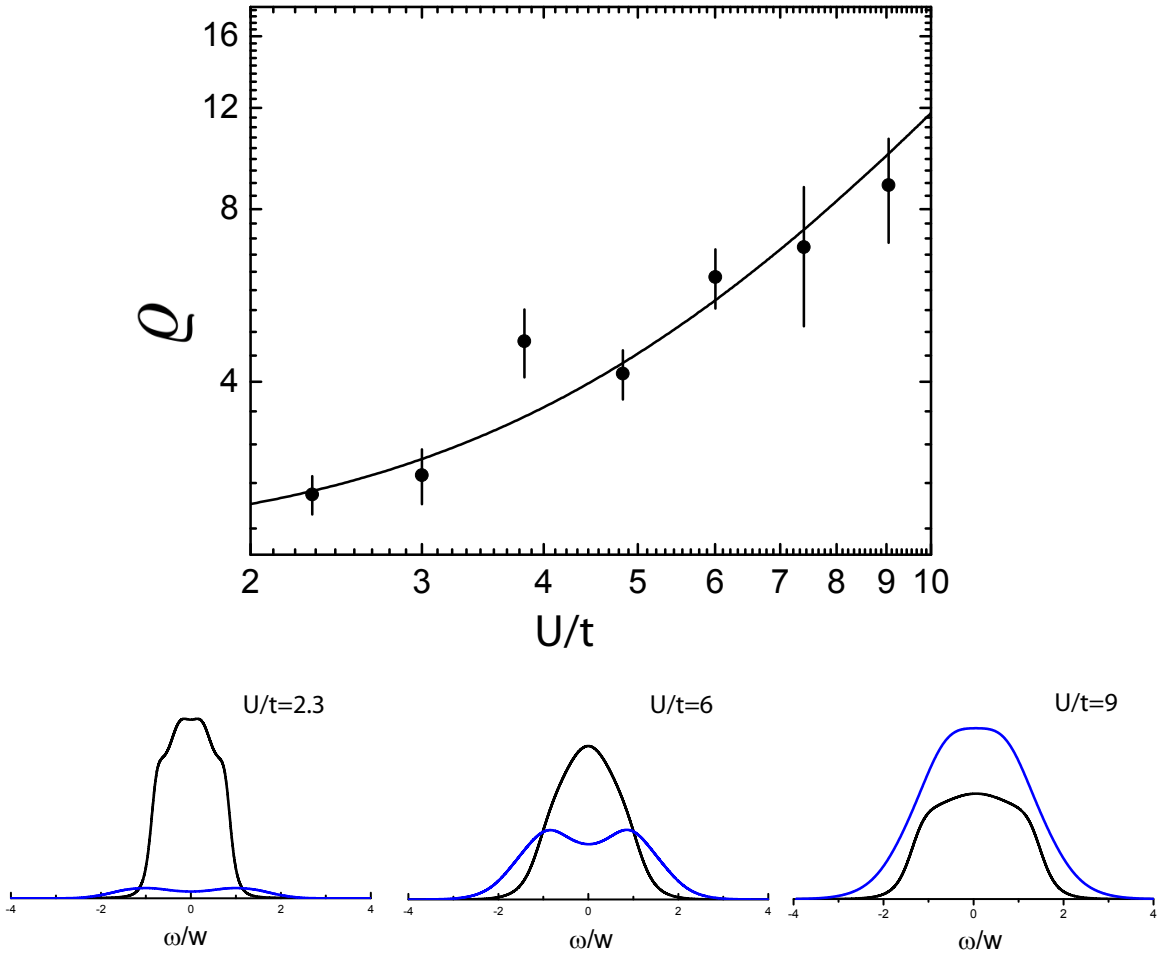

Figure 4.38: Inferred dimensionless resistivity at various interaction strength for $k_B\tilde{T}/t \approx 1.4$. The data correspond to those shown in Fig. 4.25. Data are fit to a quadratic function as predicted by DMFT, with reduced $\chi^2 = 0.99$. The bottom panel shows the spectral function and the imaginary part of the self-energy at various interaction strengths.

To our knowledge, our measurements of scaling consistent with T-linear is the first to sample temperature above the Fermi temperature in any system and the first evidence for this behavior in an ultracold gas.

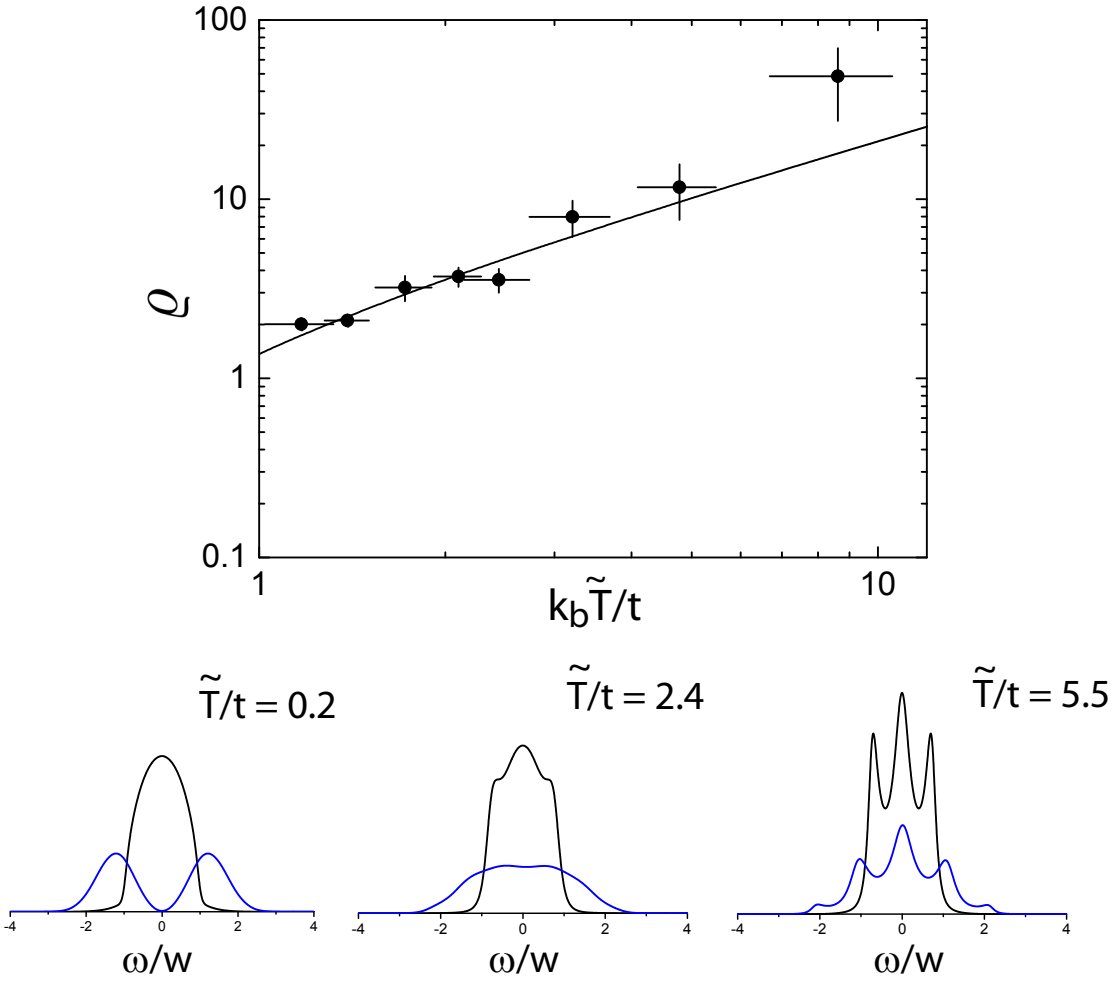

Figure 4.39: Inferred dimensionless resistivity at various temperatures for $U/t = 2.3$. The data are fit to a linear function as predicted by DMFT, with reduced $\chi^2 = 1.76$. Orthogonal distance regression is used to accommodate the horizontal error bars. The bottom panel shows the spectral function and the imaginary part of the self-energy at various temperatures. The appearance of a three-peak structure, indicative of the breakdown of quasiparticles, explains the failure of the weak scattering calculation and provides insight into the anomalous temperature scaling of resistivity from the microscopic level.

4.9 Conclusion

In this chapter, we discuss the discovery of phenomena consistent with bad-metal behaviour in the metallic regime of an optical-lattice Hubbard model. We directly measure the transport lifetime induced by interparticle scattering for a mass current of atoms excited by stimulated Raman transitions. By exploring a range of interaction strengths and a regime of temperature inaccessible to solids, we demonstrate incompatibility

with a weak scattering theory. By inferring the analog of resistivity from transport lifetime, and comparing our results to dynamical mean-field simulations, we identify three characteristics of bad metals:

- Absence of quasiparticles with a well-defined momentum:

  Via comparison to dynamical mean-field theory (DMFT) simulations, we conclude that the reduction of quasiparticle weight from strong intersections is directly related to the anomalous behavior of resistivity.

- Lack of resistivity saturation:

  The resistivity does not saturate as the Mott-Ioffe-Regel (MIR) limit is approached.

- An abnormal temperature scaling of resistivity

  In my opinion, having access to the transport behavior of strongly-correlated particles at a temperature comparable to Fermi temperature is exciting. Solid state materials melt at a temperature well below T_F. Besides, as temperature increases, phonons start to dominate, and therefore it is hard to distinguish phenomena solely due to electron-electron interactions. Although previous DMFT calculations predict a T-lienar scaling of resistivity up to $T \approx T_F/2$, as far as I know, there have been no experimental evidence in condensed matter system.

When I look back at this project, there are several improvements that we could have implemented. First, for the temperature dependence data, we could perform measurements with a higher lattice depth. The larger energy gap between the ground state and the first-excited state of the band structures allows us to approach higher temperature without populating excited bands. Moreover, after finishing this project, we updated our apparatus to have the ability to tune the interactions between atoms via a Feshbach resonance. It will be interesting to perform similar measurements, but with non-interacting two-component fermionic gas in optical lattices. A direct comparison should deliver a clearer picture for understanding the effect of strong interactions on transport lifetime.

In the future, rf spectroscopy measurements in this system may reveal information about the spectral function $A(\omega)$ directly [88]. A uniform overall confinement, like a box potential [125, 126], can be used to remove the extra complexity due to the inhomogeneous density profile present in a harmonic trap potential. Furthermore, additional effects present in solids can be added in a controllable fashion. The influence of disorder can be investigated via, e.g., applying optical speckle [127], and the impact of phonons could be explored using mixtures of different species [128].

Chapter 5

Density-dependent hopping in a Fermi-Hubbard model

5.1 Introduction

The single-band Fermi-Hubbard model, realized by loading a degenerate Fermi gas into an optical lattice, is a minimal model for describing strongly correlated electronic systems. Periodic driving forces combined with optical lattices have enabled experiments to achieve physics beyond this minimal paradigm (see Ref. [129] for a recent review). For example, magnetic phase transitions have been probed [130, 131], synthetic gauge fields have been realized [26, 27, 132], and non-trivial band structures [25] have been created using periodic driving and external fields in lattices.

In this chapter, we use applied Raman laser fields to demonstrate correlated tunneling that depends on density and spin for fermionic atoms. Correlated tunneling appears in a generalized Hubbard model in crystalline solids [133]. Consider the Hamiltonian for the Coulomb interaction in a tight-binding model:

$$H_{e-e} = \frac{1}{2} \sum_{ijkl,\sigma\sigma'} \langle ij|V_{ee}|kl\rangle \, c^\dagger_{i\sigma} c^\dagger_{j\sigma'} c_{l\sigma'} c_{k\sigma}, \tag{5.1}$$

with

$$\langle ij|V_{ee}|kl\rangle = \int d^3r d^3r' w^*(r - R_i) w(r - R_k) \frac{e^2}{|r - r'|} w^*(r' - R_j) w(r' - R_l),$$

where $w(r - R_i)$ is Wannier function.

In the original argument of Hubbard [133], the interaction terms are categorized as:

$$U = \langle ii|1/r|ii\rangle \tag{5.2}$$

$$V = \langle ij|1/r|ij\rangle \tag{5.3}$$

$$X = \langle ij|1/r|ji\rangle = \langle ii|1/r|jj\rangle \tag{5.4}$$

$$\Delta t = \langle ii|1/r|ij\rangle \, . \tag{5.5}$$

Now the indices i and j are for nearest-neighbor sites (in metals, interactions between more distant sites

are exponentially suppressed because of screening.). Terms involving more than two sites are also neglected, because they are at least one additional overlap factor smaller compared to these terms.

Hubbard gave an estimation for these four terms as $U \approx 20eV$, $V \approx 6eV$, $\Delta t \approx 0.5eV$, and $X \approx 1/40eV$, so the dominant interaction is the U term representing on-site interactions. This is the original argument that yields the famous Hubbard model. Later, after the discovery of the high temperature superconductors, physicists started to seek a new mechanism that induces effective attractive interactions among electrons to replace BCS theory. J.E. Hirsch proposed the Δt term, which he called as "bond-charge" repulsion [134]. The Hamiltonian for this term is $H_{bc} = \Delta t \sum_{\langle ij \rangle, \sigma} (c^{\dagger}_{i\sigma} c_{j\sigma} + \text{h.c.})(n_{i,\sigma} + n_{j,-\sigma})$. In solids, the strength of this term is determined by material parameters, and, physically, the ordering $U > V > \Delta t > X$ is always true.

It is desirable to manipulate this term in an independent and tunable way. The influence of correlated tunneling on transport properties has been investigated in quantum dots, where it can be tuned by gate voltages and applied electromagnetic fields [135]. Ultracold atoms in optical lattices generally realize a minimal Hubbard model without correlated tunneling, since the interactions between atoms are point-like. However, I will discuss in this chapter that periodic driving force can introduce effective correlated tunneling into the Hamiltonian. This possibility has attracted theoretical interest for inducing occupation-dependent gauge fields [136], obtaining novel phases such as holon and doublon superfluids [137], and realizing anyonic Hubbard models [138]. Thus far, density dependent tunneling has been observed for bosonic atoms trapped in optical lattices via lattice modulation [139,140]. Work discussed in the chapter is inspired by the theoretical proposal in Ref. [141]. We implement a new experimental approach based on this proposal to generate spin and density-dependent tunneling for fermionic atoms in optical lattices.

5.2 Correlated spin-flip tunneling via stimulated Raman transitions

To generate spin and density-dependent tunneling for fermionic atoms, we apply a pair of Raman beams to a spin-polarized gas. The conventional tunneling is forbidden for a spin-polarized gas by the Pauli exclusion principle. This pair of Raman beams can flip the atomic spin and induce density-dependent tunneling.

The same Raman beams described in Chapter 2 are used to induce light-assisted tunneling. A degenerate Fermi gas of ^{40}K atoms is prepared in an optical dipole trap. After evaporative cooling, the optical trap depth is increased to the same value for all the data presented in this chapter. The resulting dipole trap frequencies are (47.9 ± 1)Hz, (98 ± 1)Hz and (114 ± 2)Hz. A microwave-frequency swept magnetic field combined with a static magnetic field gradient are used to remove all atoms in one hyperfine state, thereby

preparing a spin-polarized gas, either in the $|\uparrow\rangle \equiv |F = 9/2, m_F = 9/2\rangle$ or in the $|\downarrow\rangle \equiv |F = 9/2, m_F = 7/2\rangle$ state, before we ramp on the three pairs of lattice beams in 100ms.

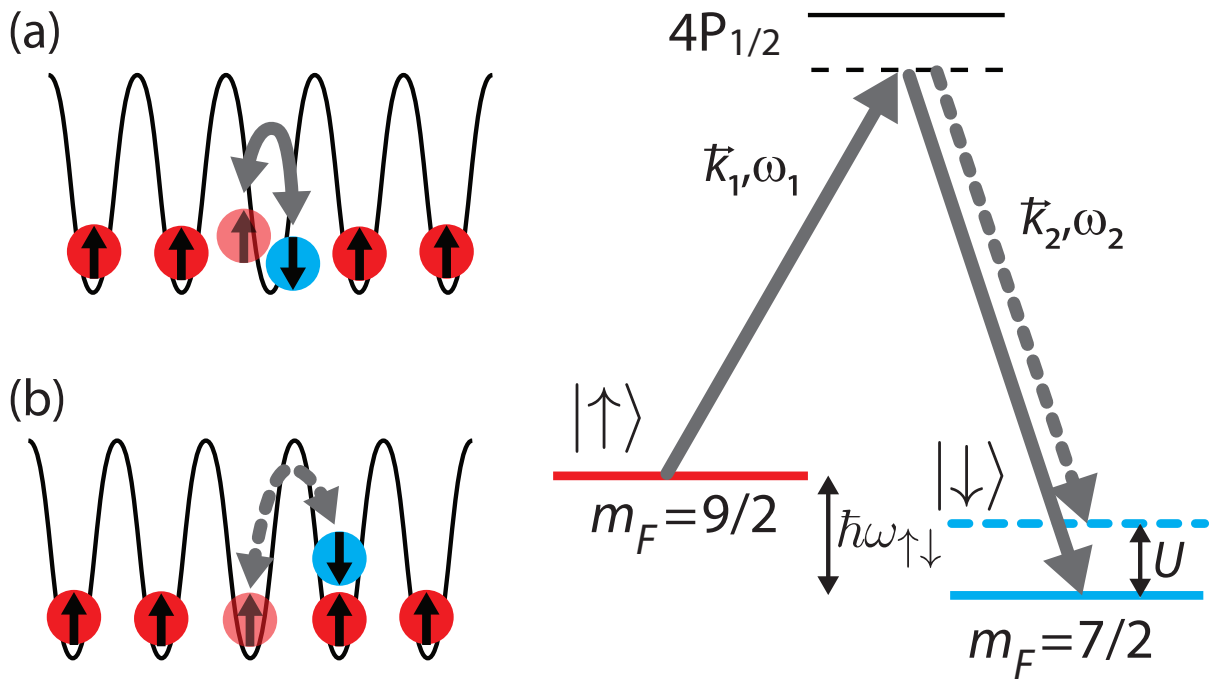

Figure 5.1: Schematic diagram of Raman transitions. A pair of Raman beams with frequencies $\omega_{1,2}$ and wavevectors $\vec{k}_{1,2}$ is applied to drive transitions between the $|\uparrow\rangle$ (red) and $|\downarrow\rangle$ (blue) states. The Raman wavevector difference $\delta\vec{k} = \vec{k}_1 - \vec{k}_2$ lies along the $(-1, -1, -1)$ direction of the lattice. Selecting between two distinct processes is achieved by fixing the laser beam frequency ω_1 and tuning ω_2. (a) If the frequency difference matches the Zeeman energy ($\delta\omega = \omega_1 - \omega_2 = \omega_{\uparrow\downarrow}$), then atoms flip their spin and remain on the same site. (b) When the laser frequency difference accommodates the Hubbard interaction energy U ($\Delta\omega = \omega_{\uparrow\downarrow} - U/\hbar$), then CSFT occurs and atoms tunnel to neighboring occupied sites and flip their spin. For $|\downarrow\rangle$ as an initial state, the condition for resonant CFST changes to $\Delta\omega = \omega_{\uparrow\downarrow} + U/\hbar$.

The Raman beams can drive two resonant precesses, depending on $\Delta\omega$. As shown in Fig. 5.1(a), if $\Delta\omega$ is tuned to the energy difference between spin states (*i.e.*, $\Delta\omega = \omega_{\uparrow\downarrow}$), then on-site spin rotations occur without induced tunneling and changes in site occupancies. We define this process as the carrier transition. By tuning the frequency difference between the beams to include U ($\Delta\omega - \omega_{\uparrow\downarrow} = \pm U/\hbar$), density-dependent tunneling accompanied by spin rotation is driven as a sideband to the carrier (Fig. 5.1(b)). We call this process correlated spin-flip tunneling (CSFT). Working in the large U limit, we use perturbation theory to find the effective CSFT Hamiltonian for this process (detailed theoretical derivations can be found in Section. 5.7, which is the work of Prof. V. Scarola and H. Hui from Virginia Polytechnic Institute and State University):

$$H_{\mathrm{CSFT}} = \sum_{i,j} \left[K_{ij} n_{i\uparrow}(1 - n_{j\downarrow}) \hat{c}^{\dagger}_{j\uparrow} \hat{c}_{i\downarrow} + K^{*}_{ij} n_{i\uparrow}(1 - n_{j\downarrow}) \hat{c}^{\dagger}_{i\downarrow} \hat{c}_{j\uparrow} \right]. \tag{5.6}$$

Eq. 5.6 has been projected into the subspace connected to the initial spin-polarized $|\uparrow\rangle$ state by resonant CSFT. This model has been verified by Scarola and Hui via determining the dynamics of the full tight-binding CSFT model by applying the time-evolving block decimation algorithm to 1D chains [142].

CSFT arises as a spin-flip transition to a virtual state offset by U, followed by a tunneling event. In contrast to the conventional tunneling term $-t\hat{c}_i^\dagger \hat{c}_j$ in the Fermi-Hubbard model, this light-induced correlated spin-flip tunneling is density-dependent and accompanied by a spin-rotation. CSFT occurs only when neighboring sites are occupied by atoms in the same spin state or when a doublon (a $|\uparrow\downarrow\rangle$-pair) on one lattice site is next to an empty site. The magnitude of the CSFT matrix element

$$|K_{ij}| \approx \frac{t}{2U}|\Omega(1 - e^{i\delta\vec{k}\cdot\vec{d}})|,$$

where $t/U \approx 0.04-0.08$ (for the work in this thesis) is controlled by lattice potential depth s, and $\delta\vec{k}\cdot\vec{d} \approx \frac{\pi}{2\sqrt{3}}$ for all lattice directions in our experiment (where $\vec{d}$ is a lattice vector). Ω is the Rabi rate for the carrier transition, which is controlled by the Raman laser intensity and can be measured via Rabi oscillations as explained in Section 5.6. In this work, $\Omega \approx 0.2U/\hbar$.

5.2.1 A two-site, two-fermion toy model

Unlike the spin-rotation driven by spatially homogeneous long-wavelength radio- or microwave-frequency radiation, our approach with Raman beams introduces a site-dependent phase $e^{i\delta\vec{k}\cdot\vec{d}}$, which is critical for this CSFT event. Here, we deliver a simple two-site, two-fermion toy model to illustrate the importance of this non-trivial Raman phase gradient.

Considering a two-site, two-fermion system, there are six possible configurations, which we label according to the site and spin occupancy in each well: $|\uparrow,\uparrow\rangle_W$, $|\downarrow,\downarrow\rangle_W$, $|\uparrow\downarrow,0\rangle_W$, $|0,\uparrow\downarrow\rangle_W$, $|\uparrow,\downarrow\rangle_W$, and $|\downarrow,\uparrow\rangle_W$. In this well-specific basis, $|\downarrow,\uparrow\rangle_W$ means that a $|\downarrow\rangle$ atom is in the left well (located at position $\vec{R}_1$) and an $|\uparrow\rangle$ atom is in the right well (located at position $\vec{R}_2$), for example.

Using a Slater determinant to explicitly write down properly symmetrized (un-normalized) two-atom

wavefunctions, we have:

$$|\uparrow,\uparrow\rangle_W = (|LR\rangle - |RL\rangle)\,|\uparrow\uparrow\rangle \tag{5.7}$$

$$|\downarrow,\downarrow\rangle_W = (|LR\rangle - |RL\rangle)\,|\downarrow\downarrow\rangle \tag{5.8}$$

$$|\downarrow\uparrow,0\rangle_W = |LL\rangle\,(|\uparrow\downarrow\rangle - |\uparrow\downarrow\rangle) \tag{5.9}$$

$$|0,\downarrow\uparrow\rangle_W = |RR\rangle\,(|\uparrow\downarrow\rangle - |\uparrow\downarrow\rangle) \tag{5.10}$$

$$|\uparrow,\downarrow\rangle_W = (|LR\rangle - |RL\rangle)(|\uparrow\downarrow\rangle + |\downarrow\uparrow\rangle) + (|LR\rangle + |RL\rangle)(|\uparrow\downarrow\rangle - |\downarrow\uparrow\rangle) \tag{5.11}$$

$$|\downarrow,\uparrow\rangle_W = (|LR\rangle - |RL\rangle)(|\uparrow\downarrow\rangle + |\downarrow\uparrow\rangle) - (|LR\rangle + |RL\rangle)(|\uparrow\downarrow\rangle - |\downarrow\uparrow\rangle), \tag{5.12}$$

where the spatial part of the wavefunction is written in the basis of $|L\rangle$ and $|R\rangle$, which are single-particle states on either the left or the right well, and the spin component is denoted as $|\uparrow\rangle$ and $|\downarrow\rangle$. For example, in this basis, $|LR\rangle\,|\uparrow\downarrow\rangle$ means that atom 1 is in the left well in the $|\uparrow\rangle$ state, and atom 2 is in the right well in the $|\downarrow\rangle$ state. The key point for this discussion is that the $|\uparrow,\downarrow\rangle_W$ and $|\downarrow,\uparrow\rangle_W$ states consist of spin singlet and triplet components. Furthermore, the relative sign between the spin and triplet components is opposite for these two states.

We focus on resonant CSFT with $\Delta\omega - \omega_{\uparrow\downarrow} = U/\hbar$. An initially spin-polarized state $|\uparrow,\uparrow\rangle_W$ (as in the experiment) can transition to a virtual state $|\uparrow,\downarrow\rangle_W$ or $|\downarrow,\uparrow\rangle_W$ via a Raman transition (see Fig. 5.2). The amplitude for this process is suppressed by a factor of $1/U$ because of the energy mismatch. The phase of the virtual state depends on which atom undergoes a spin-flip, since $\delta\vec{k} \neq 0$. Therefore, the Raman phase enters as either $e^{\delta\vec{k}\cdot\vec{R}_1}$ or $e^{\delta\vec{k}\cdot\vec{R}_2}$, where $\vec{R}_1$ and $\vec{R}_2$ differ by a lattice spacing $\vec{d}$. After the virtual state is occupied, tunneling completes the CSFT process, and a doublon is formed. Via tunneling, the sign difference between equations 5.11 and 5.12 is converted into an overall sign difference between the wavefunctions for each doublon-formation pathway. This π relative phase between the wavefunctions can be computed from the tunneling matrix elements $\langle\uparrow\downarrow,0|_W\, t(c_i^\dagger c_{i+1} + \text{h.c.})\,|\uparrow,\downarrow\rangle_W$ and $\langle\uparrow\downarrow,0|_W\, t(c_i^\dagger c_{i+1} + \text{h.c.})\,|\downarrow,\uparrow\rangle_W$.

The transition between the initial state $|\uparrow,\uparrow\rangle_W$ and the final doublon–hole state happens via these two possible channels simultaneously. The final state is a superposition of these two pathways, with a wavefunction proportional to $\left(e^{-i\delta\vec{k}\cdot\vec{R}_1} - e^{-i\delta\vec{k}\cdot\vec{R}_2}\right)(|\uparrow\downarrow,0\rangle + |0,\uparrow\downarrow\rangle)$. The probability to observe a doublon-hole state is thus proportional to $\left[1 - \cos(\delta\vec{k}\cdot\vec{d})\right]$. Without the Raman phase gradient (i.e., $\delta\vec{k} = 0$ or $\delta\vec{k}\cdot\vec{d} = 0$), destructive interference prevents tunneling, and doublons will not be formed. The Raman phase disrupts destructive interference between multiple tunneling pathways that is induced by antisymmetrization of the wavefunction. Ultimately, this interference arises from the different signs between the triplet and singlet components in equations 5.11 and 5.12—it is absent for bosons, for instance.

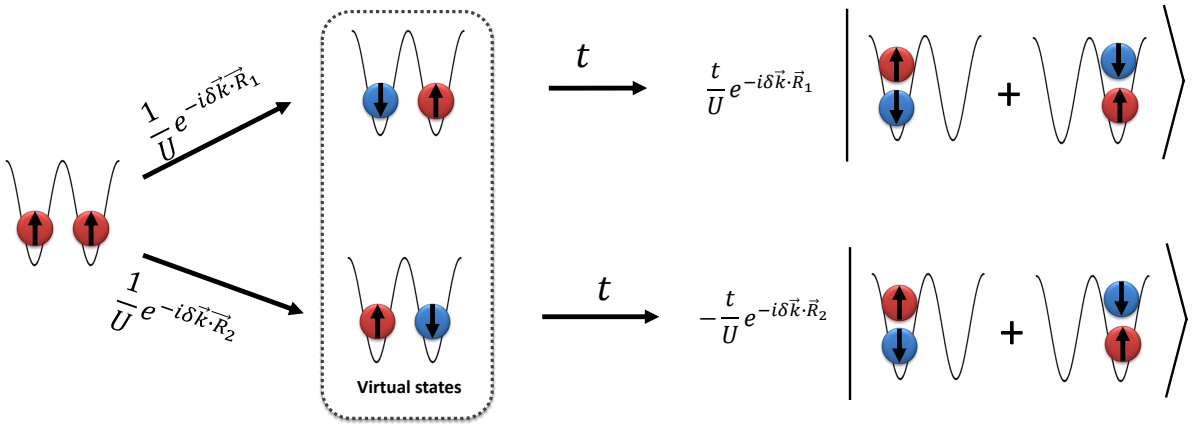

Figure 5.2: A schematic diagram showing CSFT for a two-site two-fermion system. CSFT happens as a two-step process via a virtual state. Two possible channels between the initial state $|\uparrow,\uparrow\rangle_W$ and the final state $|\uparrow\downarrow,0\rangle_W + |0,\uparrow\downarrow\rangle_W$ happen simultaneously, but with amplitudes carrying opposite signs. The probability to observe a doublon-hole pair is affected by interference between these channels.

5.2.2 Differences compared with previous approaches

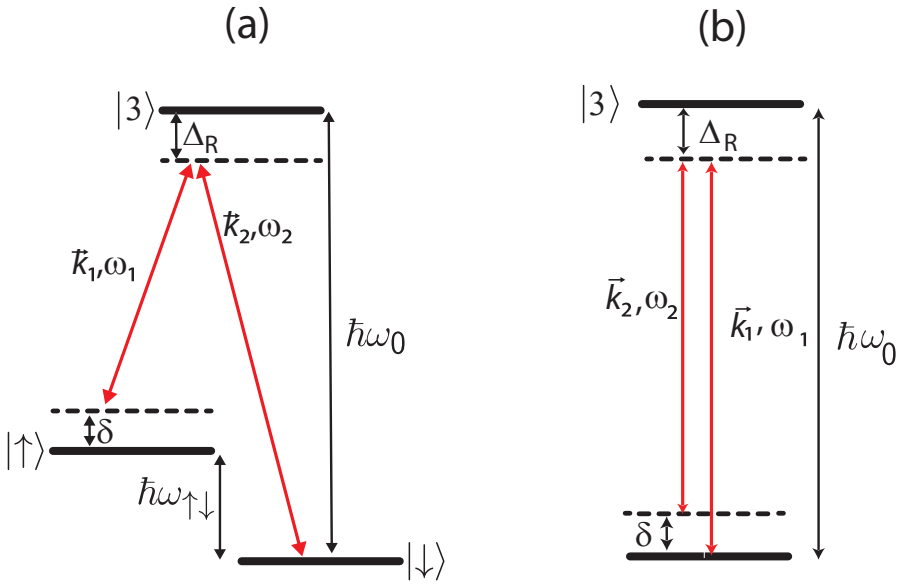

Figure 5.3: Λ three-level system involving a final state with (a): different m_F and (b): same F and m_F as the initial state. A unitary transformation exists for case (a) such the Hamiltonian becomes time-independent, while for (b), the final Hamiltonian is still time-dependent.

The spin-flip process distinguishes our approach from previous experiments [26, 140]. As have discussed

in Chapter 2, in the rotating frame and after a unitary transformation $\hat{U}$ with

$$\hat{U} = \begin{pmatrix} e^{-i\delta t} & 0 & 0 \\ 0 & 1 & 0 \\ 0 & 0 & e^{i\Delta_R t} \end{pmatrix}, \tag{5.13}$$

the Hamiltonian for our system, which includes two ground states with different magnetic quantum numbers (Fig. 5.3(a)), is:

$$H_R^{\text{2-level}} = \begin{pmatrix} \delta + \frac{\Omega_1^2 - \Omega_2^2}{4(\Delta_R+\delta)} & \frac{\Omega_1^*\Omega_2^*}{8}(\frac{1}{\Delta_R} + \frac{1}{\Delta_R+\delta})e^{-i\delta\vec{k}\cdot\vec{R}} \\ \frac{\Omega_1^*\Omega_2^*}{8}(\frac{1}{\Delta_R} + \frac{1}{\Delta_R+\delta})e^{i\delta\vec{k}\cdot\vec{R}} & 0 \end{pmatrix} \approx \begin{pmatrix} \delta + \frac{\Omega_1^2 - \Omega_2^2}{4\Delta_R} & \frac{\Omega}{2}e^{-i\delta\vec{k}\cdot\vec{R}} \\ \frac{\Omega^*}{2}e^{i\delta\vec{k}\cdot\vec{R}} & 0 \end{pmatrix} \tag{5.14}$$

which is time-independent. In other words, there exists a unitary transformation that eliminates the time dependence.

In some previous experimental approaches (such as in Ref. [26]), stimulated Bragg transitions are used to couple two states with the same F and m_F, as shown in Fig. 5.3(b). In this case, the Hamiltonian is

$$H_R = \hbar \begin{pmatrix} 0 & \Omega_1^* \cos(\vec{k_1}\cdot\vec{R} - \omega_1 t) + \Omega_2^* \cos(\vec{k_2}\cdot\vec{R} - \omega_2 t) \\ \Omega_1 \cos(\vec{k_1}\cdot\vec{R} - \omega_1 t) + \Omega_2 \cos(\vec{k_2}\cdot\vec{R} - \omega_2 t) & \omega_0 \end{pmatrix}. \tag{5.15}$$

After a unitary transformation $\mathcal{U} = \begin{pmatrix} 1 & 0 \\ 0 & e^{i\hbar\omega_1 t} \end{pmatrix}$, we have

$$H_R = \hbar \begin{pmatrix} 0 & \frac{\Omega_1^*}{2}e^{-i\vec{k_1}\cdot\vec{R}} + \frac{\Omega_2^*}{2}e^{-i\vec{k_2}\cdot\vec{R} - it\delta} \\ \frac{\Omega_1}{2}e^{i\vec{k_1}\cdot\vec{R}} + \frac{\Omega_2}{2}e^{i\vec{k_2}\cdot\vec{R} + it\delta} & \Delta_R \end{pmatrix}. \tag{5.16}$$

This Hamiltonian is still time-dependent. By diagonalizing this Hamiltonian, we find that the energy of the ground state is

$$E_g(r) = -\frac{\Omega_1^2 + \Omega_2^2}{4\Delta_R} - \frac{\Omega_1\Omega_2^*}{2\Delta_R}\cos[\delta t + \vec{R}\cdot\delta\vec{k}], \tag{5.17}$$

which contains a time-dependent term, and where $\frac{\Omega_1\Omega_2^*}{2\Delta_R} \equiv \Omega$ is the effective Rabi rate. In this case, the effect of stimulated Bragg transitions can be treated as a moving lattice potential. Transforming to the interacting picture with respect to $\mathcal{U}(t) = e^{i\int_0^t dt' H_R(t')}$ causes a first kind Bessel function $J_0(\hbar\Omega/U)$ to appear in operators like c_i, because of the cosine term in the integral. Therefore, the effective correlated

tunneling induced by this scheme is proportional to $J_0(\hbar\Omega/U)$, which is a non-linear function of Ω. For more details regarding the theoretical derivation, see Ref. [141]. On the contrary, in our approach, the amplitude of the effective tunneling depends linearly on Ω.

5.3 Spectroscopic proof for light-assisted tunneling

As illustrated in Fig. 5.1, one way to observe CSFT is to tune the frequency difference $\Delta\omega = \omega_1 - \omega_2$ between the Raman beams near to the $|\uparrow\rangle \rightarrow |\downarrow\rangle$ resonance. By measuring the number of atoms in each spin state after a Raman pulse as $\Delta\omega$ is scanned, CSFT events can be distinguished from on-site spin-flip event. We had to overcome several technical challenge to use this approach to resolve CSFT.

5.3.1 Experimental and technical challenges

Degeneracy of Raman transitions

For our standard experimental sequence, the magnitude of the quantization magnetic field, provided by a pair of coils (the imaging coils) can be up to 4.5G. The corresponding second-order Zeeman energy splitting ($E_{m_F=9/2\rightarrow 7/2} - E_{m_F=7/2\rightarrow 5/2}$) is approximately 3.1kHz, comparable to the Rabi rate of the Raman transitions. Therefore, after atoms are transferred to the $m_F = 7/2$ state when $\Delta\omega$ sweeps across $\omega_{\uparrow\downarrow}$, Raman transitions to states with $m_F < 7/2$ (Fig. 5.4) occur, which is not desirable.

Moreover, in this regime, the second-order Zeeman energy splitting is comparable to the on-site interaction U for a lattice depth of approximately $10E_R$. Raman transitions can drive multiple processes at the same time because of this degeneracy. For example, the transition frequency for a singlon (*i.e.*, one lattice site occupied by one atom) with $m_F = 9/2$ to $m_F = 7/2$ is nearly degenerate with the transition between a doublon pair consisting of an $m_F = 9/2$ and an $m_F = 7/2$ atom and two singlons with $m_F = 9/2$ and $m_F = 5/2$ (inset of Fig. 5.5). Therefore, it is challenging to distinguish each process.

Since this Raman transition degeneracy hinders a clear signal, a larger magnetic field is required to lift the degeneracy of Zeeman transitions between different m_F states. Our imaging quantization coils cannot operate high enough current. Instead, we use the anti-gravity coil mounted closer to the atoms, to create a $13G$ magnetic field, thereby providing a 27kHz difference between the $m_F = 9/2 \rightarrow m_F = 7/2$ and $m_F = 7/2 \rightarrow m_F = 5/2$ transitions (blue arrow in Fig. 5.4). Although the anti-gravity coil applies a force to the atoms due to the magnetic gradient, the in-trap position of the atoms changes less than 10μm at our operating current. Because the beam waist of the optical dipole trap, optical lattice, and Raman beams are larger than 100μm, the 10μm position shift is acceptable for our measurements. With this $13G$ magnetic

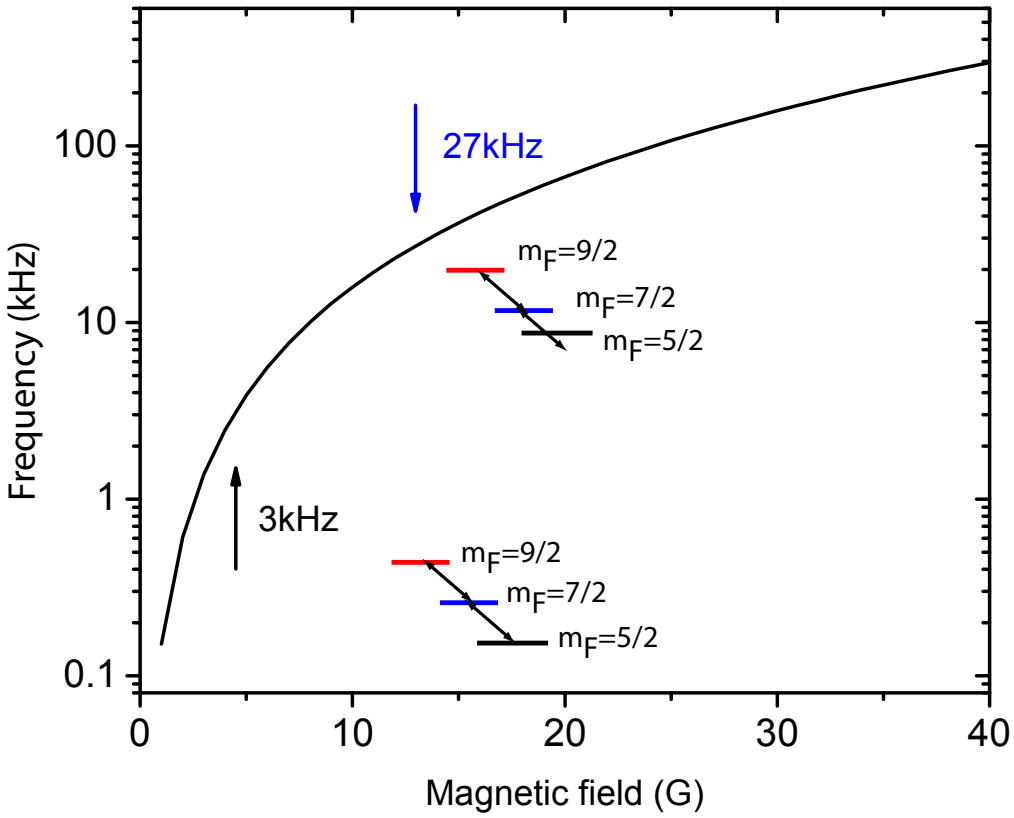

Figure 5.4: The energy difference between the $E_{m_F=9/2} - E_{m_F=7/2}$ and $E_{m_F=7/2} - E_{m_F=5/2}$ transition. The magnetic field provided by the imaging coil can not be larger than $4.5G$ (black arrow). At this magnetic field, the 3kHz energy difference is not big enough to lift the degeneracy of Raman transitions, and states with smaller m_F are populated. To avoid this, we worked at $B = 13G$ (blue arrow).

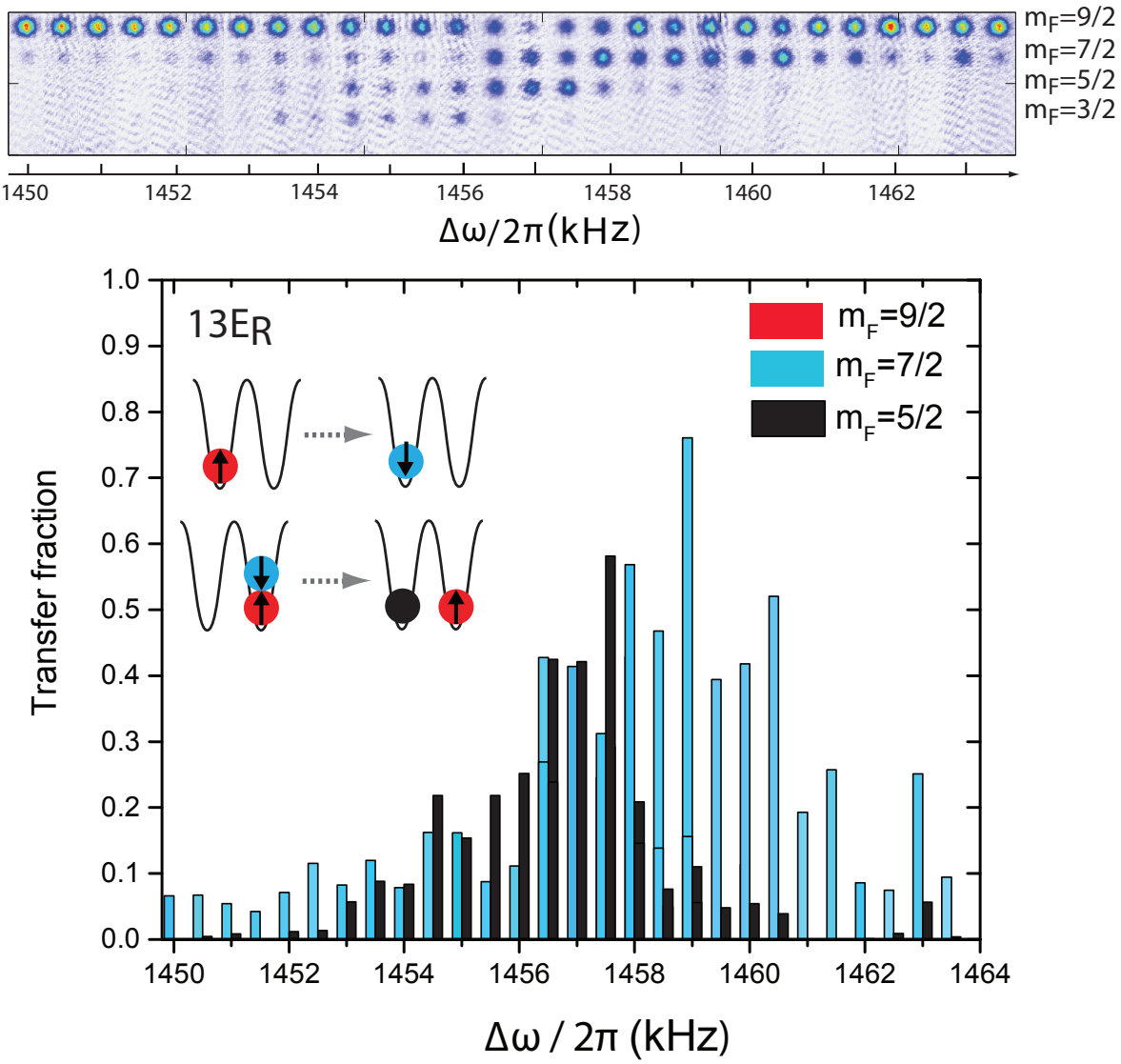

Figure 5.5: Raman spectroscopy at $s = 13E_R$ with a $4.5G$ magnetic field. Starting with a spin-polarized $|m_F = 9/2\rangle$ gas, the transfer fraction to $|m_F = 7/2\rangle$ and $|m_F = 5/2\rangle$ states is plotted as $\Delta\omega$ is swept across a range near $\omega_{\uparrow\downarrow}$. Because of the small second-order Zeeman energy shift, transfer to the $m_F = 5/2$ state is evident. In addition, CSFT and on-site spin-flip events can happen at the same time due to the degeneracy (the inset shows an example), complicating interpretation of the data and hindering an unambiguous signal of CSFT. The top panel shows the spin-resolved time-of-flight imaging as $\delta\omega$ is scanned.

field, no significant population of $m_F = 5/2$ states after applying Raman pulses has been observed within the frequency range we sample.

Magnetic field stability

The stability of the magnetic field produced by the anti-gravity coil is not as good as the imaging coil. To measure the magnetic field stability, we apply a microwave-frequency magnetic field pulse, which transfers atoms from the $|F = 9/2, m_F = 9/2\rangle$ state to the $F = 7/2$ manifold. Using microwave transitions to calibrate the $\vec{B}$ stability helped to isolate the magnetic field noise from possible Raman noise. Also, microwave transitions between hyperfine states is more sensitive to magnetic noise. The lineshape of this transition is measured via the transfer fraction to $F = 7/2$ state at various microwave frequencies. To determine the magnetic field stability, we fix the microwave frequency away from the resonance, roughly to where the transfer fraction is half of the peak value. The large slope of this frequency maximizes the sensitivity to magnetic field. By repeating the same microwave pulse many times, we can estimate the magnetic fluctuation from the standard deviation of the transfer fraction to the $F = 7/2$ state.

Comparison between Fig. 5.6(a) and (b) reveals the large fluctuations of the magnetic field generated by the anti-gravity coil, which limits the frequency resolution for Raman spectroscopy to 4.7kHz. The on-site interaction energy U for the lattice depths used in this work ranges from $h \times 3.5$kHz to $h \times 5.4$kHz. Therefore, the magnetic field noise prevented spectroscopically resolving CSFT from on-site spin-flips.

To solve this problem, we changed the servo for the anti-gravity coil to the circuit described in Chapter 2. Fig. 5.6(c) shows a factor of 5 improvement in magnetic field stability after using the new servo circuit. A 3mG fluctuation in magnetic field allows us to have a frequency resolution below 1kHz, which is sufficient for detecting CSFT.

5.3.2 Number loss during Raman transitions

Number loss and heating have been observed to be caused by the Raman pulse. The red circles in Fig. 5.7(a) plot the number of atoms remaining in the $F = 9/2$ manifold for different Raman pulse times. The number loss is accompanied by heating. Fig. 5.7(b) shows the increase in the size of gas for longer Raman pulse times. With the Raman beams on, spontaneous Raman transitions transfer atoms from the $F = 9/2$ to the $F = 7/2$ manifold. The black circles in Fig. 5.7(a) plot the increasing number of atoms in the $F = 7/2$ state. Collisions between $F = 7/2$ and $F = 9/2$ atoms lead to heating and number loss. To fully avoid this problem, we would have to further detune the Raman frequency from the D1 transition, which is beyond the tunablity range of our diode laser.

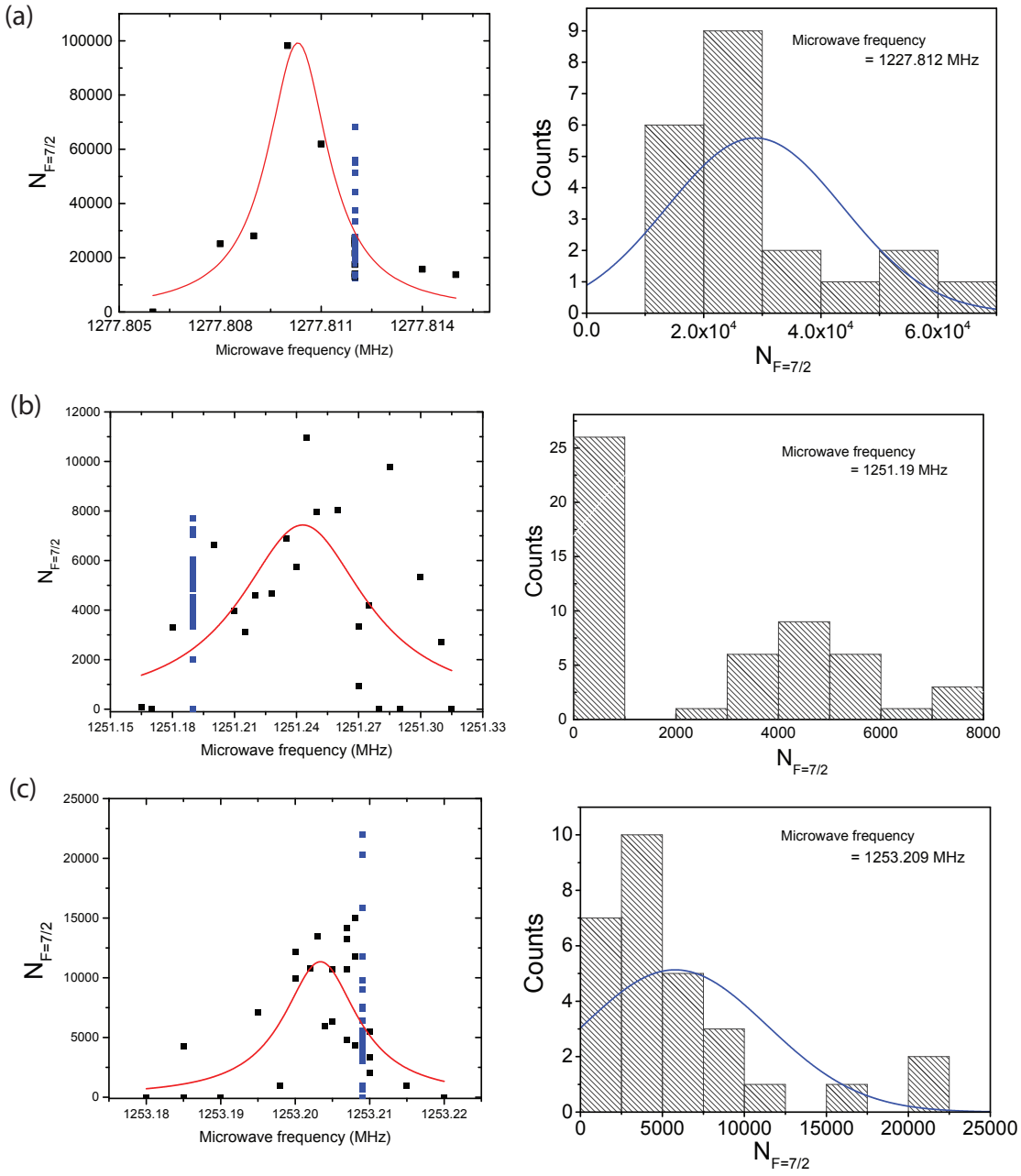

Figure 5.6: Calibration of the magnetic field stability by transferring atoms from $|F = 9/2, m_F = 9/2\rangle$ to the $|F = 7/2\rangle$ manifold by a microwave-frequency magnetic field pulse. The plots in the left column shows the lineshape of the microwave transition, and the right column shows histograms for transferred number of atoms at fixed microwave frequency. The fluctuation in magnetic field can be inferred via the standard deviation of the number measured at fixed microwave frequency and the lineshape. (a): Without the anti-gravity coil on and a 0.5ms microwave pulse, the linewidth of this transition is about 2.2kHz. This is limited by the pulse time. From the standard deviation of number, the estimated magnetic fluctuation is less than 1mG. (b): The old servo circuit had poor stability. The width of microwave transition lineshape is broader than (a) by a factor of 50. The estimated $|\vec{B}|$ stability is about 15mG, corresponding to a frequency resolution of 4.7kHz. (c): After modifying the current servo circuit for the anti-gravity coil, the magnetic field stability is significantly improved. The hourly stability is about 3mG.

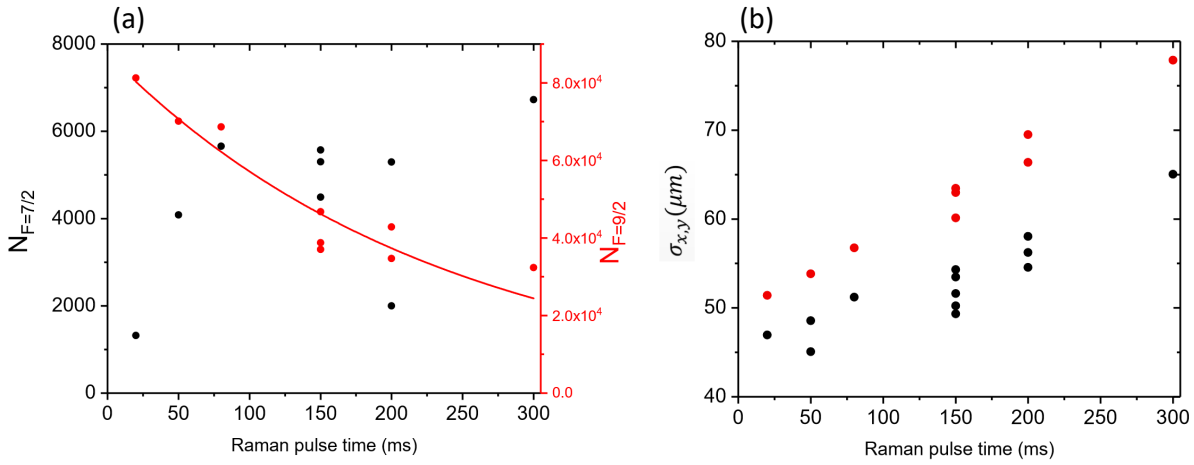

Figure 5.7: Number loss and heating during the Raman pulse. (a): The total number of atoms in the $|\uparrow\rangle$ and $|\downarrow\rangle$ states (red circle) decays with longer Raman pulse time. The red curve is a fit to an exponential decay function, with a decay time 235 ± 30ms. The number of atoms in the $F = 7/2$ manifold (black circle) increases with the Raman pulse time, and reaches a quasi-steady state after ~ 150ms. (b): The size of the gas at various Raman pulse times (red circle: σ_x; black circle: σ_y). The heating and the number loss are due to the collisions between the $F = 9/2$ and $F = 7/2$ atoms. The frequency difference between the Raman beams is fixed for this measurement.

5.3.3 Detecting CSFT with Raman spectroscopy

After lifting the second-order Zeeman degeneracy and using a higher performance current-servo circuit, we spectroscopically resolved CSFT and distinguished it from on-site spin rotations by measuring the change in spin fraction after a Raman pulse. In this work, the Raman beams are 80GHz detuned from the D1 transition. The frequency and power of each beam are controlled using an acousto-optic modulator.

Sample data are shown in Fig. 5.8(a) for the fraction $f_{\downarrow,\uparrow}$ of atoms transferred between spin states at varied $\Delta\omega$ for $s = 10E_R$ (with $t = 0.0192E_R$ and $U = 0.489E_R$). To observe the relative slowly CSFT process, the Raman pulse is 50ms long. The carrier transition, with Rabi rate $\Omega = (2\pi)650$Hz is therefore over driven. This results in a broad feature that obscures CFST: when $\Delta\omega - \omega_{\uparrow\downarrow} \approx \pm U/\hbar$, atoms undergo both detuned carrier spin-flip transitions and resonant CSFT. To overcome this complication and isolate CSFT, we subtract the data taken at identical $\Delta\omega$ with opposite initial spin configurations. Since the carrier frequency does not depend on the initial state, the contribution from the broad carrier feature is cancelled out by this procedure. In contrast, the frequency offset of the CSFT sideband changes sign with the initial spin configuration and is not removed by the subtraction. The resulting lineshape for $f_\uparrow - f_\downarrow$ shown in Fig. 5.8(b) therefore reveals the CSFT sidebands as peaks offset at approximately $\pm U \approx \pm 3.5$kHz from the carrier transition.

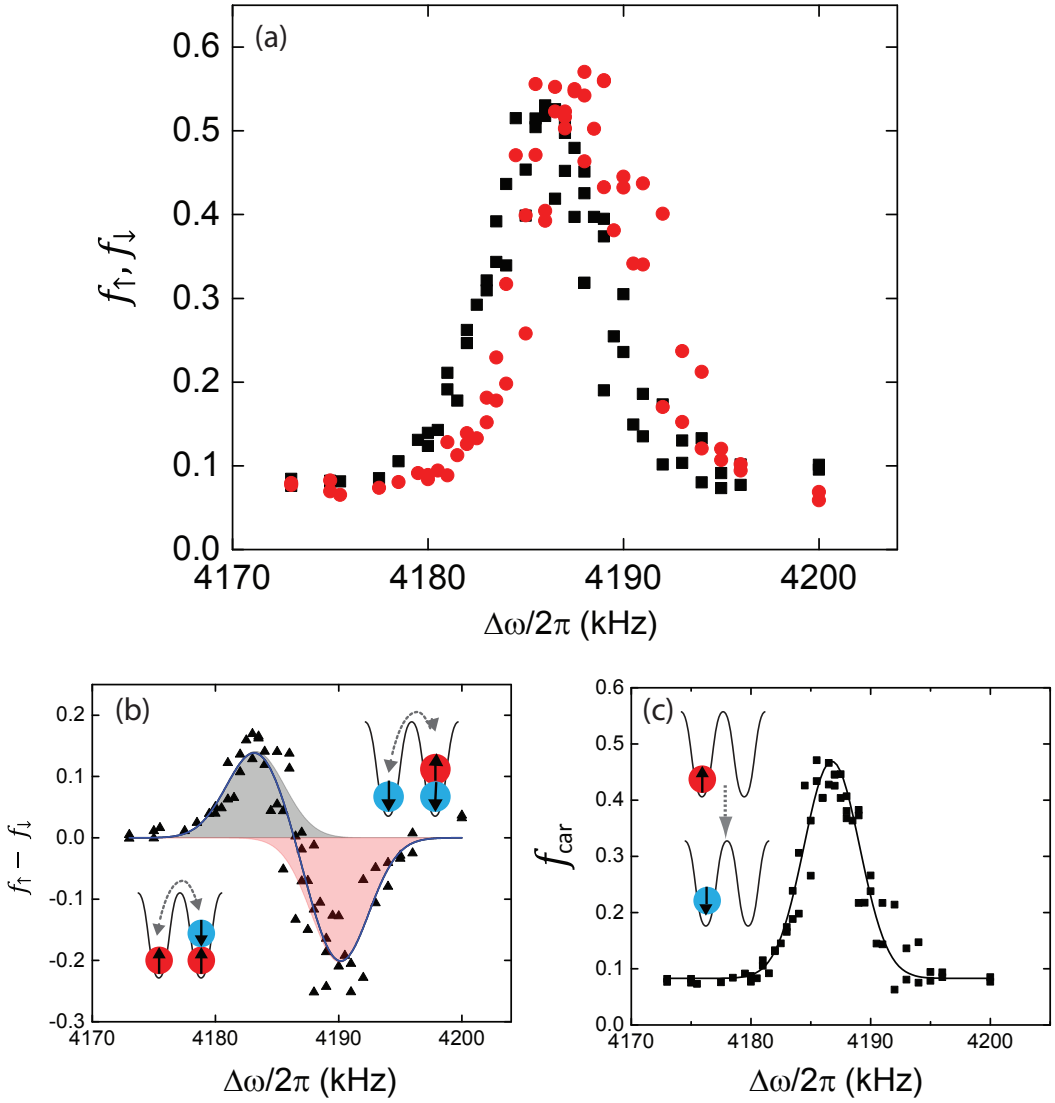

Figure 5.8: CSFT Spectroscopy. (a): The fraction of atoms transferred between spin states by a 50ms Raman pulse is shown for an initially $|\uparrow\rangle$ (black squares, $f_\uparrow$) and $|\downarrow\rangle$ (red circles, $f_\downarrow$) spin polarized state at $s = 10E_R$ for varied $\Delta\omega$. For these measurements, $N = 25400 \pm 3900$ atoms were cooled to $T/T_F = 0.24 \pm 0.08$ before turning on the lattice. (b): The difference $f_\uparrow - f_\downarrow$ for pairs of points in (a) reveals the CSFT sidebands at approximately $\pm U$. The black line shows a fit to a sum of two Gaussian functions; the individual Gaussians are displayed as shaded regions. The peak at lower (higher) frequency corresponds to CSFT for an initially $|\uparrow\rangle$ ($|\downarrow\rangle$) spin-polarized state. (c): The carrier feature inferred by subtracting CSFT sidebands from $f_\uparrow + f_\downarrow$. The width of this feature is 2.3KHz, which approximately equals to $12t$.

The predicted separation between the CSFT peaks equals to twice of the on-site interactions U. To compare our measurements with this prediction, we fit the $f_\uparrow - f_\downarrow$ lineshape to a sum of two Gaussian functions with independent central frequencies and standard deviations as free parameters. The black and red shaded regions in Fig. 5.8(b) show the individual fits to a CSFT event $|\uparrow,\uparrow\rangle \rightarrow |0,\uparrow\downarrow\rangle$ and $|\downarrow,\downarrow\rangle \rightarrow |0,\uparrow\downarrow\rangle$, respectively. Fig. 5.8(c) plots the inferred carrier spectroscopy by subtracting the two fitted Gaussian functions of CSFT sidebands from $f_\downarrow + f_\uparrow$. The width of carrier feature is 2.3kHz, and peak value is 0.5 due to decoherence caused by spontaneous Raman scattering.

The interaction energy U determined from this fit, which is half of the frequency separation of the peaks, is shown in Fig. 5.9 for data taken at different lattice potential depths. The inferred U increases less rapidly with s than the tight-binding prediction, which is shown as a dashed line. The slope for the measured U vs. E_R is (0.22 ± 0.1)kHz$/E_R$, which is 40% smaller than the predicted slope 0.368kHz$/E_R$. Renormalization of U by the Raman process (Section. 5.7) and effects from higher bands [143] may contribute to this discrepancy.

5.3.4 A simple simulation

We perform a simple simulation for the dependence of $f_\uparrow$ and $f_\downarrow$ on $\Delta\omega$ based on the Rabi formula. The transfer fraction to the other spin component is calculated by integrating:

$$f_{\uparrow(\downarrow)} = \int d^3\vec{q} \int d^3\vec{r} [0.5P(\Delta_c, \Omega_c) f(\vec{r},\vec{q}) + 0.5P(\Delta_{\mathrm{CSFT}}, \Omega_{\mathrm{CSFT}}) f(\vec{r},\vec{q})] \,, \tag{5.18}$$

with

$$\begin{aligned}
\Delta_c &= \hbar\omega_{\uparrow\downarrow} \mp \left[\epsilon(\vec{q}+\delta\vec{k}) - \epsilon(\vec{q})\right] - \hbar\Delta\omega, \\
\Delta_{\mathrm{CSFT}} &= \hbar\omega_{\uparrow\downarrow} \mp \left[\epsilon(\vec{q}+\delta\vec{k}) - \epsilon(\vec{q})\right] \mp U - \hbar\Delta\omega, \\
\epsilon(\vec{q}) &= 2t\left[3 - \cos(\frac{q_x}{\hbar}d) - \cos(\frac{q_y}{\hbar}d) - \cos(\frac{q_z}{\hbar}d)\right], \\
f(\vec{r},\vec{q}) &= \frac{1}{e^{\beta(\epsilon(\vec{q})+V(\vec{r})-\mu)}+1}, \\
P(\Delta,\Omega) &= \frac{\Omega^2}{\Omega^2+\Delta^2}.
\end{aligned}$$

Δ_c and Δ_{CSFT} are the detunings for the carrier and CSFT transitions respectively. The change in energy before and after the Raman transition because of the momentum shift is included in $\epsilon(\vec{q}+\delta\vec{k}) - \epsilon(\vec{q})$. In the expressions for Δ_c and Δ_{CSFT}, the "$-$" sign is for $f_\uparrow$, and "$+$" is for $f_\downarrow$.

For $s = 4E_R$ (Fig. 5.10(a)), conventional on-site spin-flip event dominates, and the peak positions of $f_\uparrow$ and $f_\downarrow$ are separated by $\sim 4t$. This is because the distribution of $\epsilon(\vec{q}+\delta\vec{k}) - \epsilon(\vec{q})$ centers around $2t$.

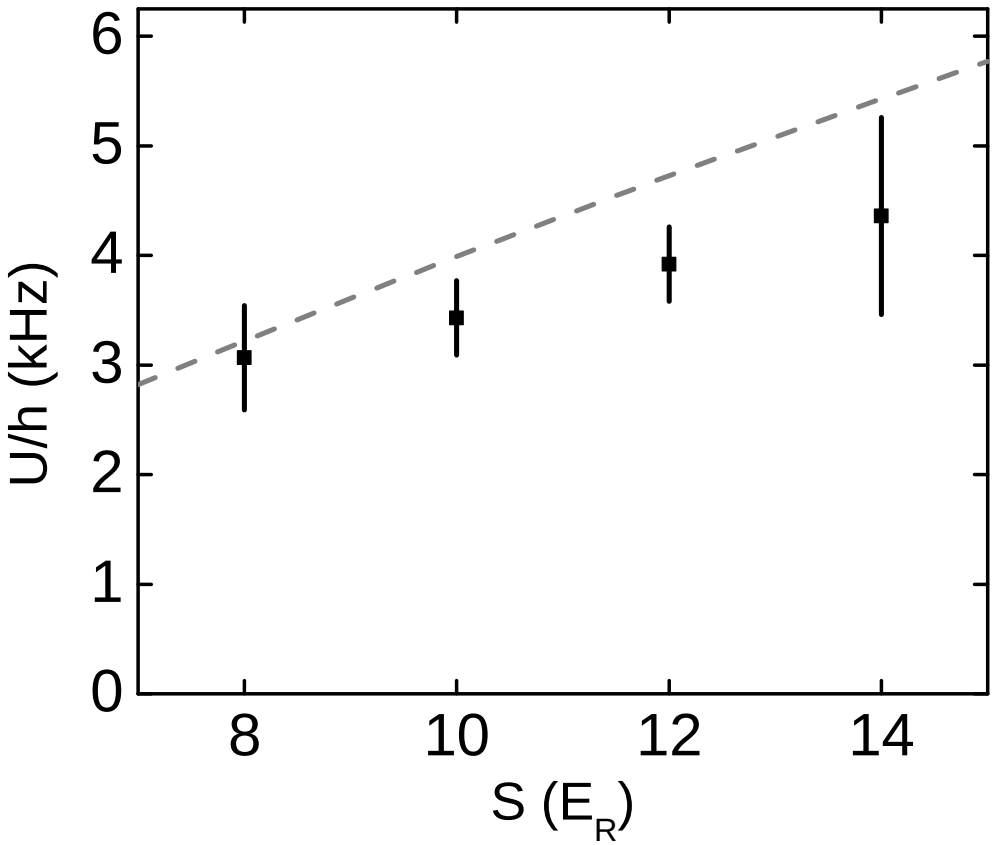

Figure 5.9: The interaction energy U inferred from fits to data such as those shown in Fig. 5.8 for varied s. The error bars are derived from the fit uncertainty. The gray dashed line is the predicted U based on the tight-binding model.

Experimental measurements for $s = 4E_R$ also show this separation. With increasing lattice depth s, the rapid decrease in t suppresses the separation between two carrier features, and $\omega_c \approx \omega_{\uparrow\downarrow}$. Peaks corresponding to CSFT events appear in Raman spectroscopy. Therefore, our procedure to infer CSFT event from $f_\downarrow - f_\uparrow$ is appropriate.

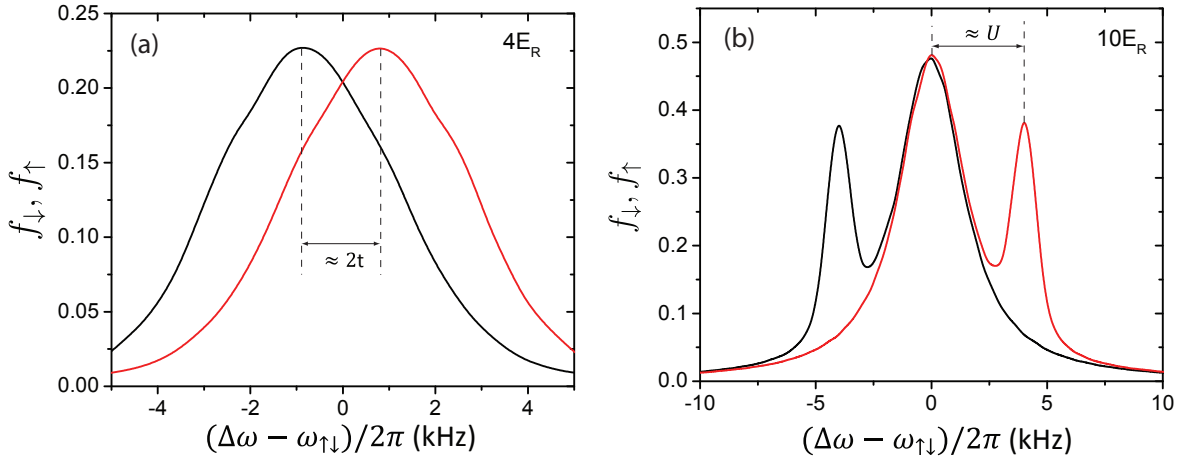

Figure 5.10: Simulation of $f_\uparrow$ (black) and $f_\downarrow$ (red) at various $\Delta\omega - \omega_{\uparrow\downarrow}$ for (a) $s = 4E_R$ and (b) $s = 10E_R$. In this simulation, $\Omega_c = 0.4 \times U/\hbar$ and $\Omega_{\mathrm{CSFT}} = 0.08 \times U/\hbar$, which are chosen to approximately match the measured transfer fractions. At low lattice depth, the separation between $f_\uparrow$ and $f_\downarrow$ is related to the momentum change during stimulated Raman transitions, and roughly equals to $\epsilon(\delta\vec{k}) - \epsilon(0) \approx 2t$. At high lattice depth, $t \ll U$, such separation becomes negligible. Therefore, the difference between $f_\uparrow$ and $f_\downarrow$ is dominated by CSFT event.

5.4 Direct doublon fraction measurements using light-assisted collisions

5.4.1 Light-assisted collisions

Each CSFT event for a spin-polarized gas is accompanied by the creation of a doublon-hole pair. To directly probe doublon generation, we measure the number loss induced by light-assisted collisions (LAC). LAC has been applied to prepare unit filling in microscopic dipole traps [144], optical lattices [145], and optical tweezers [146]. In addition, LAC provides the basis for parity imaging in quantum-gas microscopes [147]. The basic conception of LAC is shown in Fig. 5.11. The laser light used for LAC couples the electronic ground state $|S\rangle$ to the $|P\rangle$ state. An atom in an $|S\rangle$ state and an atom in a $|P\rangle$ state can form a loosely bound pair, with a long-range dipole-dipole interaction between them. If the LAC light is blue-detuned (left figure of Fig. 5.11), then the $|S + P\rangle$ state experiences a repulsive potential. If the associated kinetic energy

given by LAC light during this transition is larger than the trap potential, this bound pair leaves the trap. For the red-detuned case, $|S+P\rangle$ experiences an attractive potential. This pair can gain a large kinetic energy, leading to the loss of both atoms.

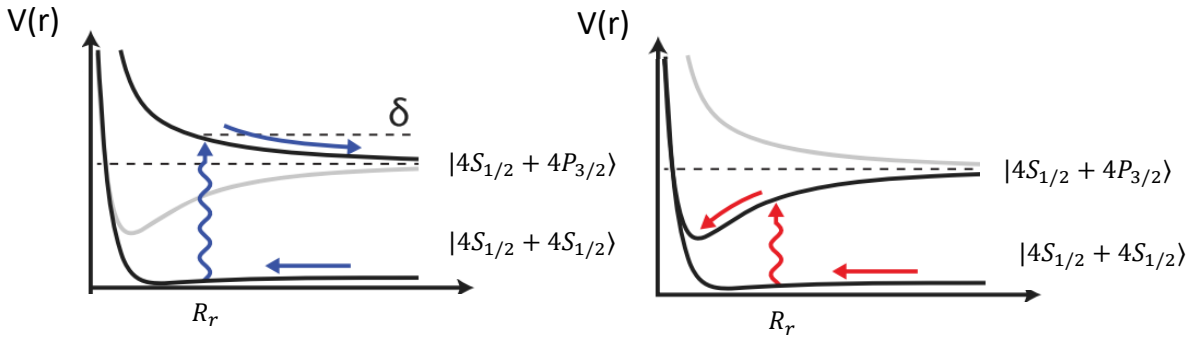

Figure 5.11: A schematic diagram showing the conception of light-assisted collisions for the blue-detuned light (left) and red-detuned light (right). At interatomic separations R_r, the ground state $|S_{1/2}+S_{1/2}\rangle$ becomes resonant with excitation to a loosely bound pair with one atom in the S state and another in the P state. The pair of atoms can gain large kinetic energy during this transition and leave the trap, leading to loss. This figure is adapted from Ref. [146].

If two atoms occupy the same lattice site, their wavefunctions are highly overlapped, and LAC causes them to be lost from the trap. Therefore, by measuring the rapid number loss induced by LAC, we can measure the fraction of doubly occupied sites. Although this procedure is conceptually simple, it seems optimizing of relevant parameters for for the light such as detuning and intensity lacks a well developed routine [148], and a patient search is required. The goal of the optimization is to separate the timescale of the two-body loss due to LAC and the timescale of the one-body loss due to heating from light scattering. However, changing the detuning and the intensity of the light change both simultaneously. It is important to check the light parameters with a band insulator (with a high fraction of doubly occupied sites) and a spin-polarized gas (with no doubly occupied site), to ensure these two timescales are well separated.

For measurements in this chapter, the LAC light is 50MHz blue-detuned from the $|F=9/2, m_F=9/2\rangle$ to $|F'=11/2, m_F=11/2\rangle$ transition. As a verification of the chosen parameters, we performed LAC measurements for two-component fermions in the band insulator regime (Fig. 5.12(a)) and a spin-polarized gas in the metallic regime (Fig. 5.12(b)). For the band insulator, the decay of the total atom number shows two loss timescales. The lost on a fast timescale corresponds to LAC removing atoms from doubly occupied sites, while the decay over a slower timescale results from single atoms ejected from the dipole trap via

heating because of spontaneous scattering. In contrast, for the spin-polarized lattice gas, for which the Pauli exclusion principle forbids the population of doubly occupied sites, only a slow decay process appears.

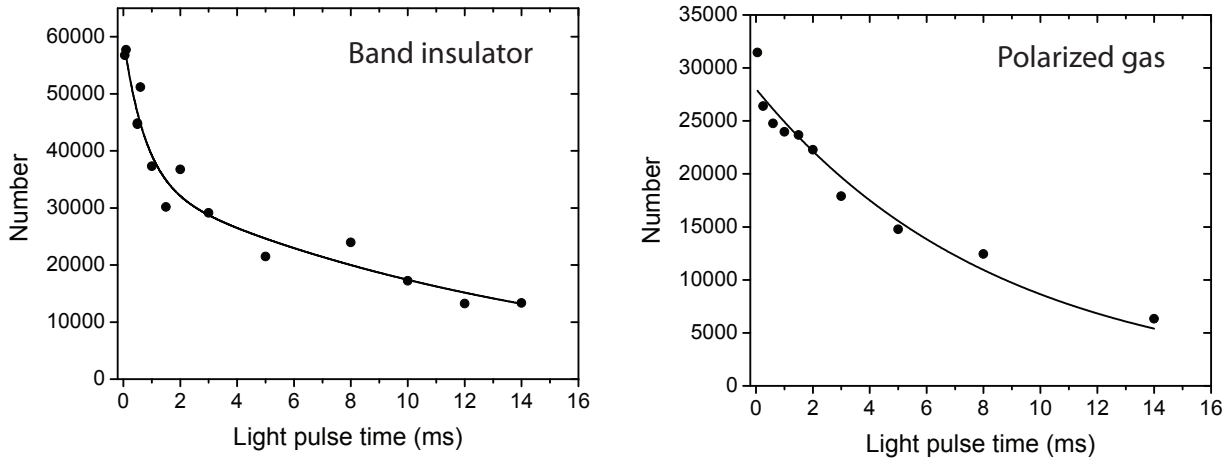

Figure 5.12: Number of remaining atoms after various duration of a near-resonant light pulse. (a): Two-component Fermi gas at $s = 4E_R$. The decay curve shows two timescales: a fast initial loss ($\tau_1 = 0.77 \pm 0.34$)ms due to LAC between atoms residing on the same lattice sites, and a slow decay due to heating ($\tau_2 = 14.5 \pm 4.2$)ms. The black line is a fit to $A_1 e^{-t/\tau_1} + A_2 e^{-t/\tau_2}$. (b): Spin-polarized Fermi gas at $s = 4E_R$. Since the Pauli exclusion principle forbids a lattice site from being occupied by two identical fermions, the short-timescale decay is absent. A fit to $A_2 e^{-t/\tau_2}$ gives ($\tau_2 = 5.9 \pm 0.6$)ms (black curve). The difference in the slow decay timescale between (a) and (b) is due to the different final optical trap depth: to access a band insulator state, a tighter confinement is required.

5.4.2 Experimental measurements of double occupancy

For measuring the population of doublons created by CSFT, we prepare a $|\uparrow\rangle$ gas with $N \approx 64000$ atoms and $T/T_F \approx 0.25$ before adiabatically loading them into an $s = 10E_R$ lattice. The carrier frequency $\omega_{\uparrow\downarrow}$ is located using Raman spectroscopy with a 0.7ms Raman pulse, which is too short to drive CSFT. A gaussian fit to this Raman spectroscopy measurements gives $\omega_{\uparrow\downarrow}$ with only few experimental cycles. Fig. 5.13 shows the procedure for double occupancy measurements. After the Raman pulse, the lattice depth is rapidly enhanced to $s = 29E_R$ (with $\hbar/t \approx 50$ms) to freeze any further dynamics. Also, the anti-gravity coil is ramped off, such that the direction of the magnetic field is along the propagation direction of the LAC light to guarantee a σ^+ polarization for driving the $|F = 9/2, m_F = 9/2\rangle \rightarrow |F' = 11/2, m_F = 11/2\rangle$ transition. The repump light is turned on during the LAC stage to bring atoms populated in the $F = 7/2$ state because of spontaneous Raman scattering back to the $F = 9/2$ state.

Fig. 5.14 plots sample data for LAC measurements with Raman frequency $(\Delta\omega - \omega_{\uparrow\downarrow})/2\pi = 3.5$kHz, which corresponds to the measured $+U$ CSFT sideband. Two loss processes are evident as the duration of

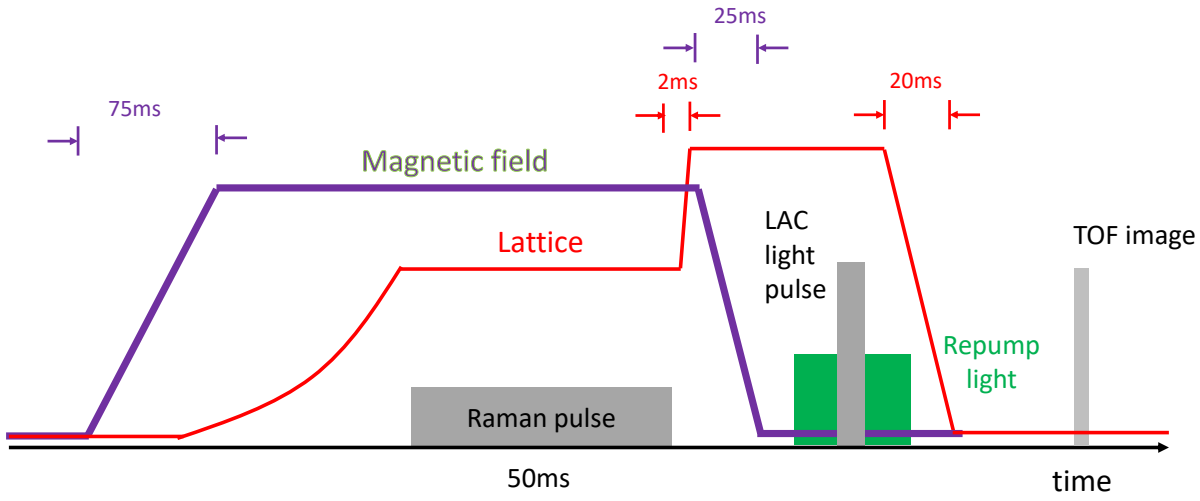

Figure 5.13: Sequence of the double occupancy measurements with light-assisted collisions. Magnetic field (green line) increases to 13G before lattice loading. Lattice (red line) is ramping to $10E_R$ in 100ms. A Raman driving field is on for 50ms, during which CSFT event happens and creates doublon-hole pair. Lattice is jumped to $29E_R$ to arrest further dynamics, before the double-occupation measurements via an LAC light pulse. Finally, a time-of-flight fluorescence imaging is taken to obtain the atom number.

the LAC pulse is changed. These data are fit to a double exponential decay function $N(t) = N_D e^{-t/t_1} + (N - N_D)e^{-t/t_2}$, with N, N_D, t_1, and t_2 as free parameters. The fraction of doubly occupied sites is determined as $D = N_D/N$.

Repeating this procedure at different $\Delta\omega$ gives the dependence of D on the Raman detuning. We find that a resonance feature for doublon creation is centered near the CFST spectroscopy sideband peak at $\Delta\omega - \omega_{\uparrow\downarrow} = \frac{U}{\hbar}$ (Fig. 5.15). Although the Raman pulse remains on for a time period much longer than the tunneling timescale, processes such as removing one atom from a doubly occupied site to a nearby empty site due to the tight-binding t term are significantly suppressed due to the energy mismatch. Hence, it is reasonable to conclude that the population of doubly occupied sites are all created via CSFT events. The data in Fig. 5.15 are compared with the fit from Fig. 5.8 to $|f_\uparrow - f_\downarrow|$, which can be interpreted as the fraction of atoms that flip their spin during CSFT. The close agreement between D and the fit imply that each spin-flip is associated with the creation of a doubly occupied site.

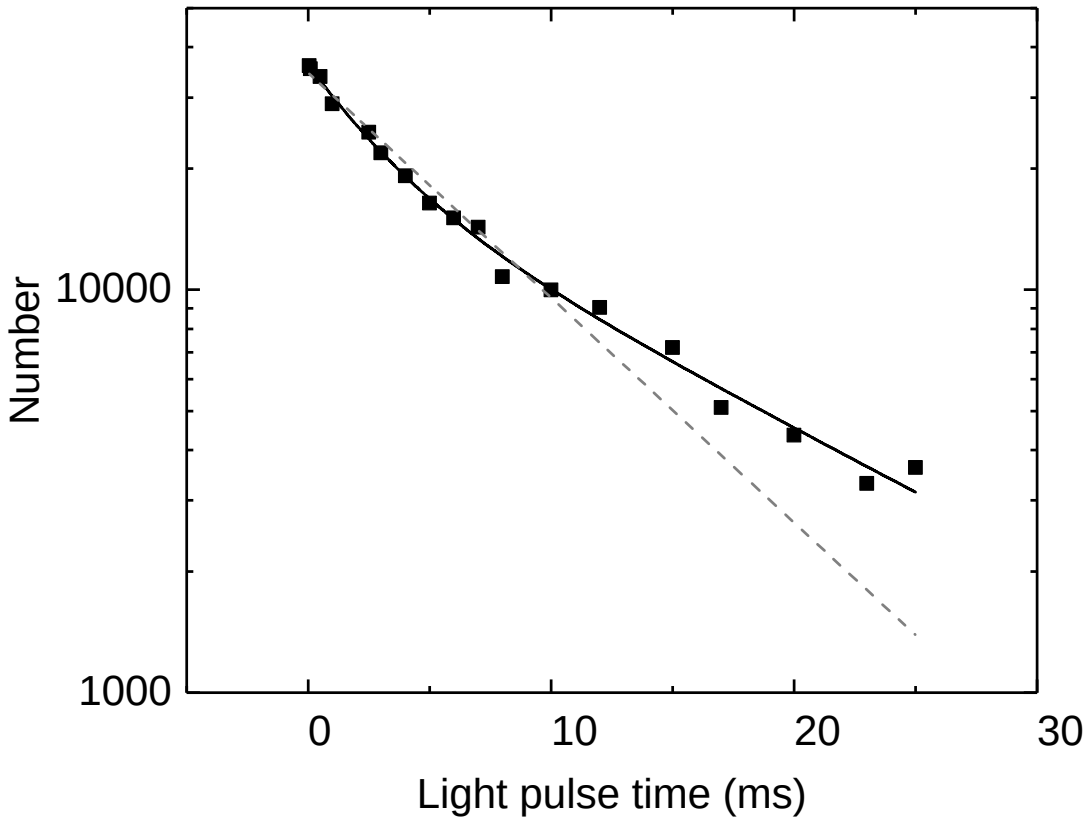

Figure 5.14: Sample data showing the LAC-induced number decay after a 50ms Raman pulse with $(\Delta\omega - \omega_{\uparrow\downarrow})/2\pi = 3.5$kHz at $s = 10E_R$. The data are fit to a double exponential decay function $N(t) = N_D e^{-t/t_1} + (N - N_D)e^{-t/t_2}$ with $t_1 = 3.1 \pm 0.77$ms and $t_2 = 13.7 \pm 2.5$ms (black solid line). We attribute the faster decay process to the collisional loss from lattice sites with double occupation. The amplitudes of these two exponential decays give the fraction of double-occupied sites. The dashed line in this figure is a fit to single exponential decay function; the deviation to measured data points is evident. The inset is the same plot but with linear axes.

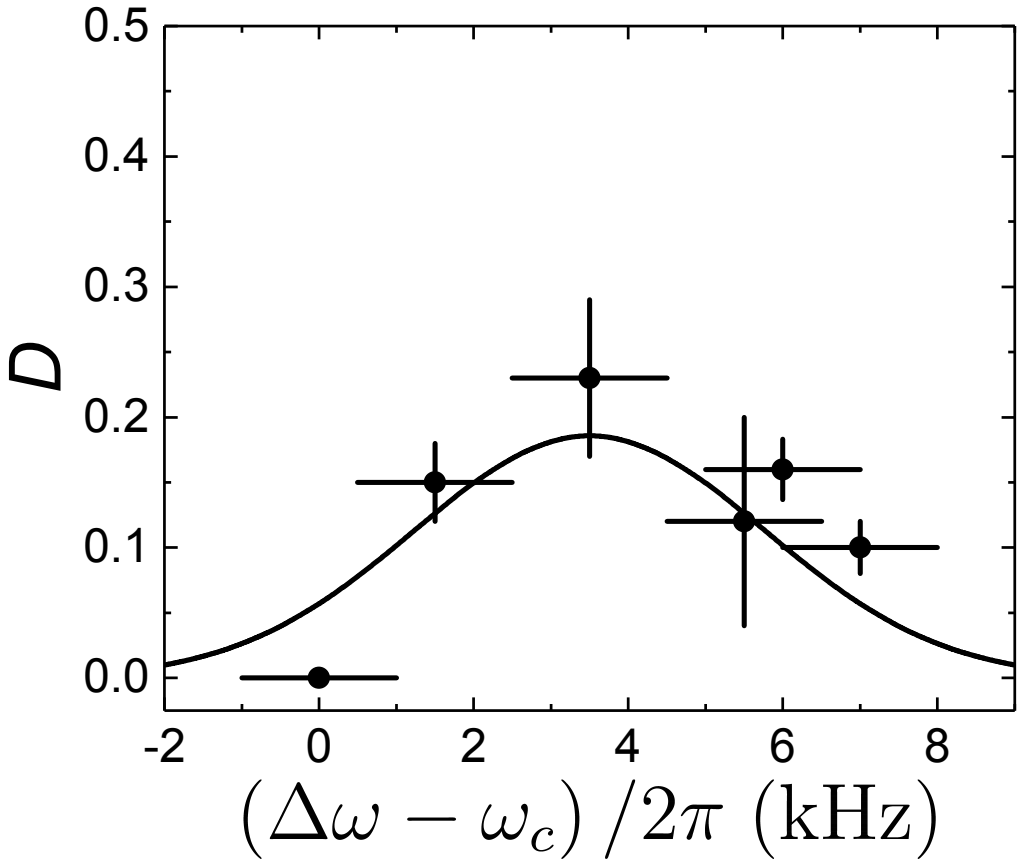

Figure 5.15: Population of doubly occupied sites D due to density-dependent tunneling. D is inferred from light-assisted collisions at various $(\Delta\omega - \omega_c)/2\pi$. The vertical error bar comes from the uncertainty in the fit to LAC data. The horizontal error bar is due to ambient magnetic field drift and is estimated from carrier frequency measurements at the beginning and the end of LAC measurements. The black curve plots $f_\uparrow - f_\downarrow$ from the fitting function in Fig. 5.8(b).

5.5 Effect of lattice filling fraction on CSFT

5.5.1 Technique to reduce filling

As a demonstration for the sensitivity of CSFT to site occupancy, we intentionally reduce atom number after loading them into optical lattices and therefore controllably introduce more vacancies. The technique involves three steps:

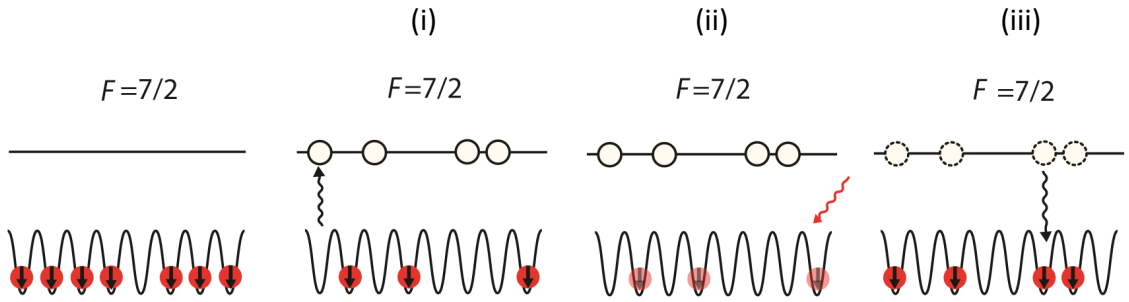

Figure 5.16: Technique used for increasing the vacancies in optical lattices by reducing number. After loading atoms into the optical lattice, (ii): a fraction of atoms are transferred to the $F = 7/2$ manifold by a microwave-frequency magnetic field sweep, (iii): a resonant probe light pulse is applied to remove atoms remaining in the $F = 9/2$ manifold, and finally (iv) atoms in the $F = 7/2$ manifold are brought back to their initial state by another magnetic field sweep. This whole procedure takes a few milliseconds; atoms will not change their positions during these steps. The fraction of atoms remaining can be adjusted by varying the power of the first microwave-frequency magnetic field sweep.

- After turning on the lattice, atoms are transferred from the $|\downarrow\rangle$ state to the $|F = 7/2, m_F = 7/2\rangle$ state via adiabatic rapid passage (ARP) driven by a microwave-frequency magnetic field. The microwave field is swept across 0.4MHz in 0.5ms, and its power is varied to control the probability of a transition between these two hyperfine states. The fraction transfered to the $F = 7/2$ state after this microwave sweep is denoted as δN (Fig. 5.16(ii)).

- A 0.5ms pulse of light, resonant with the $|F = 9/2, m_F = 9/2\rangle \rightarrow |F' = 11/2, m_F = 11/2\rangle$ transition is applied. Atoms remaining in the $|\uparrow\rangle$ state are removed from the lattice (Fig. 5.16(iii)).

- A second ARP sweep, swept across 0.8MHz in 1ms, brings all of the atoms shelved in the $F = 7/2$ manifold back to the $|\downarrow\rangle$ state (Fig. 5.16(iv)).

With this strategy, the number of atoms being removed is $1 - \delta N$, which can be simply adjusted by varying the power of the first microwave field sweep.

5.5.2 Suppression of CSFT by vacancies

After this procedure described, unoccupied sites are randomly distributed through out the spin-polarized atomic density distribution. The presence of holes suppresses CSFT, which can only occur when adjacent sites are occupied. We probe this effect by measuring changes in $|f_\uparrow - f_\downarrow|$ for a 40 ms Raman pulse with $\Delta\omega$ fixed on the $\pm U$ peaks of the CSFT sideband for a $s = 8E_R$ lattice gas (Fig. 5.17(a)). As the number of atoms is reduced and the hole density increases, $|f_\uparrow - f_\downarrow|$ decreases, indicating that fewer atoms can participate in CSFT. Panels (b) and (c) in Fig. 5.17 are sample data showing $f_\uparrow - f_\downarrow$ and the carrier feature for $\delta N = 0.57$. It is evident that while the peak height for the on-site spin-flip event almost remains unchanged, the peak heights for CSFT event reduce roughly by a factor of 2, compared with the case without removing atoms.

5.5.3 Simulation of CSFT sensitivity to vacancies

We developed a numerical simulation to determine the sensitivity of CSFT to vacancies in the lattice. We compute a density distribution in the non-interacting limit, and determine the probability that neighboring sites are occupied as atoms are randomly removed. The density distribution after turning on the lattice is generated according to

$$n\left(r_x, r_y, r_z\right) = \int \frac{d^3\vec{q}}{(2\pi)^3} \frac{1}{e^{\beta[2t[3-\cos(\pi q_x/q_B)-\cos(\pi q_y/q_B)-\cos(\pi q_z/q_B)]+V(r_x,r_y,r_z)-\tilde{\mu}]}+1},$$

where $V\left(r_x, r_y, r_z\right)$ is the total harmonic potential imposed by the optical trap and lattice beams, $\tilde{\mu}$ is the chemical potential, $\beta = 1/k_B\tilde{T}$, and $\tilde{T}$ the effective temperature in the lattice. Both $\tilde{\mu}$ and $\tilde{T}$ are solved by matching the entropy and number of atoms N to the corresponding values in the dipole trap. Non-interacting thermodynamics (including the tight-binding lattice dispersion and confining potential) are solved to relate the entropy to N and $\tilde{T}$. Each site in the simulated lattice is computed as occupied by a single atom or empty based on comparing a random number in the interval $[0, 1]$ to $n\left(r_x, r_y, r_z\right)$.

Atoms are randomly removed from the simulated density profile according to a probability δN, which corresponds to the average fraction of atoms discarded. The number of pairs N_p of adjacent occupied sites remaining after this removal procedure is counted. As shown in an inset to Fig. 5.18, atoms are only counted once if they participate in any nearest-neighbor pair. Results from this simulation for the fraction of atoms $N_p/(N\delta N)$ are shown in Fig. 5.18 for $N = 61000$ and entropy per particle $S/N = 2.89k_B$ in the lattice. This curve is also plotted in Fig. 5.17 as a comparison to experimental data points, which shows a good agreement. Codes for this simulation can be found in the Appendix.

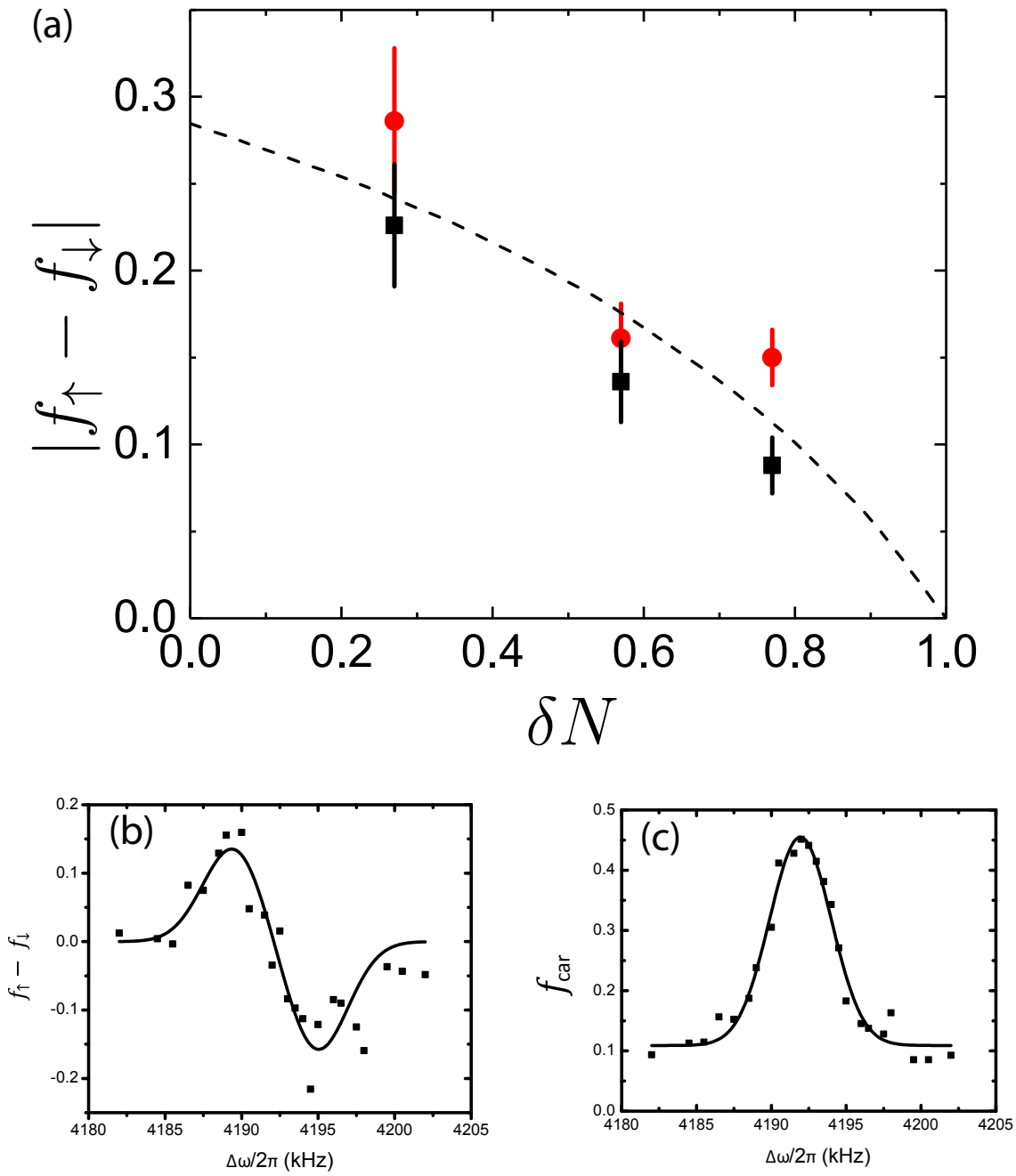

Figure 5.17: Density dependence of CSFT. (a): The CSFT spectroscopy signal taken with fixed $(\Delta\omega - \Delta\omega_{\uparrow\downarrow}) \approx \pm U/\hbar$ is shown for varied fraction δN of atoms randomly removed from an $s = 8E_R$ lattice gas. For these data, the averaged number $N = 61000$, and the gas was cooled to $T/T_F \approx 0.35$ before turning on the lattice. Data obtained with the $+U$ sideband are shown as red circles and those for $-U$ as black squares. The sideband frequencies were determined using a double-gaussian fit to CSFT spectroscopy data, as in Fig. 5.8. (b): $f_\uparrow - f_\downarrow$ for $\delta N = 0.57$. The peak height of the CSFT feature reduces roughly by a factor of two. (c): The carrier feature for $\delta N = 0.57$, inferred with the same method as for Fig. 5.8(c). The peak value roughly remains at 0.5, the same as in Fig. 5.8(c).

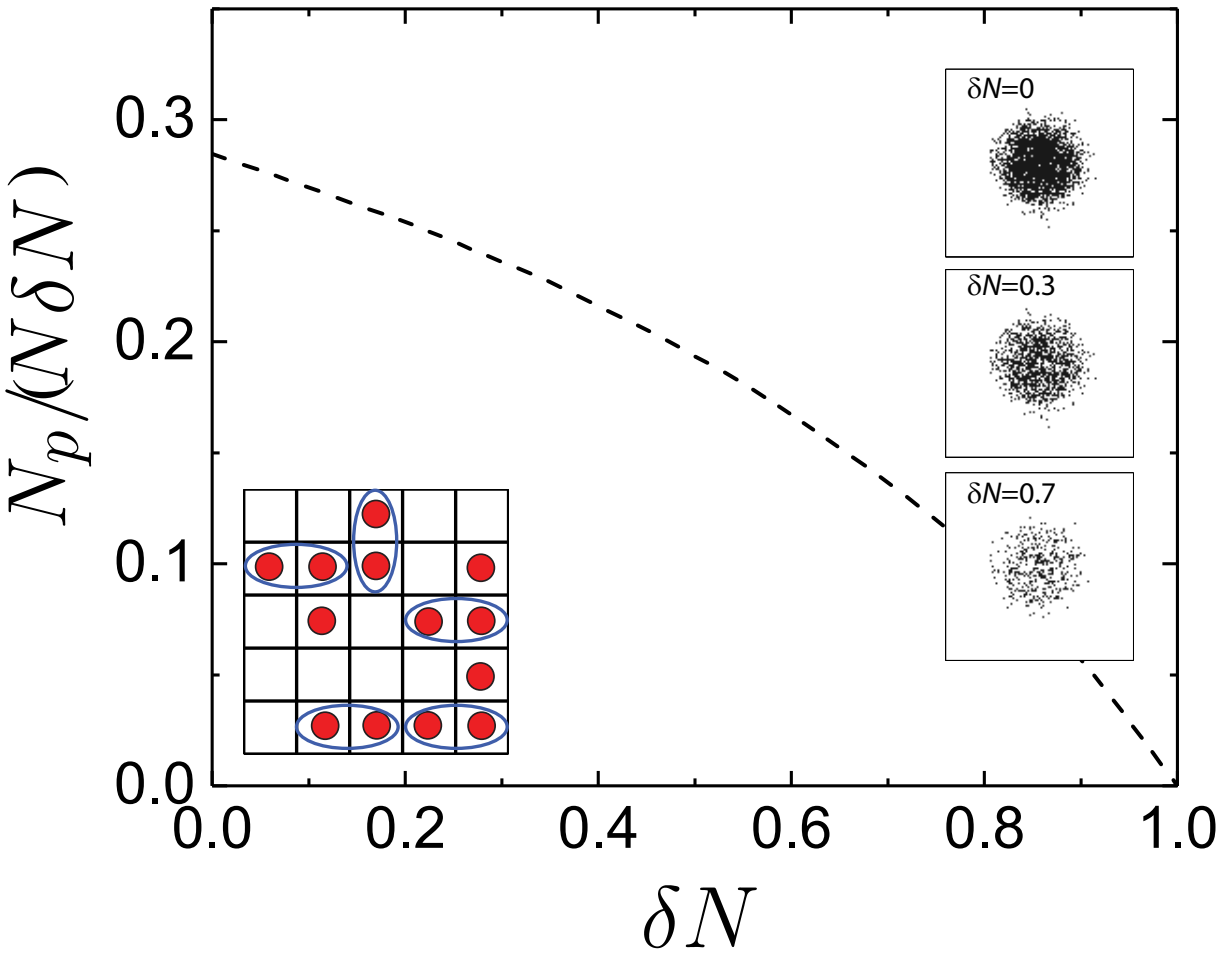

Figure 5.18: The fraction of atoms with nearest neighbors at various removal fractions δN for $N = 61000$ and $S/N = 2.89k_B$, which corresponds to $k_B\tilde{T} = 9.7t$ and chemical potential $\tilde{\mu} = 6.4t$ in the lattice. The insets at the right show sample occupation profiles (with one black dot per atom) through a central slice of the gas. The inset at bottom left schematically illustrates the procedure for counting pairs.

5.6 Rabi rate of CSFT

5.6.1 Measuring the Rabi rate of the carrier

The Rabi rate of the carrier feature can be measured using standard resonant Rabi oscillations. The carrier frequency $\omega_{\uparrow\downarrow}$ is determined using a fit of the spin transition probability vs. Raman detuning $\Delta\omega$ with a 0.7ms Raman pulse, which is too short to drive CSFT.

Fig. 5.19(a) and (b) show the sample data for carrier Rabi oscillations at different Raman power. The data are fit to a function $e^{-t/\tau}\sin^2(\frac{\Omega_{\uparrow\downarrow}}{2}t)$ to obtain the carrier Rabi rate $\Omega_{\uparrow\downarrow}$. Fig. 5.19(c) plots the relationship between Ω_c and the Raman power. A linear fit gives $\Omega_{\uparrow\downarrow} = 2\pi(I_R \times 1.13)$kHz, with I_R the intensity of Raman beams.

5.6.2 Measuring the Rabi rate of CSFT

Measuring the slower rate for CSFT requires a longer timescale. We eliminate the background contribution from the broad carrier feature using the same procedure as for Fig. 5.8. After locating the carrier frequency $\omega_{\uparrow\downarrow}$, we perform two measurements with the same Raman pulse time at $\Delta\omega = \omega_{\uparrow\downarrow} + U/\hbar$, but with different initial spin polarization (Fig. 5.20(a)). The difference between these two measurements $f_\uparrow - f_\downarrow$ only reflects the CSFT process. Fig. 5.20(b) plots the measured CSFT signal for different Raman pulse times at $s = 8\ E_R$ lattice depth.

The red curve in Fig. 5.20(b) is a fit to

$$f_{\mathrm{CSFT}}(t) = A\frac{\Omega_{\mathrm{CSFT}}^2}{2\gamma^2 + \Omega_{\mathrm{CSFT}}^2}\left\{1 - \left[\cos(\lambda t) + \frac{3\gamma}{2\lambda}\right]e^{-\frac{3\gamma}{2}t}\right\}, \tag{5.19}$$

with $\lambda = \sqrt{\Omega_{\mathrm{CSFT}}^2 + \frac{1}{2}\gamma^2}$. This expression is the solution to optical Bloch equations with damping due to spontaneous emissions in the case of resonant light [149]. With γ, A, and Ω_{CSFT} as free parameters, a fit gives $\Omega_{\mathrm{CSFT}} = (15 \pm 1)rad/s$ for the sample data shown in Fig. 5.20(b).

A similar procedure is performed at different Raman powers. Combined with the relationship between $\Omega_{\uparrow\downarrow}$ and the Raman power (Fig. 5.19(c)), we can plot the Rabi rate of CSFT vs. the carrier Rabi rate, as shown in Fig. 5.21. A linear fit gives a slope of 0.011 ± 0.001. As discussed later in Section.5.7, the predicted ratio of $|\Omega_{\mathrm{CSFT}}/\Omega_{\uparrow\downarrow}|$ is:

$$\frac{t}{U}\frac{2}{\sqrt{2}}\left[1 - \cos(\delta\vec{k}\cdot\vec{d})\right] \approx 0.047. \tag{5.20}$$

Therefore, although the measured CSFT Rabi rate presents a linear dependence on $\Omega_{\uparrow\downarrow}$, its timescale is roughly a factor of 5 slower than the theoretical prediction. The uncertainty in t and U from measurements

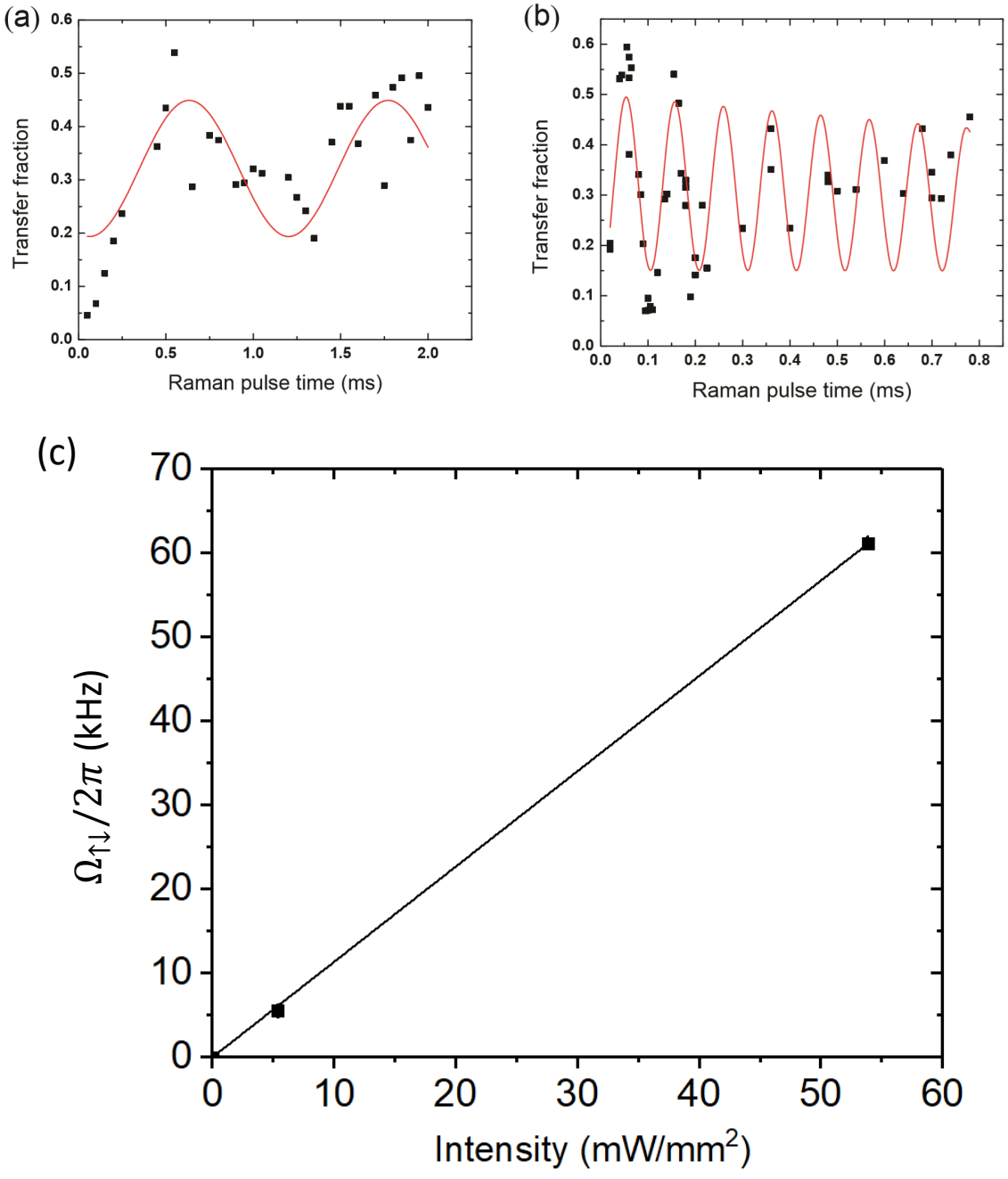

Figure 5.19: Calibration of the carrier Rabi rate. Standard resonant Rabi oscillation of the carrier $\Omega_{\uparrow\downarrow}$ are measured with the Raman beam power servoed at (a) 0.15V and (b)1.5V. The ratio between the power of a single Raman beam to the servo voltage is 1.63 ± 0.01mW/V. A fit to a damped $\sin^2$ function is used to obtain $\Omega_{\uparrow\downarrow}$. (c): Relation between $\Omega_{\uparrow\downarrow}$ and the Raman intensity.

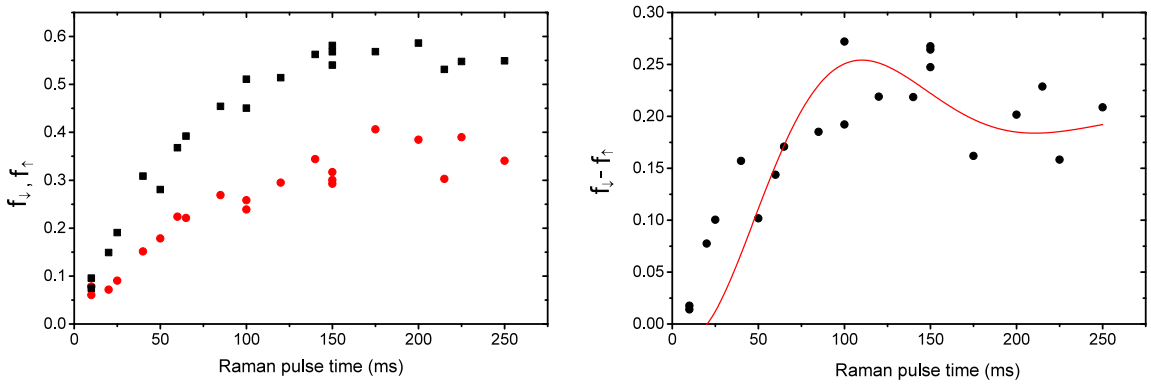

Figure 5.20: Measurements of CSFT Rabi rate with carrier Rabi rate $\Omega_{\uparrow\downarrow} = 0.2U/\hbar$. (a): The fraction of atoms transferred to the spin state is shown for an initially $|\uparrow\rangle$ (black squares) and $|\downarrow\rangle$ (red circles) spin-polarized gas at $s = 8E_R$, at various Raman pulse times. The frequency difference between two Raman beams is fixed to be $\Delta\omega - \omega_{\uparrow\downarrow} = U/\hbar$. (b): Time evolution of $|f_\downarrow - f_\uparrow|$. The red curve is a fit to the solution of the optical Bloch equations with spontaneous decay.

of the lattice potential depth are too small to explain this difference. Section. 5.7 will discuss the possible source of this discrepancy in details.

5.7 Theoretical description of effective CSFT Hamiltonian

The theoretical derivation in this section is done by Vito Scarola and Hoi Hui at Virginia Polytechnic Institute and State University.

5.7.1 Effective Hamiltonian for correlated spin-flip tunneling

As I have discussed, for the three-level system shown in Fig. 5.3(a), the single-particle Hamiltonian for the Raman beams coupling the $|\uparrow\rangle$ and $|\downarrow\rangle$ states is:

$$H_{\text{Raman}} \approx \begin{pmatrix} \delta & \frac{\Omega}{2} e^{-i\delta\vec{k}\cdot\vec{R}} \\ \frac{\Omega^*}{2} e^{i\delta\vec{k}\vec{R}} & 0 \end{pmatrix}, \tag{5.21}$$

with $\Omega = -\frac{\Omega_1^*\Omega_2}{2\Delta_R}$ as the effective Rabi rate, and $\delta\vec{k}$ is the difference in wavevectors between two Raman beams. For our case, $\Omega_1 \approx \Omega_2 \ll \Delta_R$, so the energy shift due to the AC Stark effect can be ignored.

We project this Hamiltonian onto the lowest band using localized Wannier functions as a basis, where

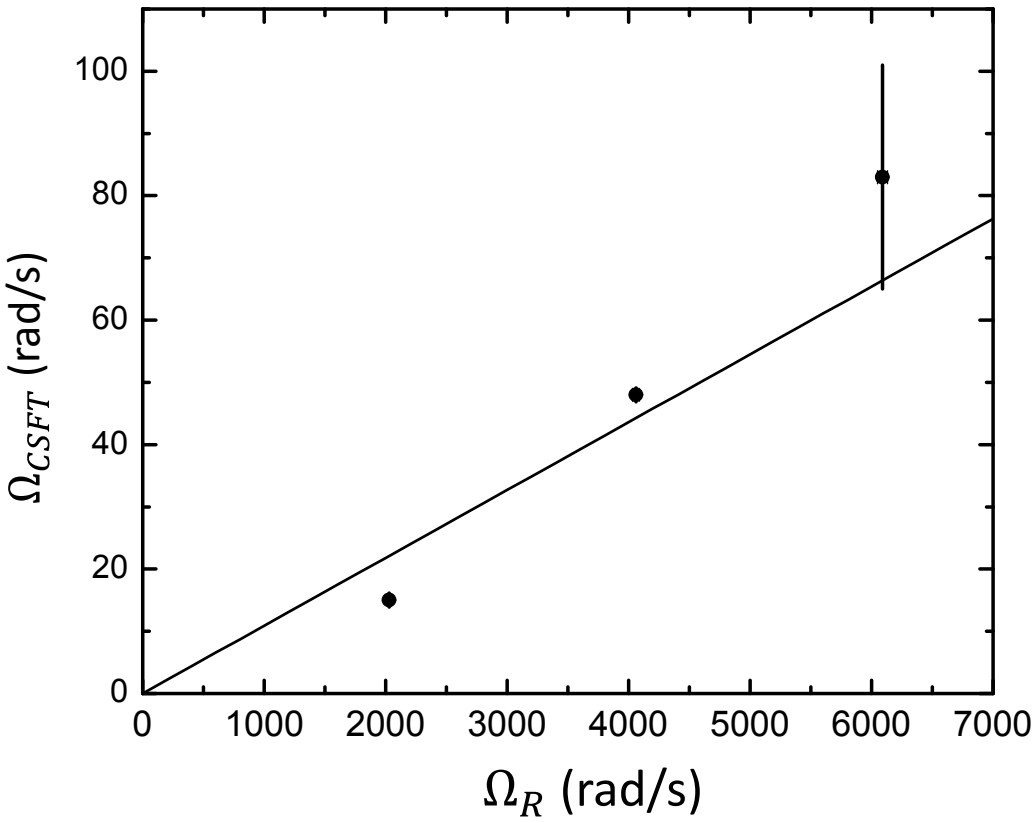

Figure 5.21: Relationship between CSFT Rabi rate and carrier Rabi rate. A linear dependence of Ω_{CSFT} on $\Omega_{\uparrow\downarrow}$ (red curve), as expected by theoretical calculation, shows here. However, the slope is a factor of 5 smaller compared with theory. A possible source of this discrepancy is the phase-noise between the Raman laser beams (more discussion on this can be found in the next section). The error bars are derived from fit uncertainty.

$|i\sigma\rangle$ denotes the localized Wannier function at the i^{th} site of the lattice with spin σ. Then we have:

$$H_{\text{Raman}} = \sum_i \left\{ \frac{\Omega}{2} |i\uparrow\rangle\langle i\uparrow| e^{-i\delta\vec{k}\cdot\vec{R}} |i\downarrow\rangle\langle i\downarrow| + \frac{\Omega^*}{2} |i\downarrow\rangle\langle i\downarrow| e^{i\delta\vec{k}\cdot\vec{R}} |i\uparrow\rangle\langle i\uparrow| \right\} + \sum_{\langle ij\rangle} \{ \frac{\Omega}{2} |i\uparrow\rangle\langle i\uparrow| e^{-i\delta\vec{k}\cdot\vec{R}} |j\downarrow\rangle\langle j\downarrow|$$
$$+ \frac{\Omega}{2} |j\uparrow\rangle\langle j\uparrow| e^{-i\delta\vec{k}\cdot\vec{R}} |i\downarrow\rangle\langle i\downarrow| + \frac{\Omega^*}{2} |i\downarrow\rangle\langle i\downarrow| e^{i\delta\vec{k}\cdot\vec{R}} |j\uparrow\rangle\langle j\uparrow| + \frac{\Omega^*}{2} |j\downarrow\rangle\langle j\downarrow| e^{i\delta\vec{k}\cdot\vec{R}} |i\uparrow\rangle\langle i\uparrow| \}, \tag{5.22}$$

where $\langle ij\rangle$ labels the indices of nearest neighbor sites. The second-quantized version of this Hamiltonian is:

$$H_{\text{Raman}} = \sum_{\langle ij\rangle} \left(\frac{\Omega}{2} \Psi_{ij} e^{-i\delta\vec{k}\cdot\frac{\vec{R}_i+\vec{R}_j}{2}} c^\dagger_{i\uparrow} c_{j\downarrow} + \frac{\Omega^*}{2} \Psi^*_{ij} e^{-i\delta\vec{k}\cdot\frac{\vec{R}_i+\vec{R}_j}{2}} c^\dagger_{i\downarrow} c_{j\uparrow} + \text{h.c.} \right)$$
$$+ \sum_i \left(\frac{\Omega}{2} \Psi_0 e^{-i\delta\vec{k}\cdot\vec{R}_i} c^\dagger_{i\uparrow} c_{i\downarrow} + \text{h.c.} \right) + \frac{\delta}{2} \sum_i \left(c^\dagger_{i\uparrow} c_{i\uparrow} - c^\dagger_{i\downarrow} c_{i\downarrow} \right) \tag{5.23}$$

where $\vec{R}_i$ is the position of the i^{th} lattice site, $\Psi_{ij} = \int d\vec{r}\; w_i^* e^{i\delta\vec{k}\cdot(\vec{R}_i - \vec{R}_j)} w_j$ is a Debye-Waller factor, and $\Psi_0 = \Psi_{00}$. The first term is spin-flip hopping term akin to spin-orbit coupling in the lattice. The second term is an on-site spin-flip term, which can be understood as an effective Zeeman term in the x, y directions. The fourth term is an effective Zeeman energy.

Therefore, the full Hamiltonian is

$$H = H_{\text{Hubbard}} + H_{\text{Raman}}$$
$$= -t \sum_{\langle ij\rangle\sigma} \left(c^\dagger_{j\sigma} c_{i\sigma} + h.c. \right) + U \sum_i n_{i\uparrow} n_{i\downarrow} + \sum_{\langle ij\rangle} \left(\frac{\Omega}{2} \Psi_{ij} e^{-i\delta\vec{k}\cdot\frac{\vec{R}_i+\vec{R}_j}{2}} c^\dagger_{i\uparrow} c_{j\downarrow} + \frac{\Omega^*}{2} \Psi^*_{ij} e^{-i\delta\vec{k}\cdot\frac{\vec{R}_i+\vec{R}_j}{2}} c^\dagger_{i\downarrow} c_{j\uparrow} + \text{h.c.} \right)$$
$$+ \sum_i \left(\frac{\Omega}{2} \Psi_0 e^{-i\delta\vec{k}\cdot\vec{R}_i} c^\dagger_{i\uparrow} c_{i\downarrow} + \text{h.c.} \right) + \frac{\delta}{2} \sum_i \left(c^\dagger_{i\uparrow} c_{i\uparrow} - c^\dagger_{i\downarrow} c_{i\downarrow} \right). \tag{5.24}$$

Two-site, two-atom system

For simplicity, we consider a two-site system with two atoms (we will generalize to many-site system later). This Hamiltonian can be separated into three parts:

$$H_0 = U \sum_{i=1,2} n_{i\uparrow} n_{i\downarrow} + \frac{\delta}{2} \sum_{i=1,2} \left(c^\dagger_{i\uparrow} c_{i\uparrow} - c^\dagger_{i\downarrow} c_{i\downarrow} \right), \tag{5.25}$$

$$H_1 = -t \sum_\sigma \left(c^\dagger_{1\sigma} c_{2\sigma} + c^\dagger_{2\sigma} c_{1\sigma} \right) + \sum_{i=1,2} \left(\frac{\Omega}{2} \Psi_0 e^{-i\vec{\delta}\cdot\vec{R}_i} c^\dagger_{i\uparrow} c_{i\downarrow} + \frac{\Omega^*}{2} \Psi^*_0 e^{i\delta\vec{k}\cdot\vec{R}_i} c^\dagger_{i\downarrow} c_{i\uparrow} \right), \tag{5.26}$$

$$H_2 = \frac{\Omega}{2} \Psi_1 e^{-i\delta\vec{k}\cdot\frac{\vec{R}_1+\vec{R}_2}{2}} a^\dagger_{1\uparrow} a_{2\downarrow} + \frac{\Omega^*}{2} \Psi^*_1 e^{i\delta\vec{k}\cdot\frac{\vec{R}_1+\vec{R}_2}{2}} a^\dagger_{2\downarrow} a_{1\uparrow} + \frac{\Omega}{2} \Psi_1 e^{-i\delta\vec{k}\cdot\frac{\vec{R}_1+\vec{R}_2}{2}} a^\dagger_{2\uparrow} a_{1\downarrow} + \frac{\Omega^*}{2} \Psi^*_1 e^{i\delta\vec{k}\cdot\frac{\vec{R}_1+\vec{R}_2}{2}} a^\dagger_{1\downarrow} a_{2\uparrow}. \tag{5.27}$$

When $U \approx \delta$, the subspace $\alpha = \{|\uparrow,\uparrow\rangle, |\uparrow\downarrow,0\rangle, |0,\uparrow\downarrow\rangle\}$ have similar energies with respect to H_0: $E_\alpha = \{\delta, U, U\}$. It is connected to the subspace $\beta = \{|\uparrow,\downarrow\rangle, |\downarrow,\uparrow\rangle\}$ (which has energy $E_\beta = 0$ with respect to H_0) by H_1. H_2 does not couple α with β, and thus we can ignore it for now and add it back later. In the basis of the $\{|\downarrow,\downarrow\rangle, |\uparrow\downarrow,0\rangle, |0,\uparrow\downarrow\rangle, |\uparrow,\downarrow,\rangle, |\downarrow,\uparrow\rangle\}$, the matrix for $H_0 + H_1$ is:

$$H_0 + H_1 = \begin{pmatrix} \delta & 0 & 0 & \frac{\Omega}{2}\Psi_0 e^{-i\vec{\delta k}\cdot\vec{R}_1} & \frac{\Omega}{2}\Psi_0 e^{-i\vec{\delta k}\cdot\vec{R}_2} \\ 0 & U & 0 & -t & t \\ 0 & 0 & U & -t & t \\ \frac{\Omega^*}{2}\Psi_0 e^{i\vec{\delta k}\cdot\vec{R}_1} & -t & -t & 0 & 0 \\ \frac{\Omega^*}{2}\Psi_0 e^{i\vec{\delta k}\cdot\vec{R}_2} & t & t & 0 & 0 \end{pmatrix}. \tag{5.28}$$

Assuming $\delta \approx U \gg 0$, H_1 can be treated as a perturbation to H_0, so we project $H_0 + H_1$ into the subspace α. The matrix element after projection is

$$\langle i,\alpha|\, \hat{P}(H_0+H_1)\,|j,\alpha\rangle = \langle i,\alpha|\, H_0+H_1\,|j,\alpha\rangle - \sum_{k\in\beta} \frac{\langle i\alpha|\, H_1\,|k\beta\rangle\,\langle k\beta|\, H_1\,|j\alpha\rangle}{2}\left(\frac{1}{E_{k\beta}-E_{i\alpha}} + \frac{1}{E_{k\beta}-E_{j\alpha}}\right).$$

Then add H_2 to obtain the effective Hamiltonian as:

$$H_{\text{eff}}^{\text{2-site}} = H_2 + \begin{pmatrix} \delta + \frac{2\Omega^2\Psi_0^2}{4\delta} & -t\Omega\Psi_0\frac{e^{-i\vec{\delta k}\cdot\vec{R}_1} - e^{-i\vec{\delta k}\cdot\vec{R}_2}}{4}\left(\frac{1}{\delta}+\frac{1}{U}\right) & -t\Omega\Psi_0\frac{e^{-i\vec{\delta k}\cdot\vec{R}_1} - e^{-i\vec{\delta k}\cdot\vec{R}_2}}{4}\left(\frac{1}{\delta}+\frac{1}{U}\right) \\ -t\Omega^*\Psi_0\frac{e^{i\vec{\delta k}\cdot\vec{R}_1} - e^{i\vec{\delta k}\cdot\vec{R}_2}}{4}\left(\frac{1}{\delta}+\frac{1}{U}\right) & U + \frac{2t^2}{U} & \frac{2t^2}{U} \\ -t\Omega^*\Psi_0\frac{e^{i\vec{\delta k}\cdot\vec{R}_1} - e^{i\vec{\delta k}\cdot\vec{R}_2}}{4}\left(\frac{1}{\delta}+\frac{1}{U}\right) & \frac{2t^2}{U} & U + \frac{2t^2}{U} \end{pmatrix}$$

We can write this effective Hamiltonian in second quantization as:

$$
\begin{aligned}
H_{\text{eff}}^{2-\text{site}} &= \left(\delta + \frac{|\Omega\Psi_0|^2}{2\delta}\right)|\uparrow,\uparrow\rangle\langle\uparrow,\uparrow| + \left(U + \frac{2t^2}{U}\right)(|\uparrow\downarrow,0\rangle\langle\uparrow\downarrow,0| + |0,\uparrow\downarrow\rangle\langle 0,\uparrow\downarrow|) \\
&\quad - \left(t\Psi_0\Omega\frac{e^{-i\delta\vec{k}\cdot\vec{R}_1} - e^{-i\delta\vec{k}\cdot\vec{R}_2}}{4}\left(\frac{1}{U}+\frac{1}{\delta}\right)(|\uparrow,\uparrow\rangle\langle\uparrow\downarrow,0| + |\uparrow,\uparrow\rangle\langle 0,\uparrow\downarrow|) + \text{h.c.}\right) \\
&\quad + \frac{2t^2}{U}(|\uparrow\downarrow,0\rangle\langle 0,\uparrow\downarrow| + |0,\uparrow\downarrow\rangle\langle\uparrow\downarrow,0|) + H_2 \\
&= \left[\left(\frac{\delta}{2} + \frac{|\Omega\Psi_0|^2}{4\delta}\right)\sum_{m=1,2} n_{m\uparrow} + \left(U + \frac{2t^2}{U} - \frac{\delta}{2} - \frac{|\Omega\Psi_0|^2}{4\delta}\right)\sum_{m=1,2} n_{m\uparrow}n_{m\downarrow} + \frac{2t^2}{U}\left(a_{1\uparrow}^\dagger a_{1\downarrow}^\dagger a_{2\uparrow}a_{2\downarrow} + \text{h.c.}\right)\right. \\
&\quad - \left(t\Omega\Psi_0\frac{e^{-iR_1k} - e^{-iR_2k}}{4}\left(\frac{1}{U}+\frac{1}{\delta}\right)\left(n_{1\downarrow}a_{2\downarrow}^\dagger a_{1\uparrow} + n_{2\downarrow}a_{1\downarrow}^\dagger a_{2\uparrow}\right) + \text{h.c.}\right) + \\
&\quad \left.\left(\frac{\Omega^*}{2}\Psi_{12}^* e^{iR_1k_R}\left(n_{1\downarrow}a_{2\downarrow}^\dagger a_{1\uparrow} + n_{2\downarrow}a_{1\downarrow}^\dagger a_{2\uparrow}\right) + \text{h.c.}\right)\right].
\end{aligned}
\tag{5.29}
$$

The last two terms in 5.29 can be viewed as tunneling accompanied with a spin-flip. The last term is proportional to Ψ_{12}, which is almost zero for the lattice depths used in this work. The second last term, with prefactor

$$
-t\Omega\Psi_0\frac{e^{-iR_1k} - e^{-iR_2k}}{4}\left(\frac{1}{U}+\frac{1}{\delta}\right) \equiv K_{12},
$$

corresponds to CSFT as observed in our measurements. The third term in this equation, proportional to t^2/U, exchanges a pair of doublons and holes at neighboring sites, *e.g.* $|\uparrow\downarrow,0\rangle \rightarrow |0,\uparrow\downarrow\rangle$.

Estimation of U using the resonance near $\delta = U$

One way the value of the Hubbard U is estimated experimentally is via CSFT by finding the resonant δ at which doublon creation is most effective. As shown in Fig. 5.9, this procedure appears to undervalue U compared with the tight-binding prediction from independent measurements of the lattice potential depth. To understand how higher order terms in H_{eff} may explain this discrepancy, we consider a two-site system with the three states $|\uparrow,\uparrow\rangle, |\uparrow\downarrow,0\rangle, |0,\uparrow\downarrow\rangle$ and solve for the value of δ at which the doublon creation rate is

maximized. Writing H_{eff} in this basis,

$$\begin{aligned} H_{\text{eff}}^{(2)} &= \begin{pmatrix} \delta + \frac{2\Psi_0^2|\Omega|^2}{\delta} & K_{12} & -K_{21} \\ K_{12}^* & U + \frac{2J^2}{U} & \frac{2J^2}{U} \\ -K_{21}^* & \frac{2J^2}{U} & U + \frac{2J^2}{U} \end{pmatrix} \\ &= \mathcal{U}^\dagger \begin{pmatrix} \delta + \frac{2\Psi_0^2|\Omega|^2}{\delta} & \sqrt{2}K_{12} & 0 \\ \sqrt{2}K_{12}^* & U + \frac{4J^2}{U} & 0 \\ 0 & 0 & U \end{pmatrix} \mathcal{U} \end{aligned} \tag{5.30}$$

where $\mathcal{U}$ transforms the basis to $\left\{ |\uparrow,\uparrow\rangle, \frac{|\uparrow\downarrow,0\rangle+|0,\uparrow\downarrow\rangle}{\sqrt{2}}, \frac{|\uparrow\downarrow,0\rangle-|0,\uparrow\downarrow\rangle}{\sqrt{2}} \right\}$, and the equality $K_{ij} = -K_{ji}$ has been used. The first two states have the same energy (and hence doublon creation is most effective) when:

$$\begin{aligned} \delta + \frac{\Psi_0^2 |\Omega|^2}{2\delta} &= U + \frac{4t^2}{U} \\ \delta &\approx U + \frac{4t^2 - |\Omega|^2 \Psi_0^2/2}{U} + \frac{2t^2 |\Omega|^2 \Psi_0^2}{U^3} \end{aligned} \tag{5.31}$$

Here we see that the resonant condition for maximal doublon creation is not exactly at $\delta = U$, but instead shows higher-order corrections. In the case that $U \gg t$, it gives $\delta = U - \frac{\Omega^2\Psi_0^2}{2U} \approx 0.02U$. These corrections contribute, but not fully accommodate, to the deviation between the measured and predicted U discussed in the main text.

Generalization to many sites

To derive an general effective Hamiltonian for CSFT with many sites, we still work in the limit $U, \delta \gg t, \Omega$ and treat the first three terms in Eq. 5.24 as perturbations. We consider the case $\delta \approx U$ and choose to require exact energy conservation between final states and the initial spin-polarized state. Off-resonant processes that can, for example, lead to sites occupied by a single spin-down atom are ignored. We therefore project our Hamiltonian onto such states where all sites obey $\langle n_{i\downarrow}(1 - n_{i\uparrow})\rangle = 0$. Let $\mathcal{P}$ be the projector onto this

space. Second-order perturbation theory then gives

$$\begin{aligned}
H_{\text{eff}} =&\mathcal{P}\Bigg[-t\sum_{\langle ij\rangle\sigma}\left(c_{i\sigma}^{\dagger}c_{j\sigma}+\text{hc}\right)-\frac{t\Psi_0}{4}\left(\frac{1}{U}+\frac{1}{\delta}\right)\sum_{\langle ij\rangle}\left(\Omega^{*}\left(e^{i\delta\vec{k}\cdot\vec{R}_i}-e^{i\delta\vec{k}\cdot\vec{R}_j}\right)c_{i\downarrow}^{\dagger}c_{j\uparrow}+i\leftrightarrow j+\text{hc}\right)\\
&+\left(\frac{\delta}{2}+\frac{|\Omega|^2\Psi_0^2}{4\delta}\right)\sum_i\left(n_{i\uparrow}-n_{i\downarrow}\right)+U\sum_i n_{i\uparrow}n_{i\downarrow}\\
&+\sum_{\langle ij\rangle}\left(\frac{\Omega}{2}e^{-i\delta\vec{k}\cdot\frac{\vec{R}_i+\vec{R}_j}{2}}\Psi_{\text{ij}}c_{i\uparrow}^{\dagger}c_{j\downarrow}+i\leftrightarrow j+\text{hc}\right)+\frac{2t^2}{U}\sum_{\langle ij\rangle}\left(c_{i\uparrow}^{\dagger}c_{i\downarrow}^{\dagger}c_{j\downarrow}c_{j\uparrow}+\text{hc}\right)\\
&+\frac{2t^2}{U}\sum_{\langle ij\rangle}\left(n_{i\uparrow}n_{i\downarrow}\left(1-n_{j\uparrow}\right)\left(1-n_{j\downarrow}\right)+i\leftrightarrow j\right)+\frac{t^2}{U}\sum_{\langle ij\rangle,\langle ij'\rangle,j\neq j'}n_{i\uparrow}c_{i\downarrow}^{\dagger}c_{j'\downarrow}c_{j\downarrow}^{\dagger}c_{i\downarrow}\\
&+\frac{t^2}{U}\sum_{\langle ij\rangle,\langle ij'\rangle,j\neq j'}\left(1-n_{i\downarrow}\right)c_{j\uparrow}^{\dagger}c_{i\uparrow}c_{i\uparrow}^{\dagger}c_{j'\uparrow}-\frac{t^2}{U}\sum_{\langle ij\rangle,\langle ij'\rangle,j\neq j'}\left(c_{j\uparrow}^{\dagger}c_{j'\downarrow}^{\dagger}c_{i\uparrow}c_{i\downarrow}+\text{hc}\right)\Bigg]\mathcal{P}.
\end{aligned}\tag{5.32}$$

Noting that $\Psi_{ij}\approx 0$ for $i\neq j$, $\Psi_0\approx 1$, and ignoring higher-order interactions, this can be written as

$$\begin{aligned}
H_{\text{eff}} =&\mathcal{P}\Bigg[-t\sum_{\langle ij\rangle\sigma}\left(c_{i\sigma}^{\dagger}c_{j\sigma}+\text{hc}\right)+\sum_{\langle ij\rangle}\left(K_{ij}c_{j\uparrow}^{\dagger}c_{i\downarrow}+K_{ji}c_{i\uparrow}^{\dagger}c_{j\downarrow}+\text{hc}\right)\\
&+\frac{\delta^*}{2}\sum_i\left(n_{i\uparrow}-n_{i\downarrow}\right)+U\sum_i n_{i\uparrow}n_{i\downarrow}\Bigg]\mathcal{P}+\mathcal{O}\left(\frac{t^2}{U}\right),
\end{aligned}\tag{5.33}$$

where

$$K_{ij}=-t\Omega\Psi_0\frac{e^{-i\delta\vec{k}\cdot\vec{R}_i}-e^{-i\delta\vec{k}\cdot\vec{R}_j}}{4}\left(\frac{1}{U}+\frac{1}{\delta}\right)\tag{5.34}$$

$$\delta^*=\delta+\frac{|\Omega\Psi_0|^2}{4\delta}.\tag{5.35}$$

H_{eff} governs the dynamics of fully polarized initial states discussed in the main text. The first term moves (but does not create) doublons and holes (e.g., $|\uparrow\downarrow,\downarrow\rangle\rightarrow|\downarrow,\uparrow\downarrow\rangle$). The second term is a spin-flip tunneling, which due to the projectors $\mathcal{P}$ is effective only if no sites with spin-down are created. We can therefore rewrite the second term by explicitly inserting the projectors: $K_{ij}n_{i\uparrow}(1-n_{j\downarrow})c_{j\uparrow}^{\dagger}c_{i\downarrow}+i\leftrightarrow j+\text{h.c.}$ This term can create doublon-hole pairs out of the fully polarized initial state and dominates the dynamics to leading order.

5.7.2 Validating the CSFT Effective Model

The effective model H_{eff} is a perturbative result, in comparison to the full tight-binding Hamiltonian H_0. To test the validity of the dynamics predicted by H_{eff}, we compare the time evolution of the double occupancy

in both models.

The dynamics of H_0 cannot be solved exactly in large systems with dimension higher than one. We therefore consider doublon dynamics in one-dimension. We initialize a one-dimensional infinite system with one spin-up fermion in each state, and evolve it with infinite time-evolving block decimation (iTEBD) [142]. The evolution of doublon fraction, defined as $D = \langle n_{i\uparrow} n_{i\downarrow} \rangle / \langle n_{i\uparrow} + n_{i\downarrow} \rangle$, is plotted in Fig. 5.22(a). The simulations performed with H_0 and H_{eff} are both presented.

Here we see that the effective model captures the qualitative features of the full Hamiltonian. The doublon creation rate at short times is essentially the same for both models. Furthermore, the long-time steady-state reveals approximately the same doublon fraction. In both models the timescale of equilibration is roughly set by $\hbar/|K_{\langle ij \rangle}| = 14\text{ms}$. We therefore see that the effective CSFT model H_{eff} captures the essential features of the full tight binding model as in in Eq. 5.24.

5.7.3 Theory–experiment comparison

CSFT timescale

Comparing the measured $|f_\downarrow - f_\uparrow|$ (Fig. 5.20) and the theoretical prediction (Fig. 5.22), it is obvious that the measured CSFT timescale is at least a factor of five larger than that of the numerical simulations, which use the experimentally determined carrier Rabi rate. The uncertainty in t and U (which determine K_{ij} and the CSFT timescale) from measurements of the lattice potential depth are too small to support this difference.

A potential source of this discrepancy is phase-noise between the Raman laser beams, which translates into fluctuations in the complex phase of Ω in H_{eff}. Phase noise with a non-uniform frequency spectrum is required to explain the discrepancy between the predicted and measured CSFT time dependence, since the predicted CSFT time dependence shown in Fig. 5.22 is constrained by all the experimental parameters, including the independent measurement of Ω using the carrier transition. In order to differentially affect the carrier and CSFT transitions, the phase-noise spectral density must be frequency dependent.

To explore this, we carry out iTEBD numerical simulations with a time-dependent $\Omega e^{i\phi(t)}$. The result, plotted as the solid line in Fig. 5.23, shows a much better agreement with the experimental result. Hoi and Vito plan to write a separate paper with more detailed discussion.

Transfer fraction vs $\Delta\omega$

By time-evolving the full Hamiltonian (Eq. 5.24) until the system reaches its steady state at different δ, it predicts the transfer fraction to the other spin-component as $\Delta\omega$ varies. Fig. 5.24 shows the comparison between experimental measurements and the spin-flip fraction predicted by simulation. While the center

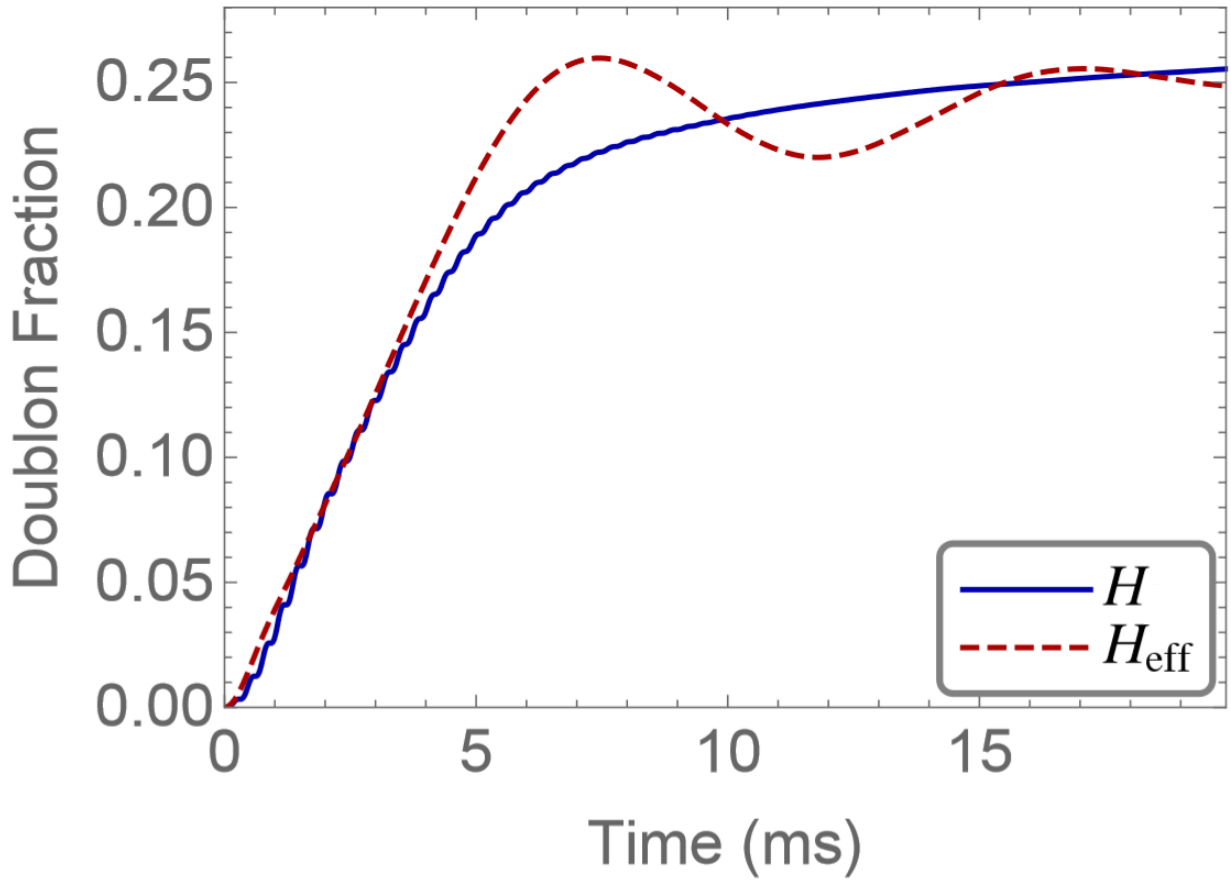

Figure 5.22: The evolution of doublon fraction $\langle n_{i\uparrow} n_{i\downarrow} \rangle / \langle n_{i\uparrow} + n_{i\downarrow} \rangle$ from a numerical simulation with constant Ω. The solid lines shows the simulation with the full Hamiltonian, while the dashed line shows that with the effective Hamiltonian H_{eff} derived from second-order perturbation theory. The states are initialized with one spin-up fermion on every site, and the parameters are determined by experiment: $t/h = 0.25$kHz, $U/h = 3.22$kHz, $\Omega = 0.2U$, and $\vec{\delta k} \cdot \vec{d} = \pi/2\sqrt{3}$. This figure was made by Vito Scarola and Hoi Hui.

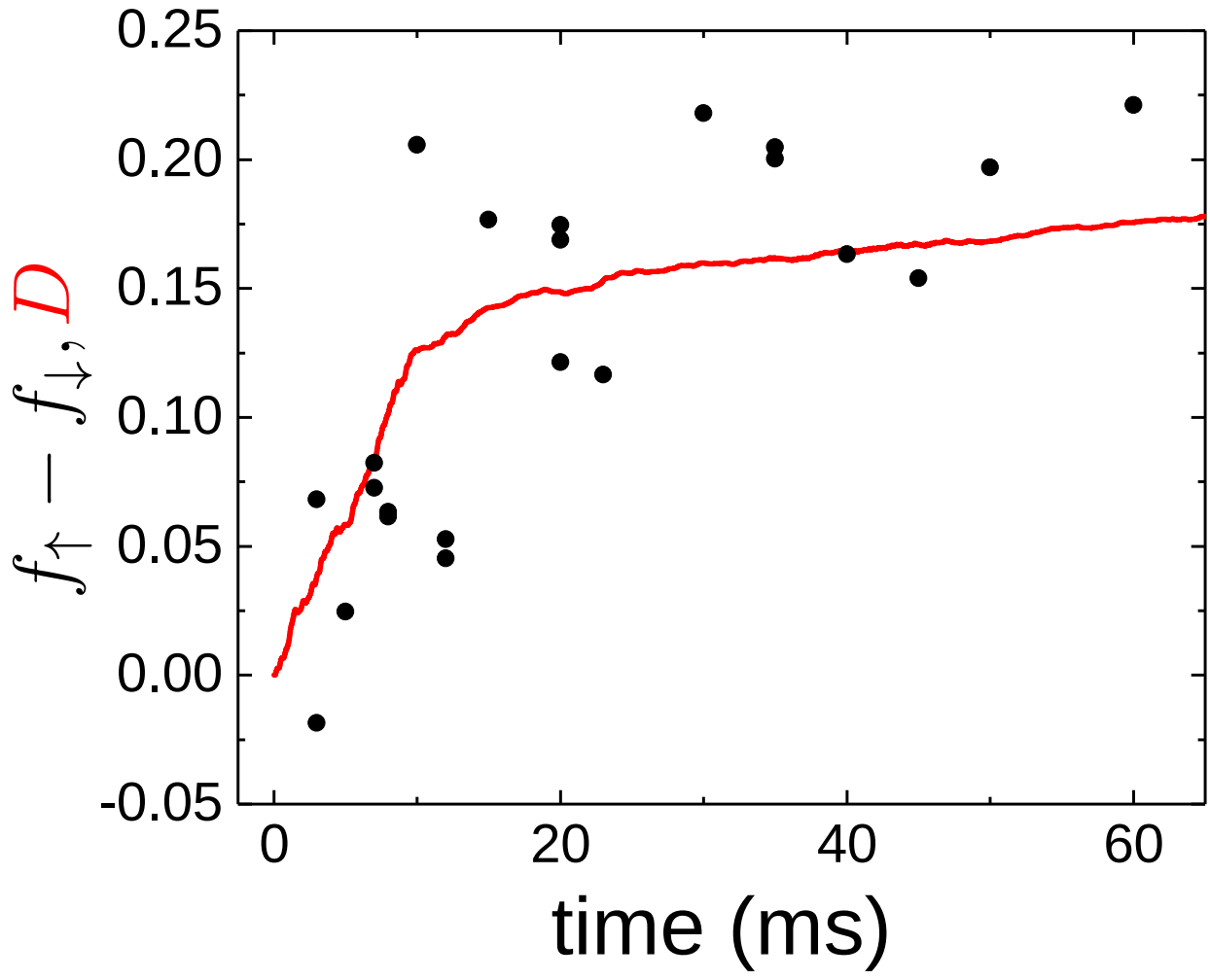

Figure 5.23: CSFT signal for varied Raman pulse time. The Raman detuning for these measurements is fixed to the $+U$ CSFT sideband. The measurements are shown using black circles, and a theoretical simulation is displayed as a red line. The simulation is performed with Ω in H_0 replaced with $\Omega e^{i\phi(t)}$, where $\langle\phi(t)^2\rangle$=8, and the characteristic timescale of the fluctuations in $\phi(t)$ is 2 ms. The dynamics has been averaged (indicated by the notation $\langle\rangle$) over five realizations of $\phi(t)$. For these parameters, the carrier Rabi oscillations are not strongly perturbed. Theoretical curve is from Vito Scarola and Hoi Hui.

positions of carrier and CSFT feature match the experimental results, the predicted linewidth is much narrower than measurements. Possible sources of such broadening may come from the phase noise on Raman laser beams.

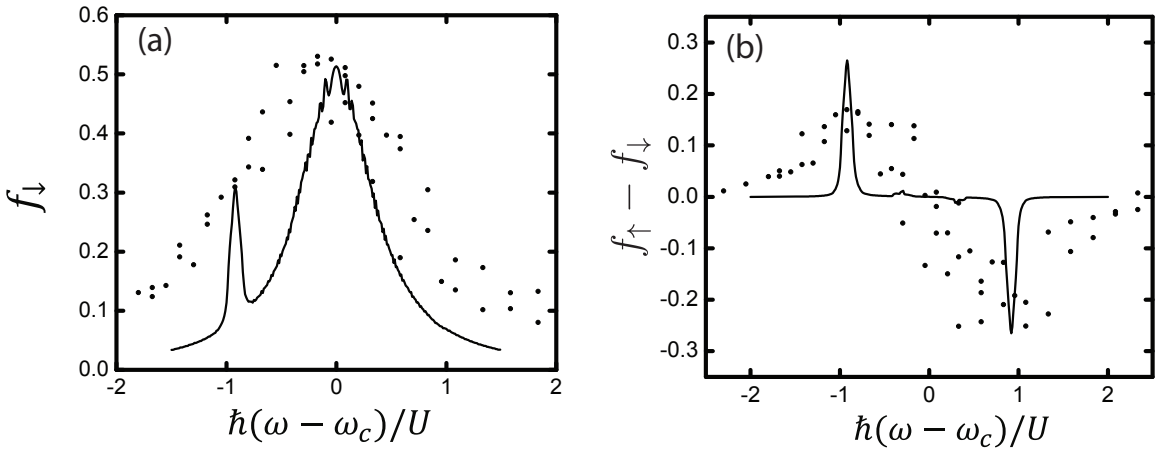

Figure 5.24: Comparison between transfer fraction at different $\Delta\omega$ of simulation (solid line) and experimental measurements (round circles). (a): Numerical simulation presents a distinguishable and narrow peak of CSFT event. (b): Peak positions in $|f_\uparrow - f_\downarrow|$ given by the simulation match the experimental results.

5.8 Conclusion and outlook

In this work, we realize correlated, density-dependent tunneling for fermionic ^{40}K atoms trapped in an optical lattice. By appropriately tunning the frequency difference between a pair of Raman beams applied to a spin-polarized gas, simultaneous spin transitions and tunneling events are induced that depend on the relative occupations of neighboring lattice sites. We spectroscopically resolve correlated spin-flip tunneling events, and the corresponding increase in doubly occupied sites is measured using number loss from light-assisted collisions. Furthermore, by controllably introducing vacancies to a spin-polarized lattice gas, we verify that the magnitude of this correlated tunneling is suppressed when neighboring lattice sites are unoccupied. This work is the first observation of density-dependent tunneling in an optical lattice Fermi-Hubbard model.

In the future, the technique we have developed may be used to observe exotic states such as bond-ordered waves, triplet paring, and hole superconductivity [141]. In addition, with combination to spin-dependent lattice [150, 151], this technique allows an arbitrary manipulation of tunneling for one spin component by selectively tuning the lattice geometry for another spin component.

Chapter 6

Rydberg Dressed States and EIT measurement

6.1 Introduction

Interactions between atoms in optical lattices are normally short-ranged and on-site only. While this feature is benefitial in terms of testing the most minimal Hubbard model, it limits the exploration on phenomena that require long-range interactions. Introducing long-range interactions in optical lattices has attracted intense interest because of the possibility to realize novel quantum phases of matter, such as quantum magnetism, topological phases, and exotic superfluidity [152–156].

Several experimental approach have been pursued, including trapping polar molecules [8, 157, 158] and atomic species with a large magnetic dipole moment [9, 159–162]. The interatomic potentials for these appraoches have a long-range and anisotropic character. Another scheme is loading atoms into an optical cavity, such that the cavity field mediates infinitely long-range interactions between all atoms [163, 164].

Rydberg atoms, which have a valence electron excited to a state with high principle quantum number n and therefore exhibit strong van der Waals interatomic interactions, are also potential candidates. The early work on Rydberg atoms includes the interaction between Rydberg states and strong external fields and dynamics of the valence electron [165]. Rydberg states are also useful for quantum information application (see Ref. [166] for a review). Quantum gates [167] and collective qubit encoding [168] have been demonstrated.

Recently manipulating Rydberg atoms to study many-body physics has attracted intense interest. Interaction-induced blockades [169] and self-assembled crystals of Rydberg atoms have been observed experimentally [170]. Arrays of single Rydberg atoms trapped in microtraps have realized Ising-like models for the study of quantum magnetism [171, 172].

The disadvantage of using Rydberg excitations is their short lifetime, which can hinder exploring exotic quantum phases. The lifetime of Rydberg atoms is on the order of tens of microseconds [173], while it takes tens of milliseconds for a typical experimental system to reach equilibrium. Recent theoretical proposals have suggested Rydberg-dressed states as a technique to avoid this problem. In this method, a small and adjustable fraction f of a Rydberg state is coherently mixed into the ground state wave function to enhance

the lifetime by a factor of $1/f^2$. In this scheme, the interaction length scale can be comparable to the lattice spacing [174, 175]. Rydberg dressing enables the study of extended Hubbard models and novel quantum phases such as charge-density waves [176]. By tuning the interaction range, the crossover from two-body interactions to collective interactions may also be observable [177]. In addition, if nP states are mixed into the ground state, it may allow simulating gauge field models [178].

Thus far, coherent interactions produced via Rydberg dressing of atoms in optical lattices has only been observed for bosonic ^{87}Rb atoms [179]. Dissipative effects have also been measured for trapped and lattice gases composed of Rb and Sr atoms [180–185], and Rydberg dressing has been used to entangle two Cs atoms confined in optical tweezers [186].

We plan to realize Rydberg-dressed interactions between fermionic ^{40}K atoms trapped in an optical lattice. Achieving this will be an exciting step toward resolving puzzles related to strongly correlated electronic solids. Also, compared to previous work with bosons (in the absence of a Feshbach resonance), Fermi statistics allows us to start from a non-interacting state. Therefore, the interactions induced by Rydberg-dressing should be easier to resolve.

In this chapter, I will report our progress on realizing long-range interactions in an optical lattice using Rydberg-dressed atoms. First, I will discuss the theory relevant to Rydberg-dressed states in detail. Calculations carried out with experimentally accessible parameters demonstrate the possibility to observe Rydberg-dressed interaction in our experiments. As a first step toward realizing Rydberg-dressed states in optical lattices, we developed a velocity-selective spectroscopy technique to measure the transition between $5P_{1/2}$ to Rydberg states via electromagnetically-induced transparency,

6.2 Properties of Rydberg-dressed atoms

6.2.1 Rydberg atoms

The potential energy from the van der Waals interaction between atoms is $U_{vdw}(R) = C_6/R^6$, where C_6 is the van der Waals coefficient, and R is the interatomic separation. For ground-state alkali metal atoms, C_6 is $10^3 - 10^4$ in atomic units [187], which is only $10^{-6} - 10^{-7}(\text{Hz} \cdot \mu\text{m}^6)$. Typical optical lattice spacings are $0.1\mu\text{m} \approx 10^4 a_0$, where a_0 is the Bohr radius. Therefore, the U_{vdw} for particles on different lattice sites can be ignored.

On the other hand, Rydberg atoms, which have a valence electron excited to an energy level with high

principle quantum number n, have exaggerated atomic properties. The energy levels of Rydberg atoms are

$$E(n,j,l) = -\frac{R'}{(n^*)^2}, \tag{6.1}$$

where R' is the Rydberg constant, $n^* = n - \delta_{nlj}$ is the effective quantum principle number, and δ_{nlj} is the state-dependent quantum defect. The quantum defects are determined from spectroscopic measurements and can be expressed as:

$$\delta_{nlj} = \delta 0_{lj} + \frac{\delta 2_{lj}}{(n-\delta 0_{lj})^2} + \frac{\delta 4_{lj}}{(n-\delta 0_{lj})^4} + ... \ , \tag{6.2}$$

where $\delta 0_{lj}$, $\delta 2_{lj}$ ... are constants called quantum defects that depend on the orbital angular momentum quantum number l and the total angular momentum quantum number j.

The wavefunction for the Rydberg valence electron is:

$$\left[-(\frac{\partial^2}{\partial r^2} + \frac{2}{r}\frac{\partial}{\partial r} - \frac{\hat{L}^2}{r^2}) + V(r)\right]\Psi(r,\theta,\phi) = E\Psi(r,\theta,\phi), \tag{6.3}$$

where $V(r)$ is the core potential. The wavefunction can be separated to radial and angular parts as $\Psi(r,\theta,\phi) = R(r)Y_l^{m_l}(\theta,\phi)$. With knowledge of the binding energies (which can be measured experimentally), for these excited states, one can solve the Schrödinger equation analytically or numerically to obtain important properties such as the orbital radius and dipole matrix elements between different atomic levels.

Compared to expansive work on Rubidium, potassium Rydberg atoms are much less explored experimentally. Here, following the numerical method in Ref. [188, 189], we calculate the wavefunctions for potassium Rydberg states, with the parameters for quantum defects from Ref. [190]. Fig. 6.1 plots the radial component $R(r)$ and the probability to find the valence electron at radius r. By comparing (c) and (d), the significant broader distribution in space is obvious for Rybderg atoms (notice the difference in the scale of x-axis).

Since the orbital scale for the valence electron can reach hundreds of nanometers (Fig. 6.1(d)), the Van der Waals interactions between Rydberg atoms are orders of magnitude stronger than those between ground state atoms. Table. 6.1 summarizes the leading order in the scaling of important quantities on the effective quantum principle number n^*.

For $l = 0$ state in potassium, $\delta_{n,l=0,j=1/2} = 2.18$ is roughly a constant for all n. Table 6.1 lists some quantities for the ground $4S$ state and $30S$ state in potassium, either based on numerically calculated wavefuntions or from polynomial functions provided by some theoretical references. Lifetime of potassium nS state is calculated as: $11.5 + 0.256(n^*) - 0.055(n^*)^2 + 1.14(n^*)^3$ in unit of ns [191]. The dispersion coefficient C_6 is calculated as: $\left[1.827 - 0.435n^* + 0.002054(n^*)^2\right](n^*)^{11}$ in atomic units. Atomic units for

Table 6.1: Properties of Rydberg levels in potassium.

Property	Scaling [192]	4S	30S
Binding energy	$(n^*)^{-2}$	4.11eV	0.0176eV (4.25THz)
Orbital radius	$(n^*)^2$	$4.94a_0$	$1167a_0$
C_6	$(n^*)^{11}$	3.945 (a.u.) [193]	-1.66×10^{17} (a.u.) [194]
Level spacing for adjacent states	$(n^*)^{-3}$	5.78THz	290GHz
Lifetime	$(n^*)^3$		24.5μs (without BBR) [191]
Dipole matrix element between $4P_{1/2}$ and nS	$(n^*)^{-1.5}$	$0.408ea_0$	$0.059ea_0$

C_6 are $\approx 1.445 \times 10^{-9}$Hz $\cdot(\mu\text{m})^6$. The effect of blackbody radiation (BBR) has not been taken into account for the lifetimes. For high n^*, the correction to the lifetime from BBR can be $10\% - 30\%$ [191].

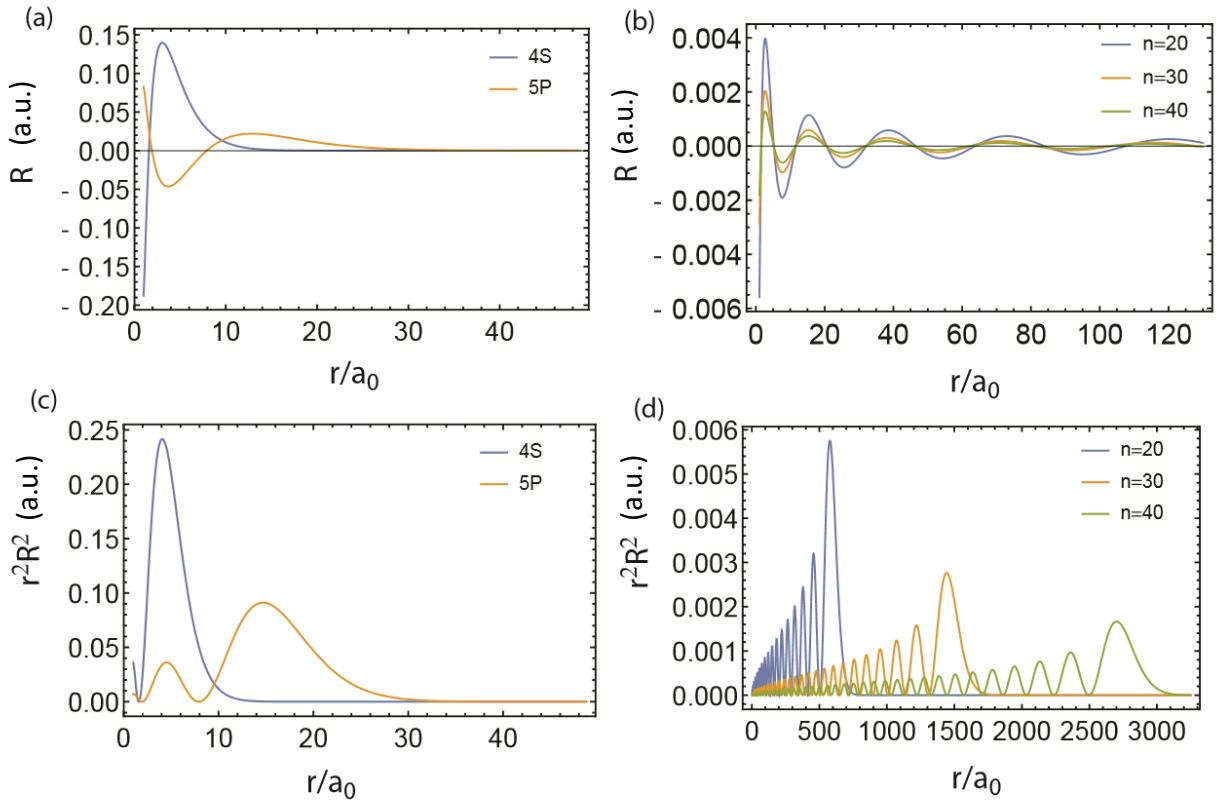

Figure 6.1: Radial wavefunction for (a): $4S$ and $5P$ and (b): Rydberg state $nS_{1/2}$. Radial probability density for (c): $4S$ and $5P$ and (b): Rydberg state $nS_{1/2}$.

6.2.2 Rydberg-dressed state

Because of the large Van der Waals interactions between Rydberg atoms, a small admixture of Rydberg character with ground states can produce atoms with interatomic interactions large enough to be observed

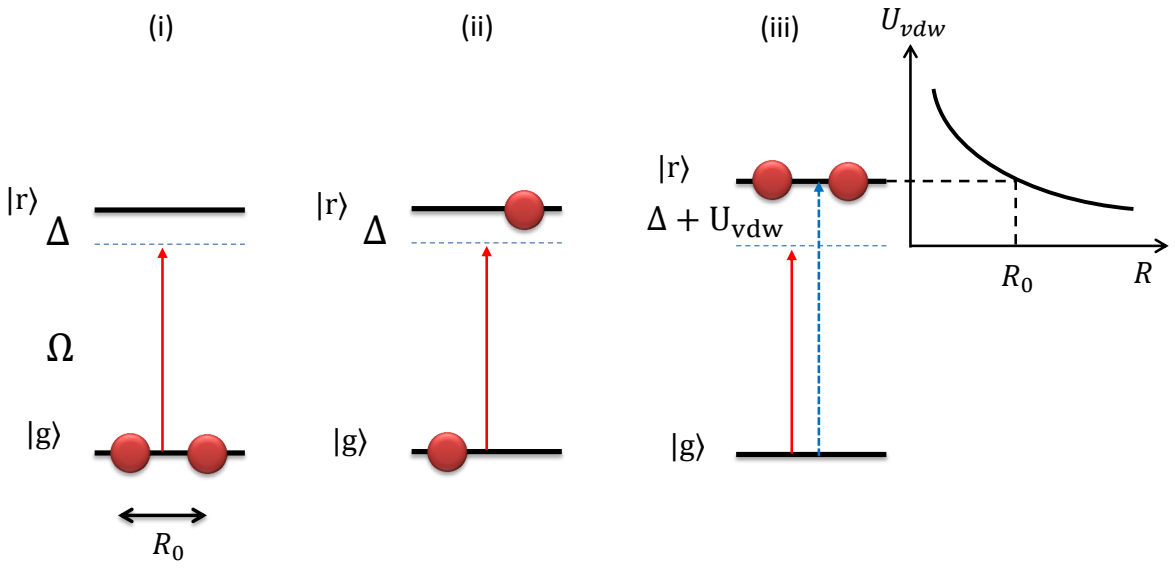

Figure 6.2: Schematic illustration of a two-atom, two-level interacting system. Laser light with Rabi rate Ω and detuning Δ couples the ground state $|g\rangle$ to Rydberg state $|r\rangle$. The energies of states (i) $|gg\rangle$ and (ii) $|gr\rangle$ are almost independent of interatomic separation due to the tiny Van der Waals interaction. However, the coupling from $|gr\rangle \to |rr\rangle$ depends on the interatomic spacing R because the energy level is shifted by the strong Van der Waals energy $U_{\rm vdw}$ (shown in (iii)). For a blue-detuned coupling light (blue arrow), there exists a interatomic separation R_0 satisfying $U_{\rm vdw}(R_0) = -\Delta$ that a two-photon resonance between $|gg\rangle$ and $|rr\rangle$ occurs.

in cold atom systems. Coherent coupling between the ground state and a Rydberg state by a laser field produces a new eigenstate of an atom called a Rydberg-dressed state. Considering a two-atom, two-level system, the ground states $|g\rangle$ are coupled to the Rydberg state $|r\rangle$ by laser light with detuning Δ and Rabi rate Ω. We choose the basis as $|gg\rangle$, $\frac{1}{\sqrt{2}}(|gr\rangle + |rg\rangle)$, and $|rr\rangle$. The Hamiltonian in the rotating frame is

$$H = \hbar \begin{pmatrix} 0 & \frac{\Omega}{\sqrt{2}} & 0 \\ \frac{\Omega}{\sqrt{2}} & \Delta & \frac{\Omega}{\sqrt{2}} \\ 0 & \frac{\Omega}{\sqrt{2}} & 2\Delta + U_{vdw}(R)/\hbar \end{pmatrix}, \tag{6.4}$$

where $U_{vdw}(R) = C_6/R^6$ is the Van der Waals interaction energy for two Rydberg atoms separated by a distance R. The antisymmetric state $\frac{1}{\sqrt{2}}(|gr\rangle - |rg\rangle)$ is ignored, because it cannot be coupled to the other states by the laser field.

Rydberg-dressed interaction

It is straightforward to obtain the eigenenergies and eigenstates by diagonalizing this matrix. Because of the interaction between atoms, the eigenenergies depend on the interatomic spacing. Figs. 6.3(a) and (c) show the energy levels for a repulsive Rydberg-Rydberg interaction $C_6 = 2\pi\times1000$MHz with Rabi rate $\Omega = 2\pi\times5$MHz,

for (a) red-detuned light ($\Delta = 2\pi \times 50$MHz) and (b) blue-detuned light ($\Delta = -2\pi \times 50$MHz). Figs. 6.3(b) and (d) show the interaction energy $V(\vec{r})$ for the Rydberg-dressed state from the two-atom interaction by subtracting the AC stark shift induced by the coupling laser.

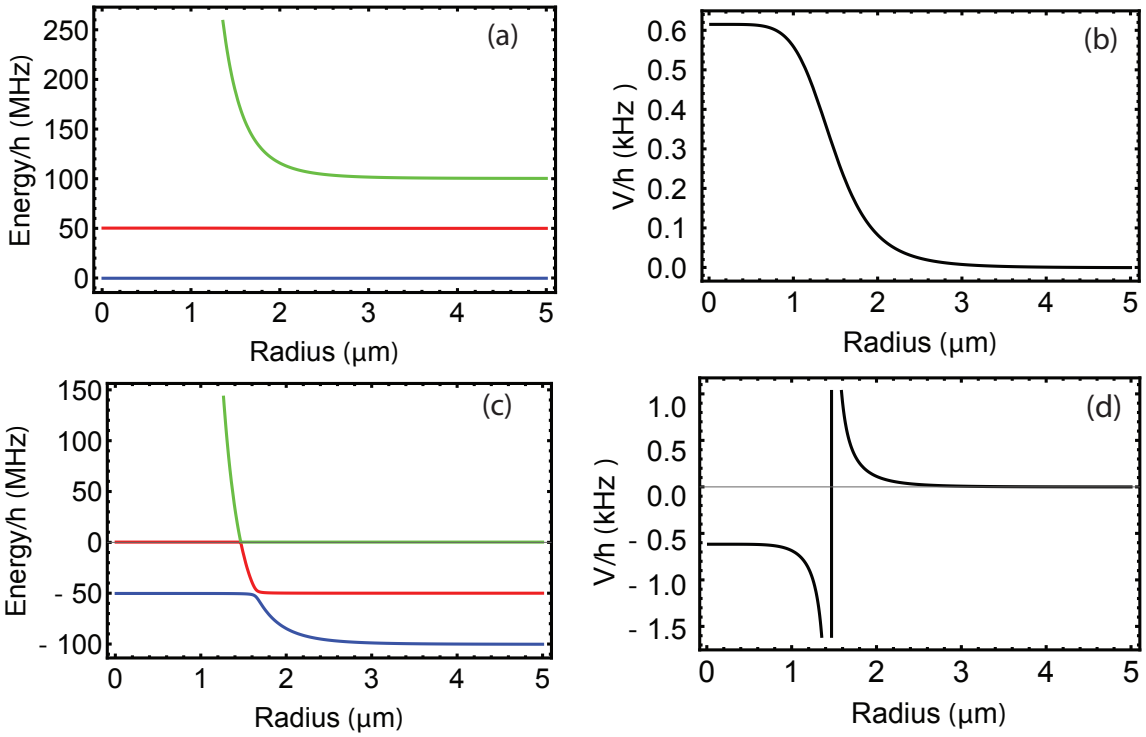

Figure 6.3: The eigenenergy levels and the interaction potential for a Rydberg-dressed state in a two-level, two-atom system., with $C_6 = 2\pi \times 1000$MHz. The coupling light has Rabi rate $2\pi \times 5$MHz. Panels (a) and (b) are for the red-detuned case, with $\Delta = 2\pi \times 50$MHz. Panels (c) and (d) are for the blue-detuned case, with $\Delta = -2\pi \times 50$MHz. With the presence of the coupling light, the eigenstates are a mixture of $|g\rangle$ and $|r\rangle$. The property of the effective interaction between Rydberg-dressed states depends on the sign of Δ. For $\Delta < 0$, $V(R)$ has a repulsive soft-core potential, while for $\Delta > 0$, $V(R)$ becomes repulsive and diverges at $R = (-C_6/2\Delta)^{1/6}$.

With a repulsive Van der Waals force, the interaction potential is repulsive for red-detuning. As the interatomic separation approaches zero, the interaction strength saturates and becomes independent of R. This is a result of the Rydberg blockade effect [195,196], which involves the strong Van der Waals interaction shifting the $|rr\rangle$ state such that exciting two Rydberg states within a small separation is strongly suppressed (see (iii) in Fig. 6.2). This soft-core interaction can extend to a distance comparable to $2-3$ lattice sites, and the tail of this potential follows a $1/R^6$ scaling at large R.

On the blue-detuned side, the interaction potential becomes attractive, and an avoided crossing occurs at $2\Delta = -C_6/R^6$, such that $V(R)$ diverges at $R = (-C_6/2\Delta)^{1/6}$. This corresponds to a two-photon resonance with the interaction-shifted $|rr\rangle$ state, as shown by the blue arrow in Fig. 6.8(iii). Inside this radius, $V(R)$ is almost independent of R.

Because we are interested in the weak coupling region, where $\Omega/\Delta \ll 1$, we can use perturbation theory to expand the ground-state energy shift in terms of Ω/Δ. Up to fourth order in Ω/Δ, we have:

$$\begin{aligned} V(R) &= \frac{|\langle gg| H \frac{1}{\sqrt{2}}(|gr\rangle + |rg\rangle)|^2}{\Delta} + \frac{|\langle gg| H \frac{1}{\sqrt{2}}(|gr\rangle + |rg\rangle) \frac{1}{\sqrt{2}}(\langle gr| + \langle rg|) H |rr\rangle|^2}{(\hbar\Delta)^2(2\hbar\Delta + U(R)/\hbar)} \\ &= \frac{\hbar^2\Omega^2}{2\Delta} + \frac{\hbar^4\Omega^4/4}{(\hbar\Delta)^2(2\hbar\Delta + U(R))} \\ &= \frac{\hbar^2\Omega^2}{2\Delta} + \frac{\Omega^4}{8\Delta^3} \cdot \frac{1}{1 + U(R)/2\hbar\Delta}, \end{aligned} \tag{6.5}$$

Omitting the term independent of R, the leading order in Rydberg-dressed interaction is

$$V(R) = \frac{\Omega^4}{8\Delta^3} \cdot \frac{1}{1 + (R/R_c)^6}, \tag{6.6}$$

where $R_c \equiv (\frac{C_6}{2\hbar\Delta})^{1/6}$. The saturation of $V(R)$ to $\frac{\Omega^4}{8\Delta^3}$ as $R \to 0$ is evident from this expression.

Eq. 6.6 indicates that the characteristic length scale of the Rydberg-dressed interaction is R_c, which is determined solely by the detuning Δ and the quantum principle number n. By coupling to a Rydberg state with $n \approx 50$, R_c can be comparable to several lattice spacings with a few MHz detuning (Fig. 6.4).

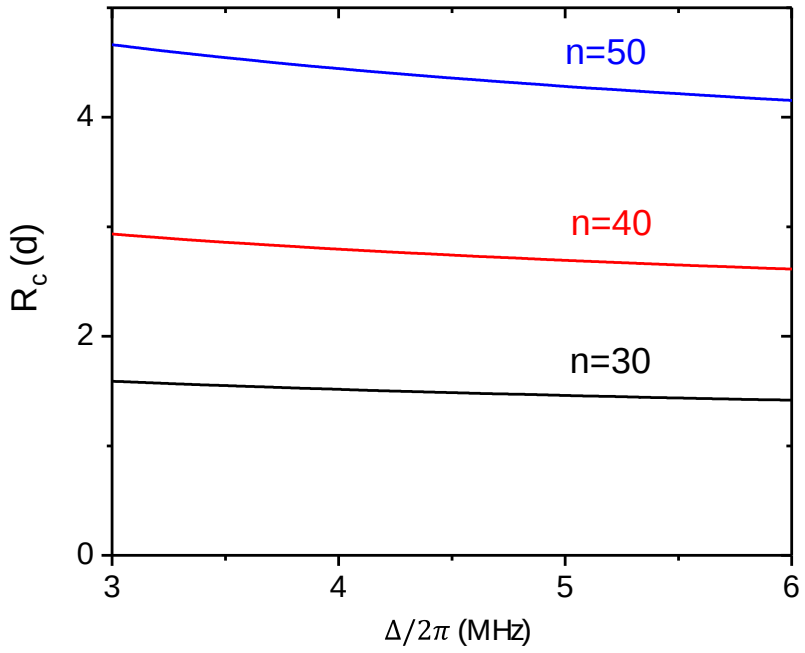

Figure 6.4: Dependence of $R_c \equiv (\frac{C_6}{2\hbar\Delta})^{1/6}$ (in units of the lattice spacing d) at various detuning for $n = 30$ (black), $n = 40$ (red) and $n = 50$ (blue).

The Rydberg-dressed interaction energy, defined as $V_m = V(R=0) - V(R \to \infty)$, at various detuning Δ with fixed $\Omega = 2\pi \times 5$MHz is plotted in Fig. 6.5. The solid line shows the result from exact diagonalization, and the dashed line is the perturbative result, $V_m = \Omega^4/8h\Delta^3$. The agreement is good for $|\Delta| > 5|\Omega|$.

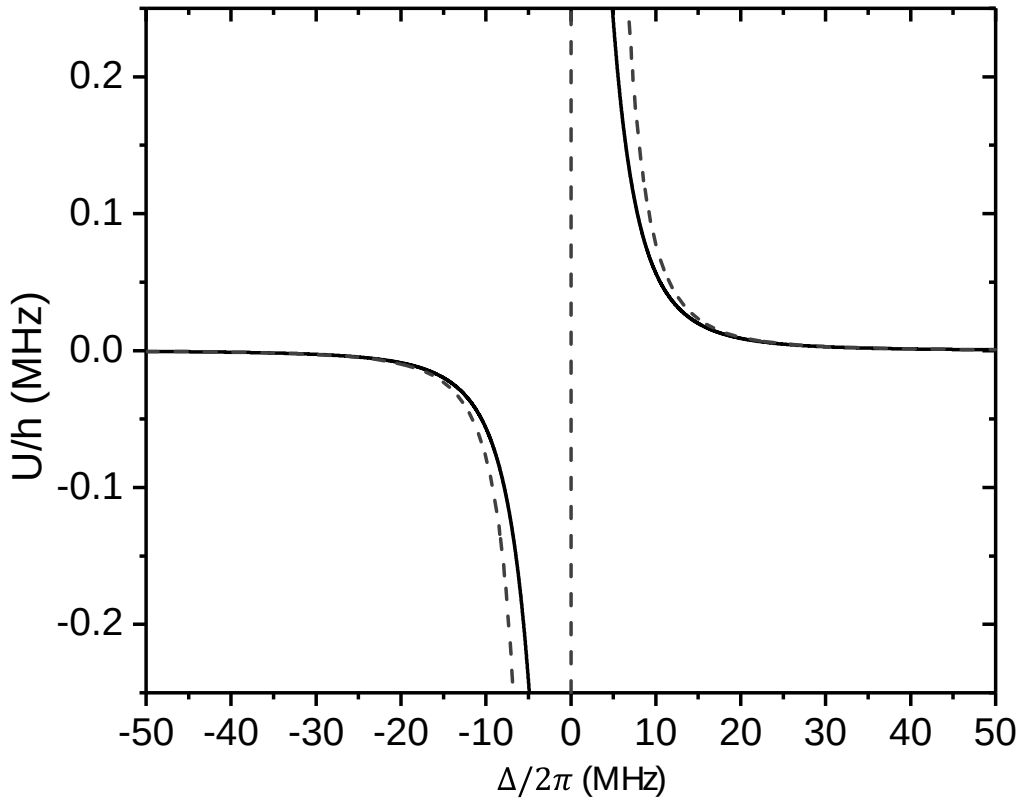

Figure 6.5: Dependence of Rydberg dressing interaction energy on laser detuning, with $\Omega = 2\pi \times 5$MHz. The solid line shows the results from exact diagonalization of Eq. 6.4. The dashed line corresponds to a perturbative result up to fourth order in Ω/Δ.

6.2.3 More than two atoms

Understanding more than two interacting atoms is a generally difficult problem. Here we only consider a simple case, with three atoms fixed to the vertices of an equilateral triangle with sides of length R, as shown

in the inset to Fig. 6.6(b). Due to the symmetry of the geometry, the Hamiltonian can be written as

$$H = \hbar \begin{pmatrix} 0 & \frac{\sqrt{3}}{2}\Omega & 0 & 0 \\ \frac{\sqrt{3}}{2}\Omega & \Delta & \Omega & 0 \\ 0 & \Omega & 2\Delta + U_{vdw}(R) & \frac{\sqrt{3}}{2}\Omega \\ 0 & 0 & \frac{\sqrt{3}}{2}\Omega & 3\Delta + 3U_{vdw}(R) \end{pmatrix}, \tag{6.7}$$

in the basis of $|ggg\rangle$, $\sqrt{\frac{1}{3}}\{|rgg\rangle + |grg\rangle + |ggr\rangle\}$, $\sqrt{\frac{1}{3}}\{|grr\rangle + |rgr\rangle + |rrg\rangle\}$, and $|rrr\rangle$.

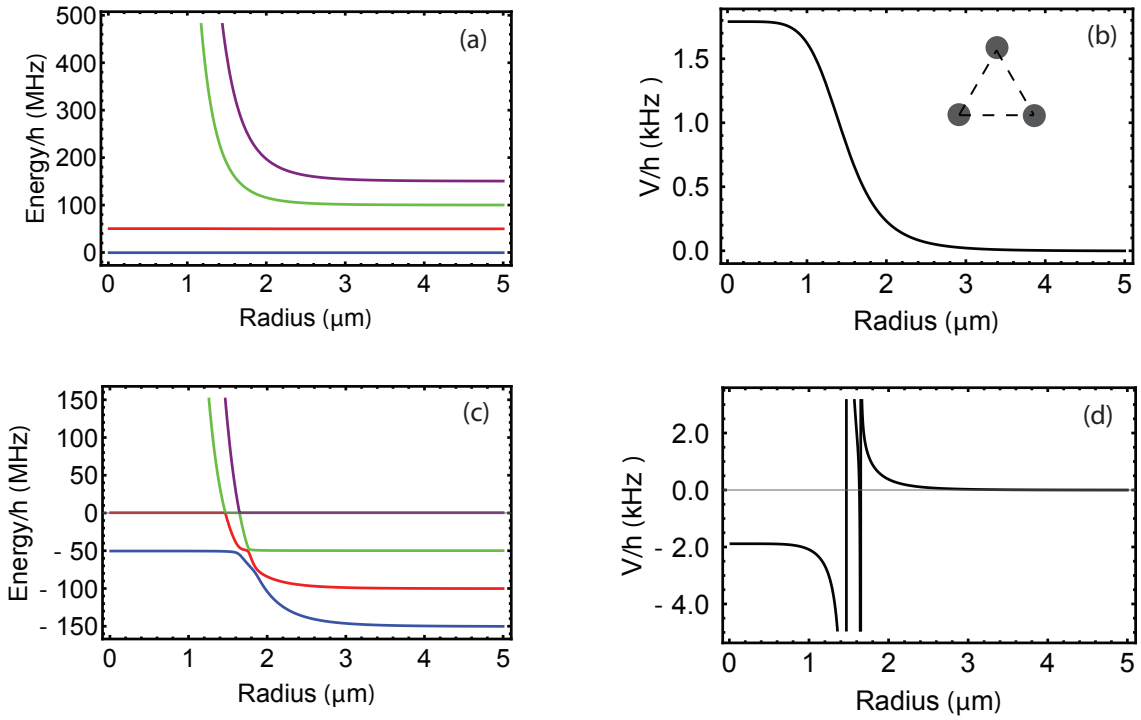

Figure 6.6: The eigenenergies and interaction potential for Rydberg-dressed states in a two-level, three-atom system. For simplicity, the geometry of the three atoms is fixed to an equilateral triangular. The same values of Ω and C_6 are used as for Fig. 6.3. For $\Delta = 2\pi \times 50$MHz, the behavior of eigenenergy levels and potential is similar to the two-atom case ((a) and (b)), with a maximum interaction strength larger by a factor of two. However, for $\Delta = -2\pi \times 50$, another avoided crossing occurs at a radius where $3\Delta = 3U_{vdw}(R)/\hbar$, corresponding to a three-photon resonant process.

Fig. 6.6 plots the eigenenergies and the interaction potential $V(R)$ between Rydberg-dressed states for $\Delta = 2\pi \times 50$MHz ((a) and (b)) and $\Delta = -2\pi \times 50$MHz ((c) and (d)). The blue detuned side has two avoided crossings, occurring at $2\Delta = -C_6/R^6$ and $3\Delta = -C_6/R^6$. The behavior on the red-detuned side is similar to the two-atom case, but the overall Rydberg-dressed interaction energy is roughly a factor of two larger. This result here suggests that it is preferable to work in a red-detuned regime to avoid multiple energy level

crossings and to magnify the energy shift due to Rydberg-dressed interactions.

6.3 Experimental approach to realize Rydberg-dressed states in potassium

6.3.1 Two-photon excitation

Directly coupling the ground and Rydberg state has been realized experimentally in Rb [179], using 297nm light generated by two-step frequency doubling. We prefer to work with a wavelength that can be generated using diode lasers. For potassium, the energy separation between the $4S_{1/2}$ and $30S_{1/2}$ states corresponds to a laser wavelength of about 300nm [197], which is not compatible with using diode lasers.

Therefore, we plan to implement Rydberg dressing using a three-level system. Instead of coupling to the Rydberg state directly, we employ a two-photon transition with $5P_{1/2}$ as an intermediate state (Fig. 6.8(a)). The transition wavelength for $4S_{1/2} \rightarrow 5P_{1/2}$ is 404.8nm; laser diodes at that wavelength are commercially available thanks to the development of BluRay. The transition wavelength from the intermediate $5P_{1/2}$ state to a high $nS_{1/2}$ state with $n \approx 20 - 50$ is approximately 1004-976nm, and high power diode laser and tapered amplifier are available in that wavelength range. Using the $5P$ state as an intermediate level enhances the Rydberg dressed lifetime compared with the D2 transition employed in experiments with Rb so far, since its natural lifetime is approximately six times longer. Also, compared to the $4S_{1/2} \rightarrow 4P_{1/2}$ D1 line in K, the electric dipole matrix element $\langle 5P_{1/2}| \, er \, |nS_{1/2}\rangle$ is more than a factor of two larger. As I will discuss, the limited Rabi rate for the $5P_{1/2} \rightarrow nS_{1/2}$ transition is one of the biggest challenges to implementing this scheme.

6.3.2 Effect of the intermediate state

Although coupling to the Rydberg state using the $5P_{1/2}$ state as an intermediate state is experimentally convenient, it has some deleterious effects.

Consider a three-level ladder system, as shown in the schematic energy diagram in Fig. 6.8. The Rabi frequency and the detuning are Ω_1 and Δ_1 for the blue laser, and Ω_2 and Δ_2 for the near-infrared (NIR) laser. The total detuning for this two-photon process is $\Delta = \Delta_1 + \Delta_2$. Similar to the analysis in the previous section, with a basis $|gg\rangle$, $(|gm\rangle + |mg\rangle)/\sqrt{2}$, $|mm\rangle$, $(|mr\rangle + |rm\rangle)/\sqrt{2}$, $|rr\rangle$, and $(|gr\rangle + |rg\rangle)/\sqrt{2}$,

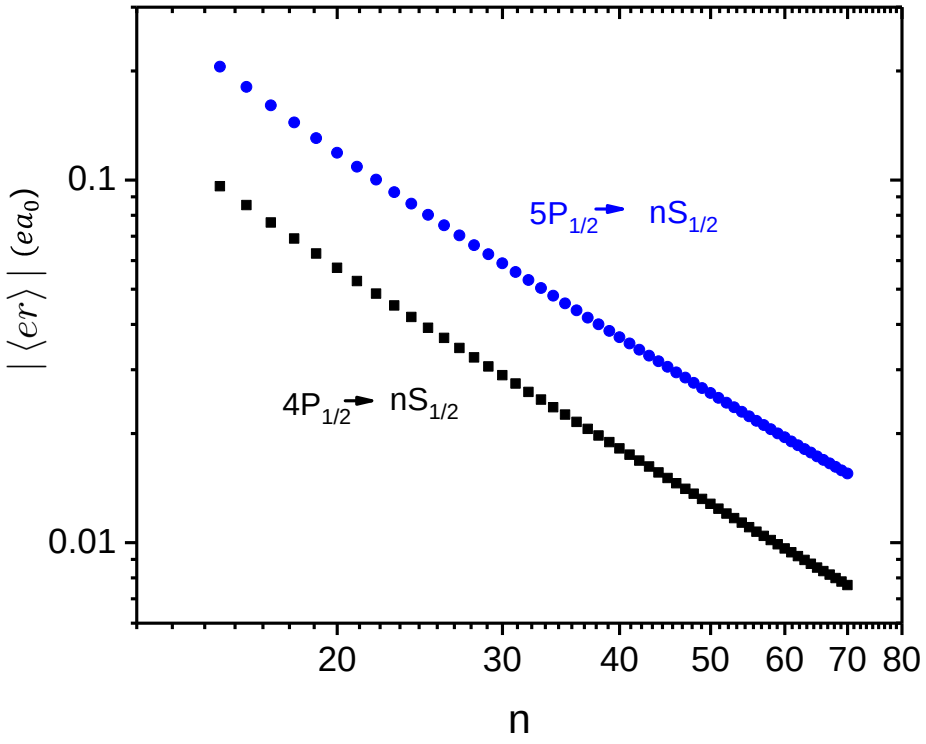

Figure 6.7: Electric dipole matrix element for $\langle 4P_{1/2}|\, er\,|nS_{1/2}\rangle$ (black) and $\langle 5P_{1/2}|\, er\,|nS_{1/2}\rangle$ (blue). We evaluate dipole matrix elements using numerical integration as $\int R_{n=4,l=1}(r) er R_{n,l=0}(r) r^2 dr$.

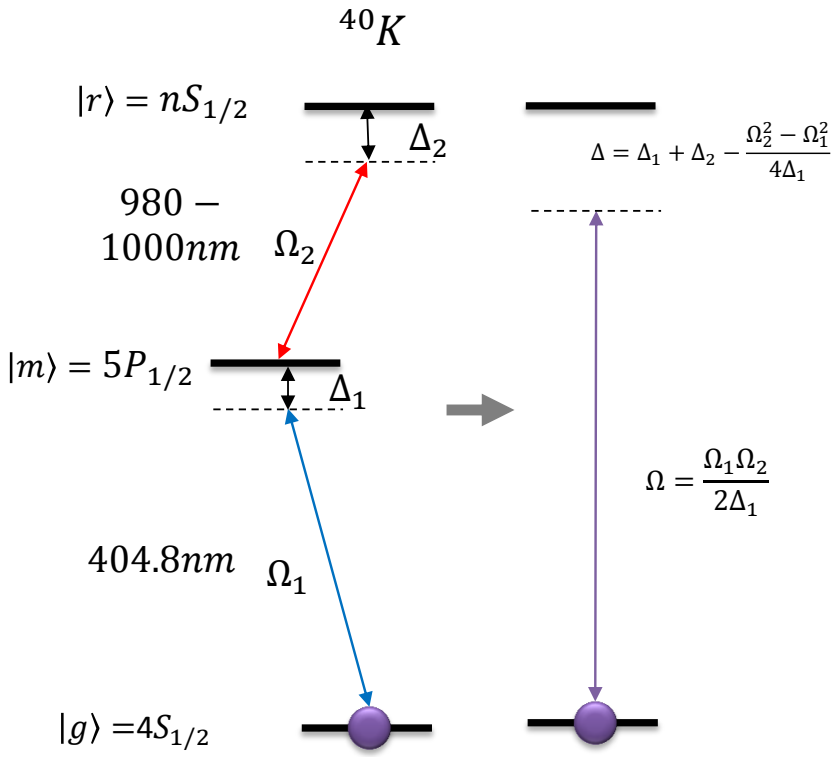

Figure 6.8: We will use a two-photon transition to excite Rydberg states in potassium through the intermediate state $|m\rangle = |5P_{1/2}\rangle$. The wavelength of light that couples these two transitions is 404.8nm and 980 − 1000nm. The corresponding Rabi rates and detunings are defined as labelled in this figure. If $\Delta_1 \gg \Omega_1$ and $\Delta_2 \gg \Omega_2$, the three-level system can be approximated as a two-level system, with effective Rabi frequency $\Omega = \frac{\Omega_1\Omega_2}{2\Delta_1}$ and detuning $\Delta = \Delta_1 + \Delta_2 - \frac{\Omega_2^2 - \Omega_1^2}{4\Delta_1}$.

the Hamiltonian in the rotating frame is written:

$$\hat{H}_{3,2\text{-}atom} = \hbar \begin{pmatrix} 0 & \Omega_1/\sqrt{2} & 0 & 0 & 0 & 0 \\ \Omega_1/\sqrt{2} & \Delta_1 & \Omega_1/\sqrt{2} & 0 & 0 & \Omega_2/2 \\ 0 & \Omega_1/\sqrt{2} & 2\Delta 1 & \Omega_2/\sqrt{2} & 0 & 0 \\ 0 & 0 & \Omega_2/\sqrt{2} & 2\Delta_1+\Delta_2 & \Omega_2/\sqrt{2} & \Omega_1/2 \\ 0 & 0 & 0 & \Omega_2/\sqrt{2} & 2(\Delta_1+\Delta_2)+U_{vdw}/\hbar & 0 \\ 0 & \Omega_2/2 & 0 & \Omega_1/2 & 0 & \Delta_1+\Delta_2 \end{pmatrix}. \tag{6.8}$$

Antisymmetric states such as $(|gm\rangle - |mg\rangle)/\sqrt{2}$ cannot be coupled to the other states by the laser fields and therefore are ignored.

Eigenenergies and interactions

Compared to a two-level two-atom, the situation here is more complicated. Whether the effective interaction between Rydberg-dressed atoms is repulsive or attractive depends not only on the sign of $\Delta_1 + \Delta_2$, but also the sign of $\Omega_1^2 - \Omega_2^2$, if $\Omega_1^2 - \Omega_2^2$ is comparable to Δ_1. Also, the lifetime for the intermediate state is about a factor of 20-30 shorter compared to the Rydberg state. To achieve a reasonable lifetime of the Rydberg-dressed state, smaller population in $|m\rangle$ is preferred. Therefore we are only interested in the case where the population in the intermediate state is very tiny, *i.e.*, $\Delta_1 \gg \Omega_1$ and $\Delta_1 \gg \Omega_2$. In the following discussion, we choose $\Omega_1 = 2\pi \times 40$MHz, $\Omega_2 = 2\pi \times 200$MHz, and $\Delta_1 = 10$GHz, which are experimentally achievable.

The lowest three eigenenergy levels and $V(r)$ are plotted in Fig. 6.9, with $\Delta_2 = -\Delta_1 + 2\pi \times 5$MHz for (a) and $\Delta_2 = -\Delta_1 - 2\pi \times 5$MHz for (b). Both have the same qualitative behavior as the two-level two-atom case.

Population in the intermediate state

With the presence of an intermediate state, the wavefunction of the Rydberg-dressed state involves three components: $|\psi\rangle = \sqrt{1 - f'^2 - f^2}\,|g\rangle + f'\,|m\rangle + f\,|r\rangle$. Fig. 6.10 plots the population P in $|g\rangle$ (red line), $|m\rangle$ (black line), and $|r\rangle$ (blue line), with an interatomic spacing $R = 0.4\mu$m, which is approximately the lattice spacing. The inset shows the population in the $|m\rangle$ state, which has a tiny contribution to $|\psi\rangle$. The minimum value of P_m occurs at $\Delta = 0$ (for a non-interacting system, this minimum value is exactly zero, *i.e.*, the so-called "dark state"). The peak of P_r and P_g shift toward the red-detuned side due to the AC Stark effect, which gives an energy shift $(\Omega_2^2 - \Omega_1^2)/4\Delta_1 = 2\pi \times 0.96$MHz. In addition, unlike a non-interacting

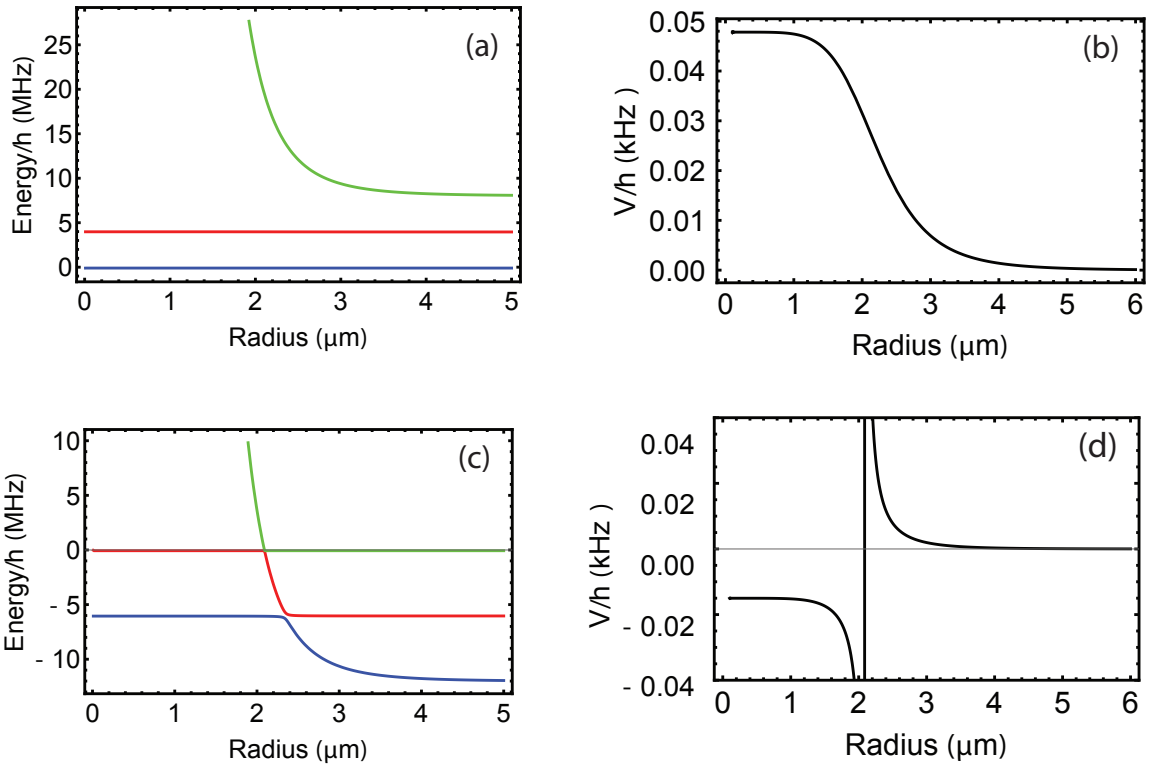

Figure 6.9: Energy levels and the interaction potential for the Rydberg-dressed states in a three-level, two-atom system. To suppress the population in the intermediate state, a large Δ_1 is preferred. Here, $\Delta_1 = 2\pi \times 10$GHz, $\Omega_1 = 2\pi \times 40$MHz, $\Omega_2 = 2\pi \times 200$MHz and $C_6 = 2\pi \times 1000$MHz. Because of the large detuning from the intermediate state, this three-level system presents a qualitatively similar behavior as a two-level system.

three-level system, the Rydberg-dressed interaction causes the maximum value of P_r to deviate from 0.5.

Indeed, due to the position-dependent Rydberg-Rydberg interactions $U_{\mathrm{vdw}}(R)$, f and f' both depend on R, especially near resonance. Fig. 6.11 plots the case when $\Delta = (\Omega_2^2 - \Omega_1^2)/4\Delta_1 + 2\pi \times 0.4\mathrm{MHz}$. The population in the intermediate state P_m is enhanced roughly by 50% as $R \to \infty$. The dependence of P on R becomes less significant with increasing detuning. With $\Delta_2 = -\Delta_1 + 2\pi \times 5\mathrm{MHz}$, the change in $P(m)$ is less than 0.2%.

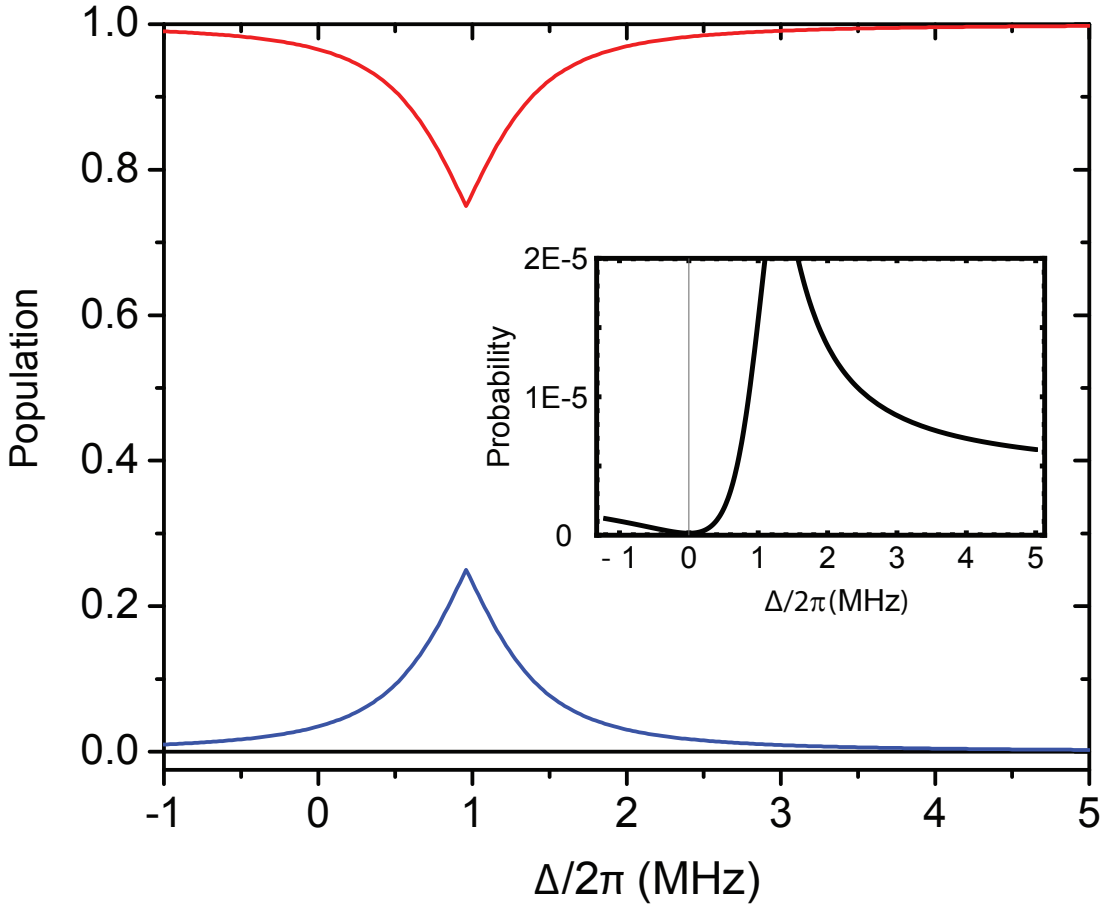

Figure 6.10: Population in ground state $|g\rangle$ (red), intermediate state $|m\rangle$ (black), and Rydberg state $|r\rangle$ (blue), for a two-atom, three-level system at various total detunings Δ. The peak position for P_r shifts to $\Delta = 2\pi \times 0.96\mathrm{MHz}$ due to the AC Stark effect. The inset shows P_m, which is strongly suppressed due to the large detuning Δ_1.

Lifetime

The most deleterious consequence of using an intermediate state $|m\rangle$ is its shorter lifetime. The total decay rate from the $5P$ state is $\Gamma_m = 7.5 \times 10^6 \mathrm{s}^{-1}$. For a Rydberg-dressed eigenstate $|\psi\rangle = \sqrt{1 - f'^2 - f^2}\,|g\rangle +$

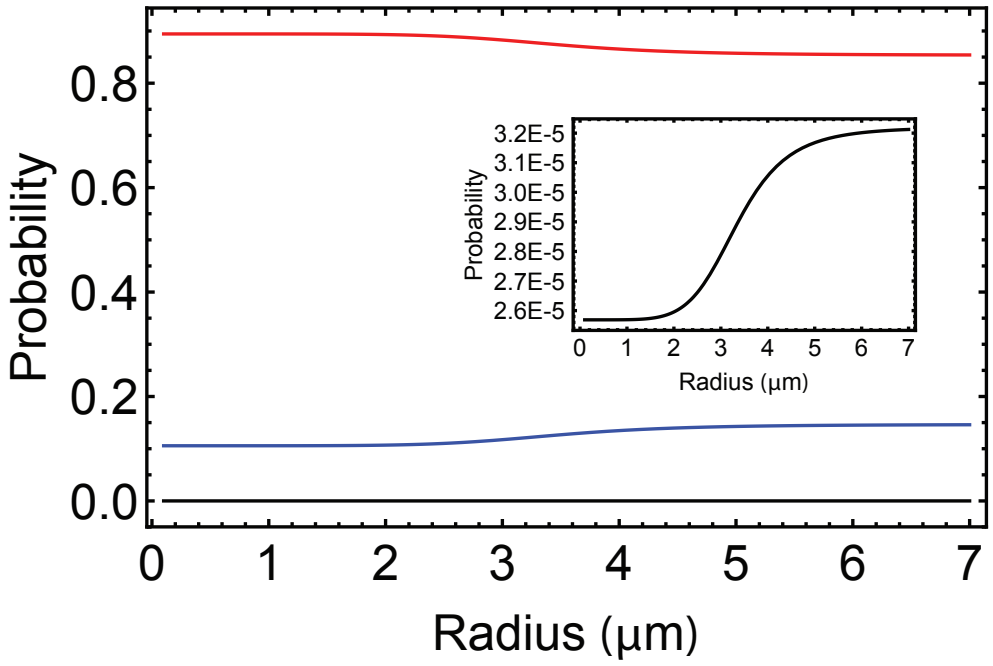

Figure 6.11: Dependence of P_g, P_m, and P_r on the interatomic spacing R, for $\Delta = (\Omega_2^2 - \Omega_1^2)/4\Delta_1 + 2\pi \times 0.4$MHz. The inset shows an expanded view for P_m.

$f'|m\rangle + f|r\rangle$, the effective scattering rate becomes $f'^2\Gamma_m + f^2\Gamma_r$, where Γ_m and Γ_r are the decay rates. Fig. 6.12 shows the effective lifetime τ_{eff} of the Rydberg-dressed state, with $\tau_{\text{eff}} = 1/(f'^2\Gamma_m + f^2\Gamma_r)$. At $\Delta = 2\pi \times 5$MHz, the lifetime is 1.5ms, which is long enough to perform spectroscopy measurements of the energy shift due to the Rydberg-dressing effect.

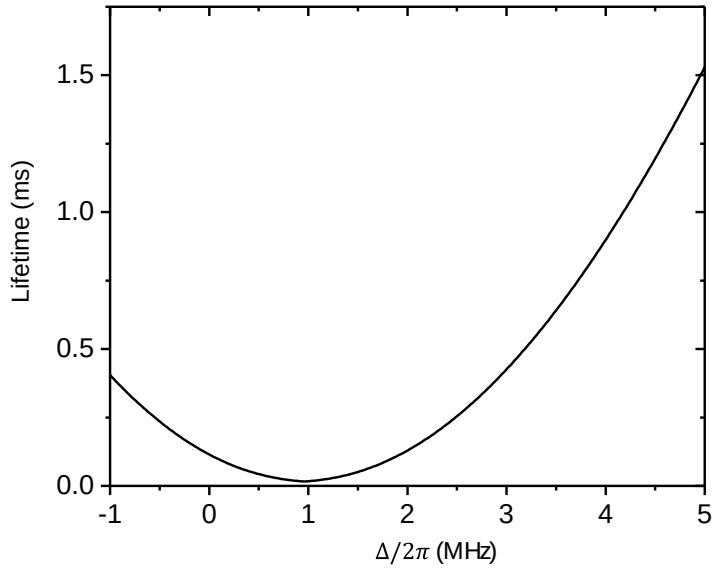

Figure 6.12: Estimated lifetime of Rydberg dressed state resulting from the decay of $|m\rangle$ and $|r\rangle$, with a separation between two atoms $R = 0.4\mu$m.

Approximation to a two-level system

As I have discussed, with a large detuning Δ_1 and total detuning $\Delta = 2\pi \times 5$MHz, the population in the intermediate state is comparatively small. Therefore, it is reasonable to reduce this three-level model to a two-level system. Ref. [198] gives a more general derivation for developing an effective two-level model for a three-level system. When the total detuning $\Delta = 0$, the three-level system can be exactly mapped to a two-level system. As discussed in Chapter 2, the Hamiltonian for the reduced two-level system is:

$$\hat{H}'_{\text{eff}} = \begin{pmatrix} -\Omega_1^2/4\Delta_1 & -\frac{\Omega_1\Omega_2}{4\Delta_1} \\ -\frac{\Omega_1\Omega_2}{4\Delta_1} & -\frac{\Omega_2^2}{4\Delta_1} + \Delta_1 + \Delta_2 \end{pmatrix}$$

As a check of the validity of this approximation, we compare the Rydberg-dressing interaction V_m obtained with the two-level approximation to exact diagonalization results of Eq. 6.8 (Fig. 6.13). The dashed line is from two-level approximation, which approaches the exact result at large Δ. We have also compared

the population in the $|g\rangle$ and $|r\rangle$ states and the time evolution of σ_{gg} and σ_{rr}. At our target detuning $\Delta = 2\pi \times 5$MHz, there is no observable difference between the two-level and three-level models.

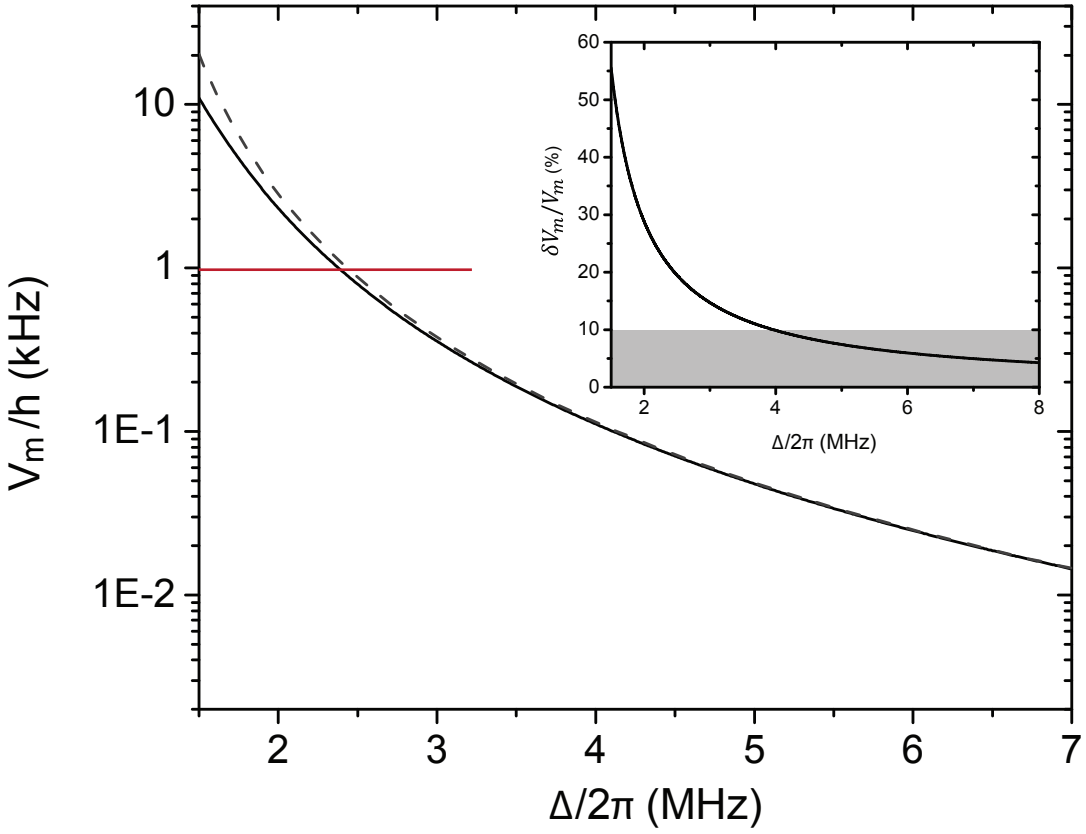

Figure 6.13: Comparison between Rydberg-dressed energy V_m at different total detunings Δ for a three-level system (solid line) and an effective two-level system (dashed line). The red line marks $V_z/h = 1$kHz. Frequency shifts larger than 1kHz are expected to be easily resolved experimentally. Inset: Sensitivity of V_z to Δ assuming a $2\pi \times 100$kHz change in Δ. $\delta V_m \equiv 2\pi 100\text{kHz} \times dV_m/d\Delta$. The gray shaded region covers values of $\delta V_m/V_m$ less than 10%.

6.3.3 Experimental feasibility

Whether we can achieve a detectable Rydberg-dressing interaction and have access to interesting quantum phases depends on three important inter-dependent parameters: the interaction range $R_c = (\frac{C_6}{2\hbar\Delta})^{1/6}$, the interaction energy V_m, and the lifetime τ_{eff} of the Rydberg-dressed state.

Because C_6 has the largest scaling exponent in $(n^*)^{11}$, R_c is mainly determined by n^* and is not sensitive to small changes in Δ (as shown in Fig. 6.4). For $n = 30 - 50$ and $\Delta = 2\pi \times 5$MHz, $R_c \approx 2 - 3$ lattice

spacings for our experiment.

Optimizing V_m and τ_{eff} is trickier, because increasing V_m is at the cost of reducing τ_{eff}. Generally speaking, large detuning Δ_1 and Rabi rate Ω_2 are preferred. Realistically, Ω_2 is limited by the NIR laser power and the minimum beam waist we choose to work with. To have a uniform Rydberg-dressing effect covering at least tens of lattice spacing, the beam waist cannot be too small. For $\Omega_2 = 2\pi \times 200$MHz, we need about 1.5W NIR laser power for a 30μm beam waist (which is limited by the numerical aperture of the lens).

Another experimental constraint is from the finite laser linewidth. The total detuning Δ cannot be too small, otherwise the variation in V_m induced by laser noise becomes too large. Assuming a 100kHz linewidth in laser light frequency, the inset in Fig. 6.13 shows $\delta V_m/V_m$, with $\delta V_m \equiv 2\pi 100\text{kHz} \times dV_m/d\Delta$. In order to reduce fluctuations in V_m less than 10%, Δ must exceed 4MHz, with a corresponding V_m/h smaller than 100Hz.

Detecting energy shifts smaller than 100Hz is experimentally challenging. However, V_m as calculated here only considers two-body effects. As discussed in the previous section, the energy shift is expected to scale roughly linearly with the number of atoms within R_c. Therefore, with $R_c \approx 2-3$ lattice spacing, V_m/h can exceed several kHz.

6.4 Detecting Rydberg states in potassium

As a first step towards observing Rydberg-dressing in ultracold ^{40}K gases, we need to locate the frequencies for the $4S_{1/2} \to 5P_{1/2}$ and $5P_{1/2} \to nS_{1/2}$ transitions. The transition between $4S_{1/2} \to 5P_{1/2}$ can be easily measured by standard saturation spectroscopy [199], while the transition between $5P_{1/2} \to nS_{1/2}$ has not been directly measured yet. On the other hand, although the absolute frequencies of the $4S \to nS$ transitions are known with approximately $\pm$10MHz uncertainty [200], the $4S \to 5P$ frequency has a relatively large reported $\pm$150MHz uncertainty [201] and, to our knowledge, a measurement of the absolute frequency had not been carried out prior to our work. Therefore, determining the $4S \to 5P$ wavelength and developing a method for spectroscopically resolving this transition is necessary step toward Rydberg dressing with ^{40}K.

For this purpose, we used electromagnetically induced transparency (EIT) [202] to probe Rydberg transitions for ^{39}K atoms contained in a heated vapor cell. The primary advantage of detecting Rydberg levels in ^{39}K is its high natural abundance compared with ^{40}K. The 235 ± 2 MHz isotope shift for the $4S_{1/2} \to 5P_{1/2}$ transition is known with high accuracy [203], and the approximately 100 MHz isotope shifts for the nS states with $n > 9$ are consistent with the Bohr mass shift within 1 MHz [204, 205]. Therefore, once the transitions

are identified using ^{39}K, the laser frequencies can be straightforwardly shifted using acousto-optic modulators to address ^{40}K.

6.4.1 Electromagnetically induced transparency (EIT)

The method we used to detect $5P \rightarrow nS$ transitions is based on electromagnetically induced transparency (EIT). EIT spectroscopy of Rydberg states has been achieved for Rb in a vapor cell at room temperature [206–208] and in cold gases [209, 210].

The principle of EIT effect involves a three-level ladder system, as shown in Fig. 6.14(a). The probe beam couples the ground state to the intermediate state with Rabi rate Ω_p and detuning Δ_p, while the coupling beam drives the transition from the intermediate state to the excited state with Rabi rate Ω_c and detuning Δ_c. Under the rotating wave approximation, the Hamiltonian describing this system can be written as

$$H = \hbar \begin{pmatrix} 0 & \frac{\Omega_p}{2} & 0 \\ \frac{\Omega_p}{2} & \Delta_p & \frac{\Omega_c}{2} \\ 0 & \frac{\Omega_c}{2} & \Delta_p + \Delta_c \end{pmatrix} \tag{6.9}$$

in the rotating frame. If we consider the case when $\Delta_p + \Delta_c = 0$, the eigenstates for this Hamiltonian become [202]

$$\begin{aligned} |+\rangle &= \sin\theta \sin\phi \, |g\rangle + \cos\phi \, |m\rangle + \cos\theta \sin\phi \, |r\rangle \\ |D\rangle &= \cos\theta |g\rangle - \sin\theta |r\rangle \\ |-\rangle &= \sin\theta \sin\phi \, |g\rangle - \sin\phi \, |m\rangle + \cos\theta \cos\phi \, |r\rangle \, , \end{aligned}$$

where θ and ϕ are the mixing angles, defined as $\tan\theta = \frac{\Omega_p}{\Omega_c}$ and $\tan 2\phi = \frac{\sqrt{\Omega_p^2 + \Omega_c^2}}{\Delta_p}$. While the $|\pm\rangle$ states are a superposition of all of the bare atomic states, $|D\rangle$ has no component from the intermediate $|m\rangle$ state, and is therefore a dark state. The probe beam can only couple to $|m\rangle$ through $|\pm\rangle$.

In the weak coupling limit ($\Omega_p \ll \Omega_c$), $\theta \rightarrow 0$, $\sin\theta \rightarrow 1$, and $\cos\theta \rightarrow 0$. If the probe beam is resonant ($\Delta_p = 0$), then it couples to the $|\pm\rangle$ states with equal amplitudes but opposite phases. Hence, destructive interference results in no absorption for the probe beam, and a transparency window appears.

A more complete analysis must take spontaneous decay from the excited states into consideration. Again, we use the Lindbald equation. In the weak coupling limit, we can assume $\sigma_{gg} = 1$, $\sigma_{mm} = 0$, and $\sigma_{rr} = 0$.

For the steady state $\frac{d}{dt}\sigma = 0$, one obtains:

$$\sigma_{gm} = \frac{i\Omega_p/2}{\Gamma_m/2 + i\Delta_p + \frac{\Omega_c^2/4}{\Gamma_r/2+i(\Delta_p+\Delta_c)}} \tag{6.10}$$

for the solution to the Lindbald equation. The complex susceptibility for the probe beam is related to the density matrix by $\chi = -\frac{2\rho_0 d_{gm}^2}{\epsilon_0 \hbar \Omega_p}\sigma_{gm}$ [211], where ρ_0 is the atomic density, and d_{gm} is the dipole matrix element. Hence the absorption, which is the imaginary part of the complex susceptibility, is:

$$\alpha = \mathtt{Im}\left[\chi\right]/\bar{\chi} = \mathtt{Im}\left[\frac{\Gamma_m/2}{\Gamma_m/2 + i\Delta_p + \frac{\Omega_c^2/4}{\Gamma_r/2+i(\Delta_p+\Delta_c)}}\right], \tag{6.11}$$

where $\bar{\chi} = 2\rho_0 d_{gm}^2/\ \epsilon_0\hbar\Gamma_m$ is the resonant susceptibility for the $|g\rangle$ to $|m\rangle$ transition.

Fig. 6.14.(a) and (b) show the absorption rate for the probe beam in two cases: (a) the coupling beam is locked to the resonant frequency while the probe beam is scanned; (b) the reverse situation, in which the probe beam is locked to the resonant frequency. In both cases, a transparency window appears near the resonant condition $\Delta_p + \Delta_c = 0$. This means once we can lock either beam to resonance, we can obtain the transition frequency for the other beam based on the EIT feature.

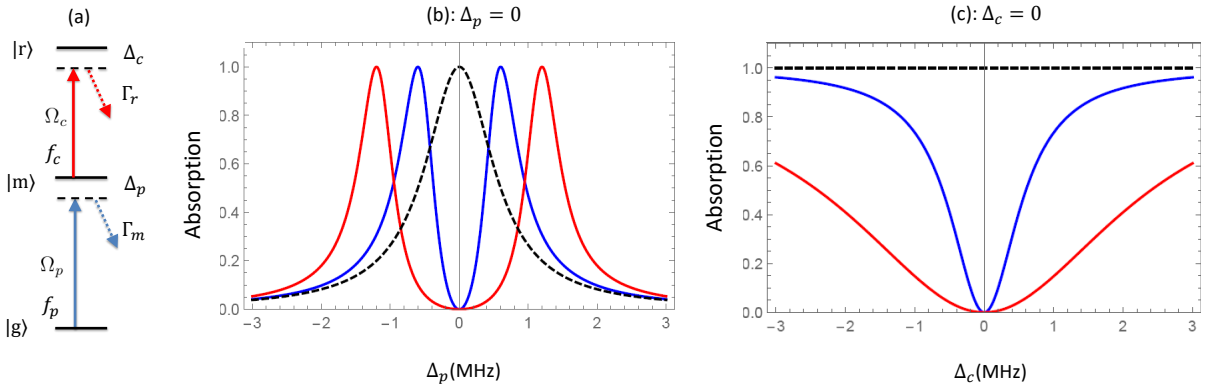

Figure 6.14: (a): A schematic diagram for an EIT 3-level system, with ground state $|g\rangle$, intermediate state $|m\rangle$ and Rydberg state $|r\rangle$. Probe light couples $|g\rangle$ and $|m\rangle$ with Rabi rate Ω_p and detuning Δ_p. The coupling light drives the transition between $|m\rangle$ and $|r\rangle$ with Rabi rate Ω_c and detuning Δ_c. The states $|m\rangle$ and $|r\rangle$ have a finite lifetime due to spontaneous emission. The decay rates are denoted as Γ_m and Γ_r respectively. The absorption for zero velocity atoms is plotted in (b) for a resonant coupling beam (while the frequency of probe beam is scanned) and in (c) for a resonant probe beam (while the frequency of coupling beam is scanned). A transparency window appears for both cases, and the linewidth of the EIT feature is proportional to Ω_c. Blue line: $\Omega_c/2\pi = \Gamma_p = 1.2$MHz, red line: $\Omega_c/2\pi = 2\Gamma_p = 2.4$MHz, and the black dashed line is a reference with $\Omega_c = 0$.

6.4.2 Dopper effect

For simplicity, we would like to carry out EIT spectroscopy in a room-temperature vapor cell. Hence, Doppler broadening must be considered. We initially did not expect any trouble from Doppler broadening, since counter-propagating coupling and probe beams are used to avoid Doppler effect for EIT measurements in Rb vapor cells. However, it turns out that whether or not this strategy works depend on the wavelength ordering for the coupling and probe beams. In our case, $\lambda_p < \lambda c$, and the Doppler effect eliminates the EIT signal (see Refs. [212] and [213] for a more general discussion of the Doppler effect for three-level systems).

To include the Doppler effect, Eq. 6.11 is rewritten as

$$\begin{aligned} \alpha(\beta) &= \frac{\Gamma_m/2}{\Gamma_m/2 + i(\Delta_p^{(0)} - f_c\beta) + \frac{\Omega_c^2/4}{i\left[\Delta^{(0)}+(f_c-f_p)\beta\right]}} \\ &= \frac{\Gamma_m/2}{\Gamma_m/2 + i\Delta_p^{(0)} + \frac{\Omega_c^2/4}{i\Delta^{(0)}} - if_p\beta + (f_c-f_p)\frac{\beta\Omega_p^2/4}{i\left[\Delta^{(0)}+(f_c-f_p)\beta\right])\Delta^{(0)}}}, \end{aligned} \tag{6.12}$$

where f_c, f_p denote the laser frequencies of the coupling and probe laser. The detuning for zero velocity atoms are $\Delta_p^{(0)}$ and $\Delta^{(0)} = \Delta_p^{(0)} + \Delta_c^{(0)}$. The parameter $\beta = v/c$, where v is the velocity in the laboratory frame, and c is the speed of light. The overall absorption is an average over the thermal distribution

$$\alpha_t = \int_{-\infty}^{\infty} d\beta G(\beta)\alpha(\beta), \tag{6.13}$$

where $G(\beta) = \frac{1}{\sqrt{2\pi}\bar{v}} e^{-\frac{\beta^2}{2(\bar{v}/c)^2}}$ is a normalized Gaussian function for the velocity distribution, with $\bar{v} = \sqrt{k_B T/m}$ as the mean speed.

Fig. 6.15 shows the result of thermal averaging. We compare two cases: the $4S_{1/2} \rightarrow 4P_{1/2} \rightarrow nS_{1/2}$ case, where $f_p < f_c$, and our case ($4S_{1/2} \rightarrow 5P_{1/2} \rightarrow nS_{1/2}$), where $f_p > f_c$. The black dashed lines gives a reference for the absorption without the coupling beam ($\Omega_c = 0$). The blue lines plot the absorption with $\Omega_c = \Gamma_m$. For the $4S_{1/2} \rightarrow 4P_{1/2} \rightarrow nS_{1/2}$ case, although the thermal average suppresses EIT, it is still detectable. On the other hand, the Doppler effect completely eliminates the EIT feature for $4S_{1/2} \rightarrow 5P_{1/2} \rightarrow nS_{1/2}$.

The sign of $f_c - f_p$ is important because the Doppler shift for the first transition in this ladder system is $\Delta_p - \Delta_p^{(0)} = -f_p\beta$, and the total detuning of the two-photon process is $\Delta - \Delta^{(0)} = (f_c - f_p)\beta$ (assuming counter-propagating probe and coupling beams). With positive $f_c - f_p$, these two shifts have the opposite sign and therefore cancel to some extent. Co-propagating pump and probe beams do not mitigate the Doppler effect for $f_c - f_p < 0$. In this case, the shift in total detuning is $(-f_c - f_p)\beta$, which always has the

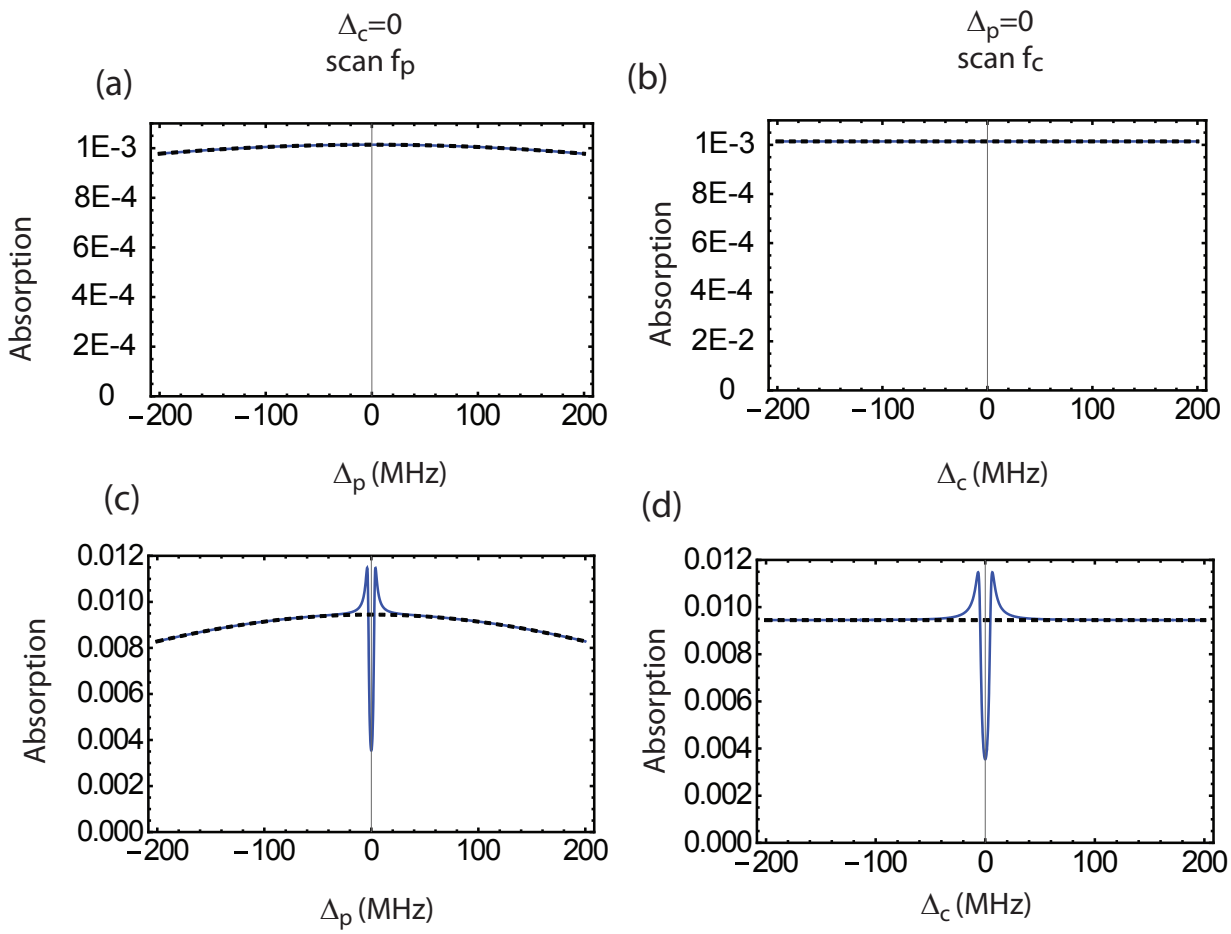

Figure 6.15: Absorption after averaging over a thermal velocity distribution. Panels (a) and (b) are for potassium with intermediate state $|m\rangle = 5P_{1/2}$ ($f_p > f_c$); (c) and (d) are for K with $|m\rangle = 4P_{1/2}$ ($f_c > f_p$). Blue line: $\Omega_c/2\pi = \Gamma_m$, which is 1.2MHz for the $4S_{1/2} \to 5P_{1/2}$ transition, and 5.9MHz for the $4S_{1/2} \to 4P_{1/2}$ transition. Black dashed line: $\Omega_c = 0$. The influence of the Doppler effect on EIT depends on the sign of $f_c - f_p$. For $|m\rangle = 5P_{1/2}$, EIT is absent, while for $|m\rangle = 4P_{1/2}$, though imperfect, the EIT feature is observable.

same sign as $\Delta_p - \Delta_p^{(0)}$.

Fig. 6.16 provides a more intuitive picture for understanding why the sign of $f_p - f_c$ matters. In this plot, the frequency of the coupling light is fixed to be resonant with the transition between the intermediate state and the Rydberg state, for zero velocity atoms. From top to bottom, the velocity of the atom increases, and the corresponding absorption for various probe frequencies is plotted. For the left column, with $f_c = 0.5f_p$, as v increases, the lower frequency peak of absorption moves to higher frequency, eventually intersecting the transparency window for zero velocity atoms. As a result, if we average over the velocity distribution, the transparency window vanishes. For the right column, with $f_c = 1.5f_p$, the influence of increasing v "squeezes" the lower frequency peak, but the position of the transparency window roughly remains unchanged. Therefore, the EIT feature survives!

6.4.3 Velocity-selective strategy

To overcome this unexpected effect, we developed a novel velocity selection scheme, that allows us to detect the EIT signal with a room-temperature vapor cell. Our idea is to ensure that the signal comes from atoms with a velocity within a narrow range near zero. Fig. 6.17 outlines our proof-of-principle approach for ^{39}K.

^{39}K has two hyperfine ground states, $F = 1$ and $F = 2$, as shown in Fig. 6.17. The energy separation between these two states is $h \times 462$MHz, and they are equally populated at room temperature. Our velocity selection scheme involves an optical pumping beam that couples the $F = 2$ ground state with the $5P_{1/2}$ state. This resonant pump beam burns a hole near $v = 0$ in the $F = 2$ velocity distribution (Fig. 6.17(a)) and transfers atoms to the $5P_{1/2}$ state. Atoms in the $5P_{1/2}$ state decay to the $F = 1$ and $F = 2$ ground states through spontaneous emission at a rate 1.07×10^6 s^{-1} [214]. Through standard optical pumping, an excess of atoms near $v = 0$ will be created in the velocity distribution of the $F = 1$ state. If the intensity of the optical pumping beam is chopped with a period much slower than the the time for inter-atomic collisions to redistribute the population imbalance between hyperfine states, the population hole and peak near $v = 0$ (Fig. 6.17(a)) will be modulated at the chopping frequency. The signal from the $v = 0$ atoms is then reconstructed by measuring the absorption of the probe beam synchronously with the chopping frequency via a lock-in amplifier.

A more general analysis reveals that the demodulated signal arises from two distinct velocity classes. In the rest frame of an atom with velocity $v = \beta c$, the Doppler-shifted frequency of the probe beam is $\tilde{f}_p = (1 - \beta)f_p$, and $\tilde{f}_{op} = (1 + \beta)f_{op}$ for the optical pumping beam (Fig. 6.17(b)). Since the demodulated signal is only non-zero for changes in the transmission of the probe caused by the optical pumping beam, the atom must be resonant with both beams. Hence, the demodulated signal is derived from atoms with

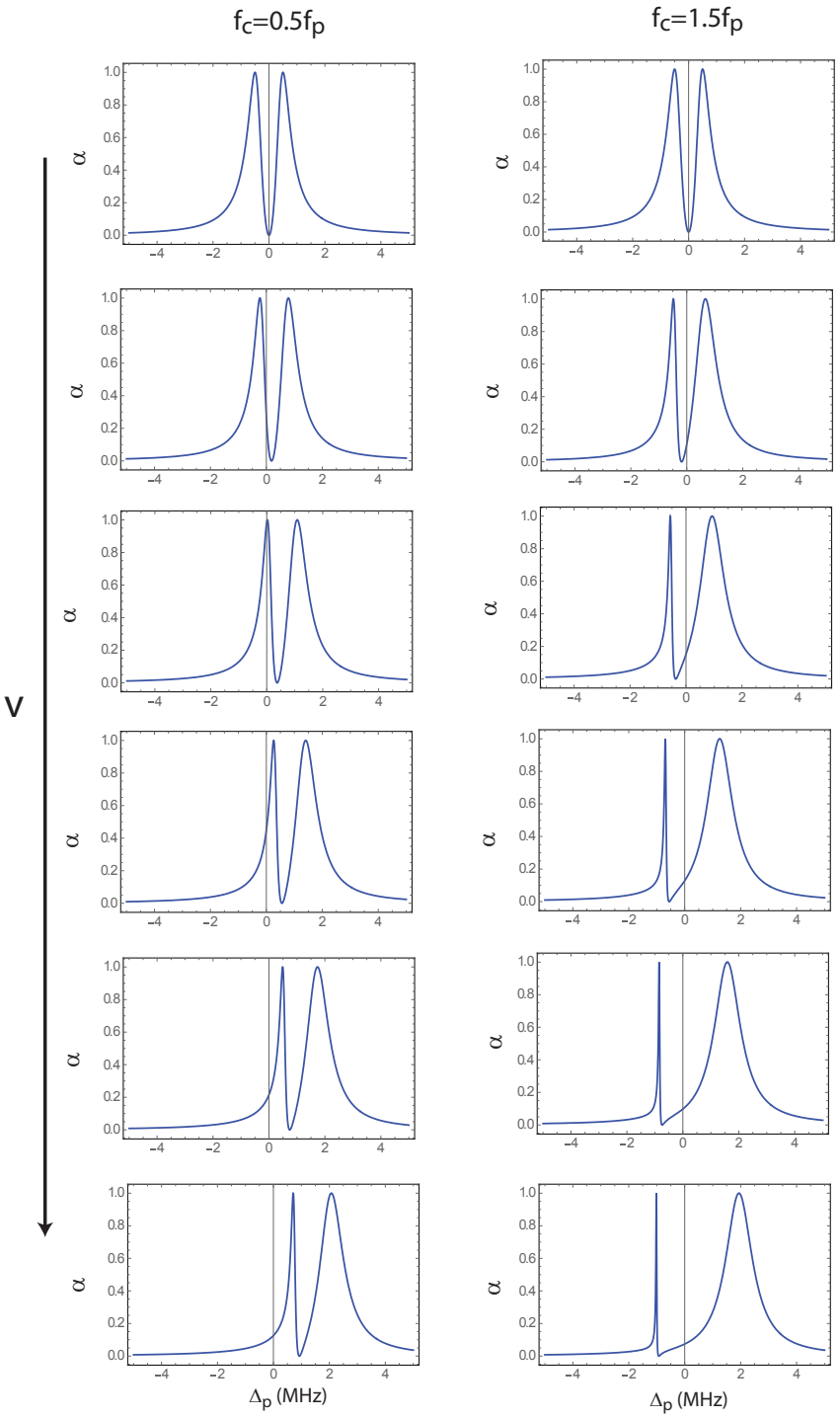

Figure 6.16: From top to bottom, the absorption is plotted for atoms with increasing velocity. In these plots, the absorption for single velocity atoms is shown, with a coupling light frequency fixed to be resonant for zero velocity atoms, and the probe laser frequency f_p is scanned. Left column ($f_c > f_p$): the lower frequency peak in the absorption spectroscopy moves toward the direction where the transparency window is for lower velocity atoms. Therefore, after averaging the absorption over the velocity distribution, the EIT feature vanishes. Right column ($f_c < f_p$): the lower frequency peak shrinks its width as the velocity of atoms increases. The position of the transparency window roughly stays at the same position, thereby robust to Doppler effect. As a result, an EIT feature exists even at room temperature.

velocities that satisfy

$$|(1+\beta)f_{op} - (1-\beta)f_p| = f_{hp},$$

or

$$\beta = \left[\pm f_{hp} - (f_{op} - f_p)\right]/(f_{op} + f_p).$$

Under the condition $f_p - f_{op} = f_{hp}$ (which is enforced in our experiment using an acousto-optic modulator), the velocity classes that give rise to a signal are $\beta = 0$ and $\beta = 2f_{hp}/(f_p + f_{op}) \approx f_{hp}/f_p$. The latter case corresponds to a velocity for which the optical pumping and probe beams in the atomic rest frame are exchanged compared with the zero-velocity case (inset of Fig. 6.17(a)), and the probe beam is resonant with the $4S, F = 2 \rightarrow 5P_{1/2}$ transition.

EIT for the probe beam is achieved when the overall detuning vanishes in the atomic rest frame, i.e., when $\tilde{f}_c + \tilde{f}_p$ is equal to the frequency difference f_0 between the $4S_{1/2}$ and $nS_{1/2}$ states, where $\tilde{f}_c$ is the frequency of the coupling beam in the rest frame of the atom. This condition for $\beta = 0$ is

$$f_c + f_p = f_0$$

and for $\beta = f_{hp}/f_p$ is

$$f_p(1-\beta) + f_c(1+\beta) = f_0 - f_{hp}.$$

With the probe beam stabilized to the $4S_{1/2}, F = 1 \rightarrow 5P_{1/2}$ transition, EIT will be observed for $f_c = f_0 - f_p$ (for the $v = 0$ atoms) and for $f_c = (f_0 - f_p)/(1 + f_{hp}/f_p) \approx f_0 - f_p - 190$ MHz (for the atoms with $v = cf_{hp}/f_p$). Two EIT features should therefore appear, separated by 190 MHz.

We perform a simulation to check our velocity-selection strategy can recover the EIT signal for potassium with $f_p > f_c$. In this simulation, only the atoms with velocity within a Lorentz distribution $L(\beta) = \frac{1}{\pi}\frac{\Gamma_v/2}{\beta^2 f_p^2 + (\Gamma_v/2)^2}$ contribute to the EIT signal, where Γ_v is the linewidth of this Lorentz distribution. Fig. 6.18 plots the ratio of absorption with and without the coupling beam for $\Gamma_v = \Gamma_e$; the EIT feature has become detectable.

6.5 Experimental setup for detecting the EIT signal

6.5.1 Oven for potassium vapor cell

The effective cross section for a Doppler broadened gas is $\sigma_{\text{eff}} = \sigma_r \sqrt{\pi \ln 2}\frac{\Gamma}{\Delta\omega_d}$ [111], where σ_r is the resonant absorption cross-section, Γ is the linewidth for the transition, and ω_d is the frequency broadening due to

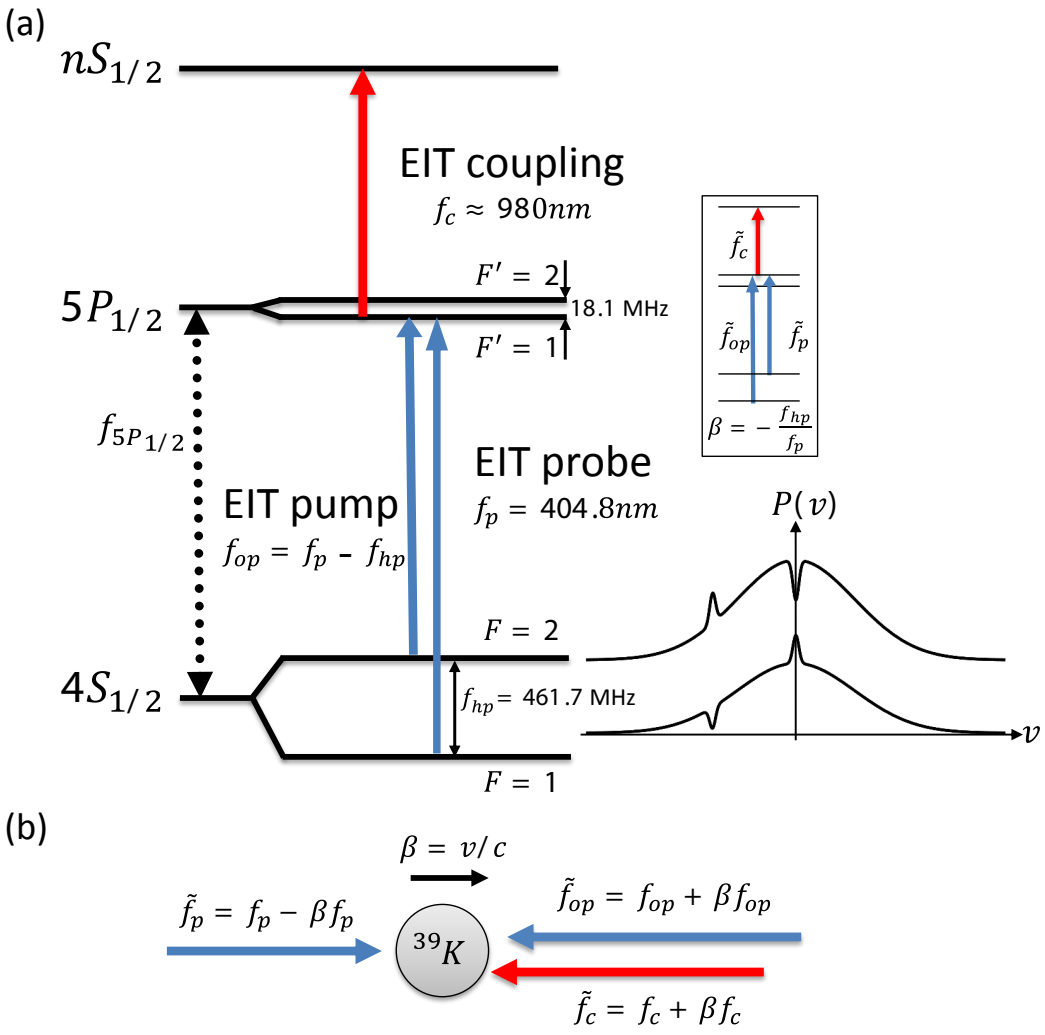

Figure 6.17: (a): Energy-level diagram of ^{39}K and corresponding transition wavelengths. The three-level ladder system used to perform the EIT measurement includes ground state $4S_{1/2}$, intermediate state $5P_{1/2}$, and Rydberg state $nS_{1/2}$. EIT pump beam is added to create an unbalance in the number of atoms within a narrow range near a certain velocity class. The Gaussian velocity distributions for the $F = 1$ and $F = 2$ states are shown. The peak and hole on the velocity distribution appear and disappear as the EIT pump beam is turned on and off. (b): Frequencies of pump beam $\tilde{f}_{pp}$, probe beam $\tilde{f}_p$, and coupling beam $\tilde{f}_c$ in the atomic frame, where $\beta = v/c$ and v is velocity. The inset shows the frequencies in the rest frame for atoms with velocity $\beta = -f_{hp}/f_p$, in which case the frequency of the EIT pump and probe beams are exchanged.

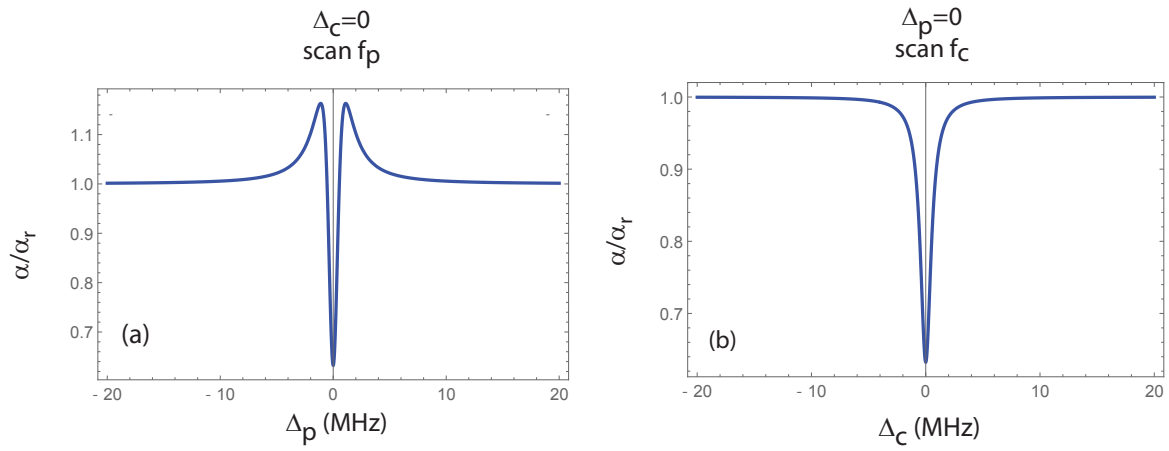

Figure 6.18: Numerical results of EIT signal with velocity-selection strategy. Assuming that the velocity of atoms is within a Lorentz distribution (with linewidth $\Gamma_v = \Gamma_e$), the change in absorption with and without coupling beam is plotted for (a): scanning probe frequency with fixed $\Delta_c = 0$ for zero velocity atoms, and (b): scanning coupling frequency with fixed $\Delta_p = 0$ for zero velocity atoms. α_r is the absorption for the probe transition.

Doppler effect. For the blue transition $4S_{1/2} \rightarrow 5P_{1/2}$ in potassium, compared with the D1 transition $4S_{1/2} \rightarrow 4P_{1/2}$, σ_r is a factor of 3.6 smaller, and the effective cross section is about a factor of 300 smaller at the same temperature. To increase the signal size for saturation spectroscopy, we heat the vapor cell to 85°C. The vapor pressure at 85°C is about 4×10^{-6}mbar, which is more than a factor of 100 compared to the vapor pressure at room temperature [16].

We constructed an oven to heat the cell (Fig. 6.19). The oven consists of a four-way cross (labeled as A in Fig. 6.19, from Kurt J. Lesker Company. C-0337-133), two nipples (B in Fig. 6.19, Kurt J. Lesker Company. FN-0337), two glass viewports (C in Fig. 6.19, Kurt J. Lesker Company. VPZL-337) for the main flanges, and two glass viewports for the side windows (D in Fig. 6.19, Kurt J. Lesker Company. VPZL-133). The side windows of the four-way cross are useful for monitoring spontaneous fluorescence light from the probe laser.

A home-made mount is used to hold the vapor cell inside this oven. This mount consists of two rings and four rods, as shown in Fig. 6.20(a) and (b). The outside dimension of the ring is roughly $0.1''$ smaller than the tube dimension of the oven, and the inside dimension of the ring is roughly $0.1''$ larger than the vapor cell dimension. The gaps between the mount, the vapor cell, and the oven are filled with aluminum foil.

Two flexible resistive heater are used to maintain the oven temperature, with three thermocouples inside the oven to monitor the temperature. To avoid potassium condensation on the window of vapor cell, we wrapped each heater tape close to the end of the 4-way cross. This allows us to heat the two ends of the vapor

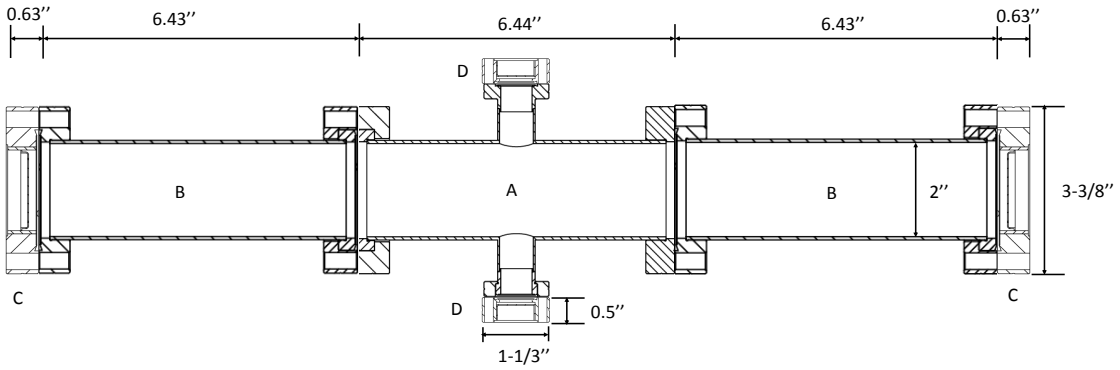

Figure 6.19: Drawings of the oven that heats up the potassium vapor cell. Oven consists of a four-way cross (labeled as A), two nipples (B), and four glass viewports (C and D). Drawings are from the vendor's website.

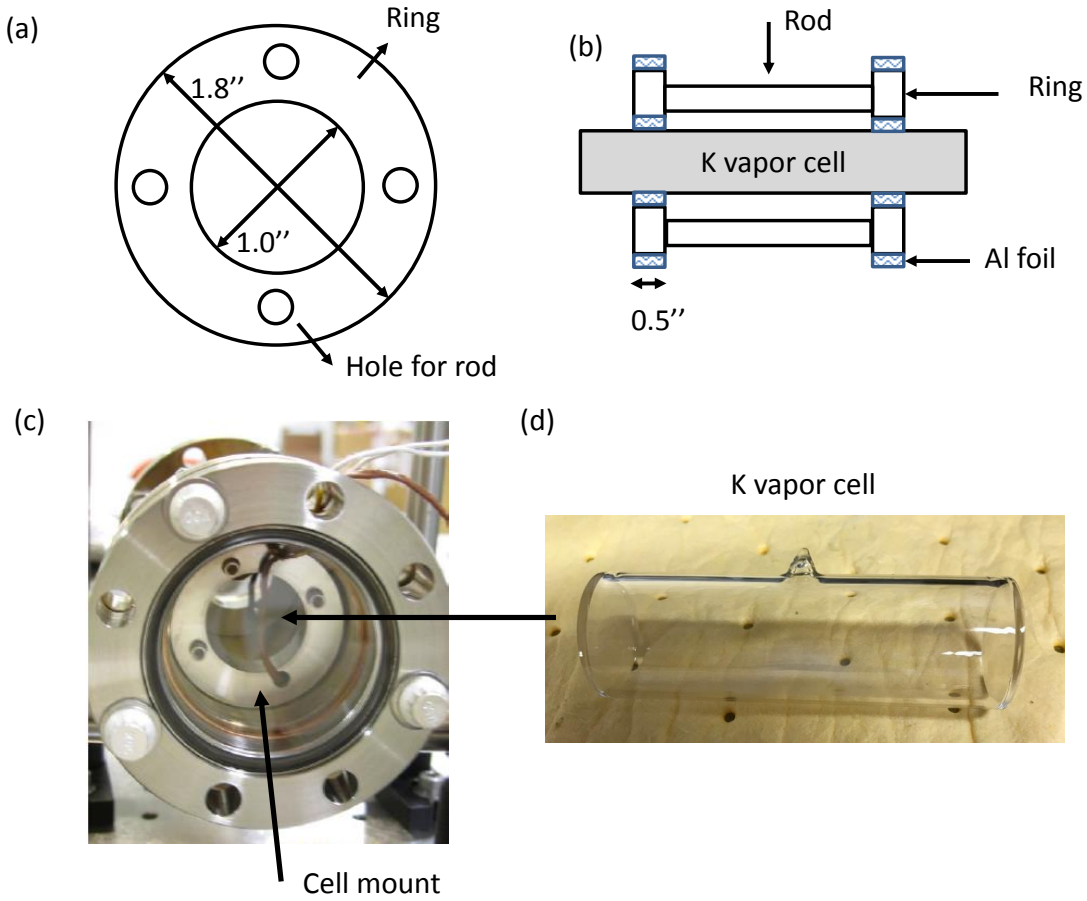

Figure 6.20: Drawings and photos of the home-made mount that holds the vapor cell in the oven. (a) and (b): The mount consists of two rings and four rods. The gap between the mount and the cell is filled with Al foil. (c): Photo for the mount and vapor cell inside the oven. (d): Potassium vapor cell used in this work.

cell hotter compared to its middle as the temperature is increased. Fiber glass insulation is wrapped around the outside of the heaters and the oven. Fig. 6.21(a) shows the photos of the oven after being wrapped by Al foil.

A constant heating of the vapor cell seems to lead to some absorption of potassium atoms by the glass. Once I used a potassium vapor cell with very little material in it. After about 1-2 months, the vapor pressure decreased and made the spectroscopy measurements become impossible. The current vapor cell in the oven contains a lot of potassium in it and works at a temperature lower than 90°C. It has been worked well for more than five years.

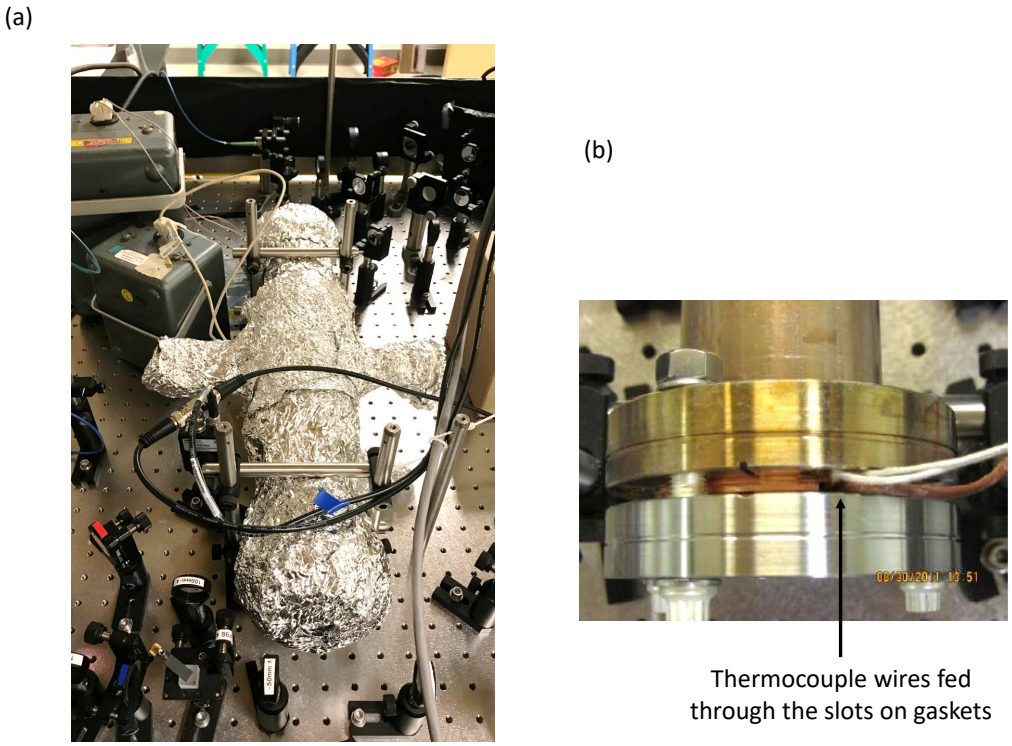

Figure 6.21: (a): Photo of the potassium vapor cell oven. Variacs are used to power two heater tapes. Temperature inside the oven is measured by three thermistors placed at different positions inside the oven. The temperature is maintained at 85°C to obtain a high vapor pressure of potassium for performing spectroscopy measurements. (b): Photo shows the thermocouple wires gone through the slots on gaskets.

6.5.2 External cavity diode laser (ECDL)

The EIT measurement involves two diode lasers: a blue diode laser (ML320G2 from Mitsubishi, bought from Thorlabs) for driving the $4S_{1/2} \rightarrow 5P_{1/2}$ transition, and a near-infrared (NIR) diode laser (JDSU 6531-J1, bought from eBay) for coupling the $5P$ state to Rydberg states. Both laser diodes are mounted in

a home-made tunable external cavity (Fig. 6.22). A Littrow configuration, containing a collimating lens and a diffraction grating, is used to tune the laser wavelength and reduce its frequency linewidth.

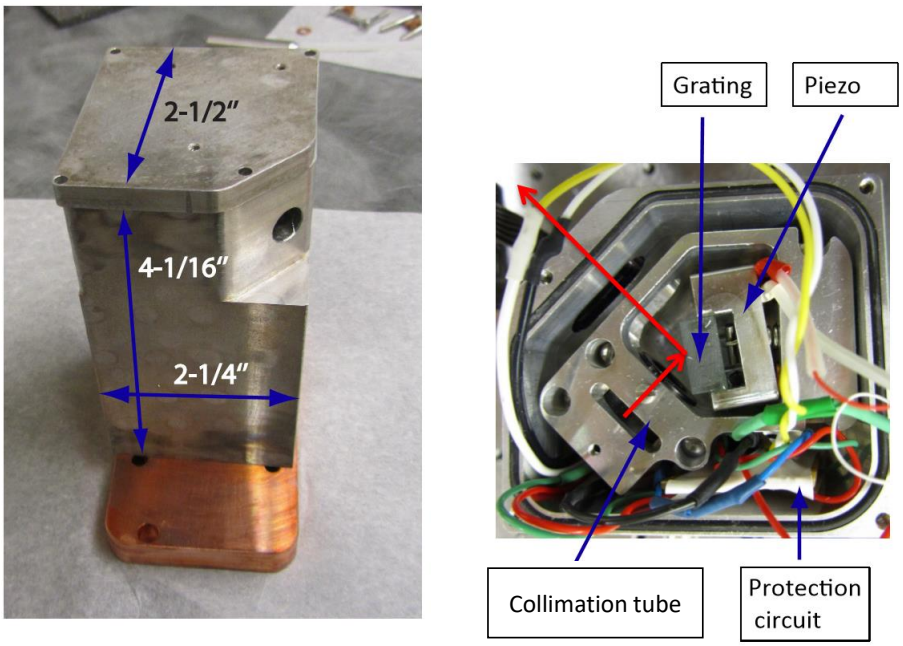

Figure 6.22: Left: Home-made external cavity housing for the blue laser diode. Right: Inside of the external cavity housing. The blue laser diode is held in a collimation tube. The grating is mounted close to the laser diode. Such a small cavity length is necessary for achieving a reasonable frequency tuning range for the blue laser diode. A piezo transducer is used to sweep the laser frequency. The red arrows represents the laser diode beam.

The design of the ECDL is compact (Fig. 6.22). A protection circuit (Fig. 6.23) is used to avoid backward voltage across the laser diode and electrical transients. The number of diodes (1N4148) used in this protection circuit depends on the wavelength of the laser diode. The blue laser diode requires a higher operating voltage (5.4V) compared to the NIR laser diodes (usually with operating voltage 1.8V-2.2V). Also, the polarity of diodes depends on the type of the laser diode (anode ground or cathode ground). A 10kΩ thermistor (Thorlabs TH10K) is mounted inside a hole on the laser diode cavity, which is near to the laser diode. A thermoelectric cooler (Thorlabs TEC 3-6) is placed under the laser diode cavity. The thermistor and the thermoelectric cooler are used for temperature servo. Table. 6.2 summaries the components used for the ECDLs.

A short cavity length is important. Compared to the near-infrared laser light, the shorter wavelength of blue light makes it harder to tune its wavelength. With a length of the home-made external cavity less than 1cm, the maximum tunable range of the blue light wavelength is less than 1nm from its free-running wavelength. To reach the desired frequency, we asked Thorlabs to do wavelength-selection for the blue laser

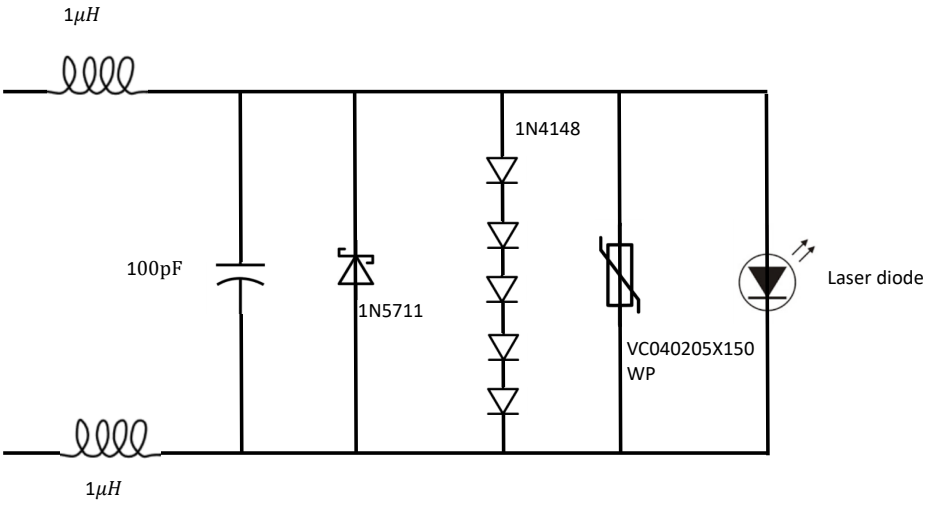

Figure 6.23: Protection circuit for the NIR laser diode (anode ground). A series of diodes (IN4148) is used to prevent transient backward voltage across the laser diode. A transient voltage suppressor (VC040205X150) provides protects from voltage transients. The capacitor and inductor form a high frequency filter. For the blue laser diode, ten 1N4148s are used.

diodes. For the NIR diode lasers, with such short cavity length, it is easy to tune its wavelength 5nm away from its free-running wavelength. By applying an AC voltage up to $200V$ to the piezo attached to the laser grating, the laser frequency can be scanned smoothly without mode hopping within 800MHz for the blue laser and across about 2GHz for the NIR laser diode.

6.5.3 Frequency modulation spectroscopy

To stabilize the frequency of the blue laser light to the $\left|4S_{1/2}, F = 2\right\rangle \rightarrow \left|5P_{1/2}\right\rangle$ transition, we apply a standard frequency modulation spectroscopy technique [215]. The probe beam passes through an electro-optic phase modulator (EO-PM-NR-C4 from Thorlabs). A 8MHz radio-frequency driving field is applied on this EOM, which is generated via direct digital synthesis (DDS, AD9959 from Analog Devices) and then amplified by a 2W amplifier (Mini circuits, ZHL-1-2W). The voltage applied on this non-resonant EOM is much lower than EOM's π voltage ($V_\pi \approx 80V$). Only about 3% of the total power has been transferred to the sidebands. Because the transfer fraction is low, it is hard to observe the sidebands directly on a Fabry-Pérot interferometer. To measure the sidebands intensity, a better method is beating the light after EOM to an unmodulated beam.

We choose $5P_{1/2}$ as the intermediate state instead of $5P_{3/2}$ because of its relative simple energy structures.

Table 6.2: List of components used in the ECDL.

Vendor	Catalog No.	Description
Lee Spring	LE 034B 01 M	Springs, 53.30 lb/in
Edmund Optics	NT43-775	1800 Grooves/mm, VIS Holographic Gratin
	NT43-774	1800 Grooves/mm, UV Holographic Grating
Ratermann manufacturing inc	KRY-GPL202-1/2OZ	Krytox GPL-202 Grease
McMaster	98385A123	Pins
	9464K351	O-ring
	9464K79	O-ring
	9452K38	O-ring
Newport	9341-K	Tiny Hex Adjustment Screw, 2.0 mm Travel, Ball Tip, 6-80
Thorlabs	AE0203D08F	Piezoelectric Actuator, Max Displacement 9.1 μm, $3.5 \times 4.5 \times 10$ mm
	F6SSN2P	Threaded Bushing, 6-80, 0.375" Long
	TEC3-6	TEC
	C230TME-A	Lens for blue laser diode
	C230TME-B	Lens for NIR laser diode
	TH10K	Thermistor
Digikey	A132-100-ND	Shielded Cable
	HR1594-ND	Connector
	HR1586-ND	Plug
Mouser Electronics	565-5223-60	RF Cable Assemblies, Triaxial 3 Lug Male, 60" Long
	565-5219	RF Connectors, Triaxial Jack

The laser cannot resolve the hyperfine states on the $5P$ manifolds [199], and therefore the exact locking frequency of the blue laser light is unknown. The $5P_{3/2}$ level has four hyperfine states. The coherent coupling between the ground state to the Rydberg state via these four different intermediate states carry various phases, which may complicate the interpretation of data.

Fig. 6.24 shows a schematic of the frequency modulation spectroscopy setup. A photodetector (Thorlabs PDA8A) with a 50MHz bandwidth is used to measure the transmitted light power after the vapor cell. The demodulated signal is shown in Fig. 6.25, which is roughly the derivative of a standard saturated spectroscopy. The zero-crossing corresponding to the $F = 2 \rightarrow F'$ transition is used for frequency locking. The quality of the demodulated signal is not perfect. Slow drift in DC offset of the error signal makes the laser become unlocked about every 30 minutes. It is possible that the probe beam polarization is not pure. After the probe beam passes through the EOM, an amplitude modulation appears becuase of the fluctuations in the temperature and beam pointing. Another possible reason for the small peak-to-peak voltage of the error signal may be because the silicon-based photodetector does not have a good response at this wavelength. Improvement of the locking will be necessary for future projects.

6.5.4 Setup for EIT measurement

A schematic of our EIT measurement apparatus is shown in Fig. 6.26. Both the EIT pump and probe beams are coupled into a polarization maintaining fiber for spatial filtering. The coupling, optical pumping, and probe beam are spatially overlapped and propagate through the potassium vapor cell in the oven. The probe and optical pumping beams (with waists 190 μm and 120 μm and powers 70 μW and 300 μW, respectively) are derived from the same ECDL. The probe beam is shifted by $f_{hp} \approx 460$ MHz from the optical pumping beam, and the power of the optical pumping beam is chopped at 25 kHz using an acousto-optic modulator. The NIR ECDL is used to generate the 15 mW near-infrared coupling beam, which is weakly focused to a 260 μm waist in the cell. The power of the coupling beam is modulated at 1.27 kHz using a chopper wheel. The transmitted probe power is measured using a photodetector (Thorlabs PDA8A), and the EIT signal is derived from double-demodulation at 25 kHz and 1.27 kHz via a mixer and lock-in amplifier. This demodulation scheme detects changes in the transmitted probe power induced by the coupling beam for atomic velocities selected by the optical pumping beam.

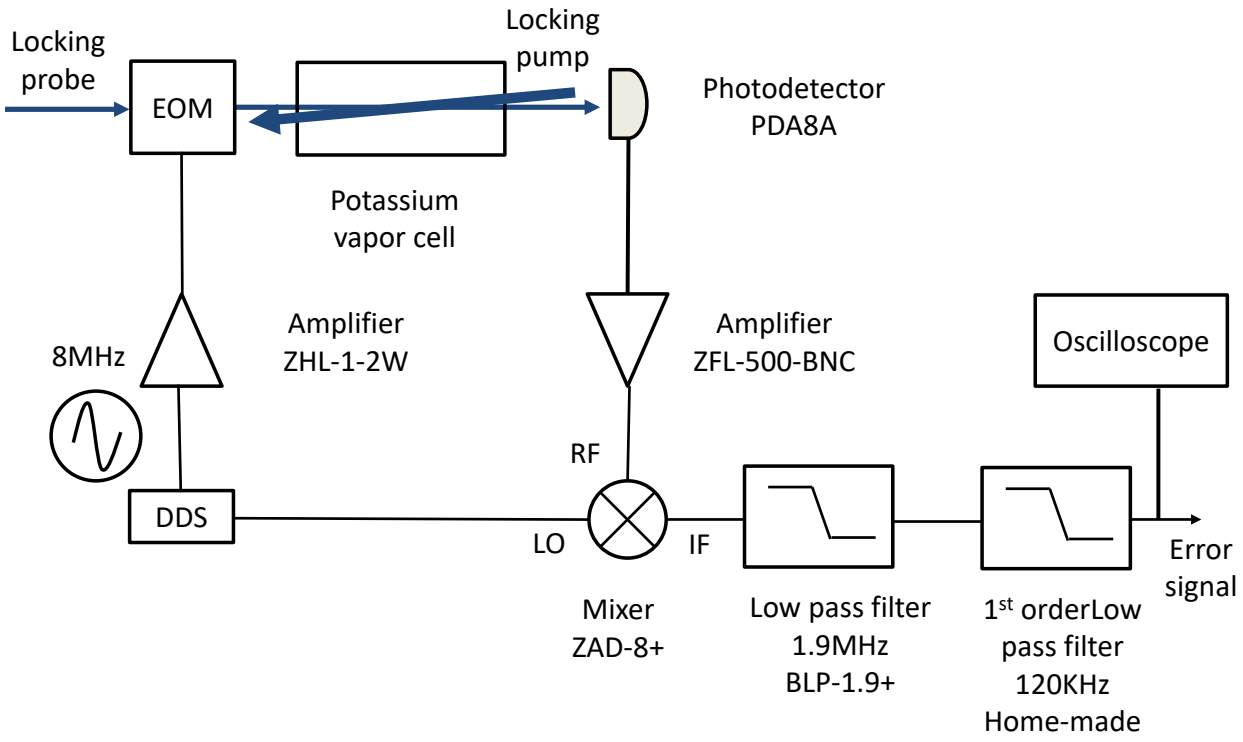

Figure 6.24: A schematic diagram of the standard frequency modulation locking setup for $4S_{1/2} \rightarrow 5P_{1/2}$ transition. The locking probe beam counter-propagates with the locking pump beam. An electro-optic phase modulator (EOM) generates 8MHz side bands on the central carrier frequency of the probe beam. The transmitted probe power is measured with a photodector (Thorlabs PDA8A). A four-channel 500 MSPS direct digital synthesize (DDS, Analog devices AD9959) is used to drive the EOM and to provide a reference signal for the mixer to demodulate the photodetector signal. The demodulated signal, after going through two low-pass filters, is used to lock the laser frequency to the $4S_{1/2}, F = 1 \rightarrow 5P_{1/2}$ transition.

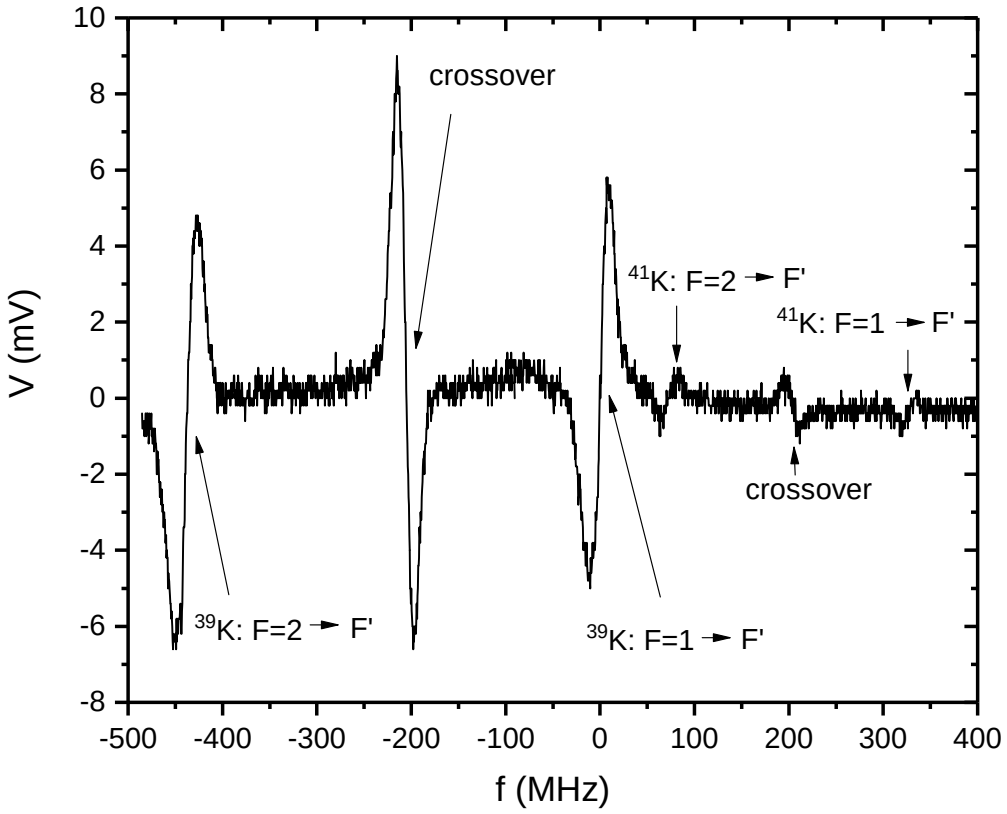

Figure 6.25: Frequency modulation spectroscopy signal for the $4S_{1/2} \rightarrow 5P_{1/2}$ transition. The blue laser is locked to the zero-crossing corresponding to the $F = 2 \rightarrow F'$ transition in ^{39}K.

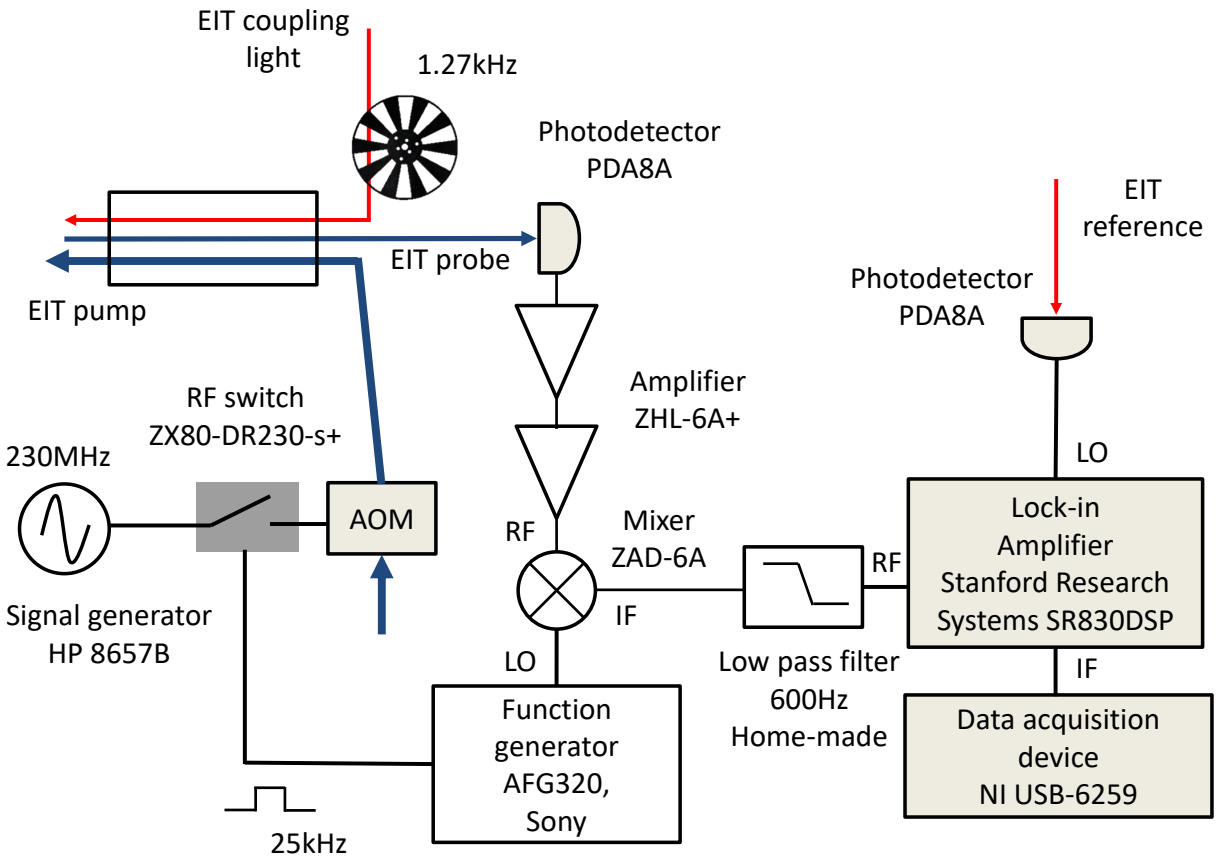

Figure 6.26: A schematic of the EIT measurement apparatus. The coupling beam counter-propagates with the probe beam and co-propagates with the optical pumping beam through a vapor cell. An acousto-optic modulator (AOM) shifts the frequency of the optical pumping beam such that the frequency difference with the probe beam matches the ground-state hyperfine splitting. A 25 kHz square-wave generator and a radio-frequency (rf) switch is used to modulate the signal generator that drives the AOM and chop the optical pumping beam. An optical chopping wheel modulates the coupling beam at 1.27 kHz. This mechanical chopping wheel generates some acoustic vibrations. To avoid the acoustic vibration coupling into the 980nm laser cavity, a cardboard box is used to cover the ECLD. The transmitted power of the probe beam is measured using a photodetector (PDA8A). The PD signal is doubly demodulated, first using a mixer followed by a low-pass (LP) filter, and then using a lock-in amplifier (Stanford Research Systems SR830DSP).

6.6 Results of EIT measurement

To measure EIT, we tune the near-infrared coupling laser close to the frequency resonant with the $5P_{1/2} \rightarrow nS_{1/2}$ transition predicted by previous measurements of the $4S \rightarrow 5P_{1/2}$ [216] and $4S \rightarrow nS$ transitions [197]. For EIT measurement in this work, the current and the resistance of the 10K thermistor are $I = 74.93$mA and $R_T = 12.996$kΩ ($T \approx 19°$C) for the blue diode laser , and $I = 99.81$mA and $R_T = 12.243$kΩ ($T \approx 20°$C) for the NIR diode laser.

The frequency of the coupling laser is scanned by a data acquisition device (DAQ, NI USB-6259 from National Instrument). An analog output on the DAQ controls the voltage applied on the piezo attached to the grating for the NIR ECDL. The voltage generated by this analog output is magnified by a factor of 17.5 with an amplifier circuit, which consists a $450V$ power operational amplifier (APEX Microtechnology PA98). The scanning rate of the piezo voltage is $0.055V/s$. Part of the NIR light is picked off by a beam sampler before the chopping wheel and fiber coupled to the input of a high resolution wavemeter (Bristol 621A). The measured wavelength is recorded by an analog input to the DAQ device. Matlab code for the NIR laser frequency scanning and wavelength recording via the DAQ device can be found in the Appendix.

The change in EIT probe light power is detected by a photodetector (PDA8A), and double-demodulated by a mixer (ZAD-6A) and a lock-in amplifier (Stanford Research Systems SR830DSP). The signal from the lock-in amplifier, which is proportional to changes in the transmitted probe power, is recorded by the DAQ device. In our EIT measurements, the lock-in amplifier is set to have a 300ms time constant and a $500\mu V$ sensitivity. Part of the NIR light after the chopping wheel is picked off by a beam sampler, and its intensity is detected by a photodetector (Thorlabs PDA8A), which is used as a reference signal for the lock-in amplifier.

Typical data for $n = 28$ are shown in Fig. 6.27. The lock-in amplifier signal is shown vs. the difference in frequency between the coupling laser and the predicted $5P_{1/2} \rightarrow nS$ transition frequency based on Refs. [197] and [216]. We assume that the wavelength measured in Ref. [216] corresponds to the frequency labeled $f_{5P_{1/2}}$ in Fig. 6.17(a). The lock-in signal vanishes on the scale shown in Fig. 6.27 if the optical pumping beam is absent. The two pairs of peaks evident in Fig. 6.27 derive from the two velocity classes that contribute to the EIT signal, whereas the doublet structure arises from EIT through the $F' = 1$ and $F' = 2$ hyperfine states in the excited $5P_{1/2}$ electronic state.

The data are fit to a sum of four Gaussian functions, which, in this case, give center frequencies of (-0.7600 ± 0.0003), (-0.737 ± 0.001), (-0.5711 ± 0.0003), and (-0.5510 ± 0.0005) GHz. For the $5P_{1/2}, F' = 2 \rightarrow nS$ transition, the absolute frequencies we measure are 303240.379, 303698.194, and 304102.870 GHz for $n = 26, 27$, and 28. We estimate that drift in the laser lock for the 404.8 nm laser adds a 1 MHz uncertainty to these frequencies; Zeeman and AC Stark shifts are negligible at this level. The 20 ± 2 MHz difference

between the closely spaced peaks is consistent with the 18.1 ± 0.2 MHz $5P_{1/2}$ hyperfine splitting [217]. The approximately 190 MHz difference between the pairs is consistent with the shift in the resonant EIT coupling frequency between atoms with $v = 0$ and $v = cf_{hp}/f_p$.

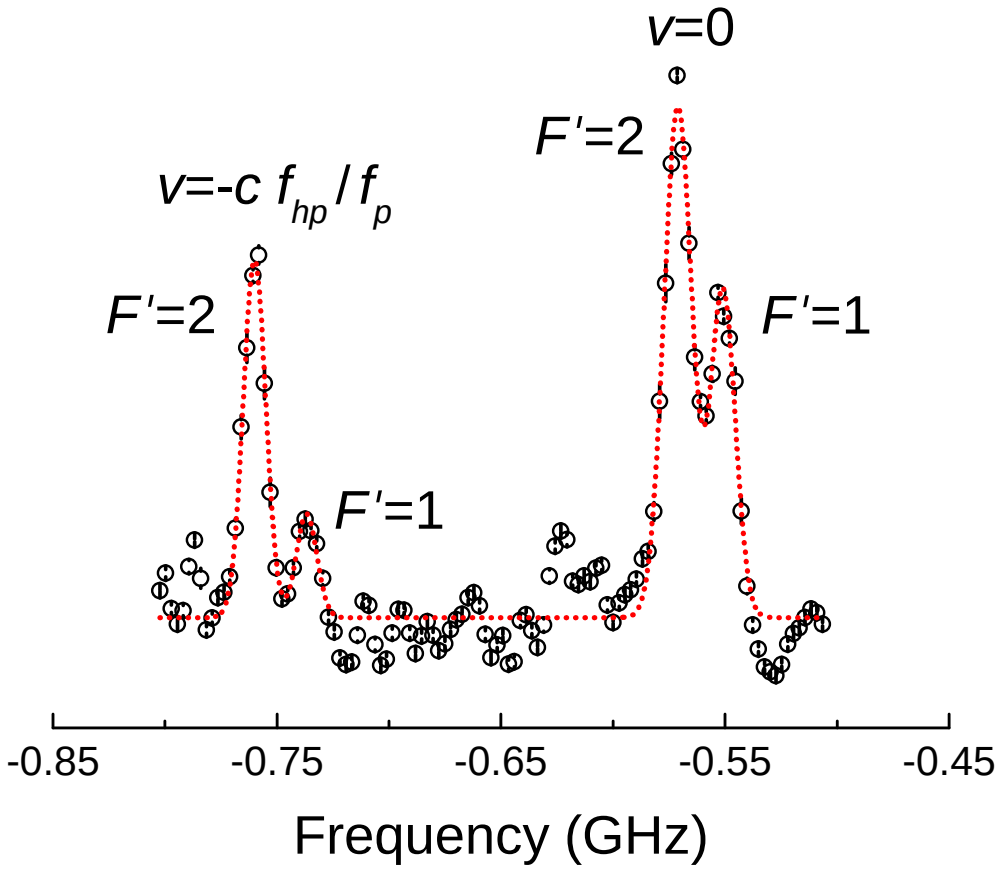

Figure 6.27: EIT spectroscopy of the $28S$ state. The signal from the lock-in amplifier, which is proportional to changes in the probe transmission, is shown as the frequency of the coupling laser is scanned. The maximum signal corresponds to approximately a 0.2% change in the transmission of the probe beam synchronous with the optical pumping and coupling beam. The abscissa is the frequency difference of the coupling laser relative to the $5P_{1/2} \rightarrow nS$ transition predicted by previous measurements of the $4S \rightarrow 5P_{1/2}$ and $4S \rightarrow nS$ transitions [197,216]. Each point is an average of 5 measurements, and the error bars are the standard error of the mean. The dotted line is a fit to the sum of four Gaussian functions. The approximately 20 MHz FWHM of the peaks is consistent with broadening expected from the spread in velocities selected by the optical pumping beam and noise from the repeatability of the wavemeter.

6.6.1 Improved accuracy for the $4S \rightarrow 5P$ transition

We measure EIT spectra for $n = 26$, 27, and 28, which spans 0.86 THz in the coupling laser frequency. Fig. 6.28 shows the center frequencies of the EIT peaks (as deviations from the frequency predicted by Refs. [197] and [216]) for $v = 0$ obtained from Gaussian fits such as those shown in Fig. 6.27. The weighted average for the frequency deviation of the transition to the $5P,\ F' = 1$ and $5P,\ F' = 2$ states is -0.573 ± 0.005

GHz and -0.552 ± 0.007 GHz, respectively. The individual measurements are consistent with these average values within the specified 10 MHz repeatability of the wavemeter. The most significant contribution to the overall measurement uncertainty is the 60 MHz accuracy of the wavemeter used to measure the absolute frequency of the coupling laser. We have verified that the wavemeter is accurate at this level for the ^{87}Rb and ^{40}K D2 transitions. We assign an additional 20 MHz uncertainty to account for the unresolved hyperfine structure of the $5P_{1/2}$ state in the setup used to stabilize the wavelength of the 404.8 nm laser, making the overall uncertainty 80 MHz.

Based on our measurement, the $4S_{1/2} \rightarrow 5P_{1/2}$ transition frequency (as labeled $f_{5P_{1/2}}$ in Fig. 6.17(a)) should be shifted by 560 ± 80 MHz from the currently accepted value [216, 218], giving 740529.36 ± 0.08 GHz for the absolute frequency of this transition. Our measurement represents a factor of two improvement in the present ± 150 MHz reported uncertainty for this transition [216]. Our results are not consistent with the currently accepted value of this transition, which was determined using a grating-based spectrometer and hollow-cathode lamp [216], and was therefore not a measurement of the absolute frequency. Also, the ground-state hyperfine structure was not accounted for in Ref. [216], potentially introducing large systematic errors. Furthermore, the source of the ± 150 MHz reported uncertainty and a justification of that value were not explained in Ref. [216].

6.7 Conclusion and outlook

This project was started six years ago as my first independent research project in our group. Around that time, introducing beyond on-site interactions in optical lattices via Rydberg-dressed states was a relatively new idea. Several groups have started this Rydberg-dressed strategy and progress has been made during the past few years, accompanied by many unexpected difficulties.

Theoretical calculations suggest that it is promising to observe Rydberg-dressing with potassium in optical lattices. As a first step toward this goal, we developed a simple method to overcome the Doppler effect and performed precision velocity-selective spectroscopy in a hot potassium vapor cell. From the EIT spectra, we measured the transition frequencies for $5P_{1/2}$ to $n = 26 - 28$, which in turn calibrate the energy separation between the ground state and $5P_{1/2}$ state.

The next step in this project will focus on measuring the lifetime and interaction shift for Rydberg dressing. The lifetime will be straightforwardly measured via atom loss, and the interaction shift by hyperfine microwave spectroscopy. For spectroscopy, we will prepare a spin-polarized non-interacting gas in the $|F = 9/2, m_F = 9/2\rangle$ state with unit filling in the center of lattice. The dressing lasers will be tuned to se-

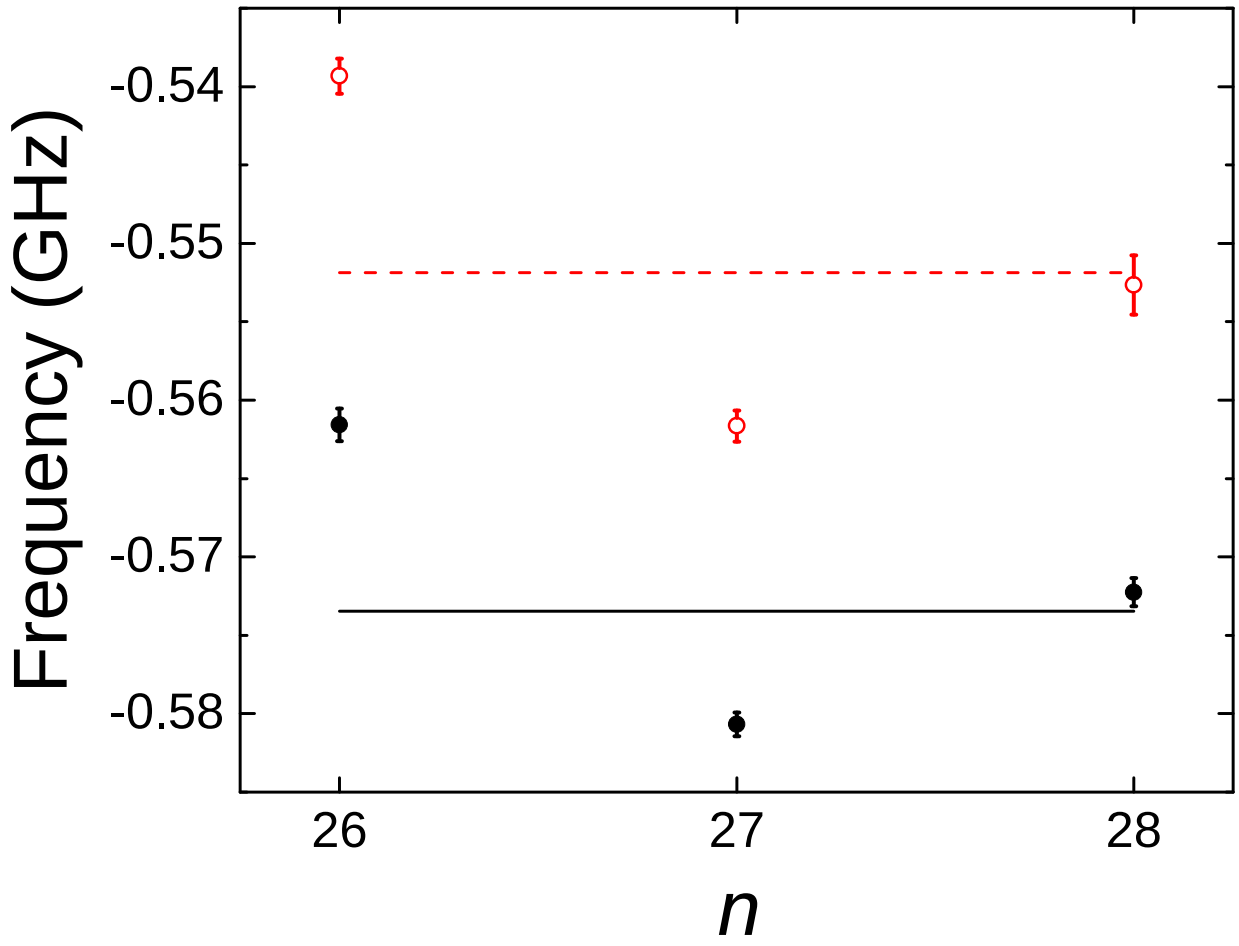

Figure 6.28: The measured frequency deviation for the $5P_{1/2} \rightarrow nS_{1/2}$ transition with principal quantum numbers $n = 26$, 27 and 28. The solid black (hollow red) points are for the transition to the $5P,\ F' = 1$ ($5P,\ F' = 2$) state. The black solid and red dashed lines are the weighted average of each set of three points for the transitions to the $5P,\ F' = 1$ and $5P,\ F' = 2$ states, respectively. The error bars show the uncertainty from the fits to data such as those in Fig. 6.27. The 60 MHz uncertainty from the accuracy of the wavemeter is not included in the error bars.

lectively address the $|F = 7/2\rangle$ manifold. The interaction shift can be measured via microwave spectroscopy on the $|F = 9/2, m_F = 9/2\rangle \rightarrow |F = 7/2, m_F = 7/2\rangle$ transition, which we routinely achieve with a 300 Hz resolution.

References

[1] Patrick A Lee, Naoto Nagaosa, and Xiao-Gang Wen. Doping a Mott insulator: Physics of high-temperature superconductivity. *Reviews of Modern Physics*, 78(1):17, 2006.

[2] Antoine Georges, Gabriel Kotliar, Werner Krauth, and Marcelo J Rozenberg. Dynamical mean-field theory of strongly correlated fermion systems and the limit of infinite dimensions. *Reviews of Modern Physics*, 68(1):13, 1996.

[3] Jean Dalibard, Fabrice Gerbier, Gediminas Juzeliūnas, and Patrik Öhberg. Colloquium: Artificial gauge potentials for neutral atoms. *Reviews of Modern Physics*, 83(4):1523, 2011.

[4] Marcos Atala, Monika Aidelsburger, Michael Lohse, Julio T Barreiro, Belén Paredes, and Immanuel Bloch. Observation of chiral currents with ultracold atoms in bosonic ladders. *Nature Physics*, 10(8):588–593, 2014.

[5] Junru Li, Wujie Huang, Boris Shteynas, Sean Burchesky, Furkan Çağrı Top, Edward Su, Jeongwon Lee, Alan O Jamison, and Wolfgang Ketterle. Spin-orbit coupling and spin textures in optical superlattices. *Physical Review Letters*, 117(18):185301, 2016.

[6] Xiong-Jun Liu, Kam Tuen Law, and Tai Kai Ng. Realization of 2d spin-orbit interaction and exotic topological orders in cold atoms. *Physical Review Letters*, 112(8):086401, 2014.

[7] Zhan Wu, Long Zhang, Wei Sun, Xiao-Tian Xu, Bao-Zong Wang, Si-Cong Ji, Youjin Deng, Shuai Chen, Xiong-Jun Liu, and Jian-Wei Pan. Realization of two-dimensional spin-orbit coupling for Bose-Einstein condensates. *Science*, 354(6308):83–88, 2016.

[8] Bo Yan, Steven A Moses, Bryce Gadway, Jacob P Covey, Kaden RA Hazzard, Ana Maria Rey, Deborah S Jin, and Jun Ye. Observation of dipolar spin-exchange interactions with lattice-confined polar molecules. *Nature*, 2013.

[9] Simon Baier, Manfred J Mark, Daniel Petter, Kiyotaka Aikawa, Lauriane Chomaz, Zi Cai, M Baranov, P Zoller, and F Ferlaino. Extended Bose-Hubbard models with ultracold magnetic atoms. *Science*, 352(6282):201–205, 2016.

[10] Renate Landig, Lorenz Hruby, Nishant Dogra, Manuele Landini, Rafael Mottl, Tobias Donner, and Tilman Esslinger. Quantum phases from competing short-and long-range interactions in an optical lattice. *Nature*, 532(7600):476–479, 2016.

[11] Martin C Fischer, Jesse W Wilson, Francisco E Robles, and Warren S Warren. Invited review article: pump-probe microscopy. *Review of Scientific Instruments*, 87(3):031101, 2016.

[12] Chih-Chun Chien, Sebastiano Peotta, and Massimiliano Di Ventra. Quantum transport in ultracold atoms. *Nature Physics*, 11(12):998–1004, 2015.

[13] Stanimir Svetoslavov Kondov. *Ultracold fermionic atoms in disordered potentials*. University of Illinois at Urbana-Champaign, 2013.

[14] William Russell McGehee. *Transport and disorder-induced localization of ultracold Fermi gases*. University of Illinois at Urbana-Champaign, 2015.

[15] B DeMarco, JL Bohn, JP Burke Jr, M Holland, and Deborah S Jin. Measurement of p-wave threshold law using evaporatively cooled fermionic atoms. *Physical Review Letters*, 82(21):4208, 1999.

[16] TG Tiecke. Properties of potassium. *University of Amsterdam, The Netherlands, Thesis*, pages 12–14, 2010.

[17] S. S. Kondov, W. R. McGehee, and B. DeMarco. Interplay of disorder and interactions in an optical lattice Hubbard model. *ArXiv e-prints*, May 2013.

[18] Ch Monroe, DM Meekhof, BE King, Steven R Jefferts, Wayne M Itano, David J Wineland, and P Gould. Resolved-sideband Raman cooling of a bound atom to the 3d zero-point energy. *Physical Review Letters*, 75(22):4011, 1995.

[19] SE Hamann, DL Haycock, G Klose, PH Pax, IH Deutsch, and Poul S Jessen. Resolved-sideband Raman cooling to the ground state of an optical lattice. *Physical Review Letters*, 80(19):4149, 1998.

[20] Andrew J Kerman, Vladan Vuletić, Cheng Chin, and Steven Chu. Beyond optical molasses: 3D Raman sideband cooling of atomic cesium to high phase-space density. *Physical Review Letters*, 84(3):439, 2000.

[21] Dian-Jiun Han, Steffen Wolf, Steven Oliver, Colin McCormick, Marshall T DePue, and David S Weiss. 3D Raman sideband cooling of cesium atoms at high density. *Physical Review Letters*, 85(4):724, 2000.

[22] David Chen, Carolyn Meldgin, Philip Russ, Brian DeMarco, and Erich Mueller. Disappearance of quasiparticles in a Bose lattice gas. *Physical Review A*, 94(2):021601, 2016.

[23] Y-J Lin, Rob L Compton, K Jimenez-Garcia, James V Porto, and Ian B Spielman. Synthetic magnetic fields for ultracold neutral atoms. *Nature*, 462(7273):628–632, 2009.

[24] Y-J Lin, K Jiménez-García, and IB Spielman. Spin-orbit-coupled Bose-Einstein condensates. *Nature*, 471(7336):83–86, 2011.

[25] Gregor Jotzu, Michael Messer, Rémi Desbuquois, Martin Lebrat, Thomas Uehlinger, Daniel Greif, and Tilman Esslinger. Experimental realization of the topological Haldane model with ultracold fermions. *Nature*, 515(7526):237–240, 2014.

[26] Hirokazu Miyake, Georgios A Siviloglou, Colin J Kennedy, William Cody Burton, and Wolfgang Ketterle. Realizing the Harper Hamiltonian with laser-assisted tunneling in optical lattices. *Physical Review Letters*, 111(18):185302, 2013.

[27] Monika Aidelsburger, Marcos Atala, Michael Lohse, Julio T Barreiro, B Paredes, and Immanuel Bloch. Realization of the Hofstadter Hamiltonian with ultracold atoms in optical lattices. *Physical Review Letters*, 111(18):185301, 2013.

[28] B. W. Shore. *Simple Atoms and Fields*. Wiley-VCH, New York, 1989.

[29] Thorsten Köhler, Krzysztof Góral, and Paul S Julienne. Production of cold molecules via magnetically tunable Feshbach resonances. *Reviews of Modern Physics*, 78(4):1311, 2006.

[30] Cheng Chin, Rudolf Grimm, Paul Julienne, and Eite Tiesinga. Feshbach resonances in ultracold gases. *Reviews of Modern Physics*, 82(2):1225, 2010.

[31] Cindy A Regal, Christopher Ticknor, John L Bohn, and Deborah S Jin. Creation of ultracold molecules from a Fermi gas of atoms. *Nature*, 424(6944):47–50, 2003.

[32] Sylvain Nascimbene, Nir Navon, KJ Jiang, Frédéric Chevy, and Christophe Salomon. Exploring the thermodynamics of a universal Fermi gas. *Nature*, 463(7284):1057–1060, 2010.

[33] Mark JH Ku, Ariel T Sommer, Lawrence W Cheuk, and Martin W Zwierlein. Revealing the superfluid lambda transition in the universal thermodynamics of a unitary Fermi gas. *Science*, 335(6068):563–567, 2012.

[34] Philip Makotyn, Catherine E Klauss, David L Goldberger, EA Cornell, and Deborah S Jin. Universal dynamics of a degenerate unitary Bose gas. *Nature Physics*, 10(2):116–119, 2014.

[35] Jit Kee Chin, DE Miller, Y Liu, C Stan, W Setiawan, C Sanner, K Xu, and W Ketterle. Evidence for superfluidity of ultracold fermions in an optical lattice. *Nature*, 443(7114):961–964, 2006.

[36] Niels Strohmaier, Yosuke Takasu, Kenneth Günter, Robert Jördens, Michael Köhl, Henning Moritz, and Tilman Esslinger. Interaction-controlled transport of an ultracold Fermi gas. *Physical Review Letters*, 99(22):220601, 2007.

[37] Lucia Hackermüller, Ulrich Schneider, Maria Moreno-Cardoner, Takuya Kitagawa, Thorsten Best, Sebastian Will, Eugene Demler, Ehud Altman, Immanuel Bloch, and Belén Paredes. Anomalous expansion of attractively interacting fermionic atoms in an optical lattice. *Science*, 327(5973):1621–1624, 2010.

[38] Ulrich Schneider, Lucia Hackermüller, Jens Philipp Ronzheimer, Sebastian Will, Simon Braun, Thorsten Best, Immanuel Bloch, Eugene Demler, Stephan Mandt, David Rasch, et al. Fermionic transport and out-of-equilibrium dynamics in a homogeneous Hubbard model with ultracold atoms. *Nature Physics*, 8(3):213–218, 2012.

[39] Debayan Mitra, Peter T Brown, Elmer Guardado-Sanchez, Stanimir S Kondov, Trithep Devakul, David A Huse, Peter Schauss, and Waseem S Bakr. Quantum gas microscopy of an attractive Fermi–Hubbard system. *Nature Physics*, 14(2):173, 2018.

[40] Alain Sewer, Xenophon Zotos, and Hans Beck. Quantum Monte Carlo study of the three-dimensional attractive Hubbard model. *Physical Review B*, 66(14):140504, 2002.

[41] JM Singer, MH Pedersen, T Schneider, H Beck, and H-G Matuttis. From BCS-like superconductivity to condensation of local pairs: A numerical study of the attractive Hubbard model. *Physical Review B*, 54(2):1286, 1996.

[42] AF Ho, MA Cazalilla, and Thierry Giamarchi. Quantum simulation of the Hubbard model: The attractive route. *Physical Review A*, 79(3):033620, 2009.

[43] N Dupuis. Berezinskii-Kosterlitz-Thouless transition and BCS-Bose crossover in the two-dimensional attractive Hubbard model. *Physical Review B*, 70(13):134502, 2004.

[44] Li Han and CAR Sá De Melo. Evolution from Bardeen–Cooper–Schrieffer to Bose–Einstein condensate superfluidity in the presence of disorder. *New Journal of Physics*, 13(5):055012, 2011.

[45] T Loftus, CA Regal, C Ticknor, JL Bohn, and Deborah S Jin. Resonant control of elastic collisions in an optically trapped Fermi gas of atoms. *Physical Review Letters*, 88(17):173201, 2002.

[46] CA Regal, C Ticknor, JL Bohn, and Deborah S Jin. Tuning p-wave interactions in an ultracold Fermi gas of atoms. *Physical Review Letters*, 90(5):053201, 2003.

[47] CA Regal and DS Jin. Measurement of positive and negative scattering lengths in a Fermi gas of atoms. *Physical Review Letters*, 90(23):230404, 2003.

[48] Jasper S Krauser, Jannes Heinze, S Götze, M Langbecker, N Fläschner, Liam Cook, Thomas M Hanna, Eite Tiesinga, Klaus Sengstock, and Christoph Becker. Investigation of Feshbach resonances in ultracold K 40 spin mixtures. *Physical Review A*, 95(4):042701, 2017.

[49] CA Regal, Markus Greiner, and Deborah S Jin. Observation of resonance condensation of fermionic atom pairs. *Physical Review Letters*, 92(4):040403, 2004.

[50] Tilman Esslinger, Immanuel Bloch, and Theodor W Hänsch. Bose-Einstein condensation in a quadrupole-Ioffe-configuration trap. *Physical Review A*, 58(4):R2664, 1998.

[51] G Reinaudi, T Lahaye, Z Wang, and D Guéry-Odelin. Strong saturation absorption imaging of dense clouds of ultracold atoms. *Optics Letters*, 32(21):3143–3145, 2007.

[52] Brian DeMarco. *Quantum behavior of an atomic Fermi gas*. University of Colorado, 2001.

[53] Alan Corney. *Atomic and laser spectroscopy*. Clarendon Press Oxford, 1978.

[54] N.W. Ashcroft and N.D. Mermin. *Solid State Physics*. Saunders College, Philadelphia, 1976.

[55] M Greiner, I Bloch, O Mandel, TW Hänsch, and T Esslinger. Bose–Einstein condensates in 1D-and 2D optical lattices. *Applied Physics B: Lasers and Optics*, 73(8):769–772, 2001.

[56] A Kastberg, William D Phillips, SL Rolston, RJC Spreeuw, and PS Jessen. Adiabatic cooling of cesium to 700 nk in an optical lattice. *Physical Review Letters*, 74(9):1542, 1995.

[57] Michael Köhl, Henning Moritz, Thilo Stöferle, Kenneth Günter, and Tilman Esslinger. Fermionic atoms in a three dimensional optical lattice: Observing Fermi surfaces, dynamics, and interactions. *Physical Review Letters*, 94(8):080403, 2005.

[58] David McKay, M White, and B DeMarco. Lattice thermodynamics for ultracold atoms. *Physical Review A*, 79(6):063605, 2009.

[59] Maxime Ben Dahan, Ekkehard Peik, Jakob Reichel, Yvan Castin, and Christophe Salomon. Bloch oscillations of atoms in an optical potential. *Physical Review Letters*, 76(24):4508, 1996.

[60] Brian P Anderson and Ma A Kasevich. Macroscopic quantum interference from atomic tunnel arrays. *Science*, 282(5394):1686–1689, 1998.

[61] M Gustavsson, Elmar Haller, MJ Mark, JG Danzl, G Rojas-Kopeinig, and H-C Nägerl. Control of interaction-induced dephasing of Bloch oscillations. *Physical Review Letters*, 100(8):080404, 2008.

[62] Marco Fattori, B Deissler, C D'ERRICO, Mattia Jona-Lasinio, M Modugno, G Roati, L Santos, A Simoni, M Zaccanti, M Inguscio, et al. Atom interferometry with a weakly interacting Bose-Einstein condensate. In *Pushing The Frontiers Of Atomic Physics*, pages 251–262. World Scientific, 2009.

[63] Vanderlei Bagnato, David E Pritchard, and Daniel Kleppner. Bose-Einstein condensation in an external potential. *Physical Review A*, 35(10):4354, 1987.

[64] DA Butts and DS Rokhsar. Trapped Fermi gases. *Physical Review A*, 55(6):4346, 1997.

[65] DC McKay and B DeMarco. Cooling in strongly correlated optical lattices: prospects and challenges. *Reports on Progress in Physics*, 74(5):054401, 2011.

[66] Christina V Kraus and J Ignacio Cirac. Generalized Hartree–Fock theory for interacting fermions in lattices: numerical methods. *New Journal of Physics*, 12(11):113004, 2010.

[67] Ana Maria Rey, Guido Pupillo, and James V Porto. The role of interactions, tunneling, and harmonic confinement on the adiabatic loading of bosons in an optical lattice. *Physical Review A*, 73(2):023608, 2006.

[68] David C Mckay. *Quantum simulation in strongly correlated optical lattices*. University of Illinois at Urbana-Champaign, 2012.

[69] Georg M Bruun and Charles W Clark. Ideal gases in time-dependent traps. *Physical Review A*, 61(6):061601, 2000.

[70] PB Blakie, A Bezett, and P Buonsante. Degenerate Fermi gas in a combined harmonic-lattice potential. *Physical Review A*, 75(6):063609, 2007.

[71] Ana Maria Rey, Guido Pupillo, Charles W Clark, and Carl J Williams. Ultracold atoms confined in an optical lattice plus parabolic potential: A closed-form approach. *Physical Review A*, 72(3):033616, 2005.

[72] Markus Greiner. *Ultracold quantum gases in three-dimensional optical lattice potentials*. PhD thesis, lmu, 2003.

[73] Russell A Hart, Pedro M Duarte, Tsung-Lin Yang, Xinxing Liu, Thereza Paiva, Ehsan Khatami, Richard T Scalettar, Nandini Trivedi, David A Huse, and Randall G Hulet. Observation of antiferromagnetic correlations in the Hubbard model with ultracold atoms. *Nature*, 519(7542):211–214, 2015.

[74] Daniel Greif, Thomas Uehlinger, Gregor Jotzu, Leticia Tarruell, and Tilman Esslinger. Short-range quantum magnetism of ultracold fermions in an optical lattice. *Science*, page 1236362, 2013.

[75] Maxwell F Parsons, Anton Mazurenko, Christie S Chiu, Geoffrey Ji, Daniel Greif, and Markus Greiner. Site-resolved measurement of the spin-correlation function in the Fermi-Hubbard model. *Science*, 353(6305):1253–1256, 2016.

[76] Martin Boll, Timon A Hilker, Guillaume Salomon, Ahmed Omran, Jacopo Nespolo, Lode Pollet, Immanuel Bloch, and Christian Gross. Spin-and density-resolved microscopy of antiferromagnetic correlations in Fermi-Hubbard chains. *Science*, 353(6305):1257–1260, 2016.

[77] Lawrence W Cheuk, Matthew A Nichols, Katherine R Lawrence, Melih Okan, Hao Zhang, Ehsan Khatami, Nandini Trivedi, Thereza Paiva, Marcos Rigol, and Martin W Zwierlein. Observation of spatial charge and spin correlations in the 2d Fermi-Hubbard model. *Science*, 353(6305):1260–1264, 2016.

[78] AA Kordyuk. Pseudogap from arpes experiment: Three gaps in cuprates and topological superconductivity. *Low Temperature Physics*, 41(5):319–341, 2015.

[79] A Kaminski, J Mesot, H Fretwell, JC Campuzano, MR Norman, M Randeria, H Ding, T Sato, T Takahashi, T Mochiku, et al. Quasiparticles in the superconducting state of $Bi_2Sr_2CaCu_2O_{8+\delta}$. *Physical Review Letters*, 84(8):1788, 2000.

[80] 11 VJ Emery and SA Kivelson. Superconductivity in bad metals. *Physical Review Letters*, 74(16):3253, 1995.

[81] Andrea Damascelli, Zahid Hussain, and Zhi-Xun Shen. Angle-resolved photoemission studies of the cuprate superconductors. *Reviews of Modern Physics*, 75(2):473, 2003.

[82] CM Varma, P Be Littlewood, S Schmitt-Rink, E Abrahams, and AE Ruckenstein. Phenomenology of the normal state of cu-o high-temperature superconductors. *Physical Review Letters*, 63(18):1996, 1989.

[83] Nandan Pakhira and Ross H McKenzie. Absence of a quantum limit to charge diffusion in bad metals. *Physical Review B*, 91(7):075124, 2015.

[84] Clifford V Johnson and Peter Steinberg. What black holes teach about strongly coupled particles. *Phys. Today*, 63(5):29–33, 2010.

[85] Thomas Faulkner, Nabil Iqbal, Hong Liu, John McGreevy, and David Vegh. From black holes to strange metals. *arXiv preprint arXiv:1003.1728*, 2010.

[86] Sean A Hartnoll and Andreas Karch. Scaling theory of the cuprate strange metals. *Physical Review B*, 91(15):155126, 2015.

[87] R Jaramillo, Sieu D Ha, DM Silevitch, and Shriram Ramanathan. Origins of bad-metal conductivity and the insulator-metal transition in the rare-earth nickelates. *Nature Physics*, 10(4):304–307, 2014.

[88] Yoav Sagi, Tara E Drake, Rabin Paudel, Roman Chapurin, and Deborah S Jin. Breakdown of the Fermi liquid description for strongly interacting fermions. *Physical Review Letters*, 114(7):075301, 2015.

[89] Chenglin Cao, Ethan Elliott, J Joseph, H Wu, J Petricka, T Schäfer, and JE Thomas. Universal quantum viscosity in a unitary Fermi gas. *Science*, 331(6013):58–61, 2011.

[90] Ariel Sommer, Mark Ku, Giacomo Roati, and Martin W Zwierlein. Universal spin transport in a strongly interacting Fermi gas. *Nature*, 472(7342):201–204, 2011.

[91] DJ Thouless. Relation between the Kubo-Greenwood formula and the Boltzmann equation for electrical conductivity. *Philosophical Magazine*, 32(4):877–879, 1975.

[92] G De Filippis, V Cataudella, A de Candia, AS Mishchenko, and N Nagaosa. Alternative representation of the Kubo formula for the optical conductivity: A shortcut to transport properties. *Physical Review B*, 90(1):014310, 2014.

[93] Gerald D Mahan. *Many-particle physics*. Springer Science & Business Media, 2013.

[94] Philip Warren Anderson. *Basic notions of condensed matter physics*. Benjamin-Cummings, 1984.

[95] Antoine Georges and Thierry Giamarchi. Strongly correlated bosons and fermions in optical lattices. *arXiv preprint arXiv:1308.2684*, 2013.

[96] John J Quinn and Richard A Ferrell. Electron self-energy approach to correlation in a degenerate electron gas. *Physical Review*, 112(3):812, 1958.

[97] JM Luttinger. Analytic properties of single-particle propagators for many-fermion systems. *Physical Review*, 121(4):942, 1961.

[98] Andrew J Schofield. Non-Fermi liquids. *Contemporary Physics*, 40(2):95–115, 1999.

[99] MM Qazilbash, KS Burch, D Whisler, D Shrekenhamer, BG Chae, HT Kim, and DN Basov. Correlated metallic state of vanadium dioxide. *Physical Review B*, 74(20):205118, 2006.

[100] DA Bonn, Ruixing Liang, TM Riseman, DJ Baar, DC Morgan, Kuan Zhang, P Dosanjh, TL Duty, A MacFarlane, GD Morris, et al. Microwave determination of the quasiparticle scattering time in YBa_2 Cu_3 O_6.95. *Physical Review B*, 47(17):11314, 1993.

[101] JAN Bruin, H Sakai, RS Perry, and AP Mackenzie. Similarity of scattering rates in metals showing T-linear resistivity. *Science*, 339(6121):804–807, 2013.

[102] J Vučičević, D Tanasković, MJ Rozenberg, and V Dobrosavljević. Bad-metal behavior reveals Mott quantum criticality in doped Hubbard models. *Physical Review Letters*, 114(24):246402, 2015.

[103] Subir Sachdev and Bernhard Keimer. Quantum criticality. *Phys. Today*, 64(arXiv: 1102.4628):29, 2011.

[104] Thomas Faulkner, Nabil Iqbal, Hong Liu, John McGreevy, and David Vegh. Strange metal transport realized by gauge/gravity duality. *Science*, 329(5995):1043–1047, 2010.

[105] Sean A Hartnoll. Theory of universal incoherent metallic transport. *arXiv preprint arXiv:1405.3651*, 2014.

[106] Hong Liu. From black holes to strange metals. *Physics Today*, 65(6):68, 2012.

[107] AF Ioffe and AR Regel. Non-crystalline, amorphous and liquid electronic semiconductors. *Prog. Semicond*, 4:237–291, 1960.

[108] NF Mott. Conduction in non-crystalline systems ix. the minimum metallic conductivity. *Philosophical Magazine*, 26(4):1015–1026, 1972.

[109] O Gunnarsson, M Calandra, and JE Han. Colloquium: Saturation of electrical resistivity. *Reviews of Modern Physics*, 75(4):1085, 2003.

[110] NE Hussey?, K Takenaka, and H Takagi. Universality of the Mott–Ioffe–Regel limit in metals. *Philosophical Magazine*, 84(27):2847–2864, 2004.

[111] Christopher J Foot. *Atomic physics*, volume 7. Oxford University Press, 2005.

[112] D Chen, C Meldgin, and Bryan DeMarco. Bath-induced band decay of a Hubbard lattice gas. *Physical Review A*, 90(1):013602, 2014.

[113] B DeMarco, SB Papp, and DS Jin. Pauli blocking of collisions in a quantum degenerate atomic Fermi gas. *Physical Review Letters*, 86(24):5409, 2001.

[114] B DeMarco and Deborah S Jin. Spin excitations in a Fermi gas of atoms. *Physical Review Letters*, 88(4):040405, 2002.

[115] David C McKay, Carolyn Meldgin, David Chen, and Brian DeMarco. Slow thermalization between a lattice and free Bose gas. *Physical Review Letters*, 111(6):063002, 2013.

[116] Walter Metzner and Dieter Vollhardt. Correlated lattice fermions in d=8 dimensions. *Physical Review Letters*, 62(3):324, 1989.

[117] Gabriel Kotliar and Dieter Vollhardt. Strongly correlated materials: Insights from dynamical mean-field theory. *Physics today*, 57(3):53–60, 2004.

[118] Martin Eckstein, Marcus Kollar, Krzysztof Byczuk, and Dieter Vollhardt. Hopping on the Bethe lattice: Exact results for densities of states and dynamical mean-field theory. *Physical Review B*, 71(23):235119, 2005.

[119] Antoine Georges and Gabriel Kotliar. Hubbard model in infinite dimensions. *Physical Review B*, 45(12):6479, 1992.

[120] Olivier Parcollet, Michel Ferrero, Thomas Ayral, Hartmut Hafermann, Igor Krivenko, Laura Messio, and Priyanka Seth. Triqs: A toolbox for research on interacting quantum systems. *Computer Physics Communications*, 196:398–415, 2015.

[121] Markus Aichhorn, Leonid Pourovskii, Priyanka Seth, Veronica Vildosola, Manuel Zingl, Oleg E Peil, Xiaoyu Deng, Jernej Mravlje, Gernot J Kraberger, Cyril Martins, et al. Triqs/dfttools: A TRIQS application for ab initio calculations of correlated materials. *Computer Physics Communications*, 204:200–208, 2016.

[122] Henrik Kajueter and Gabriel Kotliar. New iterative perturbation scheme for lattice models with arbitrary filling. *Physical Review Letters*, 77(1):131, 1996.

[123] Xiaoyu Deng, Jernej Mravlje, Michel Ferrero, Gabriel Kotliar, Antoine Georges, et al. How bad metals turn good: spectroscopic signatures of resilient quasiparticles. *Physical Review Letters*, 110(8):086401, 2013.

[124] M Jarrell and Th Pruschke. Anomalous properties of the Hubbard model in infinite dimensions. *Physical Review B*, 49(2):1458, 1994.

[125] Alexander L Gaunt, Tobias F Schmidutz, Igor Gotlibovych, Robert P Smith, and Zoran Hadzibabic. Bose-Einstein condensation of atoms in a uniform potential. *Physical Review Letters*, 110(20):200406, 2013.

[126] Biswaroop Mukherjee, Zhenjie Yan, Parth B Patel, Zoran Hadzibabic, Tarik Yefsah, Julian Struck, and Martin W Zwierlein. Homogeneous atomic Fermi gases. *Physical Review Letters*, 118(12):123401, 2017.

[127] SS Kondov, WR McGehee, W Xu, and B DeMarco. Disorder-induced localization in a strongly correlated atomic Hubbard gas. *Physical Review Letters*, 114(8):083002, 2015.

[128] Kenneth Günter, Thilo Stöferle, Henning Moritz, Michael Köhl, and Tilman Esslinger. Bose-Fermi mixtures in a three-dimensional optical lattice. *Physical Review Letters*, 96(18):180402, 2006.

[129] André Eckardt. Colloquium: Atomic quantum gases in periodically driven optical lattices. *Rev. Mod. Phys.*, 89:011004, Mar 2017.

[130] Colin V Parker, Li-Chung Ha, and Cheng Chin. Direct observation of effective ferromagnetic domains of cold atoms in a shaken optical lattice. *Nature Physics*, 9(12):769–774, 2013.

[131] Julian Struck, Christoph Ölschläger, R Le Targat, Parvis Soltan-Panahi, André Eckardt, Maciej Lewenstein, Patrick Windpassinger, and Klaus Sengstock. Quantum simulation of frustrated classical magnetism in triangular optical lattices. *Science*, 333(6045):996–999, 2011.

[132] Julian Struck, Christoph Ölschläger, Malte Weinberg, Philipp Hauke, Juliette Simonet, André Eckardt, Maciej Lewenstein, Klaus Sengstock, and Patrick Windpassinger. Tunable gauge potential for neutral and spinless particles in driven optical lattices. *Physical Review Letters*, 108(22):225304, 2012.

[133] John Hubbard. Electron correlations in narrow energy bands. In *Proceedings of the Royal Society of London A: Mathematical, Physical and Engineering Sciences*, volume 276, pages 238–257. The Royal Society, 1963.

[134] JE Hirsch. Bond-charge repulsion and hole superconductivity. *Physica C: Superconductivity*, 158(3):326–336, 1989.

[135] Wilfred G Van der Wiel, Silvano De Franceschi, Jeroen M Elzerman, Toshimasa Fujisawa, Seigo Tarucha, and Leo P Kouwenhoven. Electron transport through double quantum dots. *Reviews of Modern Physics*, 75(1):1, 2002.

[136] S Greschner, G Sun, D Poletti, and L Santos. Density-dependent synthetic gauge fields using periodically modulated interactions. *Physical Review Letters*, 113(21):215303, 2014.

[137] Ákos Rapp, Xiaolong Deng, and Luis Santos. Ultracold lattice gases with periodically modulated interactions. *Physical Review Letters*, 109(20):203005, 2012.

[138] Sebastian Greschner and Luis Santos. Anyon hubbard model in one-dimensional optical lattices. *Physical Review Letters*, 115(5):053002, 2015.

[139] Ruichao Ma, M Eric Tai, Philipp M Preiss, Waseem S Bakr, Jonathan Simon, and Markus Greiner. Photon-assisted tunneling in a biased strongly correlated Bose gas. *Physical Review Letters*, 107(9):095301, 2011.

[140] Florian Meinert, Manfred J Mark, Katharina Lauber, Andrew J Daley, and H-C Nägerl. Floquet engineering of correlated tunneling in the Bose-Hubbard model with ultracold atoms. *Physical Review Letters*, 116(20):205301, 2016.

[141] Alejandro Bermudez and Diego Porras. Interaction-dependent photon-assisted tunneling in optical lattices: a quantum simulator of strongly-correlated electrons and dynamical gauge fields. *New Journal of Physics*, 17(10):103021, 2015.

[142] Guifre Vidal. Classical simulation of infinite-size quantum lattice systems in one spatial dimension. *Physical Review Letters*, 98(7):070201, 2007.

[143] Mateusz Lkacki, Dominique Delande, and Jakub Zakrzewski. Numerical computation of dynamically important excited states of many-body systems. *Physical Review A*, 86(1):013602, 2012.

[144] Nicolas Schlosser, Georges Reymond, Igor Protsenko, and Philippe Grangier. Sub-poissonian loading of single atoms in a microscopic dipole trap. *Nature*, 411(6841):1024, 2001.

[145] Marshall T DePue, Colin McCormick, S Lukman Winoto, Steven Oliver, and David S Weiss. Unity occupation of sites in a 3d optical lattice. *Physical Review Letters*, 82(11):2262, 1999.

[146] Brian J Lester, Niclas Luick, Adam M Kaufman, Collin M Reynolds, and Cindy A Regal. Rapid production of uniformly filled arrays of neutral atoms. *Physical Review Letters*, 115(7):073003, 2015.

[147] Waseem S Bakr, Jonathon I Gillen, Amy Peng, Simon Fölling, and Markus Greiner. A quantum gas microscope for detecting single atoms in a Hubbard-regime optical lattice. *Nature*, 462(7269):74, 2009.

[148] A Fuhrmanek, R Bourgain, Yvan RP Sortais, and A Browaeys. Light-assisted collisions between a few cold atoms in a microscopic dipole trap. *Physical Review A*, 85(6):062708, 2012.

[149] Sun Kyung Lee and Hai-Woong Lee. Damped population oscillation in a spontaneously decaying two-level atom coupled to a monochromatic field. *Physical Review A*, 74(6):063817, 2006.

[150] D Jaksch, H-J Briegel, JI Cirac, CW Gardiner, and P Zoller. Entanglement of atoms via cold controlled collisions. *Physical Review Letters*, 82(9):1975, 1999.

[151] Gregor Jotzu, Michael Messer, Frederik Görg, Daniel Greif, Rémi Desbuquois, and Tilman Esslinger. Creating state-dependent lattices for ultracold fermions by magnetic gradient modulation. *Physical Review Letters*, 115(7):073002, 2015.

[152] Alexey V. Gorshkov, Salvatore R. Manmana, Gang Chen, Jun Ye, Eugene Demler, Mikhail D. Lukin, and Ana Maria Rey. Tunable superfluidity and quantum magnetism with ultracold polar molecules. *Phys. Rev. Lett.*, 107:115301, Sep 2011.

[153] N. R. Cooper and G. V. Shlyapnikov. Stable topological superfluid phase of ultracold polar fermionic molecules. *Phys. Rev. Lett.*, 103:155302, Oct 2009.

[154] RMW van Bijnen and T Pohl. Quantum magnetism and topological ordering via Rydberg dressing near Förster resonances. *Physical Review Letters*, 114(24):243002, 2015.

[155] Alexander W Glaetzle, Marcello Dalmonte, Rejish Nath, Christian Gross, Immanuel Bloch, and Peter Zoller. Designing frustrated quantum magnets with laser-dressed Rydberg atoms. *Physical Review Letters*, 114(17):173002, 2015.

[156] Andrew C Potter, Erez Berg, Daw-Wei Wang, Bertrand I Halperin, and Eugene Demler. Superfluidity and dimerization in a multilayered system of fermionic polar molecules. *Physical Review Letters*, 105(22):220406, 2010.

[157] K.-K. Ni, S. Ospelkaus, M. H. G. de Miranda, A. Pe'er, B. Neyenhuis, J. J. Zirbel, S. Kotochigova, P. S. Julienne, D. S. Jin, and J. Ye. A high phase-space-density gas of polar molecules. *Science*, 322(5899):231–235, 2008.

[158] Steven A Moses, Jacob P Covey, Matthew T Miecnikowski, Bo Yan, Bryce Gadway, Jun Ye, and Deborah S Jin. Creation of a low-entropy quantum gas of polar molecules in an optical lattice. *Science*, 350(6261):659–662, 2015.

[159] Mingwu Lu, Nathaniel Q Burdick, and Benjamin L Lev. Quantum degenerate dipolar Fermi gas. *Physical Review Letters*, 108(21):215301, 2012.

[160] Jürgen Stuhler, Axel Griesmaier, Tobias Koch, Marco Fattori, Tilman Pfau, Stefano Giovanazzi, Paolo Pedri, and Luis Santos. Observation of dipole-dipole interaction in a degenerate quantum gas. *Physical Review Letters*, 95(15):150406, 2005.

[161] K Aikawa, A Frisch, M Mark, S Baier, A Rietzler, R Grimm, and F Ferlaino. Bose-Einstein condensation of erbium. *Physical Review Letters*, 108(21):210401, 2012.

[162] Igor Ferrier-Barbut, Holger Kadau, Matthias Schmitt, Matthias Wenzel, and Tilman Pfau. Observation of quantum droplets in a strongly dipolar Bose gas. *Physical Review Letters*, 116(21):215301, 2016.

[163] Kristian Baumann, Christine Guerlin, Ferdinand Brennecke, and Tilman Esslinger. Dicke quantum phase transition with a superfluid gas in an optical cavity. *Nature*, 464(7293):1301–1306, 2010.

[164] Julian Léonard, Andrea Morales, Philip Zupancic, Tilman Esslinger, and Tobias Donner. Supersolid formation in a quantum gas breaking a continuous translational symmetry. *Nature*, 543(7643):87–90, 2017.

[165] RF Stebbings and FB Dunning. *Rydberg states of atoms and molecules*. Cambridge University Press, 1983.

[166] Mark Saffman, TG Walker, and Klaus Mølmer. Quantum information with Rydberg atoms. *Reviews of Modern Physics*, 82(3):2313, 2010.

[167] L Isenhower, E Urban, XL Zhang, AT Gill, T Henage, TA Johnson, TG Walker, and M Saffman. Demonstration of a neutral atom controlled-not quantum gate. *Physical Review Letters*, 104(1):010503, 2010.

[168] Etienne Brion, Klaus Mølmer, and Mark Saffman. Quantum computing with collective ensembles of multilevel systems. *Physical Review Letters*, 99(26):260501, 2007.

[169] M Viteau, MG Bason, J Radogostowicz, N Malossi, D Ciampini, O Morsch, and E Arimondo. Rydberg excitations in Bose-Einstein condensates in quasi-one-dimensional potentials and optical lattices. *Physical Review Letters*, 107(6):060402, 2011.

[170] Peter Schauß, Marc Cheneau, Manuel Endres, Takeshi Fukuhara, Sebastian Hild, Ahmed Omran, Thomas Pohl, Christian Gross, Stefan Kuhr, and Immanuel Bloch. Observation of spatially ordered structures in a two-dimensional Rydberg gas. *Nature*, 491(7422):87–91, 2012.

[171] Henning Labuhn, Daniel Barredo, Sylvain Ravets, Sylvain De Léséleuc, Tommaso Macrì, Thierry Lahaye, and Antoine Browaeys. Tunable two-dimensional arrays of single Rydberg atoms for realizing quantum Ising models. *Nature*, 534(7609):667–670, 2016.

[172] Hannes Bernien, Sylvain Schwartz, Alexander Keesling, Harry Levine, Ahmed Omran, Hannes Pichler, Soonwon Choi, Alexander S Zibrov, Manuel Endres, Markus Greiner, et al. Probing many-body dynamics on a 51-atom quantum simulator. *arXiv preprint arXiv:1707.04344*, 2017.

[173] Constantine E Theodosiou. Lifetimes of alkali-metalatom Rydberg states. *Physical Review A*, 30(6):2881, 1984.

[174] T. Macrìand T. Pohl. Rydberg dressing of atoms in optical lattices. *Phys. Rev. A*, 89:011402, Jan 2014.

[175] JE Johnson and SL Rolston. Interactions between Rydberg-dressed atoms. *Physical Review A*, 82(3):033412, 2010.

[176] JE Hirsch. Charge-density-wave to spin-density-wave transition in the extended hubbard model. *Physical Review Letters*, 53(24):2327, 1984.

[177] Jens Honer, Hendrik Weimer, Tilman Pfau, and Hans Peter Büchler. Collective many-body interaction in Rydberg dressed atoms. *Physical Review Letters*, 105(16):160404, 2010.

[178] Alexander W Glaetzle, Marcello Dalmonte, Rejish Nath, Ioannis Rousochatzakis, Roderich Moessner, and Peter Zoller. Quantum spin-ice and dimer models with Rydberg atoms. *Physical Review X*, 4(4):041037, 2014.

[179] Johannes Zeiher, Rick Van Bijnen, Peter Schauß, Sebastian Hild, Jae-yoon Choi, Thomas Pohl, Immanuel Bloch, and Christian Gross. Many-body interferometry of a Rydberg-dressed spin lattice. *Nature Physics*, 12(12):1095, 2016.

[180] Jonathan B Balewski, Alexander T Krupp, Anita Gaj, Sebastian Hofferberth, Robert Löw, and Tilman Pfau. Rydberg dressing: understanding of collective many-body effects and implications for experiments. *New Journal of Physics*, 16(6):063012, 2014.

[181] EA Goldschmidt, T Boulier, RC Brown, SB Koller, JT Young, AV Gorshkov, SL Rolston, and JV Porto. Anomalous broadening in driven dissipative Rydberg systems. *Physical Review Letters*, 116(11):113001, 2016.

[182] N Malossi, MM Valado, S Scotto, P Huillery, P Pillet, D Ciampini, E Arimondo, and O Morsch. Full counting statistics and phase diagram of a dissipative Rydberg gas. *Physical Review Letters*, 113(2):023006, 2014.

[183] H Schempp, G Günter, M Robert-de Saint-Vincent, CS Hofmann, D Breyel, A Komnik, DW Schönleber, Martin Gärttner, Jörg Evers, S Whitlock, et al. Full counting statistics of laser excited Rydberg aggregates in a one-dimensional geometry. *Physical Review Letters*, 112(1):013002, 2014.

[184] C Gaul, BJ DeSalvo, JA Aman, FB Dunning, TC Killian, and T Pohl. Resonant Rydberg dressing of alkaline-earth atoms via electromagnetically induced transparency. *Physical Review Letters*, 116(24):243001, 2016.

[185] JA Aman, BJ DeSalvo, FB Dunning, TC Killian, S Yoshida, and J Burgdörfer. Trap losses induced by near-resonant Rydberg dressing of cold atomic gases. *Physical Review A*, 93(4):043425, 2016.

[186] Y-Y Jau, AM Hankin, T Keating, IH Deutsch, and GW Biedermann. Entangling atomic spins with a Rydberg-dressed spin-flip blockade. *Nature Physics*, 12(1):71–74, 2016.

[187] A Derevianko, JF Babb, and A Dalgarno. High-precision calculations of van der waals coefficients for heteronuclear alkali-metal dimers. *Physical Review A*, 63(5):052704, 2001.

[188] Myron L Zimmerman, Michael G Littman, Michael M Kash, and Daniel Kleppner. Stark structure of the Rydberg states of alkali-metal atoms. *Physical Review A*, 20(6):2251, 1979.

[189] Jonathan D Pritchard. *Cooperative Optical Non-linearity in a blockaded Rydberg ensemble*. Springer Science & Business Media, 2012.

[190] Thomas F Gallagher. *Rydberg atoms*, volume 3. Cambridge University Press, 2005.

[191] Xinghong He, Baiwen Li, Aiqiu Chen, and Chengxiu Zhang. Model-potential calculation of lifetimes of Rydberg states of alkali atoms. *Journal of Physics B: Atomic, Molecular and Optical Physics*, 23(4):661, 1990.

[192] Robert Löw, Hendrik Weimer, Johannes Nipper, Jonathan B Balewski, Björn Butscher, Hans Peter Büchler, and Tilman Pfau. An experimental and theoretical guide to strongly interacting Rydberg gases. *Journal of Physics B: Atomic, Molecular and Optical Physics*, 45(11):113001, 2012.

[193] M Marinescu, HR Sadeghpour, and A Dalgarno. Dispersion coefficients for alkali-metal dimers. *Physical Review A*, 49(2):982, 1994.

[194] Kilian Singer, Jovica Stanojevic, Matthias Weidemüller, and Robin Côté. Long-range interactions between alkali Rydberg atom pairs correlated to the ns–ns, np–np and nd–nd asymptotes. *Journal of Physics B: Atomic, Molecular and Optical Physics*, 38(2):S295, 2005.

[195] D Jaksch, JI Cirac, P Zoller, SL Rolston, R Côté, and MD Lukin. Fast quantum gates for neutral atoms. *Physical Review Letters*, 85(10):2208, 2000.

[196] MD Lukin, M Fleischhauer, R Cote, LM Duan, D Jaksch, JI Cirac, and P Zoller. Dipole blockade and quantum information processing in mesoscopic atomic ensembles. *Physical Review Letters*, 87(3):037901, 2001.

[197] C-J Lorenzen, K Niemax, and LR Pendrill. Precise measurement of 39k ns and nd energy levels with an evacuated wavemeter. *Optics Communications*, 39(6):370–374, 1981.

[198] Ying Wu and Xiaoxue Yang. Effective two-level model for a three-level atom in the ξ configuration. *Physical Review A*, 56(3):2443, 1997.

[199] Alexandra Behrle, Marco Koschorreck, and Michael Köhl. Isotope shift and hyperfine splitting of the 4 s→5 p transition in potassium. *Physical Review A*, 83(5):052507, 2011.

[200] C-J Lorenzen, K Niemax, and LR Pendrill. Precise measurements of 39k ns and nd energy levels with an evaluated wavemeter. *Optics Communications*, 39(6):370–374, 1981.

[201] I Johansson and N Svendenius. An intensity problem in the spectrum of potassium. *Physica Scripta*, 5(3):129, 1972.

[202] Michael Fleischhauer, Atac Imamoglu, and Jonathan P Marangos. Electromagnetically induced transparency: Optics in coherent media. *Reviews of Modern Physics*, 77(2):633, 2005.

[203] Alexandra Behrle, Marco Koschorreck, and Michael Köhl. Isotope shift and hyperfine splitting of the 4 s→5 p transition in potassium. *Physical Review A*, 83(5):052507, 2011.

[204] K Niemax and LR Pendrill. Isotope shifts of individual nS and nD levels of atomic potassium. *Journal of Physics B: Atomic and Molecular Physics*, 13(15):L461, 1980.

[205] LR Pendrill and K Niemax. Isotope shifts of energy levels in 40K and 39K. *Journal of Physics B: Atomic and Molecular Physics*, 15(5):L147, 1982.

[206] Markus Mack, Florian Karlewski, Helge Hattermann, Simone Höckh, Florian Jessen, Daniel Cano, and József Fortágh. Measurement of absolute transition frequencies of Rb 87 to nS and nD Rydberg states by means of electromagnetically induced transparency. *Physical Review A*, 83(5):052515, 2011.

[207] AK Mohapatra, TR Jackson, and CS Adams. Coherent optical detection of highly excited Rydberg states using electromagnetically induced transparency. *Physical Review Letters*, 98(11):113003, 2007.

[208] Atreju Tauschinsky, Richard Newell, HB van Linden van den Heuvell, and RJC Spreeuw. Measurement of 87 Rb Rydberg-state hyperfine splitting in a room-temperature vapor cell. *Physical Review A*, 87(4):042522, 2013.

[209] KJ Weatherill, JD Pritchard, RP Abel, MG Bason, AK Mohapatra, and CS Adams. Electromagnetically induced transparency of an interacting cold Rydberg ensemble. *Journal of Physics B: Atomic, Molecular and Optical Physics*, 41(20):201002, 2008.

[210] JD Pritchard, D Maxwell, Alexandre Gauguet, KJ Weatherill, MPA Jones, and CS Adams. Cooperative atom-light interaction in a blockaded Rydberg ensemble. *Physical Review Letters*, 105(19):193603, 2010.

[211] Julio Gea-Banacloche, Yong-qing Li, Shao-zheng Jin, and Min Xiao. Electromagnetically induced transparency in ladder-type inhomogeneously broadened media: Theory and experiment. *Physical Review A*, 51(1):576, 1995.

[212] JR Boon, E Zekou, D McGloin, and MH Dunn. Comparison of wavelength dependence in cascade-, λ-, and vee-type schemes for electromagnetically induced transparency. *Physical Review A*, 59(6):4675, 1999.

[213] A Urvoy, C Carr, R Ritter, CS Adams, KJ Weatherill, and R Löw. Optical coherences and wavelength mismatch in ladder systems. *Journal of Physics B: Atomic, Molecular and Optical Physics*, 46(24):245001, 2013.

[214] Jean E Sansonetti. Wavelengths, transition probabilities, and energy levels for the spectra of potassium (ki through k xix). *Journal of Physical and Chemical Reference Data*, 37(1):7–96, 2008.

[215] Gary C Bjorklund, MD Levenson, W Lenth, and C Ortiz. Frequency modulation (FM) spectroscopy. *Applied Physics B: Lasers and Optics*, 32(3):145–152, 1983.

[216] I Johansson and N Svendenius. An intensity problem in the spectrum of potassium. *Physica Scripta*, 5(3):129, 1972.

[217] E Arimondo, M Inguscio, and P Violino. Experimental determinations of the hyperfine structure in the alkali atoms. *Reviews of Modern Physics*, 49(1):31, 1977.

[218] A. Kramida, Yu. Ralchenko, J. Reader, and and NIST ASD Team. NIST Atomic Spectra Database (ver. 5.5.3), [Online]. Available: `https://physics.nist.gov/asd` [2018, March 19]. National Institute of Standards and Technology, Gaithersburg, MD., 2018.

Appendix A

3D matrix for calculating band structures

```
function m=blochmatrix3d_2(qx,qy,qz,Vx,Vy,Vz)
global trunc

% structure of H matrix
%-|-----------------kx=-1-------------------------|------kx=0----|----kx=1-----
% |----ky=-1------|-----ky=0-----  |-----  ky=-1----|  ..............
% |kz=-1,kz=0,kz=1|kz=-1,kz=0,kz=1|kz=-1,kz=0,kz=1|  ..............



m=zeros(trunc^3,trunc^3);


for l=1:trunc*trunc*trunc

% convert matrix indices labeling to quasimomentum labeling along x, y and z.
    if floor(l/(trunc*trunc))==l/(trunc*trunc) && l~=0
        index_x = floor(l/(trunc*trunc))-1;
    else
        index_x = floor(l/(trunc*trunc));
    end

    if floor((l-index_x*trunc*trunc)/trunc)==...
            (l-index_x*trunc*trunc)/trunc && l~=0
        index_y = floor((l-index_x*trunc*trunc)/trunc)-1;
    else
        index_y = floor((l-index_x*trunc*trunc)/trunc);
    end

    index_z = l-index_x*trunc*trunc-index_y*trunc-1;

    index_x = index_x-floor(trunc/2);
    index_y = index_y-floor(trunc/2);
    index_z = index_z-floor(trunc/2);

% construct diagonal terms in H
    m(l,l) = (2.*(index_x)+qx)^2+...
        (2.*(index_y)+qy)^2+...
        (2.*(index_z)+qz)^2;

% off-diagonal terms along z
    if l<trunc*trunc*trunc && mod(l,trunc) ~= 0
        m(l+1,l)=-Vz/4.;
        m(l,l+1)=-Vz/4.;
    end
end

% off-diagonal terms along y
for l=1:trunc*trunc-1
    for ll=1:trunc
```

```
51          if mod(l,trunc) ~= 0
52              m(l*trunc+ll,(l-1)*trunc+ll)=-Vy/4;
53              m((l-1)*trunc+ll,l*trunc+ll)= -Vy/4;
54          end
55
56      end
57  end
58
59  % off-diagonal terms along x
60  for l=1:trunc-1
61      for ll=1:trunc*trunc
62          m(l*trunc*trunc+ll,(l-1)*trunc*trunc+ll)= -Vx/4.;
63          m((l-1)*trunc*trunc+ll,l*trunc*trunc+ll)= -Vx/4.;
64      end
65  end
```

Appendix B

EIT measurement

```
format short
close all

% add analog output channel (applied on piezo) and digital input channel (reading out wavelength)
ao=analogoutput('nidaq','Dev1');
ochan=addchannel(ao,0);
ai=analoginput('nidaq','Dev1');
ichan=addchannel(ai,0);

set(ai,'SampleRate',10000);

libName='BristolLibrary';

libLoaded = libisloaded(libName);
if(libLoaded)
    unloadlibrary(libName)
end

f0=303240.44;

loadlibrary('CLDevIface.dll','cldevdll.h','alias',libName);
BristolDevHandle = calllib(libName,'CLOpenUSBSerialDevice',8);
test = calllib(libName,'CLSetLambdaUnits',BristolDevHandle,1);
test=calllib(libName,'CLSetMedium',BristolDevHandle,0);

f1=figure
hold on
f2=figure
hold on


aa=1;

inavg=zeros(1,aa);
lavg=zeros(1,aa);
bavg=zeros(1,aa);

vbegin=0.025;  %0.073
vend=0.05;     %0.3
vsteps=800; %10000

dv=(vend-vbegin)/vsteps;


volt=vbegin;

nn=vsteps;

idata=zeros(1,nn);
ldata=zeros(1,nn);
```

```
ebar=zeros(1,nn);
lbar=zeros(1,nn);
base=zeros(1,nn);

% apply a voltage on piezo
putsample(ao,volt);
pause(0.5);

i=1;
count=1;

basecounts=10;
% scan voltage of piezo
while volt<vend

    if count==basecounts

        test=calllib(libName,'CLGetLambdaReading',BristolDevHandle);
        test-f0
        ldata(i-basecounts+1:i-1)=test;
         count=1;


    end

     putsample(ao,volt);
     volt=volt+dv;
     pause(0.010);

    for j=1:aa

     inavg(j)=getsample(ai);   % read the wavelength

    end


    idata(i)=mean(inavg);
    ebar(i)=std(inavg);


    i=i+1;
    count=count+1;

end

test = calllib(libName,'CLCloseDevice',BristolDevHandle)
unloadlibrary(libName)
delete(ao)
clear ao
print('done.')

%% delete the device
test = calllib(libName,'CLCloseDevice',BristolDevHandle)
unloadlibrary(libName)
delete(ao)
clear ao
print('done.')
```

Appendix C

Simulating atom removal

```
% 2017/9/19 Wenchao Xu

% Code for counting the number of doublon pairs after number removing
% procedure
% The first part used William R McGehee's code to get the temperature and
% chemical potential in optical lattices. I added some comments to help
% understanding.


% load S/N as a function of T/T_F data
load('Z:\Pubs\William R. McGehee\wrm_thesis\matlab\totf_to_son.mat')
polyx=totf_to_son(:,1);
polyy=totf_to_son(:,2);
sntotf=spline(polyx,polyy);

% To get the entropy at konwn T/TF:
% ppval(sntotf,0.15)

%% do non-interacting thermodynamics for lattice

%%%%
% Sampling q space for integration over reciprocal lattice space
npoints = 5000000;
cosq = 3-sum(cos(pi*(1-2*rand(npoints,3))),2);
% cosq: sampling the momentum space, and getting the distribution of energy
% the range of cosq is from [0,6]
nq = 100;
cosq_vals = linspace(0,6,nq);
% cosq_vals: it deals with ENERGY, not momentum.
% It should cover the SAME range as cosq, not from 0 to 2pi!
cosq_prob = hist(cosq(),cosq_vals);
% make a histgram. It is the density of states with lattice dispersion
cosq_prob = cosq_prob/npoints;
% cosq_prob transfers the integral over q to dE \rho(E), with
% \rho(E) as density-of-state.
% It needs to be renormalized to 1, because integrating over q:
% (1/\pi)^3 \int \d^3 q, with q from -pi to pi, gives 1

% Sampling x space for integrating over positions
rmax = 60;
nr = 60+1;
xlist = linspace(0,rmax,nr);
rprob = 4*pi*(rmax/nr)*linspace(0,rmax,nr).^2;
% rprob is 4 pi r^2 dr

%
[qprob,xprob] = meshgrid(cosq_prob,rprob);
[qval, xval] = meshgrid(cosq_vals,xlist);
% this generates a "phase space" in kinetic energy (lattice) and position
% qprob: the possibility that kinetic energy equals to cosq_vals.
```

```
51
52  %convert all to columns
53  qval = qval(:);
54  xval = xval(:);
55  qprob = qprob(:);
56  xprob = xprob(:);
57
58  %A test for this methor. Mathematica gives 5605
59  %t = 0.0395;
60  %gamma = 3.71e-08 * (112.8)^2;
61  %sum(qprob.*xprob.*1./(...
62  %         exp((2*t*qval+gamma*xval.^2-4.78*t)./(1.48*t))+1))
63
64
65  %% do some thermodynamic calculatoins, to get T and mu in lattice
66
67  % t = 0.0862; %s = 4ER
68  %t = 0.0395;  %s= 7ER
69  t = 0.0308; %s= 8ER
70  %t = 0.01919; %s=10ER
71  gamma = 3.71e-08 * (118)^2; % in units of ER per lattice site^2. 118HZ: 8ER
72  %gamma = 3.71e-08 * (100)^2; %100Hz, 4ER
73  gridpoints = 80;
74  [TT,mumu] = meshgrid(linspace(0,0.3,gridpoints),linspace(0.01,1,gridpoints));
75  TT_col = TT(:);
76  mumu_col = mumu(:);
77
78  entropy_mc = zeros(size(TT_col));
79  number_mc = zeros(size(TT_col));
80  for i = 1:numel(TT),
81      T = TT_col(i);
82      mu = mumu_col(i);
83      number_mc(i) = sum(qprob.*xprob.*1./(...
84          exp((2*t*qval+gamma*xval.^2-mu)./T)+1));
85      entropy_mc(i) = sum(qprob.*xprob.*(log(1+exp((mu-2*t*qval-gamma*xval.^2)./T))...
86          -((mu-2*t*qval-gamma*xval.^2)./T).*...
87          (1./(exp(-1*(mu-2*t*qval-gamma*xval.^2)./T)+1))));
88  end
89  entropy_mc = reshape(entropy_mc,size(TT));
90  number_mc = reshape(number_mc,size(TT));
91
92  %% number and entropy matching
93  number_constraint = 61000;
94  entropy_constraint = 2.89;
95
96  fracerror = abs(number_mc-number_constraint)/number_constraint+...
97      abs(((entropy_mc./number_mc)-entropy_constraint)/entropy_constraint);
98  fracerror = fracerror(:);
99
100 [x,indx] = min(fracerror);
101 T = TT_col(indx);
102 mu = mumu_col(indx);
103 [T,mu,entropy_constraint,number_constraint/1000,T/t,mu/t]'
104
105 %% double check the number & entropy
106 % If the matching is poor, may try increase the gridpoints
107
108 num = sum(qprob.*xprob.*1./(...
109         exp((2*t*qval+gamma*xval.^2-mu)./T)+1))
110
111 entropy_mc = sum(qprob.*xprob.*(log(1+exp((mu-2*t*qval-gamma*xval.^2)./T))...
112         -((mu-2*t*qval-gamma*xval.^2)./T).*...
113         (1./(exp(-1*(mu-2*t*qval-gamma*xval.^2)./T)+1))));
114
```

```
entropy_mc/num



%% generate the distribution of atoms in real space
[x,y,z]=meshgrid(-50:1:50,-50:1:50,-50:1:50);
nr = @(nx,ny,nz) sum(cosq_prob.*1./(...
        exp((2*t*cosq_vals+gamma*(nx.^2+ny.^2+nz.^2)-mu)./T)+1));

% generate distribution in 3D real space
a = zeros(101,101,101);
for i = 1:1:101
    for j = 1:1:101
        for k = 1:1:101
            a(i,j,k)=nr(i-50,j-50,k-50);
        end
    end
end

sum(sum(sum(a)))   % number check
imagewrm(a(:,:,51))
colorbar
caxis([0,1])
%% counting the number of pairs at various removal fraction
close all

% check initial occupation
ini = rand([length(x),length(x),length(x)]);
ini = (a>ini);
imagewrm(double(ini(:,:,51)))
colorbar
colorbar('off')
set(gca,'XTick',[])
set(gca,'YTick',[])
colormap([1 1 1; 0.1 0.1 0.1])
caxis([0,1])

% make a plot for given mu,T, and vary p
data = [];
% for a large enough region, where no atom at the boundary, the
% length(tar)-1 shouldn't cost underestimate counting of pairs.
%tar = tar;
for p=0:0.05:1.0   % removal fraction
    count = 0;

    %generate initial occupation
    ini = rand([length(x),length(x),length(x)]);
    ini = (a>ini);

    % remove some depends on the propobility
    remove = rand([length(x),length(x),length(x)]);
    fin = ini.*double(remove>p);
    %fin: distribution of atoms after number reduction
    tar = fin;
    for i = 1:length(tar)-1
        for j = 1:length(tar)-1
            for k = 1:length(tar)-1
                if tar(i,j,k)==1
                    if tar(i,j,k+1)==1
                        tar(i,j,k)=0;
                        tar(i,j,k+1)=0;
                        count = count+1;
                    elseif tar(i,j+1,k)==1
                        tar(i,j,k)=0;
```

```
                        tar(i,j+1,k)=0;
                        count = count+1;
                    elseif tar(i+1,j,k)==1
                        tar(i,j,k)=0;
                        tar(i+1,j,k)=0;
                        count = count+1;
                    end
                end
            end
        end
    end
    % above loops: count number of pairs. A pair is removed after counting.
    data = cat(1,data,[p,count/sum(sum(sum(fin)))]);
    % count/sum(sum(sum(fin))): max number of possible doublons/total number
    % of atoms after removal procedure.
end
```